VOLUME 80 JUNE 17, 1976 NUMBER 13

JPCHAx

THE JOURNAL OF PHYSICAL CHEMISTRY

PUBLISHED BIWEEKLY BY THE AMERICAN CHEMICAL SOCIETY

THE JOURNAL OF

PHYSICAL CHEMISTRY

Published by the
AMERICAN CHEMICAL SOCIETY
BOOKS AND JOURNALS DIVISION
D. H. Michael Bowen, Director

Editorial Department: Charles R. Bertsch, Head; Marianne C. Brogan, Associate Head; Celia B. McFarland, Joseph E. Yurvati, Assistant Editors
Graphics and Production Department: Bacil Guiley, Head
Research and Development Department: Seldon W. Terrant, Head

Advertising Office: Centcom, Ltd., 50 W. State St., Westport, Conn. 06880.

Published biweekly by the American Chemical Society at 20th and Northampton Sts., Easton, Pennsylvania 18042. Second class postage paid at Washington, D.C. and at additional mailing offices.

Editorial Information

Instructions for authors are printed in the first issue of each volume. Please conform to these instructions when submitting manuscripts.

Manuscripts for publication should be submitted to *The Journal of Physical Chemistry*, Department of Chemistry, University of Minnesota, Minneapolis, Minn. 55455. Correspondence regarding **accepted papers and proofs** should be directed to the Editorial Department at the ACS Easton address.

Page charges of $60.00 per page are assessed for papers published in this journal. Ability to pay does not affect acceptance or scheduling of papers.

Bulk reprints or photocopies of individual articles are available. For information write to Business Operations, Books and Journals Division at the ACS Washington address.

Requests for **permission to reprint** should be directed to Permissions, Books and Journals Division at the ACS Washington address. The American Chemical Society and its Editors assume no responsibility for the statements and opinions advanced by contributors.

Subscription and Business Information

1976 Subscription rates—including surface postage

	U.S.	PUAS	Canada, Foreign
Member	$24.00	$29.75	$30.25
Nonmember	96.00	101.75	102.25
Supplementary material	15.00	19.00	20.00

Air mail and air freight rates are available from Membership & Subscription Services, at the ACS Columbus address.

New and renewal subscriptions should be sent with payment to the Office of the Controller at the ACS Washington address. **Changes of address** must include both old and new addresses with ZIP code and a recent mailing label. Send all address changes to the ACS Columbus address. Please allow six weeks for change to become effective. **Claims** for missing numbers will not be allowed if loss was due to failure of notice of change of address to be received in the time specified; if claim is dated (a) North America—more than 90 days beyond issue date, (b) all other foreign—more than 1 year beyond issue date; or if the reason given is "missing from files". Hard copy claims are handled at the ACS Columbus address.

Microfiche subscriptions are available at the same rates but are mailed first class to U.S. subscribers, air mail to the rest of the world. Direct all inquiries to Business Operations, Books and Journals Division, at the ACS Washington address or call (202) 872-4444. **Single issues** in hard copy and/or microfiche are available from Special Issues Sales at the ACS Washington address. Current year $4.75. Back issue rates available from Special Issues Sales. **Back volumes** are available in hard copy and/or microform. Write to Special Issues Sales at the ACS Washington address for further information. **Microfilm** editions of ACS periodical publications are available from volume 1 to the present. For further information, contact Special Issues Sales at the ACS Washington address. **Supplementary material** must be ordered directly from Business Operations, Books and Journals Division, at the ACS Washington address.

Microfiche	U.S.	PUAS, Canada	Other Foreign
Photocopy	$2.50	$3.00	$3.50
1–7 pages	4.00	5.50	7.00
8–20 pages	5.00	6.50	8.00

Orders over 20 pages are available only on microfiche, 4 × 6 in., 24X, negative, silver halide. Orders must state photocopy or microfiche if both are available. Full bibliographic citation including names of all authors and prepayment are required. Prices are subject to change.

American Chemical Society
1155 16th Street, N.W.
Washington, D.C. 20036
(202) 872-4600

Member & Subscription Services
American Chemical Society
P.O. Box 3337
Columbus, Ohio 43210
(614) 421-7230

Editorial Department
American Chemical Society
20th and Northampton Sts.
Easton, Pennsylvania 18042
(215) 258-9111

Notice to Authors last printed in the issue of January 1, 1976

THE JOURNAL OF

PHYSICAL CHEMISTRY

Volume 80, Number 13 June 17, 1976

JPCHAx 80(13) 1393-1518 (1976)

ISSN 0022-3654

COMMUNICATIONS TO THE EDITOR

There is no supplementary material for this issue.

* In papers with more than one author, the asterisk indicates the name of the author to whom inquiries about the paper should be addressed.

AUTHOR INDEX

THE JOURNAL OF
PHYSICAL CHEMISTRY

VOLUME 80, NUMBER 13 JUNE 17, 1976

Multistep Collisional Deactivation of Chemically Activated Methylcyclobutane[1]

Richard J. McCluskey and Robert W. Carr, Jr.*

Department of Chemical Engineering and Materials Science, University of Minnesota, Minneapolis, Minnesota 55455

(Received December 4, 1975)

Publication costs assisted by the University of Minnesota

The photolysis of ketene at 334 nm, in the presence of cyclobutane and small amounts of oxygen, was investigated at pressures between 297 and 2 Torr at 298 K. Chemically activated methylcyclobutane was formed at energies about 50 kcal/mol in excess of the threshold energy for unimolecular decomposition to propylene and ethylene by the addition of $CH_2(^1A_1)$ to cyclobutane. The data, plotted as the ratio of propylene yield to methylcyclobutane yield vs. reciprocal collision frequency, showed concave upward curvature indicative of multistep collisional deactivation. In these experiments, cyclobutane was the major collision partner. Theoretical calculations, using RRKM theory and a stepladder deactivation model, showed that the data could be fit by deactivation step sizes in the range 4 to 6 kcal/mol. The dependence of the results on collision number and molecular frequency model for the activated complex were examined in detail.

Introduction

One of the most attractive methods for producing chemical species with large nonequilibrium amounts of internal energy is the addition of $CH_2(^1A_1)$ to hydrocarbons. In favorable cases the molecular adducts are chemically activated to energies in the vicinity of 40–50 kcal/mol above the critical energy for unimolecular isomerization or decomposition of the adduct. Because of uncertainties in $\Delta H_f°(CH_2(^1A_1))$, as well as any nonthermal equilibrium amounts of energy carried by $CH_2(^1A_1)$ from its method of genesis, the energy distribution and mean energy of the adduct is correspondingly uncertain. At these high excess energies, several deactivating collisions, even with a polyatomic collision partner, may be required to stabilize the hot adduct. This can be experimentally tested at low pressures where conventional plots of the ratio of decomposition products to deactivated products vs. $(\text{pressure})^{-1}$ are concave upward if multistep deactivation occurs. At higher pressures curvature is slight, experimental data appear to be linear with $(\text{pressure})^{-1}$ due to random errors, and no information is obtained on whether or not multistep deactivation occurs. Thus, data taken only at higher pressures are frequently treated within the framework of the strong collision hypothesis. The application of unimolecular rate theory then leads to an overestimate of the average rate coefficient, and hence the average energy, of the chemically activated species.[2a] This can be misleading in methylene chemical activation systems because of uncertainty in level of energization, discussed above. In fact, the high pressure linear region can be fit equally well by any combination of average energy and average step size that is consistent with bounding values of the system thermochemistry, all other factors remaining constant.[2b] Large values of average deactivation step size result in larger values of activated species average energy required to fit the data, and vice versa.

The data reported in all but one[3] of the studies of methylene chemical activation studies in which the complicating reactions of $CH_2(^3B_1)$, and of secondary decomposition reactions, have been taken into account have been confined to the higher pressure region. There is need for more data in the low pressure region to test whether the strong collision hypothesis is an adequate approximation for polyatomic collision partners. In this paper we report data on chemically activated methylcyclobutane, formed from $CH_2(^1A_1)$ insertion into the C–H bonds of cyclobutane, over a wide range of pressures. Application of RRKM theory would be expected to provide information on deactivation step size and level of energization in the sense that any low pressure curvature would have to be predicted by the average deactivation step size, and the high pressure slope, which is most sensitive to energy, would have to be matched for the same step size.

Two recent studies of chemically activated methylcyclobutane, both done in the high pressure regime, led the investigators to different conclusions from the application of

RRKM theory to their data. Frey, Jackson, Thompson, and Walsh[4] discovered that the theoretically predicted energy of methylcyclobutane formed from ketene photolysis at 325 nm in the presence of cyclobutane was larger than the upper bound energy allowed by system thermochemistry. The authors concluded that either the strong collision hypothesis used in the calculations must be rejected, or the assumption that all vibrational modes of the activated molecule are active is incorrect, or some combination of the two. Simons, Hase, Phillips, Porter, and Growcock[5] were able to obtain agreement between RRKM theory and experiment in the methylcyclobutane chemical activation system, using the strong collision hypothesis, by employing molecular transition state models based upon different values[6,7] of the Arrhenius preexponential factor than the one used[8] by Frey et al.[4]

Experimental Section

Experiments were done on a conventional all glass vacuum apparatus capable of evacuation to 10^{-5} Torr, and employing PTFE-glass needle valves in the reaction product handling system. A chemical light filter, consisting of 5 cm of an aqueous 0.1 g/cm^3 of $NiSO_4 \cdot 6H_2O$ solution, and 1 cm of 0.1 M naphthalene in isooctane, isolated the 334.1-nm emission of a Hanovia 673A 500-W medium pressure Hg arc from other Hg emission lines in the ketene absorption region above the Pyrex cutoff. Transmission of the adjacent 313- and 366-nm lines was negligible. Photolyses were done at room temperature (ca. 300 K) in either a cylindrical 55.2-cm^3 Pyrex reactor (10 cm × 2.7 cm i.d.), used for experiments at pressures greater than 10 Torr, or a spherical 1-l. Pyrex reactor of ca. 13 cm i.d., used for experiments at lower pressures.

All analyses were performed on a Barber-Colman 5000 gas chromatograph equipped with a flame ionization detector. A 7.0 m 3% squalane on firebrick column at 0 °C, with 140 cm^3/min of He carrier at 40 psig, was used for routine analyses. Relative peak areas were determined by the product of peak height and half-height peak width. The relative sensitivities of propylene and methylcyclobutane were determined from calibration mixtures prepared from authentic samples.

Gas chromatographic analysis of cyclobutane purchased from Merck Sharp and Dohme of Canada, Ltd., revealed ca. 0.05% methylcyclobutane as an impurity. This was used only in higher pressure photolyses where the methylcyclobutane yield could be corrected with little error. Cyclobutane from the Farchan Division of Storey Chemical Co. contained ca. 0.1% methylcyclobutane impurity which was removed by gas chromatographic separation before use in all other experiments. Ketene, prepared by pyrolysis of acetic anhydride,[9] was purified by several trap to trap distillations at −78 and −196 °C before use. Oxygen was Chemetron industrial grade which was used as received.

Pressure measurements were made using a conventional Hg manometer for pressures greater than 10 Torr, and by means of a cathetometer and large bore differential manometer for pressures less than 10 Torr. The cathetometer vernier was calibrated to 0.05 mm; experimental pressures were determined to ±0.1 mm by averaging three measurements.

Photolyses were performed on mixtures of cyclobutane, ketene, and oxygen having the ratios cyclobutane:ketene:oxygen of 5:1:1, 10:1:1, and 10:2:1.

Results

The reaction products observed were methylcyclobutane, ethylene, propylene, and 1-pentene. These are the products predicted by the mechanism given below, which is consistent with the behavior of methylene as currently understood.

$$CH_2CO + h\nu \rightarrow CH_2(^1A_1) + CO$$

$$CH_2(^1A_1) + c\text{-}C_4H_8 \rightarrow MCB^*$$

$$CH_2(^1A_1) + CH_2CO \rightarrow C_2H_4 + CO$$

$$MCB^* \rightarrow C_2H_4 + C_3H_6$$

$$MCB^* \rightarrow 1\text{-}C_5H_{10}$$

$$MCB^* + M \rightarrow MCB + M$$

$$CH_2CO + h\nu \rightarrow CH_2(^3B_1) + CO$$

$$CH_2(^3B_1) + O_2 \rightarrow CO, CO_2, H_2, H_2O, \ldots$$

MCB represents methylcyclobutane, and the asterisk a chemically activated species. The chemically activated methylcyclobutane may either react or be deactivated by collision with cyclobutane, ketene, or oxygen. The deactivation is represented as a one step process for simplicity: actually it is (see below) a multistep process. The yields of ethylene, propylene, methylcyclobutane, and 1-pentene were pressure dependent products, as predicted by the mechanism. The ratios of 1-pentene to methylcyclobutane were never larger (at the lowest pressures) than 0.036 and were less than 0.01 above 6 Torr. Thus we neglected 1-pentene formation in the analysis to follow. With oxygen present, $CH_2(^3B_1)$ was scavenged[10] and its possible complications could be safely ignored.

The qualitative shape of P/MCB vs. ω^{-1} can be determined by the following simple kinetic models. For one-step deactivation (strong collision hypothesis) a steady-state on MCB* yields the following relationship:

$$\langle k_a \rangle = \omega(\mathrm{P/MCB}) \qquad (1)$$

between $\langle k_a \rangle$, the average unimolecular rate constant, ω, the collision frequency of MCB*, and P/MCB where P represents propylene. For multistep deactivation with uniform deactivation stepsize, P/MCB is given by

$$\mathrm{P/MCB} = \prod_{i=1}^{n} (1 + k_i/\omega) - 1 \qquad (2)$$

where the index i runs over the energy levels above the critical energy, k_i is the unimolecular rate constant which is a function of energy level, and ω is independent of energy. (In deriving eq 2, up transitions are neglected, but the qualitative behavior would be the same if they were included, as they were in the theoretical calculations.) Equation 1 predicts that P/MCB vs. ω^{-1} is linear, while (2) predicts concave upward shape. Thus the existence of curvature provides a basis for determining whether multistep deactivation is important. The collision diameters for the calculation of ω which have been used by different investigators vary widely.[4,5,11] Since there is no basis for the selection of one set over another, we have used two sets of collision diameters which embrace this range. One set gives a reasonable low collision number, the other a reasonable high collision number. This not only allows comparisons with previous work, but in the calculations to follow allows an assessment of the effect of variations in collision number.

The experimental data are presented in Figure 1 for ω calculated from the lower collision number. For the higher collision number the plot would be almost identical except for compression of the abscissa by the factor Z_{low}/Z_{high}. The curvature of Figure 1 demonstrates the occurrence of multistep deactivation with cyclobutane as the principal collision partner. In the high pressure limit P/MCB vs. ω^{-1} becomes

TABLE I: Collision Diameters and Efficiencies

Species	"Low set" σ^a	Ref	β^b	Ref	"High set" σ^a	Ref	β^b	Ref
MCB*	5.2	11	1	5, 11	6.8	5	1	5
c-C_4H_8	5.1	11	1	5, 11	6.49	5	1	5
CH_2CO	4.7	4	0.6	11	5.45	5	1	5
O_2	3.43	11	0.38	11	3.6	5	0.25	5

[a] Hard sphere collision diameter. [b] Collisional efficiency.

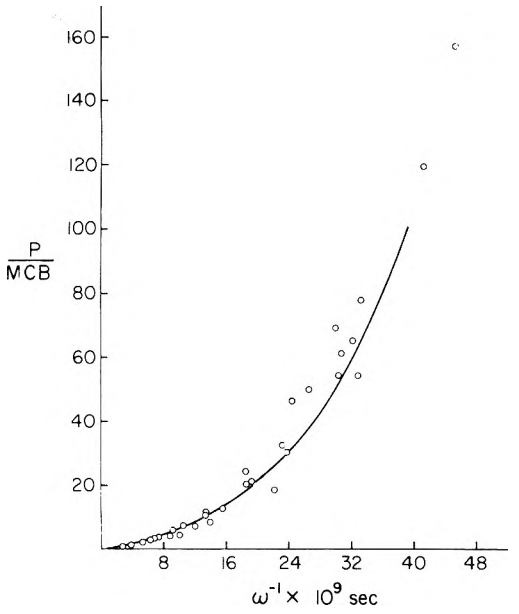

Figure 1. P/MCB experimental data; solid line: calculated curve for model I with Z_{high}, $\langle E \rangle$ = 115.4 kcal/mol, and ΔE = 6.9 kcal/mol.

nearly linear, implying that $\langle k_a \rangle$ is nearly constant. Figure 2 shows the high pressure region; note the zero intercept, as predicted by the mechanism. The values of $\langle k_a \rangle$ computed by (1) at pressures greater than 100 Torr yielded the average value of $3.16 \pm 0.14 \times 10^8$ s^{-1}, where the error is reported as $\pm\sigma$. Thus $\langle k_a \rangle$ may be considered constant, within experimental error, in the high pressure region. Average values of $\langle k_a \rangle$ from this work are reported in Table II along with those reported by previous investigators.[4,5,11] The agreement is satisfying. The experimental P/MCB values at lower pressures (Figure 1) have estimated errors of ±15%. The reasons for the greater uncertainty at low pressures are: (1) The reduced quantity of reaction sample available for analysis permitted fewer replicate gas chromatographic analyses of the same sample and (2) the relative error in pressure measurement becomes larger. Although we were able to obtain data at P/MCB values as large as 157, we are uncertain about the reliability of the data at P/MCB greater than about 60 to 80.

Theoretical Computations

Mathematical Model. A mathematical model of the unimolecular decomposition of MCB was made on the University of Minnesota Cyber 74 computer. The model uses RRKM theory to give specific microcanonical rate constants, $k(E)$, for each energy level of MCB, and the stepladder scheme to describe the stabilization process.

The RRKM expression for the microcanonical rate constant is given by

TABLE II: Comparison of High Pressure $\langle k_a \rangle$, Assuming Strong Collisions, with Earlier Work

Z(10:1:1) × 10^{-7} s^{-1} Torr^{-1}	1.106	1.87
Ref	$\langle k_a \rangle \times 10^{-8}$ s^{-1}	
4	2.9	5.0
11	3.6	5.9
5	3.2	5.4
This work	3.2	5.4

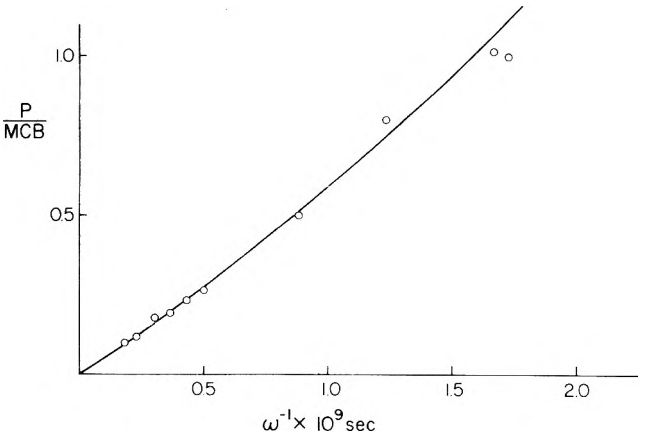

Figure 2. Higher pressure P/MCB experimental data; solid line: calculated curve for model I with Z_{high}, $\langle E \rangle$ = 115.4 kcal/mol, and ΔE = 6.9 kcal/mol.

$$k(E) = L^{\neq}(Q_1^{+}/Q_1) \sum_{E=E_0}^{E} P(E - E_0)/hN(E) \qquad (3)$$

where the symbols have their conventional meaning.[12,13] Four molecular models of the activated complex, necessary for calculation of the sums of quantum states in (3), have been reported in the literature.[4,5] Since the frequency assignments were made for agreement with each of the three reported entropies of activation[6-8] we have adopted those models in these calculations for consistency and ease of comparison. The harmonic oscillator model of Frey, Jackson, Thompson, and Walsh,[4] called model I here, is consistent with the entropy of activation derived from the experimental high pressure thermal decomposition data of Das and Walters.[8] In the three molecular frequency models reported by Simons, Hase, Phillips, Porter, and Growcock,[5] the methyl group is treated as a one-dimensional free rotor, the remainder of the frequencies as harmonic oscillators. Model S-1 is consistent with the Das and Walters[8] thermal data, model S-2 fits the preexponential factor reported by Pataracchia and Walters,[6]

and model S-3 gives agreement with the A factor reported by Thomas, Conn, and Swinehart.[7]

For model I the sums and densities were computed using the Beyer and Swinehart algorithm[14] with a grain size of 10 cm^{-1}. The round-off error introduced by this grain size was less than 2%, as judged by comparison of a direct count, i.e., a grain size of 1 cm^{-1}. For models S-1, S-2, and S-3, the sums and densities were calculated by the Whitten and Rabinovitch[15] approximation. At energies too low for this approximation to be accurate, the energy levels of the internal rotor were approximated by harmonic oscillator levels and the sums and densities computed by the Beyer and Swinehart[14] algorithm.

The ratio P/MCB was computed from the matrix formulation[16]

$$\frac{P}{P + MCB} = \frac{1}{\omega}\sum_i \left[\mathbf{k}\left(\mathbf{I} - \mathbf{P} + \frac{\mathbf{k}}{\omega}\right)^{-1} \boldsymbol{f}\right]_i \qquad (4)$$

In (4), $\mathbf{k}$ is a main diagonal matrix with $k(E)$ as its elements, $\mathbf{I}$ is the unit matrix, $\mathbf{P}$ is a matrix with elements P_{ij}, and $\boldsymbol{f}$ is a vector with elements $f(E)$, the energy distribution function of MCB*. The collisional transition probabilities from state j to state i, $P_{ij} = 0$ unless $j - i$ = specified stepsize. The principles of detailed balance, $P_{ij} = P_{ji}[N(E_i)/N(E_j)] \exp[(E_j - E_i)/kT]$, and completeness, $\Sigma_i P_{ij} = 1$, were adhered to.

In all of the calculations to be presented, the energy distribution of MCB* was approximated by a delta function located at the average energy of MCB*. To examine the effect of broadening the distribution function, several calculations were made using an approximation suggested by Forst,[17] with the additional constraint that $f(E)\,dE = 0$ at $E = E_{min}$, and also using a distribution function derived by application of the principle of microscopic reversibility to the reverse of the methylene–cyclobutane addition. The former had a width (variance) of 1.6 kcal/mol, and the latter a width (variance) of 1.9 kcal/mol. Test calculations with MCB* average energies in the vicinity of 112 kcal/mol showed that the high pressure $\langle k_a \rangle$ was 2 and 4% larger, respectively, than with a delta function, well within experimental error, so that the delta function certainly is an adequate approximation at high pressures. There was more sensitivity to $f(E)\,dE$ at low pressures. For example, the 2.7 Torr value of P/MCB decreased by 13 and 20%, respectively, relative to a delta function. The former is barely within the estimated low pressure error (±15%) and the latter lies outside. The effect of energy distribution function on the conclusions will be presented below.

Computational Results. Values of P/MCB as a function of pressure were obtained from eq 4 for combinations of $\langle E \rangle$, the average MCB* energy, and deactivation stepsize, ΔE for each of the four activated complex models for both Z_{high} and Z_{low}. The grain size used in the matrix was 200 cm^{-1}. Test calculations showed the results to be insensitive to the graining at this level. Sets of input data yielding a high pressure $\langle k_a \rangle$ within ±10% (±2σ) of the experimental value, and P/MCB within ±15% of the experimental value at 2.7 Torr were considered "good" data fits. The value of $\langle E \rangle$, moreover, had to be consistent with thermochemistry. The maximum possible energy of MCB*, $\langle E \rangle_{max}$, can be computed from the overall photoreaction

$$CH_2CO + c\text{-}C_4H_8 + h\nu\ (334\ nm) = MCB^* + CO \qquad (5)$$

by assuming that all of the exothermicity and excess photon energy is pooled into MCB*. The energy balance is given by

$$\langle E \rangle_{max} = -\Delta H^\circ_0 + N_a h\nu + E_{th} \qquad (6)$$

TABLE III: Computer Calculations of $\langle k_a \rangle_\infty$ and P/MCB[a]

Energy parameters		Calculational results	
Initial energy, kcal/mol	Stepsize, kcal/mol	$\langle k_a \rangle_{200}$ Torr × 10^{-8}, s^{-1}	D/$S_{2.7}$ Torr
$Z = Z_{low}$ (10:1:1) = 1.106 × 10^7 s^{-1} $Torr^{-1}$			
109.1	4.6	2.75	73.1
110.2	4.6	3.32	123.9
	5.7	2.84	57.4
111.3	4.6	4.00	217.0
	5.7	3.40	91.4
	6.9	3.02	51.5
112.5	5.7	4.07	149.3
	6.9	3.60	78.6
	8.0	3.29	49.8
113.6	6.9	4.29	122.5
	8.0	3.90	73.7
	9.1	3.63	50.4
Exptl		2.9–3.5	60–80
$Z = Z_{high}$ (10:1:1) = 1.87 × 10^7 s^{-1} $Torr^{-1}$			
112.5	4.6	4.68	81.4
113.6	4.6	5.58	135.8
	5.7	4.74	61.4
114.8	5.7	5.62	96.2
	6.9	4.98	53.4
115.9	6.9	5.87	80.4
	8.0	5.34	50.4
117.1	8.0	6.28	73.5
	9.1	5.82	49.9
Exptl		4.9–5.9	60–80

[a] Model I: $f(E)$ = delta function.

N_a is Avogadro's number, and E_{th} is the thermal energy of the reactants. Using $\Delta H^\circ_0 = -22.0$ kcal/mol, $N_a h\nu = 85.6$ kcal/mol and $E_{th} = 4.5$ kcal/mol results in $\langle E \rangle_{max} = 112.1$ kcal/mol. A lower bound to the energy of MCB*, $\langle E \rangle_{low}$, can be calculated from the exoergicity of

$$CH_2(^1A_1) + c\text{-}C_4H_8 = MCB^* \qquad (7)$$

and is given by

$$\langle E \rangle_{low} = -\Delta H^\circ_0 + E_{th} + E_{act} \qquad (8)$$

In this calculation, $CH_2(^1A_1)$ is assumed not to carry any excess photon energy. E_{act} is the activation energy for $CH_2(^1A_1)$ addition to $c\text{-}C_4H_8$. To obtain the lower bound a low value of the heat of formation of singlet methylene, $\Delta H_f^\circ{}_0(CH_2(^1A_1)) = 96$ kcal/mol was used, and E_{act} was assumed to be zero. This resulted in $\langle E \rangle_{low} = 104.2$ kcal/mol. However, larger values of the heat of formation of methylene have been reported and if $\Delta H_f^\circ{}_0(CH_2(^1A_1)) = 101$ kcal/mol is used,[18] along with $E_{act} = 1$ kcal/mol (methylene additions occur extremely rapidly, and presumably have low activation energies), then $\langle E \rangle = 110.8$ kcal/mol is deduced from eq 8, and the upper and lower limit are very close. This is a reflection of the fact that the photon energy at 334 nm is close to the dissociation limit in ketene, and very little excess photon energy is available.

A tabulation of computer results for various input values of $\langle E \rangle$ and ΔE, using model I, is given in Table III. For Z_{high}, it is apparent that at an energy of 112.5 kcal/mol and a stepsize of 4.6 kcal/mol the high pressure $\langle k_a \rangle$ is too low while the D/S ratio at 2.7 Torr is too high. If the stepsize were decreased to bring up the $\langle k_a \rangle$ the D/S ratio would go even higher. Thus no stepsize will give an adequate fit to the data at this input energy. Examination of the computer data for an energy of 116 kcal/mol shows that the experimental data could be fit with

TABLE IV: Energy Parameters that Reproduce the Experimental Results[a]

Model	Z_{low}		Z_{high}	
	E_{range}, kcal/mol	ΔE_{range}, kcal/mol	E_{range}, kcal/mol	ΔE_{range}, kcal/mol
I	109.5–112.5	5–7.5	113.5–116.5	5–7.5
S-I	108–111.5	4.5–7.5	112–115	5–7.5
S-II	106–109	4.5–7	110–112.5	4.5–7
S-III	102.5–105.5	4–6.5	106–108.5	4–6.5

[a] All data were obtained using $f(E) = \delta(E)$. More representative distribution functions reduce the energy and ΔE by about 1 kcal/mol. See text.

a range of stepsizes from 6.9 to about 7.6 kcal/mol, the stepsize range being limited by the low pressure data. As energy is increased further the computer results show that at 117 kcal/mol any stepsize fitting the low pressure data would give too high a value for the high pressure rate constant. The same trends were seen in the results for the low collision number and for all the other molecular frequency models examined. At too low an energy the model's high pressure constant is too low and the low pressure D/S is too high; for too large an energy the high pressure result becomes too high and the low pressure D/S too low.

How well a computer model constrained to fit $\langle k_a \rangle_\infty$ and the low pressure D/S matches the intermediate pressure data can be seen in Figures 1 and 2 which show a plot of calculated D/S vs. ω^{-1} for model I and Z_{high}, at $\langle E \rangle = 115.4$ kcal/mol and $\Delta E = 6.9$ kcal/mol. Fits could also be obtained for other molecular models, energies, and stepsizes.

The result for all the different molecular models are summarized in Table V. The range of stepsizes which allow a fit to the experimental data are almost the same for both collision numbers, the stepsize values for the two collision numbers differing by less than 0.5 kcal/mol. The $\langle E \rangle$ values which permit a data match are about 3–4 kcal/mol smaller for the lower collision number. These results are independent of the molecular frequency model.

For every frequency model a data fit is obtained at approximately the same ratio of $k(\langle E \rangle)/\omega$. Hence models giving higher microcanonical rate constants require lower energies to fit the data. There is also a slight reduction in stepsize which accompanies this lowering of $\langle E \rangle$.

Discussion

We interpret the curvature of the data plotted in Figure 1 as evidence for multistep deactivation of MCB*. The comparisons with RRKM theory summarized in Table IV show the nature of RRKM data fits very clearly. The best fits for model I and S-I, using Z_{high}, are obtained at values of $\langle E \rangle$ larger than allowed by system thermochemistry, and can be disregarded. However, the same two models work satisfactorily for Z_{low}. It could also be argued that the data fit for model S-III and Z_{low} is obtained for $\langle E \rangle$ which is marginally on the low side, and should be disregarded. Nevertheless, each model gives a fit to the data for some combination of deactivation stepsize, $\langle E \rangle$ (in the accessible range), and collision number. Thus the difficulty of determining the average energy, $\langle E \rangle$, of chemically activated species by this technique is amply illustrated. In the present case the uncertainty is about 10 kcal/mol.

On the other hand, Table IV shows that the values of ΔE are relatively insensitive to $\langle E \rangle$, Z, and the activated complex model. This fortunate circumstance means that studies of collisional energy transfer can be accomplished even in systems where these quantities are not very well known.

TABLE V: Thermochemical Estimates of $\Delta H_f°_0(CH_2(^1A_1))$

Model	$\Delta H_f°_0(^1CH_2) + E_{xs}$, kcal/mol
I	98.5–102
S-I	97–102
S-II	95–102
S-III	94–98.5

TABLE VI: Thermochemical Data

Species	$\Delta H_f°_0$, kcal/mol	Ref
MCB	6.7	*a*
c-C_4H_8	12.2	*b*
CH_2CO	−10.7	*c*
CO	−27.2	*d*

[a] W. D. Good, R. T. Moore, A. G. Osborn, and D. R. Douslin, *J. Chem. Thermodyn.*, **6**, 303 (1975). [b] M. Kh. Karapet'yants and M. L. Karapet'yants, "Thermodynamic Constants of Inorganic and Organic Compounds", Translated by J. Schmorak, Humphrey Science Publishers, Ann Arbor, Mich., 1970, p 343. [c] R. L. Nuttall, A. H. Laufer, and M. V. Kilday, *J. Chem. Thermodyn.*, **3**, 167 (1971). [d] D. D. Wagman, W. H. Evans, I. Halow, V. B. Parker, S. M. Bailey, and R. H. Schumm, *Natl. Bur. Stand. (U.S.) Techn. Note*, **No. 270-1** (1965).

The effect of using a broader, more realistic distribution function was tested by trial calculations using the two distributions referred to above with model I. The effect was to lower the range of $\langle E \rangle$ and ΔE for which a good fit could be obtained by about 1 kcal/mol. The effect is relatively minor, and the delta function distribution is not an unreasonable approximation to use. However, the ranges of $\langle E \rangle$ and ΔE reported in Table IV must be regarded as being 0.5 to 1 kcal/mol higher than those that would be obtained by using a more accurate distribution function. We conclude that a stepladder model with stepsizes in the range 4–3 kcal/mol is adequate to describe the multistep deactivation of MCB* by c-C_4H_8 collider.

The apparent failure of RRKM theory to adequately describe the MCB* system, which was reported by Frey, Jackson, Thompson, and Walsh,[4] can be attributed to use of the strong collision hypothesis in their theoretical treatment. (They suggested this as a possible failing at the time.) Our experiments (Figure 1) clearly show evidence for multistep deactivation, and we were able to quantitatively account for the data with RRKM theory using the same molecular frequency model for the activated complex (model I). The other possible causes of failure which they discussed,[4] collisional deactivation inefficiency (elastic collision) or fewer active vibrational modes, are not necessary to obtain agreement between theory and experiment. However, the effects of elastic collisions can be simulated by decreasing collision diameters.

Simons, Hase, Phillips, Porter, and Growcock[5] reported RRKM calculated values of $\langle E \rangle$ for MCB* from CH_2CO at 334 nm for each of the four molecular frequency models used here, but with the strong collision hypothesis. For each of the four models, $\langle E \rangle$ was larger than the allowable thermochemical maximum. This was used as a basis for judging "goodness" of the models, and hence a basis for evaluation of Arrhenius preexponential factors. The data in Table IV,

however, show that multistep deactivation yields values of $\langle E \rangle$ which are energetically allowable for each of the four frequency models, and hence reveals another aspect of the inadequacy of the strong collision hypothesis in methylene chemical activation systems. Taken alone, the calculations done here allow no basis for discrimination among the three published values of the preexponential factor.

The values of $\langle E \rangle$ obtained as a "best fit" to the data for each of the models and collision numbers can be related to the sum of the heat of formation of $CH_2(^1A_1)$ plus the excess photon energy carried by methylene at the time of addition through

$$\Delta H_f°_0(CH_2(^1A_1)) + E_{xs} = \langle E \rangle - E_{th} - \Delta H_f°_0(c\text{-}C_4H_8) + \Delta H_f°_0(MCB) \quad (9)$$

The results are shown in Table V. Although E_{xs} at 334 nm is unknown, it must be small, probably no more than 1–2 kcal/mol at most. Thus the data are consistent with a range of values of $\Delta H_f°_0(CH_2(^1A_1))$, and it is quite apparent that nothing very precise can be learned about its value from this type of experiment. The data are not inconsistent with either the low value previously put forward from this laboratory, or the somewhat higher value reported in a previous RRKM study.[18]

Acknowledgment. This work was supported by the U.S. Energy Research and Development Administration under Contract No. E(11)-1 2026.

References and Notes

(1) USERDA Document No. COO-2026-25.
(2) (a) D. W. Setser, *Phys. Chem. Ser. One*, 1972–1973, **9**, 11 (1972); (b) R. W. Carr and M. G. Topor, *J. Chem. Phys.*, **58**, 757 (1973).
(3) J. D. Rynbrandt and B. S. Rabinovitch, *J. Phys. Chem.*, **74**, 1679 (1970).
(4) H. M. Frey, G. R. Jackson, M. Thompson, and R. Walsh, *Trans. Faraday Soc.*, **69**, 2054 (1973).
(5) J. W. Simons, W. L. Hase, R. J. Phillips, E. J. Porter, and F. B. Growcock, *Int. J. Chem. Kinet.*, to be published.
(6) A. F. Pataracchia and W. D. Walters, *J. Phys. Chem.*, **68**, 3894 (1964).
(7) T. F. Thomas, P. J. Conn, and D. F. Swinehart, *J. Am. Chem. Soc.*, **91**, 7611 (1969).
(8) M. N. Das and W. D. Walters, *Z. Phys. Chem.*, **15**, 22 (1958).
(9) A. D. Jenkins, *J. Chem. Soc.*, 2563 (1952).
(10) R. L. Russell and F. S. Rowland, *J. Am. Chem. Soc.*, **90**, 1671 (1968).
(11) R. L. Russell, Ph.D. Thesis, University of California, Irvine, Calif., 1971.
(12) P. J. Robinson and K. A. Holbrook, "Unimolecular Reactions", Wiley, New York, N.Y., 1972.
(13) W. Forst, "Theory of Unimolecular Reactions", Academic Press, New York, N.Y., 1973.
(14) T. Beyer and D. F. Swinehart, *Commun. ACM*, **16**, 379 (1973); S. E. Stein and B. S. Rabinovitch, *J. Chem. Phys.*, **58**, 2438 (1973).
(15) G. Z. Whitten and B. S. Rabinovitch, *J. Chem. Phys.*, **38**, 2466 (1963).
(16) M. Hoare, *J. Chem. Phys.*, **38**, 1630 (1963).
(17) Reference 13, p 214.
(18) W. L. Hase, R. J. Phillips, and J. W. Simons, *Chem. Phys. Lett.*, **12**, 161 (1971).

Transition State Characterization for the Hydrogen Elimination from 1,4-Cyclohexadiene

D. C. Tardy,*[1] A. S. Gordon, and W. P. Norris

Michelson Laboratory, Naval Weapons Center, China Lake, California 93555 *(Received November 21, 1975)*

Publication costs assisted by the Naval Weapons Center

The gas phase thermal decomposition of various isotopically substituted 1,4-cyclohexadienes was studied in the 275–375 °C temperature region to obtain transition state information for the Woodward–Hoffman symmetry allowed hydrogen elimination reaction. Competitive decompositions with (i) a 1:1 mix of 1,4-cyclohexadiene and perdeuterio-1,4-cyclohexadiene or (ii) 1,2,3,4,5,6-hexadeuterio-1,4-cyclohexadiene produced (*i*) H_2 and D_2 or (*ii*) H_2, D_2, and HD. The difference in E_a for H_2 and D_2 elimination was 2.1 ± 0.4 and 2.4 ± 0.8 kcal/mol for systems (i) and (ii), respectively; the difference in E_a for H_2 and HD was 1.5 ± 0.4 kcal/mol. The results indicate a tight transition state which resembles benzene in its vibrational frequency assignment while the reaction coordinate is predominately the concerted breaking of two carbon–hydrogen bonds.

The decomposition of 1,4-cyclohexadiene[2] has previously been reported. The only detectable reaction is the homogeneous first-order intramolecular stereospecific elimination of molecular hydrogen[3]

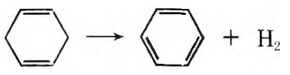

The reaction has been studied in the unimolecular high pressure region and the temperature dependence of the rate constant between 330 and 390 °C is best described by the equation

$$\log k = 12.4 - \frac{43\,800}{2.303\,RT}$$

where R is 1.98 cal/K mol.

The activation energy (E_a = 43.8 kcal/mol) for this elimination reaction is approximately 18 ± 3 kcal/mol lower than the reported E_a's of analogous Woodward–Hoffman allowed hydrogen elimination reactions, i.e., cyclohexene[4,5] (E_a = 62 ± 3 kcal/mol) and *cis*-butene-2[6] (E_a = 65 ± 2 kcal/mol).[6,7] The present work was undertaken to obtain information of the A and E factors which are involved in the reaction process and to further test the concerted mechanism for the reaction.

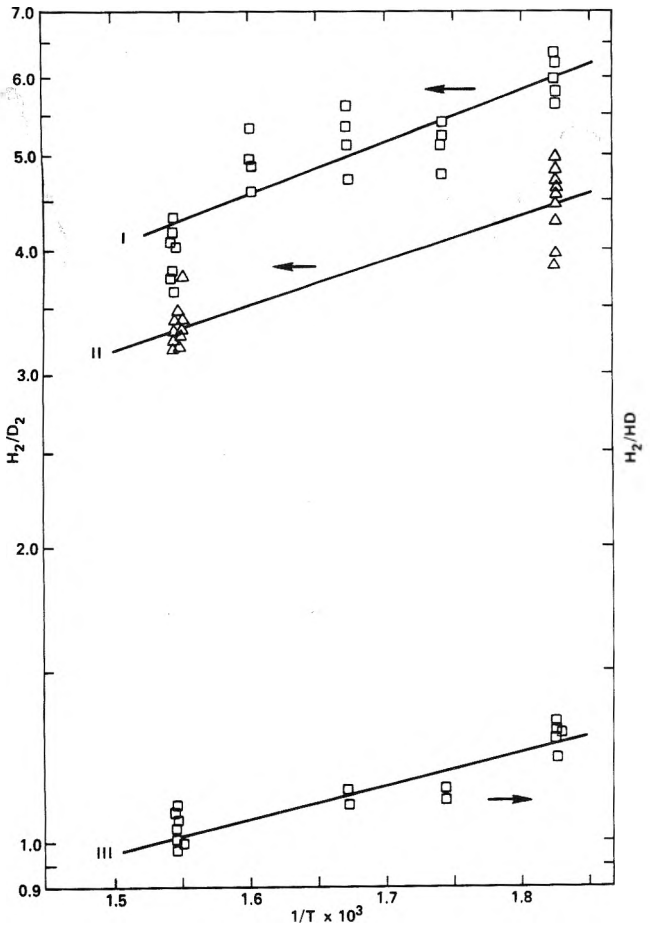

Figure 1. Yield plots of H_2/D_2 for intermolecular (II) and intramolecular (I) comparisons and H_2/HD for intramolecular (III) comparison as a function of temperature. The least-squares analysis (solid lines) yielded slopes (kcal/mol) and intercepts of: (I) -2.38 ± 0.8, 0.67 ± 0.4; (II) -2.06 ± 0.4, 0.67 ± 0.4; (III) -1.46 ± 0.4, 0.33 ± 0.2.

These particular objectives can be obtained through the studies of isotopically substituted cyclohexadienes. Two studies will be reported in this note:

(i) The intermolecular competitive eliminations of various hydrogens from a 1:1 mix of 1,4-cyclohexadiene (CH)[8] and perdeuterio-1,4-cyclohexadiene (CD).[8] No HD was detected in conformity with the intramolecular molecular hydrogen elimination mechanism of Alfassi et al.[7]

(ii) The intramolecular competitive elimination of H_2, HD, and D_2 from 1,2,3,4,5,6-hexadeuterio-1,4-cyclohexadiene (CHD).[8,9]

Most of the pyrolyses were done between 275 and 375 °C at pressures of approximately 600 Torr in a seasoned vessel with a surface-to-volume ratio of 1.3 cm^{-1}. A few pyrolyses were carried out with a surface-to-volume ratio of 6.1 cm^{-1} and showed the reaction to be homogeneous. The hydrogen isotopes were quantitatively analyzed with a mass spectrometer calibrated with known compositions of H_2, HD, and D_2. The hydrogen ratios were found to be independent of reaction time and pressure.

Assuming Arrhenius behavior, a two-parameter (the activation energy difference ΔE and A factor ratio ΔA) least-squares analysis of the data in Figure 1 was performed. For the H_2 and D_2 elimination ΔE is -2.06 ± 0.4[10] and -2.38 ± 0.8 kcal/mol[10] while ΔA is 0.67 ± 0.4[10] and 0.67 ± 0.4[10] for the intermolecular and intramolecular comparisons, respectively. No quantitative conclusions on the fact that the intramolecular comparison exhibits the largest isotope effect will be made since within experimental error there is no difference in ΔA or ΔE for the two comparisons. However, the magnitude of ΔE suggests a mechanism where the C–H stretch participates in the reaction coordinate since the difference in zero point energies (ZPE) of a C–H and C–D stretch is -1.2 kcal/mol as compared to that of -0.6 kcal/mol for the respective bends.

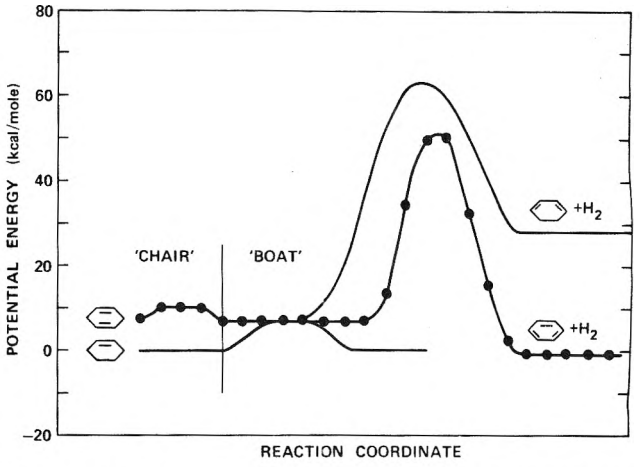

Figure 2. Potential energy versus reaction coordinate for the reactions:

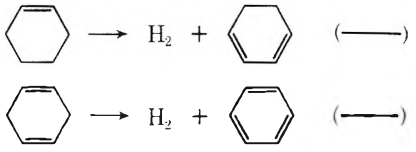

For comparative purposes the zero point energies of a and b in the boat forms are taken as equal, while the zero point energy of a in the half boat form is arbitrarily taken as zero.

For the CHD system $\Delta A(H_2/HD)$ is experimentally determined to be one-half of $\Delta A(H_2/D_2)$. This is in agreement with the fact that the CHD was not formed stereospecifically and thus there are twice as many isomers producing HD as compared to H_2 or D_2. $\Delta E(H_2/HD)$ is approximately half of $\Delta E(H_2/D_2)$ as to be expected by a simple difference in ZPE.

An analogous isotope effect in the thermal decomposition of cyclopentene has been brought to our attention by one of the referees. Knecht[11] reported $\Delta E(H_2/D_2)$ and $\Delta E(H_2/HD)$ of -2.50 and -1.25 kcal/mol while $\Delta A(H_2/D_2)$ and $\Delta A(H_2/HD)$ were 0.63 and 0.99, respectively. These values are remarkably similar to our results even though the activation energy in the cyclopentene system is 57.8 kcal/mol. Knecht's results for $\Delta A(H_2/HD)$ may be in error since his value was obtained from a 23.3% cyclopentene-d_7 impurity in the cyclopentene-d_8.

The previously reported A factors[4,5] suggest a tight transition state (TS). A TS theory calculation in which the cyclohexadiene ring modes were tightened to simulate those of benzene and the reaction coordinate was taken as the carbon hydrogen stretch, gives a H_2/D_2 yield ratio which is greater for the intramolecular comparison, in accordance with the experimental data. This was not true for other models. Hence, the data support a tight TS which resembles benzene in its vibrational frequency assignments while the reaction coordinate is predominately the breaking of carbon hydrogen bonds in the 3 and 6 positions of the cyclohexadiene ring.

The allowed cis elimination requires that the hydrogen atoms in the 3 and 6 positions must be either sufficiently close for a bonding interaction or sufficiently extended for the σ electrons associated with the C–H bond to be delocalized in

the π electron system of the nascent benzene. In either case the ring conformation of the TS must have boatlike characteristics. From x-ray data[12] the stable conformation of CH has the nonvinylic carbon atoms approximately 156° from the plane formed by the vinylic carbon atoms, thus supporting a boatlike ground state. With this geometry the hydrogens are approximately 3 Å from one another, too large for sufficient bonding overlap to give TS stabilization. A discussion of the energetics and TS of the elimination in the CH, cyclohexene, and cyclopentene systems is presented in ref 4b. Since strain energy builds very rapidly with displacement, the observed E_a cannot bring these H's close enough to interact. Hence, the relatively low E_a for the reaction must reflect the influence of the π bonds on partly decoupling the σ bonds of the allylic hydrogens.

The difference of 18 kcal/mol between the E_a's for the analogous eliminations of H_2 from CH and cyclohexene can be understood with an energy profile as depicted in Figure 2. A difference of 6 kcal/mol[13] in E_a can be accounted for by the conformation difference of the reactants since cyclohexene is predominately in a half-boat configuration. The remaining difference of 12 ± 3 kcal/mol must be due to stabilization of the TS by about one-third of the benzene resonance energy of 35.95 kcal/mol.[14] It is interesting that this resonance energy is present when the TS is in a boat configuration.

References and Notes

(1) Associate Professor, University of Iowa, Iowa City, Iowa 52240.
(2) (a) R. J. Ellis and H. M. Frey, *J. Chem. Soc. A*, 553 (1966); (b) S. W. Benson and R. Shaw, *Trans. Faraday Soc.*, **63**, 985 (1967).
(3) I. Fleming and E. Wildsmith, *Chem. Commun.*, 223 (1970).
(4) (a) S. R. Smith and A. S. Gordon, *J. Phys. Chem.*, **65**, 1125 (1961). (b) The study in (a) has been pursued in greater detail by Ireton, Gordon, and Tardy (manuscript in preparation) and gives E_a = 61.6 kcal/mol and not 71.2 kcal/mol as reported in (a).
(5) S. W. Benson and H. E. O'Neal, *Natl. Stand. Ref. Data Ser., Natl. Bur. Stand.*, **No. 21** (1970).
(6) A. Lifshitz, S. H. Bauer, and E. L. Resler, *J. Chem. Phys.*, **38**, 2056 (1963).
(7) Z. B. Alfassi, D. M. Golden, and S. W. Benson, *Int. J. Chem. Kinet.* **5**, 991 (1973).
(8) Purified by gas chromatography.
(9) Synthesized by the Birch reduction of perdeuteriobenzene. Labeling purity was checked by ^{13}C and ^{1}H NMR and found to be more than 99 mol % D.
(10) The uncertainties stated correspond to a 95% confidence limit.
(11) D. A. Knecht, *J. Am. Chem. Soc.*, **95**, 7933 (1973).
(12) H. Oberhammer and S. H. Bauer, *J. Am. Chem. Soc.*, **91**, 10 (1969).
(13) (a) R. Bucourt and D. Hanaut, *Bull. Soc. Chem. Fr.*, 4563 (1967); (b) R. Bucourt in "Topics in Stereochemistry," Vol. 8, E. L. Eliel and N. L. Allinger, Ed., Wiley, New York, N.Y., 1974.
(14) J. D. Cox and G. Pilcher, "Thermochemistry of Organic and Organometallic Compounds", Academic Press, New York, N.Y., 1970.

Ethyl Radical Isomerization. A 1,2-Hydrogen (Deuterium) Shift in the Pyrolysis of 1,1,1-Trideuterioethane

A. S. Gordon, D. C. Tardy,* and R. Ireton[1]

Research Department, Chemistry Division, Naval Weapons Center, China Lake, California 93555

(Received January 14, 1976)

Publication costs assisted by the Naval Weapons Center

1,1,1-Trideuterioethane has been pyrolyzed in the temperature range 500–600 °C. The reaction products are formed via chains initiated by C–C bond cleavage of ethane, but the hydrogen and deuterium content of the ethylene products and the H_2, HD, and D_2 yields are not predicted by the conventional mechanism. The results may be understood in terms of a mechanism involving isomerization of ethyl radical by a 1,2-H (or -D) shift along the carbon skeleton competing with abstraction from the parent and decomposition. The kinetic evidence suggests that the E_a for decomposition of ethyl radical and the 1,2 isomerization are within 1.5 kcal/mol, the difference in rate constants reflecting the difference in preexponential factors.

Introduction

The intramolecular shift of hydrogen in free radicals has been well documented[2] in the liquid and gas phases for transfers involving cyclic transition states larger than five members; i.e., 1,4- and 1,5-hydrogen shifts via five- and six-membered transition states, respectively, have been observed. These studies have been performed using both thermal and chemical activation techniques.

Due to geometrical considerations (i.e., strain energy) 1,2- and 1,3-hydrogen shifts should have high energy barriers as compared to 1,4 and 1,5 shifts; barriers between 18 and 12 kcal/mol have been measured for 1,4 and 1,5 shifts. The small rate constant associated with these high barriers have large experimental uncertainties and hence, the evidence is somewhat controversial.

Jackson and McNesby[3] have studied the thermal isomerization of labeled isopropyl radicals and concluded that the 1,2 isomerization rate constant is approximately 9 ± 2% of the rate constant for breaking a carbon–hydrogen bond to give a hydrogen atom and propylene between 472 and 553 °C. However, Heller and Gordon[4] have also studied the thermal decomposition of isopropyl radicals generated by the photolysis of diisopropyl ketone, and their results suggest that approximately 50% of the isopropyl radicals isomerize. Both studies revealed that the fraction isomerized was independent of temperature. Kerr and Trotman-Dickenson[5] have studied the isomerization of the isobutyl radical, and their results

* Address correspondence to this author at the Department of Chemistry, University of Iowa, Iowa City, Iowa 52242.

indicate that the isomerization becomes less important as the temperature is increased. Using chemical activation techniques Tardy[6] has shown qualitatively and semiquantitatively that 1,2 or 1,3 shifts do occur in the *n*-pentyl radical system with critical energies of approximately 31 kcal/mol.

The above-mentioned systems suffer from chemical complexities and the presence of a rapid competitive process, carbon–carbon bond rupture. To measure the slow isomerizations, competitive paths should have rate constants with a similar value as that of the isomerization, and the number of reaction paths should also be minimized. The ethyl radical meets these requirements. Labeled ethyl radicals were produced by the pyrolysis of 1,1,1-trideuterioethane (1,1,1-TDE). The pyrolysis[7] is a chain reaction that involves the initial formation of methyl radicals

$$CH_3CD_3 \rightarrow CH_3 + CD_3 \qquad (I)$$

which abstract a hydrogen or deuterium from the parent ethane

$$CH_3 + CH_3CD_3 \rightarrow CH_3H + \dot{C}H_2CD_3 \text{ or } CH_3D + CH_3\dot{C}D_2 \qquad (II)$$

$$CD_3 + CH_3CD_3 \rightarrow CD_3H + \dot{C}H_2CD_3 \text{ or } CD_3D + CH_3\dot{C}D_2 \qquad (III)$$

producing the marked ethyl radicals. The ethyl radical can in turn (a) decompose, (b) abstract, or (c) isomerize followed by (a) or (b). The main products, hydrogens and ethylenes, indicate that decomposition predominates. Both hydrogen and ethylene are found to follow first-order kinetics and are formed homogeneously.

The present work was undertaken to further document 1,2-hydrogen shifts in free radicals and to obtain Arrhenius *A* and *E* factors for this process so that a physical model for the hydrogen transfer could be postulated.

Experimental Section

Three different batches of 1,1,1-TDE were purchased from Merck Sharpe and Dohme, Montreal, Canada. Two of the batches were special orders involving preparation of CD_3CH_2Br and CH_3CD_2Br in which a Grignard was formed from the ethyl bromide and treated with the appropriate water. All of the 1,1,1-TDE was purified by gas chromatography.

Mass spectrometer analysis established that there was no d_4 content in any of the 1,1,1-TDE samples synthesized by three different routes. It was much more difficult to establish d_2 content and whether 1,1,2-TDE was present. The parent peak mass spectra indicated that the d_2 content was probably less than 4%. The similar ethylene-d_3 and ethylene-d_2 ratios in the products of ethane synthesized by different methods was considered good evidence that little or no 1,1,2-TDE was present in the ethane. ^{13}C and ^1H NMR analysis also indicated the mole ratio of 1,1,2-TDE to 1,1,1-TDE was less than 0.03.[12]

The pyrolyses were performed either in a cylindrical quartz reaction vessel, 5-cm in diameter, 100-cm^3 volume, with a surface/volume ratio of 1.3 cm^{-1}, or in a similar vessel packed with quartz shell tubing whose axes were parallel to the axis of the reaction vessel and had a S/V of 6.1 cm^{-1}.

The reacted mix was expanded through a 5-cm^3 U-trap packed with silica sand into a sample flask at 77 K. The volatile products from liquid N_2 were analyzed with a mass spectrometer and the remaining material was separated by gas chromatography. The ethylene fraction was trapped and examined with a mass spectrometer for parent ion peaks. The validity of the experimental procedure was checked by subjecting known mixes of ethylene and ethylene-d_4 as well as H_2, HD, and D_2 to the above procedure.

Experimental Results

The data in Table I show the H_2/D_2 and HD/D_2 ratios with variation of temperature, pressure of reactant, and time of reaction. It may be seen that temperature has an effect on the ratios; both H_2/D_2 and HD/D_2 ratios decrease with increasing temperature. The total amount of H atom/total amount of D atom ($\Sigma H/\Sigma D$) calculated by $(2 \times \text{yield}_{H_2} + \text{yield}_{HD})/(2 \times \text{yield}_{D_2} + \text{yield}_{HD})$ is always larger than unity, decreasing with increasing temperature. The effect of methyl radical on the distribution of deuterium marking is very slight since the hydrogen/methane ratio is about 100.[7]

The ethylene-d_3/ethylene-d_2 ratios indicate that ethylene-d_3 increases from 4 to 10% of the ethylene-d_2, as the pressure decreases from 960 to 40 Torr. The d_3 percentage tends to be somewhat higher at higher temperatures, but this small effect is somewhat masked by data scatter. Within the limits of the data scatter (not over 10%) there is no effect of time of reaction, temperature, or surface on the ethylene-d_3/ethylene-d_2 ratio.

The ethylene-d_1/ethylene-d_2 ratios are less reliable than the ethylene-d_3/ethylene-d_2 ratios due to extraneous background at masses 27, 28, and 29. Hence, conclusions in this paper will not depend on the quantitative analysis of this ratio.

The addition of carbon dioxide or xenon slightly increased the ethylene-d_3/ethylene-d_2 ratio: the increase is slightly larger than the experimental error associated with these measurements. However, the $\Sigma H/\Sigma D$ ratio did decrease as the "inert" gas was added.

Reaction vessels of high and low surface-to-volume ratios were used. The yield ratios H_2/D_2, HD/D_2, $\Sigma H/\Sigma D$, $CHDCD_2/CH_2CD_2$, and CH_2CHD/CH_2CD_2 were within experimental error, independent of S/V.

Discussion

H Abstraction. If the H_2, HD, and D_2 are formed via abstraction by H and D atoms, then the following reactions are of importance:

$$CH_3\dot{C}D_2 \rightarrow H + CH_2CD_2 \qquad (1)$$

$$\dot{C}H_2CD_3 \rightarrow D + CH_2CD_2 \qquad (2)$$

$$H + CH_3CD_3 \rightarrow H_2 + \dot{C}H_2CD_3 \qquad (3)$$

$$H + CH_3CD_3 \rightarrow HD + CH_3\dot{C}D_2 \qquad (4)$$

$$D + CH_3CD_3 \rightarrow HD + \dot{C}H_2CD_3 \qquad (5)$$

$$D + CH_3CD_3 \rightarrow D_2 + CH_3\dot{C}D_2 \qquad (6)$$

Assuming H and D atoms discriminate similarly in abstraction of H and D atoms from hydrocarbons, the ratio of rate constants k_3/k_4 should equal k_5/k_6. Setting $r = k_3/k_4$ then

$$\frac{(H_2)}{(D_2)} = \frac{k_3(H)}{k_6(D)}$$

and

$$\frac{(HD)}{(D_2)} = \frac{k_4(H)(CH_3CD_3) + k_5(D)(CH_3CD_3)}{k_6(D)(CH_3CD_3)} = \frac{1}{r}\left(\frac{H_2}{D_2}\right) + r$$

Substituting the experimental ratios of hydrogens and using the larger root since r is known to be greater than 1, it is seen that for low S/V, r equals 2.0 at 578 °C and 2.1 at 520 °C.

TABLE I: Ratios of Hydrogens and Ethylenes Formed in the Decomposition of CH_3CD_3 as a Function of Experimental Variables

Temp, °C	P (total), Torr	Inert CH_3CD_3	Time, s	H_2/D_2	HD/D_2	$\Sigma H/\Sigma D$	$CHDCD_2/CH_2CD_2$	CH_2CHD/CH_2CD_2
520	40	0	360	1.69	2.97	1.28	0.091	0.040
520	40	0	600	1.62	2.89	1.25	0.097	0.030
520	40	0	600	1.66	2.86	1.27	0.094	0.036
520	40	0	750	1.64	2.82	1.27	0.095	0.033
520	40	0	1200	1.69	2.90	1.28	0.092	0.041
520	150	0	120	1.70	2.86	1.29	0.076	0.036
520	150	0	180	1.78	2.94	1.32	0.068	0.028
520	150	0	180	1.72	2.92	1.29	0.070	0.028
520	154	0	1200	1.78	2.88	1.32	0.095	0.047
520	960	0	180				0.045	0.028
520	960	0	360	1.72	2.86	1.28	0.056	0.026
520	920	0	600	1.73	2.89	1.29	0.045	0.032
	Inert = CO_2							
520	968	22.2:1	180	1.52	2.88	1.21	0.102	0.042
520	968	22.2:1	360	1.54	2.86	1.22	0.105	0.041
520	968	22.2:1	360	1.43	2.74	1.18	0.097	0.038
520	968	22.2:1	360	1.52	2.83	1.21	0.106	0.047
520	968	22.2:1	360	1.50	2.83	1.21	0.107	0.040
520	968	22.2:1	360	1.48	2.74	1.20	0.108	0.027
520	968	22.2:1	600	1.55	2.82	1.23	0.119	0.053
520	968	22.2:1	1200	1.48	2.72	1.20	0.142	0.056
520	968	22.2:1	1800	1.58	2.73	1.24	0.160	0.082
	Inert = Xenon							
520	982	22.2:1	180	1.60	2.86	1.24	0.097	
520	1002	22.2:1	180	1.48	2.74	1.20	0.108	0.036
520	982	22.2:1	180	1.58	2.80	1.24	0.100	0.048
520	946	22.2:1	180	1.60	2.89	1.25	0.113	0.050
520	982	22.2:1	180	1.62	2.81	1.26	0.105	0.040
520	860	22.2:1	180	1.63	2.91	1.26	0.102	0.037
520	960	22.2:1	180	1.55	2.84	1.23	0.105	0.042
520	982	22.2:1	240	1.62	2.85	1.26	0.103	0.038
520	1150	22.2:1	240	1.61	2.82	1.25	0.108	0.044
520	900	22.2:1	360	1.74	2.89	1.30	0.106	0.037
520	800	22.2:1	360	1.69	2.95	1.28	0.091	0.035
520	860	22.2:1	1800	1.59	2.85	1.24	0.196	0.053
578	40	0	30	1.45	2.75	1.19	0.099	0.056
578	40	0	45	1.46	2.74	1.19	0.098	0.036
578	153	0	15	1.46	2.64	1.20	0.091	0.039
578	153	0	30	1.52	2.80	1.22	0.085	0.029
578	153	0	45	1.56	2.81	1.23	0.092	0.046
578	153	0	150	1.54	2.78	1.23	0.107	0.048

Similarly, for high S/V, r equals 2.0 at 600 °C and 2.2 at 510 °C. Thus, within experimental error, S/V has no effect on the ratio of abstraction of H or D. The small change in r with temperature indicates that the difference in energy of activation for abstraction of H and D must be small. If the value of r at the high and low temperatures of the range studied is substituted in the Arrhenius equation, then the ratio of preexponential factors for abstraction of H and D atoms, A_H/A_D, is calculated to be 1.25 and the corresponding energy of activation difference $E_D - E_H = 800$ cal/mol. Both values are in harmony with unpublished data of Gordon and Smith on studies of abstraction of H and D from hydrocarbons by H or D atoms, and those reported by McNesby.[8]

Ethyl Abstraction and Isomerization. Reactions 1–6 comprise a self-regulating closed system in which $\Sigma H/\Sigma D$ and H_2/D_2 should be unity. The deficiency of D atoms (which only show when $D_2 < H_2$) suggests that D atoms are buried in other products. Two possibilities exist:

(1) Exchange of $CH_3\dot{C}D_2$ and $\dot{C}H_2CD_3$ radicals via an abstraction reaction from the parent ethane.

$$CH_3\dot{C}D_2 + CH_3CD_3 \rightarrow CH_3CD_2H + \dot{C}H_2CD_3 \quad (7)$$

$$\dot{C}H_2CD_3 + CH_3CD_3 \rightarrow CD_3CH_2D + CH_3\dot{C}D_2 \quad (8)$$

(2) Isomerization of $CH_3\dot{C}D_2$ and $\dot{C}H_2CD_3$.

$$CH_3\dot{C}D_2 \rightarrow \dot{C}H_2CD_2H \quad (9)$$

$$\dot{C}H_2CD_3 \rightarrow CH_2D\dot{C}D_2 \quad (10)$$

followed by decomposition

$$\dot{C}H_2CD_2H \rightarrow CH_2CD_2 + H \quad (11)$$

$$\dot{C}H_2CD_2H \rightarrow CH_2CDH + D \quad (11')$$

$$CH_2D\dot{C}D_2 \rightarrow CHDCD_2 + H \quad (12)$$

$$CH_2D\dot{C}D_2 \rightarrow CH_2CD_2 + D \quad (12')$$

or abstraction

$$\dot{C}H_2CD_2H + CH_3CD_3 \rightarrow CH_3CHD_2 + \dot{C}H_2CD_3 \quad (13)$$

$$\dot{C}H_2CD_2H + CH_3CD_3 \rightarrow CH_2DCHD_2 + CH_3\dot{C}D_2 \quad (13')$$

$$CH_2D\dot{C}D_2 + CH_3CD_3 \rightarrow CH_2DCD_3 + CH_3\dot{C}D_2 \quad (14)$$

$$CH_2D\dot{C}D_2 + CH_3CD_3 \rightarrow CH_2DCD_2H + \dot{C}H_2CD_3 \quad (14')$$

A competition between decomposition or isomerization followed by abstraction is suggested. Both processes are moderated by abstraction. Abstraction will dominate at high ethane pressures. Consequently, at high ethane pressures the D atoms are buried in the ethane-d_4 for the most part. At low ethane pressure the ethylene-d_3 mainly accounts for the D-atom deficiency.

The presence of ethylene-d_3 supports the possibility for isomerization. However, other paths producing ethylene-d_3 must first be eliminated. Four such paths are: (i) heterogeneous decomposition of $C_2H_3D_3$; (ii) homogeneous decomposition of $C_2H_2D_4$; (iii) homogeneous decomposition of CH_2DCD_2H; (iv) addition of D to $C_2H_2D_2$. Path (i) is dismissed since the $CHDCD_2/CH_2CD_2$ yield ratio was found to be independent of S/V. Likewise, (ii) and (iii) are eliminated since there is only a small percentage of ethane-d_4 and -d_3 generated during the reaction and the initial $C_2H_3D_3$ contained only 1,1,1-trideuterioethane. The formation of ethylene-d_3 by path (iv) would involve the addition of D atoms to a primary product, ethylene-d_2

$$D + CH_2CD_2 \rightarrow CH_2D\dot{C}D_2 \quad (15)$$

followed by

$$CH_2D\dot{C}D_2 \rightarrow H + CHDCD_2 \quad (16)$$

$$CH_2D\dot{C}D_2 \rightarrow D + CH_2CD_2 \quad (16')$$

If reaction 15 was important, then increasing the time of reaction should markedly increase the d_3/d_2 ratio. Since the ethylene is a product of the reaction, a longer reaction time permits a larger average reaction of D atoms and 1,1-dideuterioethylene. The ethylene-d_3/d_2 ratios remained constant, within experimental error, for small percentage of decomposition (see Table I). The evidence clearly indicates that reaction 15 is not important in our reaction system, and that the ethylene-d_3 is probably the result of reaction 10 followed by reactions 12 and 14.

If we ignore the hydrogen and deuterium atoms buried in the d_2 and d_4 ethane products, the $\Sigma H/\Sigma D$ may be calculated from the ethylenes and compared with the same ratio from the hydrogens. Every CH_2CD_2 in the products results in one hydrogen plus one deuterium atom being injected into the product hydrogens and similarly ethylene-d_3 and -d_1 results in two hydrogen plus no deuterium and two deuterium plus no hydrogen atom, respectively.

Assuming that all the deficient D atoms are buried in the ethylenes then $\Sigma H/\Sigma D$ can be calculated from the ethylene-d_1, -d_2, and -d_3 yields by

$$\left.\frac{\Sigma H}{\Sigma D}\right|_{\text{ethylene}} = \left[1 + 2\frac{(CHDCD_2)}{(CH_2CD_2)}\right] \Big/ \left[1 + 2\frac{(CH_2CHD)}{(CH_2CD_2)}\right]$$

where $(\Sigma H/\Sigma D)|_{\text{ethylene}}$ is the $\Sigma H/\Sigma D$ calculated from the ethylenes. From the experimental ethylene yields, the calculated $(\Sigma H/\Sigma D)|_{\text{ethylene}}$ decreases from 1.10 to 1.04 as the ethane pressure increases from 40 to 960 Torr, while the observed $\Sigma H/\Sigma D$ from the product hydrogens remains constant at 1.27 within experimental error (see Table I). Thus, D atoms may be buried in ethane products in addition to those buried in the ethylenes.

To check this hypothesis, steady-state and time-dependent computer experiments using reactions 1–8 with literature values[9] for the rate constants and isotope effects were performed. From these hydrogen yields based on the above calculations, $\Sigma H/\Sigma D$ was 1.32; changing the isotope effect for ethyl abstraction of H and D by 20% altered $\Sigma H/\Sigma D$ by approximately 10%. Thus, the deviation of $\Sigma H/\Sigma D$ from unity is due both to abstraction from the parent and to isomerization to form ethylene-d_3 and -d_1.

The competition between ethyl radical abstraction and isomerization/decomposition is shown by the fact that the experimental $CHDCD_2/CH_2CD_2$ ratio decreases as the ethane pressure increases, but remains constant for a given ethane concentration when the pressure is increased with an inert gas such as CO_2 or Xe. The results with CO_2 and Xe also indicate that the $CH_2D\dot{C}D_2$ radical precursor of the ethylene-d_3 decomposes from a thermalized population distribution (see Table I).

The competition is also qualitatively shown by the temperature dependence of the H_2/D_2 or $\Sigma H/\Sigma D$ ratios. These ratios decrease with an increase of temperature since the decomposition reactions 1, 2, 9–12 have a higher activation energy than the abstraction reactions 7, 8, 13, and 14.

Ethyl Steady State. As the reaction goes from the decomposition region (low pressure) to the abstraction region (high pressure), the steady-state concentrations calculated from the model are affected as shown below.

Assuming (a) that the H and D atoms behave similarly in abstraction reactions and (b) reactions 7–14 are unimportant, the steady state $\dot{C}H_2CD_3/CH_3\dot{C}D_2$ ratio is

$$\dot{C}H_2CD_3/CH_3\dot{C}D_2 = (k_1/k_2)r$$

The difference in activation energy between reactions 1 and 2 is the bond strength difference between C–D and C–H, so $k_1/k_2 = 2.5$ at 520 °C. Thus, the $\dot{C}H_2CD_3/CH_3\dot{C}D_2$ ratio at 520 °C is approximately 5.3.

However, if reactions 7 and 8 are very rapid compared to reactions 1 and 2, then the $\dot{C}H_2CD_3/CH_3\dot{C}D_2$ ratio would be lowered to 2.1 at 520 °C. The decrease of $\dot{C}H_2CD_3/CH_3\dot{C}D_2$ with an increase of pressure in the transition region suggests that $CHDCD_2/CH_2CHD$ will decrease since $\dot{C}H_2CD_3$ and $CH_3\dot{C}D_2$ are the precursors to $CHDCD_2$ and CH_2CHD, respectively. This prediction is in accord with the experimental findings.

Isomerization Rate Constant. The rate constant for isomerization can be estimated by extrapolating the $CH_2CD_2/CHDCD_2$ ratio to zero pressure: the extrapolated value is approximately 10. Thus, one $CHDCD_2$ is observed for 10 CH_2CD_2 in the decomposition environment. The $CHDCD_2$ is produced from $CH_2D\dot{C}D_2$ which can also produce a CH_2CD_2. In the temperature range of this study, the rate of loss of an H atom is about 2.5 times the loss of a D atom. Therefore, 1.2 CH_2DCD_2 must decompose for every $CHDCD_2$ formed. CH_2CD_2 is formed from two dominant radicals: $\dot{C}H_2CD_3$ and $CH_3\dot{C}D_2$. Since they are in a steady-state ratio of ~5.1 and have a decomposition rate constant ratio of 0.4, approximately 6.8 of the 10 observed CH_2CD_2 originate from the $\dot{C}H_2CD_3$ radical. Thus, the relative rate of D isomerization to D splitoff is 0.18. Using the preferred Arrhenius parameters for the decomposition of ethyl radicals,[9] the A factor and activation energy for isomerization are $10^{12.8\pm1.1}$ s^{-1} and 40.7 ± 4.0 kcal/mol, respectively.

Computer experiments were performed using reactions 1–8 and 11–14 and their published rate constants.[9] Within the uncertainties in these rate constants it was concluded that the isomerization rate constant is 0.2 ± 0.1 of the competitive decomposition rate constant, this is in qualitative agreement with the simple reasoning given above.

Isomerization Mode The fact that $CH_2CD_2/CHDCD_2$ is independent of temperature in the range 520–586 °C suggests that reactions 2 and 10 have similar critical energies (within 1.5 kcal/mol) and thus the difference in rate constants is due solely to the difference in A (steric) factors. This fact strongly suggests that in both reactions the initial reaction coordinate is similar, and as the hydrogen or deuterium carbon bond lengthens ($C_2 \cdots H$), there is a certain probability (approximately 0.1) that the "expelled" hydrogen or deuterium will be "captured" by the

$$\dot{C}_1—\dot{C}_2\cdot^H$$

radical carbon (C_1). This can be visualized with two models:

(i) The C_1C_2H bending motion in similar decomposition complexes[10] is taken to be approximately 150 cm^{-1}. Assuming a Boltzmann energy distribution and a temperature of 550 °C (midway in the experimental temperature range), the average occupied vibrational quantum state of the bending motion is $n = 3$. In this quantum state the classical maximum amplitude of oscillation is ±75°, and the probability of an amplitude greater than 55° is approximately 0.1. The corresponding C_1C_2H bond angle would be less than 54°. The process can thus be envisioned as one in which the hydrogen is stretching and bending and that ~10% of the time it is captured by the adjacent carbon atom, C_1.

(ii) Preliminary quantum calculations (MINDO/II′) have been performed for various configurations of the ethyl radical.[11] The minimum path for the process in which $H + C_2H_4$ is formed has been computed. This minimum path involves the carbon–hydrogen stretch such that the hydrogen is "exiting" in a direction toward the nonbonded carbon (C_1); the maximum energy on the minimum path corresponds to the hydrogen and two carbon atoms at the vertices of an isosceles triangle. From a static (motionless) point of view, the atom in this configuration has three possible paths: (a) decomposition to $H + C_2H_4$; (b) addition to carbon 1 producing an ethyl radical, or (c) addition to carbon 2 also producing an ethyl radical. The actual probability of each path depends on the trajectories (motions) involved.

Introducing the kinematic factor in both models, one would expect atoms with low velocities to be trapped by the adjacent carbon atom, while high velocity atoms will fly off, producing $H + C_2H_4$. Consequently, D would be expected to isomerize more rapidly than H in these systems.

Acknowledgment. D.C.T. expresses his appreciation to the Office of Naval Research for support. R.I. is grateful for an NRC postdoctoral fellowship supported by NWC.

References and Notes

(1) NRC Postdoctoral Fellow.
(2) (a) J. W. Wilt, "Free Radical Rearrangements", in "Free Radicals", Vol. 1, J. K. Kochi, Ed., Wiley, New York, N.Y., 1973, pp 332–502; (b) M. Julia, *Pure Appl. Chem.*, **15**, 167 (1967).
(3) W. M. Jackson and J. R. McNesby, *J. Chem. Phys.*, **36**, 2272 (1962).
(4) C. A. Heller and A. S. Gordon, *J. Phys. Chem.*, **62**, 709 (1958).
(5) J. A. Kerr and A. F. Trotman-Dickenson, *Trans. Faraday Soc.*, **54**, 921 (1958).
(6) D. C. Tardy, *Int. J. Chem. Kinet.*, **6**, 291 (1974).
(7) See papers by M. Back, A. S. Gordon, and R. H. Knipe in "The Mechanisms of Pyrolysis Oxidation and Burning of Organic Materials", *Natl. Bur. Stand. (U.S.), Spec. Publ.*, **No. 357** (1972).
(8) J. R. McNesby, *J. Phys. Chem.*, **64**, 1671 (1960).
(9) (a) A. F. Trotman-Dickenson and G. S. Milne, *Natl. Stand. Ref. Data Ser., Natl. Bur. Stand.*, **No. 9** (1967); (b) S. W. Benson and H. E. O'Neal, *ibid.*, **No. 21** (1970).
(10) B. S. Rabinovitch, R. F. Kubin, and R. E. Harrington, *J. Chem. Phys.*, **38**, 405 (1963).
(11) K. Sando and N. Ertz, private communication.
(12) The authors thank D. W. Moore of these laboratories for the analyses.

Laser Augmented Decomposition. 2. D_3BPF_3

K-R. Chien and S. H. Bauer*

Department of Chemistry, Cornell University, Ithaca, New York 14853 *(Received January 12, 1976)*

We continued the study of the accelerated decomposition of H_3BPF_3 induced by laser radiation (930–950 cm^{-1}), and extended it to the fully deuterated species. While in all essential respects the kinetics of the ir photolysis for the two compounds are identical, the few differences which were uncovered proved crucial in pointing to interesting features of the mechanism. These verified predictions based on a normal mode analysis for the distribution of potential energy among the internal coordinates. For the laser augmented decomposition, $E_a^L = 3.5 \pm 1$ kcal/mol, compared with $E_a^{th} = 29.3$ kcal/mol for the thermal process. The quantum efficiency is low, $\approx 4 \times 10^4$ photons/molecule decomposed. The rates of decomposition depend on the isotopic content and are sensitively dependent on the frequency of the irradiating line. For example, with P(24) large fractionation ratios were found for D_3BPF_3 vs. H_3BPF_3, and small differences for $D_3{}^{11}BPF_3$ vs. $D_3{}^{10}BPF_3$. The levels of decomposition induced by the sequential three-photon absorption have been semiquantitatively accounted for.

Introduction

We previously reported[1] (designate I) on the laser augmented decomposition:

$$2H_3BPF_3 \xrightarrow{10.6\ \mu} B_2H_6 + 2PF_3 \qquad (1)$$

and demonstrated that (i) the enhanced rate at room temperature is a consequence of vibrational excitation, not of thermal heating; (ii) the effect is highly specific, being sensitively dependent on the P(J) value of the irradiating CO_2 laser line; (iii) vibration–vibration pumping appears to be ineffective for augmenting the rate of the strictly analogous reaction

$$2H_3BCO \rightarrow B_2H_6 + 2CO$$

when the carbonyl was admixed with the perfluorophosphine adduct; and, (iv) the dependence of decomposition on power levels indicated participation of three or more photons.

At this time we report on further studies of reaction 1, with primary emphasis on D_3BPF_3. A vibrational normal mode analysis for these compounds indicated that the augmentation factor may be increased by deuteration, and that in D_3BPF_3 the difference in rates for $^{10}B/^{11}B$ may be detectable. We also undertook to determine directly the dependence of the laser-induced decomposition on time, pressure, laser power, and ambient temperature. We have estimated the quantum efficiency.

These experiments were designed to generate critical information on multiphoton absorption processes and on questions pertaining to intramolecular energy migration.

Experimental Section

1. *Preparations and Spectral Analysis.* The D_3BPF_3 was prepared in a high-pressure bomb by mixing 1 part B_2D_6 with 10 parts of PF_3, at a total pressure of about 3 atm. The mixture attained equilibrium at room temperature in about 30 h. It was fractionated through a −160 °C trap (2-methylbutane) into a liquid nitrogen trap; the D_3BPF_3 remained in the −160 °C vessel, from which it was transferred to sample tubes. The product was characterized by its infrared absorption spectrum (Perkin-Elmer No. 521) and mass analyzed (CEC21-103A). To ascertain the extent of any hydrogen impurity, the sample was submitted for a high resolution, mass spectral analysis (AEI-MS-902); D_2HBPF_3 was present at 8.5%, with no significant levels of DH_2BPF_3.

Moderate resolution infrared spectra in the P–F stretching region for the hydrogenic and deuterated adducts are shown in Figure 1. Except for the hatched region including the sharp, unassigned feature at 931 cm^{-1} present in H_3BPF_3, the band shifts to higher frequency by ≈ 12 cm^{-1}, without substantial changes in shape. This has been checked for several independent preparations. Thus, it appears that the shifted band has the character of the normal mode ν_3, ascribed primarily to the P–F symmetric stretching vibration.[2] To confirm our previous conclusion that there is no substantial rotational fine structure at this region[3] we measured, line by line, the low power absorption coefficient for D_3BPF_3 [α_{10}] with the sample external to the cavity, utilizing a spectrophone. The results are shown in Figure 2, wherein the $\alpha_{1,0}$'s for H_3BPF_3 were included for comparison. These band shapes reproduce the shapes recorded with the PE 521. Clearly there is no indication of significant rotational fine structure in these bands. However, at very low pressures the absorption coefficient is pressure dependent. Thus, for P(28), α_{10} [for H_3BPF_3] declines from 6.8×10^{-2} at 150 mTorr to 1.24×10^{-2} at 43 mTorr, indicating that saturation is a factor. Pressuring the sample with He has very little effect, but added Xe, even when present in the ratio of only 2/1, increases α_{10} by 2.3.

2. *Details of Experimental Operations.* The apparatus and experimental method were described in I. The salient points are as follows. Before each run, the D_3BPF_3 sample at −160 °C, was pumped on to remove residual B_2D_6 and PF_3. Pressures in the intracavity reaction cell were 2–5 mTorr, but on occasion was raised to 15 mTorr. The samples were irradiated with selected laser lines for specified periods, generally 12 min. Laser powers were monitored with a Coherent Radiation No. 201 power meter which fed into a strip chart recorder for time averaging of the signal. Since a 95% reflecting output mirror was used, the total irradiating laser power was 40× the measured output power. The irradiated sample was then trapped in a U tube cooled with liquid nitrogen, and transferred for mass spectral analysis, or collected in a small cell for ir spectral analysis. The percent decomposition was estimated from the relative peak heights at mass 103 ($D_2BPF_3{}^+$) for the irradiated and nonirradiated samples. The ratio of mass 88 ($PF_3{}^+$) to mass 103 was also used to check on the composition. The inlet

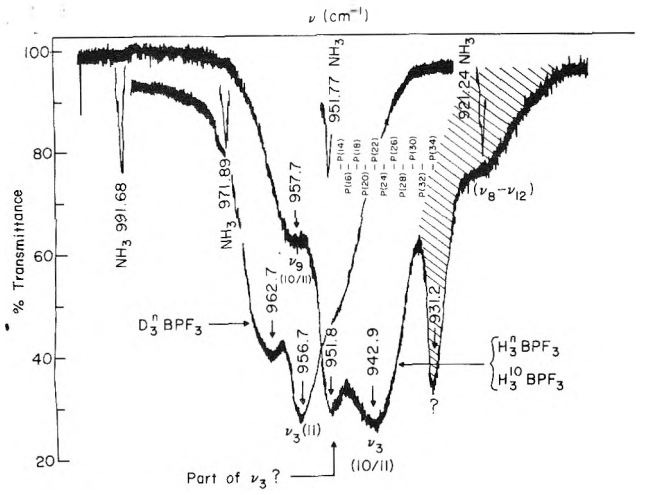

Figure 1. Absorption spectrum, recorded with the PE No. 521: sample pressure, 1.7 Torr; cell temperature, room temperature; cell length, 7.5 cm; spectrometer resolution, 0.2 cm^{-1}. The assignments shown are those given by Taylor and Bissot.[2a] The reassignments proposed in ref 2b for the vapor at −126 °C show four unaccounted frequencies (vs + vvs); indeed, our normal mode analysis appears to be in better agreement with the 1956 assignments.

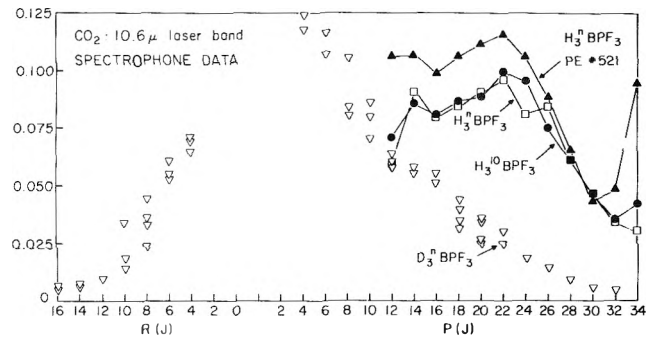

Figure 2. Absorption coefficients $[\alpha_{1,0}]$ at low power levels [0.3 W/cm^2] with the sample at ≃300 mTorr. The coefficients peak at P(4) for D_3BPF_3 and at P(22) for H_3BPF_3.

system of the mass spectrometer (CEC-103A) is equipped with a capacitance manometer, so that the initial sample pressures could be controlled.

With the cell at room temperature the compound was irradiated with different P(*J*) lines, for selected laser power and time, to determine the most effective line for augmenting the decomposition. With the grating set on that line, we determined the dependence of decomposition rate, for a set laser power, on sample pressure, and on irradiation time. Then, we also determined the dependence of the extent of decomposition on laser power (which ranged from 50 to 120 W). Finally many runs were repeated at a higher sample temperature (38 °C) so that we could estimate an "activation energy" for the augmented rate.

To determine the photon conversion efficiency we measured changes in laser output levels due to intracavity power absorption by the sample, at the laser power levels used for the moderate photolysis runs (approximately 60 W). Samples were injected into the intracavity cell, and the decrease in power was rapidly recorded. The *mean* absorption coefficients $\langle\alpha\rangle$ were calculated following the analysis of Kaufman and Oppenheim.[4] These authors developed relations between the absorption coefficients measured for gaseous samples external to the cavity, at specified power levels, and changes in the laser output with the same absorbers intracavity. Thereby they were able to determine the laser parameters under high gain operation. They found that laser output decreased essentially linearly with $(1 - e^{-\alpha D})$ until lasing was quenched; D is the intracavity absorption cell length and α is in cm^{-1}. Write $J_L/J_L{}^0 = 1 - \beta(1 - e^{-\alpha D})$. For their CO_2 laser, at the P(20) line the unsaturated single-pass gain coefficient, $g_0 = 0.0053$ cm^{-1} and $\beta = 3.33$. It follows that for lasing conditions with known β, the effective intracavity absorption coefficient can be determined from measurement of the decrement in laser output produced by the injected sample.

$$\alpha D = \ln\left[\frac{\beta}{(\beta - 1) + J_L/J_L{}^0}\right] \qquad (2)$$

To obtain $\langle\alpha\rangle$ values for our sample, we assumed $\beta = 3.33$, since our lasers are of very similar construction, and the results are not sensitive to small changes in β. Also, $\alpha = \langle\alpha\rangle p$ at these low pressures. Typically, for H_3BPF_3 at P(32) (J/J_0) is plotted vs. p(sample) in Figure 3, and the $\langle\alpha\rangle$ coefficients for selected lines are listed in Table I; their absolute uncertainty is about 75% due to the instability in the laser power output; their *relative* magnitudes are much more reliable. $\langle\alpha\rangle$ differs from $\alpha_{1,0}$ in magnitude and P(J) dependence because the former measures multiphoton processes.

The isotopic compositions of the sample [$^{10}B/^{11}B$ and $D_2H^{11}B/D_3{}^{10}B$] were first estimated from the high resolution spectral scans. The mixture used consisted of approximately 92% D_3BPF_3 and 8% HD_2BPF_3; under these conditions the contribution to mass 11 from ^{10}BH was negligible. Hence the m/e ratio for 10/11 obtained with the low resolution spectrometer was used to ascertain the isotopic selectivity of the laser driven photolysis. The mixture of reaction products (B_2D_6, PF_3, and D_3BPF_3) was kept at −160 °C, so that the PF_3 and B_2D_6 vented into the inlet line of the spectrometer first. The boron isotope ratios were then measured for both the product, B_2D_6, and the remaining reactant. The isotopic composition relative to H/D was determined by combining the ratio of the peak heights for 10/11 with those for 104/105 [$(HD_2{}^{11}BPF_3 + D_3{}^{10}BPF_3)/D_3{}^{11}BPF_3$]. In these experiments the laser power level was kept at 120 W with the sample pressure at 2 mTorr. Products from thermal decomposition driven to the same extent as were the laser irradiated samples were analyzed concurrently to establish the specificity for isotope separation by laser irradiation.

Summary of Results

1. *P(J) Dependence.* The percent of decomposition of D_3BPF_3 and H_3BPF_3 for 12-min irradiation times, utilizing selected laser lines at the specified laser powers, are plotted in Figure 4. We estimate the precision of each point to be ≈35%, due to the combined uncertainties introduced by fluctuations in laser power, losses during handling of the sample, and the analytical methods. Note that the highest decompositions are produced by P(32) for H_3BPF_3 and by P(24) for D_3BPF_3. In each case *the most efficient frequency does not correspond to the maximum in the $\alpha_{1,0}$ values but to maxima in the $\langle\alpha\rangle$'s;* refer to Table I. Furthermore, the highest yield for D_3BPF_3 is larger than the corresponding one for H_3BPF_3. Finally, the percent decomposition increases nonlinearly with laser power. In view of the low efficiency for decomposition of D_3BPF_3 at P(32) where the rate for H_3BPF_3 is a maximum [and, vice versa for P(24)] this procedure provides a basis, albeit not a practical one, for the separation of H/D isotopes. For this process, the CO laser augmented decomposition of D_3BCO will prove more efficient.

TABLE I: Mean Absorption Coefficients $\langle\alpha\rangle$ (cm^{-1} $Torr^{-1}$) and Quantum Efficiencies φ (photons absorbed/molecule decomposed)

	D_3BPF_3		H_3BPF_3	
Laser line	$\langle\alpha\rangle$	φ	$\langle\alpha\rangle$	φ
P(20)	1.07×10^{-2}			
P(24)	3.20×10^{-2}	4.24×10^4		
P(26)	2.24×10^{-2}			
P(32)			3.00×10^{-2}	5.48×10^4

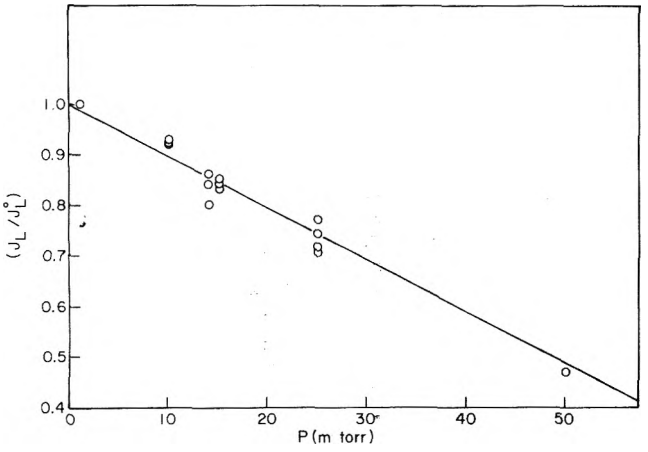

Figure 3. Changes in laser output at P(32) with increasing sample pressure. p(H_3BPF_3) in mTorr: D = 110 cm, T = 298 K.

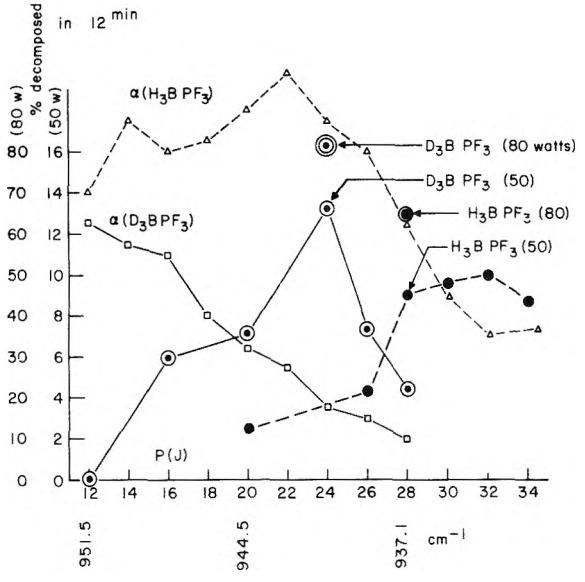

Figure 4. Percent of reactant decomposed during 12 min of irradiation at the indicated power levels.

2. *Power Dependence.* The percent decomposition at two temperatures, as a function of the total laser flux in the cavity, is plotted in Figure 5; it is not linearly dependent on the power. Graphs of log(percent decomposition of D_3BPF_3) vs. log(laser power), Figure 6, were linear, with slopes ≈3.1, similar to our previously reported values for H_3BPF_3.[1] This indicates that at least three photons are required per mole of reactant for the augmented decomposition. Our data are not sufficiently precise to determine whether there is a threshold power level.

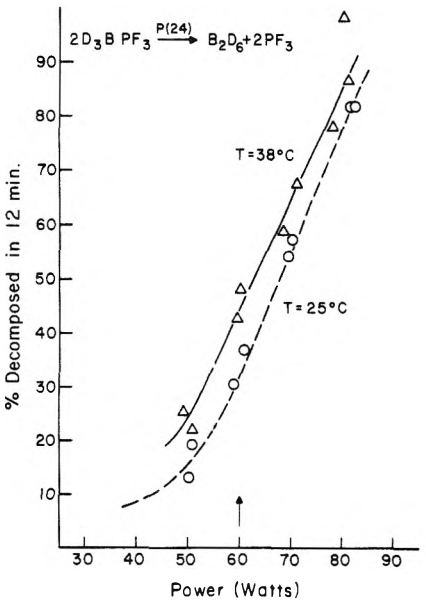

Figure 5. Percent decomposed in 12 min of irradiation, as a function of irradiating power (intracavity), at two temperatures.

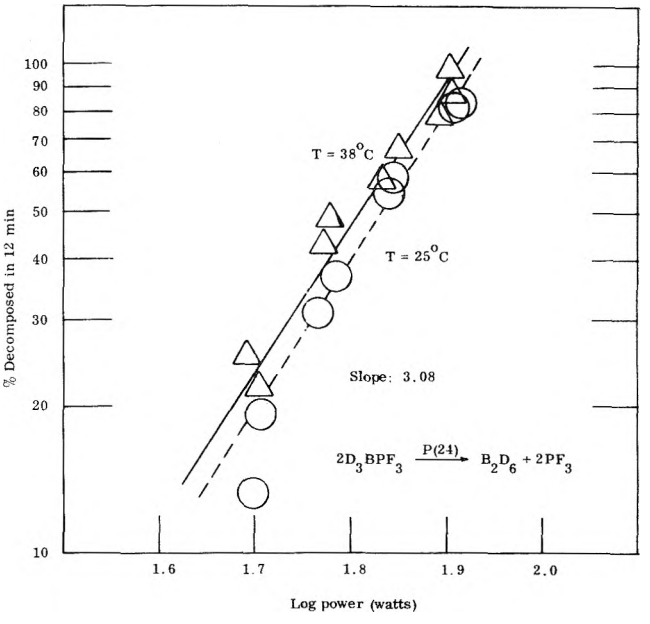

Figure 6. Percent decomposed vs. irradiating power, in log–log coordinates.

3. *Proof of Specificity.* In I we found that when H_3BCO was added to H_3BPF_3 and the mixture irradiated, there was no augmented decomposition of the carbonyl while the rate of decomposition of the perfluorophosphine adduct remained unaltered. This demonstrates that a specific mode of vibration had to be excited to induce decomposition of the H_3BCO, and that v–v transfer was inadequate. Similar tests were made with D_3BPF_3 plus H_3BCO mixtures, with identical results.

4. *Rate Constant and Activation Energy.* We found that the augmented rate, i.e., percent of H_3BPF_3 decomposed by P(32), was independent of the sample pressure from 1 to 15 mTorr, which suggests that the reaction is essentially first order. When the pressure was raised to 25 mTorr and later to 50 mTorr the rate increased by factors of 2 and 3, respectively. We interpret the enhanced rate at the higher pressure as a thermal contribution to the overall rate. For runs below 15

TABLE II: Rate Constants and "Activation Energies"

Compd	Laser line and power level	k (wall temperature)		E_a^L, kcal/mol
H_3BPF_3	P(32); 50 W	1.46×10^{-4} s^{-1} (25 °C)		
	P(32); 60 W	4.37×10^{-4} s^{-1} (25 °C)	5.58×10^{-4} s^{-1} (36 °C)	4.03
D_3BPF_3	P(24); 50 W	3.06×10^{-4} s^{-1} (25 °C)	3.75×10^{-4} s^{-1} (38 °C)	2.65
	P(24); 60 W	5.67×10^{-4} s^{-1} (25 °C)	8.30×10^{-4} s^{-1} (38 °C)	5.90
	P(24); 70 W	1.14×10^{-3} s^{-1} (25 °C)	1.39×10^{-3} s^{-1} (38 °C)	2.61
	P(24); 80 W	2.38×10^{-3} s^{-1} (25 °C)	2.83×10^{-3} s^{-1} (38 °C)	2.46

mTorr the rate constants at several laser powers were calculated on the basis of a first-order rate law; the reaction time was kept constant at 12 min. The results are summarized in Table II. The "activation energies" (E_a^L) were deduced from pairs of rate constants at two wall temperatures: 25 and 38 °C. The magnitudes of E_a^L range from 2.5 to 5.9 kcal/mol, with a mean value of 3.5 kcal/mol. At this stage we assumed that the increment in average gas temperature (which must be somewhat higher than the wall temperature) is equal to the increment in wall temperature.

5. *Power–Time Relations.* Figure 7 illustrates the time dependence of augmented rates for several laser powers and sample temperatures. Curves a and b show induction periods, for low powers (50–60 W) at room temperature. However, curves c and d are linear with time for high powers (120 W at room temperature) or low powers at higher temperatures, 60 W at 36 °C.

6. *Selectivity of Decomposition Rate on $^{10}B/^{11}B$ Content.* Define $\kappa \equiv R_I/R_N$ where R_N in the natural abundance ratio ($^{10}B/^{11}B$) and R_I is the ratio present in either the undecomposed material or in the product after laser irradiation. In Table III we listed values of κ for boron and hydrogen for several irradiation times with P(24); $R_N[^{10}B/^{11}B]$ was measured to be 0.248 ± 0.006, and $R_N[(HD_2{}^{11}BPF_3 + D_3{}^{10}BPF_3)/D_3{}^{11}BPF_3]$ was 0.338 ± 0.008. These experiments show that $\kappa_{max}(^{10}B/^{11}B)$ occurs in about 5 min of irradiation time. We anticipate the separation factor to be small based on the computed small shift in the normal mode frequencies for this molecule due to $^{11}B/^{10}B$ substitution. In contrast, κ_{max}(H/D) was found to increase with time, consistent with the large difference in frequencies at which $\langle\alpha\rangle_{max}$ occurs for the two species. To ensure that the differential isotope effects were due to laser irradiation, we analyzed mixtures decomposed thermally to comparable levels; κ remained unchanged.

TABLE III: Isotope Enrichment Factors ($\kappa_{thermal}$ = 1.00)

	Time, min			
	1	3	5	8
B(10)/B(11)[a]	0.85	0.87	0.82	0.96
B(10)/B(11)[b]	1.09	1.35	1.53	1.36
H/D[c]	1.16	1.79	4.19	8.10

[a] Calculated from ratio of $B(10)^+$ to $B(11)^+$ mass peaks, from B_2D_6. [b] Calculated from ratio of $B(10)^+$ and $B(11)^+$ mass peaks, from D_3BPF_3. [c] Calculated from the ratio of $B(10)^+$ to $B(11)^+$ mass peaks, and from ratio of $D_2H^{11}BPF_3^+$ and $D_3{}^{11}BPF_3^+$ mass peaks from D_3BPF_3; laser power = 120 W at P(24); P = 2 Torr.

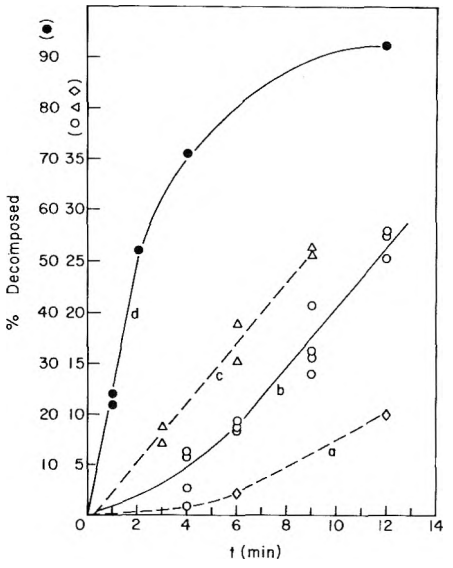

Figure 7. Time dependence of percent decomposed at the specified power levels and temperatures: (a) H_3BPF_3, 50 W [P(32)] at room temperature (23 °C); (b) H_3BPF_3, 60 W [P(32)] at room temperature; (c) H_3BPF_3, 60 W [P(32)] at 36 °C; (d) D_3BPF_3, 120 W [P(24)] at room temperature.

Discussion

The two elementary steps which account for the thermal reaction[5] are:

$$H_3BPF_3 \underset{k_{-1}}{\overset{k_1}{\rightleftharpoons}} H_3B + PF_3 \qquad \Delta H_1^\circ \approx 24.5 \text{ kcal/mol} \qquad (1a, -1a)$$

$$H_3B + H_3BPF_3 \xrightarrow[k_b]{} B_2H_6 + PF_3 \qquad \Delta H_b^\circ \approx -13.4 \text{ kcal/mol} \qquad (1b)$$

During laser photolysis ir energy is absorbed in the ν_3 mode (nominally the symmetric P–F stretch) and this enhances the overall rate of steps 1a,1b which require the scission of the B–P bond. Nevertheless, the augmentation is highly specific, since v–v energy transfer, which cannot be avoided in H_3BPF_3/H_3BCO mixtures, is not effective for decomposing the carbonyl. Furthermore, although the magnitude of the $\langle\alpha\rangle$'s with P(24) for D_3BPF_3 and with P(34) for H_3BPF_3 are very nearly equal (Table I), the efficiency for decomposing the deuterated compound with P(24) is considerably greater than that for the hydrogenic specie with P(32), Figure 4. Clearly, the average number of photons absorbed per molecule, that is, the total vibrational energy content is not the only parameter which determines the rate of reaction. Finally, the fact that no differential rate for $^{10}B/^{11}B$ was found for H_3BPF_3, while a measurable difference was found for D_3BPF_3, is evidence that the effects of laser pumping are sensitive to the molecular dynamics. A normal mode analysis proved illuminating. In Table IV we listed a set of adjusted force constants for a Urey–Bradley potential function for borane–trifluorophosphine, based on the reported raman and infrared spectra. Similar lists of force constants were proposed by Taylor[3] and

TABLE IV: Force Constants (Symmetry Coordinates) Used in Normal Mode Analysis Based on a Urey–Bradley Force Field

$F_1 = f_{BH} + 2f_{BH,BH'} = 3.376$
$F_2 = f_{PB} = 2.3423$
$F_3 = f_{PF} + 2f_{PF,PF'} = 6.4530$
$F_4 = 1/2f_{HBH} + 1/2f_{PBH} + f_{(HBH),(HBH)'} - f_{(PBH),(PBH)'} = 0.4770$
$F_5 = 1/2f_{FPF} + 1/2f_{BPF} + f_{(FPF),(FPF)'} - f_{(BPF),(BPF)'} = 1.4000$
$F_6 = f_{BH} - f_{BH,BH'} = 3.1525$
$F_7 = f_{PF} - f_{PF,PF'} = 5.7323$
$F_- = f_{HBH} - f_{(HBH),(HBH)'} = 0.3538$
$F_9 = f_{PBH} - f_{(PBH),(PBH)'} = 0.3801$
$F_{10} = f_{FPF} - f_{(FPF),(FPF)'} = 1.3080$
$F_{11} = f_{BPF} - f_{(BPF),(BPF)'} = 0.3163$
$F_{12} = f_{PBtorsion} = 0.0916$
$F_{13} = \sqrt{6}(f_{PB,FPF} - f_{PB,FPB}) = 0.383$
$F_{14} = 2\sqrt{2}(f_{PF,FPF} - f_{PF,BPF}) = 0.3722$
$F_{15} = 2\sqrt{3}f_{PB,PF} = 0.4503$

Sawodny and Goubeau.[6] Several interesting features appear. While ν_9 is unaffected by either D/H or $^{11}B/^{10}B$ substitution, the computed value for ν_3 in H_3BPF_3 is 932 cm^{-1}, irrespective of the boron isotope, while in D_3BPF_3 the computed value for ν_3 appears at a considerably higher frequency for the ^{11}B species (986 cm^{-1}) and at a still higher value for $D_3{}^{10}BPF_3$. True, the computed frequencies for these normal modes show substantial discrepancies from those observed, which indicates that the assignments are incomplete, but the analysis does provide a rationalé for the observed trend in the chemical behavior produced by isotopic substitution. This becomes clearer when one compares the potential energy distribution in symmetry coordinate space,[7] as is illustrated in Figure 8. The internuclear distances were derived from microwave spectra[3] while the bracketed numbers show the proportions of the energy in ν_3 allocated to each type of internal vibration. The upper values are for the D_3 compound and the lower for the H_3 species. On the basis of this *sho* approximation we propose that when the adduct absorbs infrared (in normal mode ν_3) a larger fraction of the energy is deposited into the B–P stretching vibration for D_3BPF_3 than for H_3BPF_3. We have yet to calculate analogous energy partitions for multiexcited molecules, where allowance will have to be made for finite amplitude motions.[8]

An estimate of the gross photochemical efficiency was obtained, as follows. The laser power extracted by the sample in the cavity per passage through the cell is $20J_L(1 - e^{-\langle\alpha\rangle pD})$, where J_L is the power read with the monitoring meter, through the output mirror (95% reflecting). At 3 mTorr (298 K), there are $\sim 10^{18}$ molecules in the cell, of which ≈30% decompose in 12 min. The number of photons absorbed is

$$\frac{40J_L\langle\alpha\rangle pD \cdot 10^7\Delta t}{h\nu} \qquad (3)$$

The ratio of photons absorbed/molecule decomposed is $\sim 4 \times 10^4$ (Table I). This low efficiency[9] and the observed low value for $E_a{}^L$ (mean 3.5 ± 1.1 kcal/mol), in contrast to the overall thermal value of 29.3 kcal/mol, may be accounted for by considering: (a) the geometry of the reaction cell, (b) the previously estimated thermal activation energy, $E_a{}^{th}(1b) \approx$ 5 kcal/mol, and (c) the slope of the log (percent decomposition) vs. log(power) line.

The reaction cell was made 12 cm i.d. to provide a large enough volume so that a sufficient amount of material could be manipulated for analysis at the 2–3 mTorr level. The illuminated core is 12 mm in diameter, approximately 2/3 of a

TABLE V: Calculated and Observed Wave Numbers (cm^{-1})

	$H_3{}^{11}BPF_3$		$H_3{}^{10}BPF_3$	$D_3{}^{11}BPF_3$		$D_3{}^{10}BPF_3$
Mode	Calcd	Obsd	Calcd	Calcd	Obsd	Calcd
ν_1	2393	2385	2394	1700	1717	1702
ν_2	1081	1077	1100	854		867
ν_3	932	944	932	986	957	1000
ν_4	613	607	618	571	572	571
ν_5	436	441	443	400	421	405
ν_6	197	197	197	142		142
ν_7	2455	2455	2470	1843	1845	1864
ν_8	1115	1117	1118	813	807	817
ν_9	960	957	960	959	958	959
ν_{10}	689	697	692	514		517
ν_{11}	366	370	366	365	362	365
ν_{12}	191	196	193	179	169	180

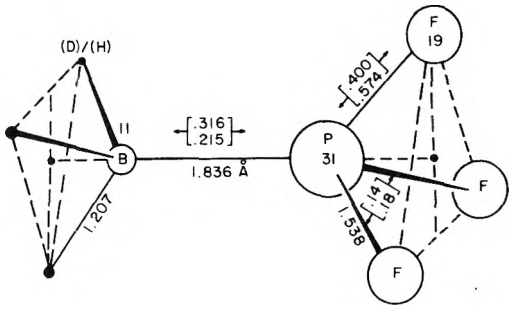

Figure 8. Structure of and energy partition in borane–trifluorophosphine.

mean free path (mpf). It is plausible to assume that the vibrationally excited adducts do dissociate to a greater extent than via the thermal reaction. Under high flux irradiation, the D_3BPF_3 (ν_3; ν_9) leave the illuminated core and collide with unexcited adducts and dissociation fragments in the larger encompassing volume. They lose their excess energy by v–v and v–T energy transfer, or react. Those that reach the wall probably decompose to produce small amounts of hydrogen, as previously reported. However, since BD_3's recombine to B_2D_6 and D_3BPF_3 with essentially kinetic cross sections, its concentration level in the encompassing volume is no more than a factor of 10 higher than under thermal conditions. This accounts for the fact that there is no significant enhancement of the H_3BCO decomposition when the latter is admixed with the trifluorophosphine adduct. Most of the infrared energy is thus dissipated at the walls of the reactor. The augmented rate is produced by $D_3BPF_3{}^\dagger$ which enter the annular region around the illuminated core and there encounter BD_3's. A semiquantitative account follows.

(a) First consider the mean temperature in the encompassing volume. Clearly it must be somewhat higher than the wall temperature, to provide a driving gradient for removal of energy extracted from the laser by the illuminated core. The absence of detectable decomposition of admixed H_3BCO (in a 12 min run) merely imposes an upper limit of ≈45 °C.

(b) A conventional steady-state condition on $[BD_3]$ leads to:

$$[BD_3]_{ss} = \left(\frac{k_1}{k_{-1}}\right)\frac{1-\xi}{\gamma\xi + (k_b/k_{-1})(1-\xi)} \qquad (4)$$

where ξ is the fraction of D_3BPF_3 decomposed at the specified time, and γ ranges from 2 (at early times, when $[BD_3] \simeq [PF_3]$)

to unity, when $[PF_3] \gg [BD_3]$. Since $[BD_3]_{ss}$ is *independent* of the initial concentration of the adduct, it is not surprising that we observed an overall order of unity.

(c) For thermal reactions 1a,1b at 45 °C: $(k_1/k_{-1}) = 3.35 \times 10^{-14}$ mol/cm^3 and $(k_b/k_{-1}) \approx 1.5 \times 10^{-3}$ ($k_{-1} \equiv 10^{12}$, ref 10); so that at $\xi \simeq 0.1$, $[D_3B]_{ss} \approx 3 \times 10^{-13}$ mol/cm^3 [Note: the steady-state concentration must be less than the equilibrium value, calculated from (1a); at 45 °C, $[BD_3]_{eq} = 2.3 \times 10^{-12}$ mol/cm^3].

(d) Under laser irradiation both k_1 and k_b increase. Thus, for those adducts that accumulate $3\nu_3$, about 3 kcal/mol reside in B–P extension (refer to Figure 8). Since $E_b^{th} = 4.8$ kcal/mol and $E_{1a}^{th} = 24.5$ kcal/mol, we postulate that

$$k_1^{(3\nu_3)} = 2.4 \times 10^{15} \exp\left[-\frac{21\,500}{RT}\right]$$

$$k_b^{(3\nu_3)} = 3 \times 10^{12} \exp\left[-\frac{1800}{RT}\right]$$

Application of eq 4 gives $[BD_3]_{ss}^{\ddagger} \approx 1.2 \times 10^{-11}$ mol/cm^3, when $\xi \rightarrow 0.1$, and $T = 318$ K. This concentration level applies only to the annular region, 1 mfp thick, surrounding the illuminated core (volume of reaction cell 1.2×10^4 cm^3; of annulus 1.3×10^3 cm^3).

(e) The number of adducts that enter and leave the illuminated core (per second) is 2.8×10^{20}, when the molecule density is 10^{14} cm^{-3} (3 mTorr) [derived from $N\bar{c}A/4$]. Their mean exposure time (met) to the radiation is 4×10^{-5} s. During one such period 1.12×10^{16} D_3BPF_3 enter and leave; concurrently, from eq 3, 1.4×10^{15} photons are absorbed; i.e., *on the average* one out of eight adducts picks up a single photon. Indeed, Goodman deduced, for our experimental conditions, that one out of six picks up a single photon, that one out of 17 picks up two, and one out of 79 picks up three in a *coherent sequential* process.[11] Thus, $\approx 1.8 \times 10^{13}$ $D_3BPF_3^{(3\nu_3)}$ enter the annular region (1 mfp = 1.5 cm) per met. These either get deexcited or react with a D_3B prior to entering the remaining volume.

The total moles of B_2D_6 produced during a 12 min run, at the 60 W level, via

$$D_3BPF_3^{(3\nu_3)} + BD_3 \xrightarrow{k_b^{\ddagger}} B_2D_6 + PF_3$$

$$\mathcal{M} = \left(\frac{720}{4 \times 10^{-5}}\right) \frac{1.8 \times 10^{13}}{6.02 \times 10^{23}} \frac{1}{1300} [2 \times 10^{11}][BD_3]_{ss} \qquad (5)$$

If we accept the above estimate (d) for $[BD_3]_{ss}^{\ddagger}$, $\mathcal{M} = 9.9 \times 10^{-7}$ mol, compared with 3.9×10^{-6} mol of the adduct initially present; that is, a conversion of $\approx$25%, close to that observed.

The significance of this calculation is that $[BD_3]_{ss}^{\ddagger}$ is primarily determined by the transient $D_3BPF_3^{(3\nu_3)}$ population and the local temperature in the annular region adjacent to the illuminated core. Only secondarily does the steady-state level depend on the wall temperature. Thus, it is difficult to assign a precise physical significance to the apparent activation energy of 3.5 kcal/mol. From Figure 5, one merely notes that raising the wall temperature by 18 °C accelerates the net rare of decomposition by the factor 1.4 due to an increase in $[BD_3]_{ss}^{\ddagger}$. This corresponds to a rise in temperature in the effective volume from 318 to 321 K. At these temperatures, contributions from the thermal reaction are within the analytical noise.

(f) Left unaccounted for are the induction times found when we used low power levels at room temperature (Figure 7). A qualitative explanation hinges on the time required to reach steady state concentration levels of BD_3 in the reactive volume. If that is the case, more precise measurements of the delays, over a wider range of pressures and power levels, should permit us to estimate the augmented rate for step 1a. Another factor may be the time required to establish the temperature gradient from the illuminated core to the colder wall.

Our case contrasts with the model developed by Letokhov and Makarov[12] in which multiphoton absorptions are predicated upon the intervention of rotational relaxation between successive steps. Even at the low pressures used in these experiments rotational spectra of these species are sufficiently broadened so that a virtual continuum is present. The mismatch due to anharmonicity although small and easily accomodated within the average overlap of adjacent states nevertheless limits the quantum efficiency by reducing the upward radiation transition probability. Our case also contrasts with the very high levels of radiation required to affect separation of the isotopes of sulfur in the laser pyrolysis of SF_6, as explained by Bloembergen.[13] The power levels used here ($\leq$150 W/cm^2) are minuscule compared to the 10^9 levels used for SF_6 and similar decompositions.[14]

Acknowledgments. This work was supported by the Army Research Office—Durham, under Contract No. DA-ARO-D-31-124-73-G195.

References and Notes

(1) E. R. Lory, S. H. Bauer, and T. Manuccia, *J. Phys. Chem.*, 79, 545 (1975).
(2) (a) R. C. Taylor and T. C. Bissot, *J. Chem. Phys.*, **25**, 780 (1956). Our normal mode analysis is in better agreement with this earlier assignment, than with the more recent one proposed by (b) R. C. Taylor, et al., *J. Raman. Spectrosc.*, **2**, 175 (1974).
(3) Microwave spectrum reported by R. L. Kuczkowski and D. R. Lide, Jr., *J. Chem. Phys.*, **46**, 357 (1967).
(4) Y. J. Kaufman and U. P. Oppenheim, *Appl. Opt.*, **13**, 374 (1974). Also, refer to R. A. Keller, et al., *J. Opt. Soc. Am.*, **61**, 746 (1971); **62**, 319 (1972); **63**, 1552 (1973).
(5) A. B. Burg and Y. C. Fu, *J. Am. Chem. Soc.*, **86**, 176 (1964).
(6) W. Sawodny and J. Goubeau, *Z. Anorg. Allg. Chem.*, **356**, 289 (1968).
(7) We acknowledge, with thanks, an unpublished table for potential energy distribution in symmetry coordinates, sent to us by Professor R. C. Taylor.
(8) A discussion of this problem is being prepared by Professor Aron Kupperman.
(9) Incidentally, a similar low efficiency ($\approx 10^5$ photons/molecule decomposed) is indicated for the isotopically selective photolysis of SF_6 by CO_2 laser radiation. Estimates are based on: R. V. Ambartzumian and V. S. Letokhov, *Laser Focus*, 48 (July 1975); J. L. Lyman, et al., *Appl. Phys. Lett.*, **27**, 87 (1975). This conclusion was also reached by G. Hancock, et al., *Opt. Commun.*, **16**, 177 (1976).
(10) The room temperature recombination rate constants for BF_3 with various amines range from 2.7×10^{10} to 9.3×10^{12} (mol^{-1} cm^3 s^{-1}). Hence $k_{-1} \simeq 10^{12}$ is a reasonable assumption. S. H. Bauer, *Adv. Chem. Ser.*, **No. 32**, 88 (1961); **No. 42**, 35 (1964). See also T. P. Fehlner, *Int. J. Chem. Kinet.*, **7**, 633 (1975).
(11) J. Stone, E. Thiele, and M. F. Goodman, *J. Chem. Phys.*, **63**, 2936 (1975). We akcnowledge, with sincere thanks, Dr. Goodman's help in applying this analysis to our experiment.
(12) V. S. Letokhov and A. A. Makarov, *Sov. Phys. JETP (Engl. Transl.)*, **36**, 1091 (1973).
(13) N. Bloembergen, *Opt. Commun.*, **15**, 416 (1975).
(14) R. V. Ambartzumian, N. V. Chekalin, V. S. Letokhov, and E. A. Ryabov, *Chem. Phys. Lett.*, **36**, 301 (1975).

Gas to Liquid to Solid Transition in Halogen Hot Atom Chemistry. 3. Evidence for an Excited Reaction Intermediate in the (n,γ)-Activated Reactions of Iodine with Acetylene[1]

Kar-Chun To, M. E. Berg, W. M. Grauer, and E. P. Rack*

Department of Chemistry, University of Nebraska, Lincoln, Nebraska 68588 and General Medical Research, V.A. Hospital, Omaha, Nebraska 68105 *(Received December 30, 1975)*

Publication costs assisted by the U.S. Energy Research and Development Administration

The reactions of ^{128}I activated by radiative neutron capture with acetylene occur primarily through an addition channel forming an electronically excited reaction intermediate. Acetylene is unlike olefins in that no photochemical addition occurs under conditions simulating sample handling. In an excess of gaseous acetylene, at 1 atm 14.9 ± 0.6% of ^{128}I is stabilized as organic activity to the following extent: CH_3I 0.49%, CH_2I_2 0.70%; C_2H_3I 0.40%, C_2H_5I 9.30%; i-C_3H_7I 2.71%; $CH_3CH_2CHICH_3$ 1.10%, $CH_3(CH_2)_3I$ 0.20%. The effects of rare gas additives in moderating ^{128}I with gaseous C_2H_2 were determined in an effort to ascertain the nature of the activation process. Only the $C_2H_5{}^{128}I$ yield is decreased by the presence of rare gases, suggesting that both hot ^{128}I ions and thermal $I^+(^1D_2)$ and other excited ions are involved in the primary addition to acetylene. The gas to condensed phase studies showed a depletion of all C_1, vinyl iodide, C_3, and C_4 ^{128}I-labeled products; where the only product observed in high pressure gas and condensed phase systems was $C_2H_5{}^{128}I$. A reaction scheme is proposed which postulates the existence of an excited complex reaction intermediate. The properties of the proposed complex are compared qualitatively to those predicted by RRKM, "caged" complex, and caging radical theories of enhancement yields.

Introduction

Since the significant studies of Richardson and Wolfgang[2] employing the gas to condensed phase transition in the hot ^{18}F reactions with CH_3F, the density variation technique has become very popular in suggesting the relative importance of cage and molecular reactions, resulting in an active discussion in the recent literature.[3-6]

In our attempt to resolve the nature of enhancement yields in the condensed phase as due to molecular, complex (cage), or radical (cage) reactions we tried to find a hot atom system resulting in an electronically excited intermediate. It would then be of interest to observe the effects of the gas to condensed phase transition on this species.

We selected the system ^{128}I activated by radiative neutron capture (CF_3I source) in acetylene for several reasons. Acetylene is a low mass, two carbon system with a triple bond to which iodine does not add photochemically in simulated sample handling conditions. CF_3I not only provides an iodine source but also assures that acetylene is the sole source of hydrogen atoms. Radiative neutron capture activated iodine provides a large diameter atom (often as a positive ion) which not only can possess electronic excitation energy but possesses a low translational energy[7] compared to other hot atom activations. Rowland[8] has studied the production of excited radicals in the reactions of acetylene with near thermal ^{18}F.

Experimental Section

Materials. Xenon, helium, and krypton were obtained from Matheson Chemical Co. (Research Grade) with stated purities of 99.995 mol % and were used without further purification. Acetylene (Matheson Research Grade) and trifluoroiodomethane (Pierce Chemical Co.) were used after repeated degassing on the vacuum line. Methyl iodide (Analytical Grade) obtained from Mallinckrodt was stored under vacuum with copper turnings. Iodine was sublimed from a mixture of Mallinckrodt reagent grade I_2, Baker reagent grade KI, and calcium oxide.

Preparation of Reaction System. A description of the techniques used to produce atmospheric, high pressure gas and condensed phase samples has recently been reported.[5] High pressure gaseous samples were prepared by freezing 0.2 ± 0.01 Torr of iodine and 5 Torr of the iodine source into the ampoule, followed by the measured quantity of acetylene. Rare gas moderators used in the 1-atm samples were filled in the customary manner.[5]

Liquid samples were prepared by first freezing known quantities of (6.8×10^{-4} mole fraction) iodine into the ampoule followed by a known quantity of acetylene.

All samples were wrapped in aluminum foil and stored under liquid nitrogen until just prior to irradiation.

Neutron Irradiation. All irradiations were performed in the Omaha, Nebraska V.A. Hospital TRIGA reactor at a thermal neutron flux of 1.1×10^{11} neutrons cm^{-2} s^{-1} and an accompanying γ ray flux of 3×10^{17} eV g^{-1} min^{-1}. The samples were irradiated from 0.5 to 30 min and back extrapolated to zero irradiation time for correction of radiation damage.[5]

Extraction Procedure. After irradiation, the ampoules for total organic product yields (TOPY)[9] were broken in a separatory funnel containing 5 ml each of CCl_4 + I_2 and 0.5 M Na_2SO_3 solution. The organic and aqueous phase (3 ml each) were counted separately on an Ortec single-channel analyzer employing a 3 × 3 in. NaI(Tl) detector. The samples containing xenon moderator were counted on a Harshaw 12.2% efficient Ge(Li) detector interfaced with a Nuclear Data 2400 1024-channel analyzer. The liquid phase samples were irradiated immersed under ice or dry ice. The density of the reaction mixture was determined by the method of Willard and

* Address correspondence to this author at The University of Nebraska.

Rice[10] and compared to literature values.[11] No temperature greater than 25 °C[12] or lower than −78 °C[13] was attempted.

Radiogas Chromatographic Separations of the Activated Mixtures. Gaseous samples were injected into the radiogas chromatograph, as previously described.[5] A mixture of known carrier composition was simultaneously injected into the helium stream and detected by means of a thermal conductivity cell for purposes of calibration and identification of products. Liquid samples were extracted,[5] and a known portion of the organic phase was injected into the chromatograph.

The column used was a 3-m stainless steel coil containing 5% by weight di-(2-ethylhexyl)sebacate on 50/60 mesh firebrick. Linear temperature programming from 25 to 150 °C was used. Individual product yields were determined by triplicate radiogas chromatographic runs. Integration of the chromatograms produced relative yields which were normalized to the total organic product yield to give the absolute individual organic product yields (IOPY) for a particular mole fraction additive. A radiation dose curve was established for each sample condition by evaluating yields for 0.5-, 1.0-, 2.0-, 5.0-, 10.0-, 15.0-, 20.0-, and 30.0-min irradiations. Extrapolation to zero irradiation time produced TOPY and IOPY values corrected for radiolytic contributions.

Results and Discussion

Energetics of Recoil Iodine. The reactivity of ^{128}I in methane[15] and halomethane[7] and olefin[17] systems has been discussed in detail. Iodine-128 activated by the radiative neutron capture process can possess a variety of energy states composed of translational and/or electronic excitation energy in addition to possessing a positive charge. Carlson and White[14] reported that iodine atoms as a result of activation can possess a positive charge ranging from +1 to +13 due to Auger and secondary electron emission. If an iodine ion is in an environment possessing an ionization potential intermediate of the first and second ionization potentials of iodine the ion will undergo charge transfer reactions and rapidly be reduced to the +1 state. Iodine can then react as an ion or neutral atom.

In addition to charge, iodine can react as an electronically excited species. This energy due to excited electronic states of iodine can be utilized during the course of chemical reactions. $I^+(^1D_2)$ from rare gas additive experiments in the reactions of ^{128}I with methane,[15] ^{123}I with methane and ethane,[16] and ^{128}I in lower excited states in reaction with olefins[17] have been assumed as a reactive species.

Yoong et al.,[7] utilizing Monte Carlo and three-dimensional random walk in space techniques, investigated the (n,γ) recoil spectrum of ^{128}I. The calculated kinetic energy spectrum ranged from 0 to 194 eV with a maximum probability at 152 eV.

Reactions of Gas Phase ^{128}I with C_2H_2. The Suggestion of the Formation of a Charged Reaction Intermediate. Depicted in Figure 1 is a plot of total organic product yield (TOPY) vs. mole fraction of the three moderators helium, krypton, and xenon. This plot is qualitatively similar to that reported by Rack and Gordus[15] in their study of (n,γ)-activated ^{128}I with gaseous methane in that our plots extrapolate from the unmoderated 1 atm, room temperature gas yield (14.9%) to 12.9% for He and Kr and to a lower value (8.8%) for Xe. The interpretation is that of 14.9% TOPY, 3.6% is the result of hot (translational) reaction (as IOPY data will reveal) and 11.3% is thermal in character. Xenon undergoes charge transfer with iodine ions in the $^1D_2$ electronic states. The larger reduction in TOPY by Xe is due to (4.1%) quenching of excited iodine

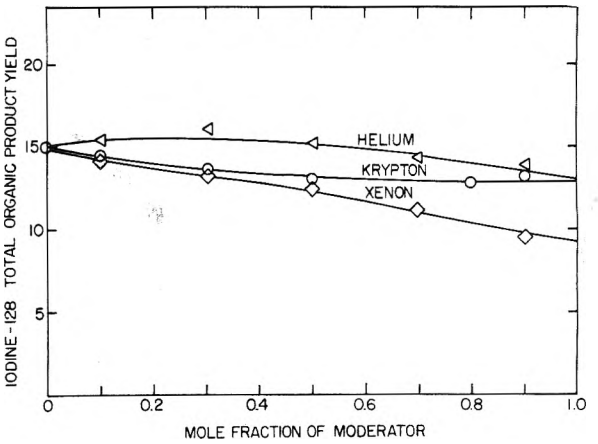

Figure 1. Effect of mole fraction of moderator on gas phase TOPY. The moderators are helium (△), krypton (○), and xenon (◇).

ions and to kinetic energy moderation (3.6% hot reaction). Of 14.9% ^{128}I organically bound, 3.6% TOPY may be attributed to hot (kinetic energy dependent) reactions and 11.3% to thermal (kinetic energy independent) reactions. The thermal reactions may be classified as the result of $I^+(^1D_2)$ (4.1%) and other thermal processes (7.2%) probably involving iodine ions in ground or low-lying electronic states.

Employing radiogas chromatography it is possible to obtain individual organic product yields (IOPY values).[9] Summarized in Table I are the observed absolute yields of the individual products (IOPY) formed in the reaction of (n,γ)-activated ^{128}I with acetylene at room temperature and 1 atm total pressure. Ethyl iodide (9.30%) is the major product. Six other products of varying magnitude are also observed. It would appear from the identity of products observed that the primary reaction of ^{128}I is *addition* to acetylene. Iodine has been observed to add to olefins in hot,[17] photochemical,[18] and thermal[19] reactions. In contrast, preliminary experiments duplicating sample handling techniques have shown *no change in total organic product yield* even when exposed to ambient light for periods of 30 min. A further investigation of acetylenic photochemical reactivity is being conducted. No attempt was made to quantitate the inorganic products H ^{128}I produced by abstraction or ^{128}I–I from thermal exchange with scavenger because of the rapid thermal exchange between I_2 and HI. An additional shortcoming in this type of experiment[20] is that any product formed by reaction involving expulsion or nonretention of the radioiodine cannot be observed.

In order to determine the relative importance of hot and thermal reactions, especially $I^+(^1D_2)$,[21] we studied individual organic product yields as a function of mole fraction of helium, krypton, and xenon (Figures 2–4). Minor products were not plotted due to difficulties in determining small yields and CH_3I and CH_2I_2 were plotted as a single organic product combination (COPY).[9] In all three plots the $CH_3I + CH_2I_2$ COPY is insensitive to moderators indicating complete thermal character. Although the yield of stabilization product, vinyl iodide, is too small to plot the ethyl iodide product shows a decrease in IOPY from 9.3 ± 0.5% to 5.7 ± 0.5% in krypton (6.1 ± 0.5% in helium). This ~4% drop is the result of kinetic energy dependent (hot) reactions. We suggest that the additional 4.1% drop of ethyl iodide in Xe is due to $I^+(^1D_2)$ reactions. Since ethyl iodide is the only product which is sensitive to kinetic energy moderators and electronically deexcited by xenon we may ascribe a 3.6% "hot" IOPY and 4.1% $I^+(^1D_2)$ IOPY to ethyl iodide formation.

TABLE I: TOPY, COPY, and IOPY Values of the Reaction of $^{127}I(n,\gamma)^{128}I + C_2H_2$ in the Gas Phase without Additives

Product	IOPY	Carbon length COPY
CH_3I	0.49 ± 0.02	
CH_2I_2	0.70 ± 0.05	
		1.19 ± 0.07 ΣC_1
C_2H_3I	0.40 ± 0.05	
C_2H_5I	9.30 ± 0.46	
		9.70 ± 0.51 ΣC_2
i-C_3H_7I	2.71 ± 0.43	2.71 ± 0.43 ΣC_3
$CH_3CH_2CHICH_3$	1.10 ± 0.20	
$CH_3(CH_2)_3I$	0.20 ± 0.03	
		1.30 ± 0.23 ΣC_4
		TOPY = 14.9 ± 0.6%

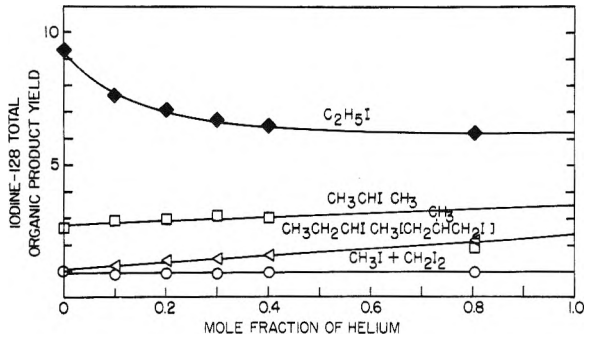

Figure 2. Effect of mole fraction of helium on gas phase IOPY: C_2H_5I (◇), CH_3CHICH_3 (□), $CH_3CH_2CHICH_3$ ($CH_3CH(CH_3)CH_2I$)[23] (△), $CH_3I + CH_2I_2$ as COPY (○). Other product yields are too small to plot.

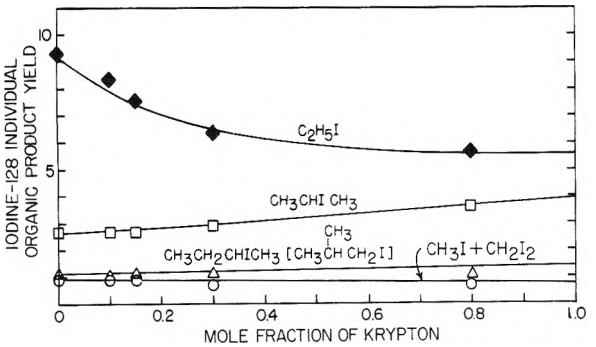

Figure 3. Effect of mole fraction of krypton on gas phase IOPY: C_2H_5I (◇), CH_3CHICH_3 (□), $CH_3CH_2CHICH_3$ (△), $CH_3I + CH_2I_2$ as COPY (○).

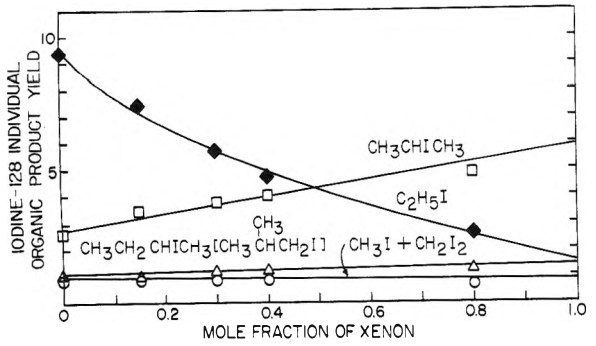

Figure 4. Effect of mole fraction of xenon on gas phase IOPY: C_2H_5I (◇), CH_3CHICH_3 (□), $CH_3CH_2CHICH_3$ (△), $CH_3I + CH_2I_2$ as COPY (○).

The secondary addition products, 2-iodopropane and 2-iodobutane (1-iodobutane has too small a yield to plot), show an interesting property by increasing with increasing mole fraction of moderator, the magnitude of the 2-iodopropane increases being in the order He < Kr < Xe. This increase in yield partially compensates for the reduction of "hot" ethyl iodide; thus giving the illusion of a 2% hot yield in Figure 1. A similar phenomenon has been reported by Loberg and Welch[16] for ^{123}I (EC/β^+) activated reactions with methane. This moderator trend may be indicative of a molecular ion complex or the presence of ion–molecule reactions.[17]

We studied the effect of 30 mol % O_2 on total and individual organic product yields and found a reduction but not a total quenching of reaction products. At this concentration, O_2 may exhibit kinetic energy moderator and/or competing substrate characteristics in addition to being a radical scavenger. Analysis of product identification and yield shows no observable oxygen containing organic compounds. The reduction in the total organic yield is greater than expected from purely kinetic energy moderation arguments. The TOPY value is reduced from 14.9 to 7.0%. The C_2H_5I yields dropped to 4.8 from 9.3%. The minor products vinyl iodide and isopropyl iodide were reduced to 0.36 and 1.83%, respectively. No other products were observed. It should be noted that the vinyl iodide IOPY values are equal, within experimental error, for O_2 additive and (ambient) I_2 systems. The observance of only three products, with reduction in two, suggests the presence of some radical reactions, but that the reaction pathways are not solely radical in nature.

The yield data summarized in Table I when compared to higher density values (to be discussed in the next section) reveal a pattern emerging from groupings of individual organic product yields. These groupings will be referred to as combined organic product yields (COPY).[9] We grouped *individual products* into the following three classes. The classes of reactions leading to final stabilization of radioiodine containing products are (1) decomposition, (2) stabilization, and (3) secondary addition. The decomposition class (ΣC_1 COPY) is characterized by the products CH_3I and CH_2I_2 where carbon–carbon bond scission occurs as a result of high internal energies; the $\cdot CH^{128}I$ fragment might be stabilized by further reaction[22] or scavenged by I_2. Stabilization (ΣC_2 COPY) occurs by collisional deexcitation and abstraction of hydrogen to form the major product C_2H_5I or its precursor vinyl iodide (C_2H_3I). It should be noted that in the reaction system ($CF_3I + C_2H_2 + I_2$) the only source of hydrogen atoms is acetylene. The labeled molecules 1- and 2-iodobutane[23] can be formed by the joining of a second acetylene molecule (secondary addition) to an iodine–acetylene reaction intermediary followed by deexcitation and hydrogen abstraction. An alternative to collisional deexcitation could be the expulsion of a carbon (with attendant atoms) to remove excess energy as translational (rotational and/or vibrational energy). Such an expulsion, followed by H· abstraction, would lead to formation of 2-iodopropane. (The expulsion of a C_2 unit must also be considered but would lead to the same products as the stabilization class; therefore, such expulsion could be regarded as a slow (long term) collision.)

The above product analysis suggests *the formation of an iodine–acetylene reaction complex as the first step in stable product formation.* The $[C_2H_2I^+]_{exc}$ complex may (a) decompose, (b) stabilize by collisional deexcitation and hydrogen abstraction, or (c) undergo a further (addition) reaction with acetylene leading to longer chain iodohydrocarbons. Our tentative reaction mechanism for such a complex is shown in

Scheme I

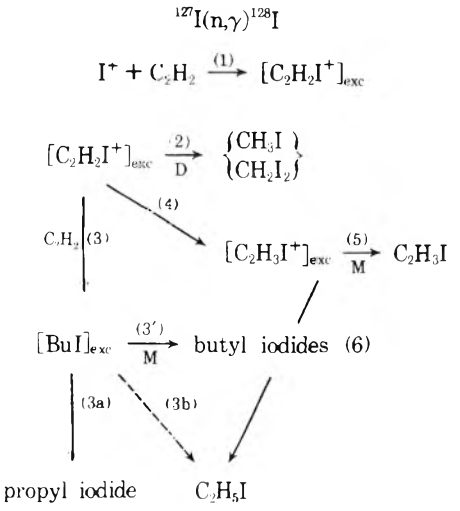

Scheme I where reaction A is the activation of ^{128}I resulting in excess kinetic energy, positive charge and/or electronic excitation energy, and (1) is the creation of the iodine–acetylene reaction complex, (2) the decomposition of the complex to form (following abstraction or scavenging) CH_3I or CH_2I_2, (3) the addition of a second C_2H_2 molecule to form butyl iodides[24] (3′) or decomposition to propyl iodide (3a) (or possibly ethyl iodide (3b)), (4) the formation of a vinyl iodide secondary intermediate which may stabilize (5) or abstract H· (6) to form ethyl iodide.

Although a kinetics study has not been undertaken, something of the relative magnitudes of these reaction pathways can be ascertained by the observed organic product distribution.[25] Reaction 1 can be correlated with total organic product yields since, as previously mentioned, abstraction and substitution products were not observed and addition can be initiated by hot or $I^+(^1D_2)$ ions or other thermal iodine species in ground or low electronic states. Reaction 2 is effectively blocked at 1 atm as evidenced by the small ΣC_1 COPY. Of the alternatives to reaction 2, reaction 4 appears larger than (3) in that ΣC_2 COPY > $\Sigma(C_3 + C_4)$ COPY and further (3a) > (3′) and (6) > (5). As will be shown, the reaction pathway designated by (4) is sufficiently large that pathway 3 is eliminated at higher pressures and that hydrogen abstraction (6) from the reactive cage wall overshadows collisional deexcitation (5).

In contrast to iodine addition to acetylene, Rowland and Williams[8] reported on the reaction of near-thermal ^{18}F with acetylene and found abstraction and substitution products of about 2–3% yield. No addition product was found unless HI was added where >50% CH_2=CHF was formed; the other products remaining unchanged. The additional product CH_3F was found in 0.1% yield when HI was added. Additional HI decreased the vinyl fluoride yield from competition by the exothermic reaction F + HI → HF + I. Hot ^{18}F is known[26] to react as a neutral atom. Fluorine has a small atomic radius and low polarizability. Therefore, it would appear that positive charge, a larger atomic radius, higher polarizability, and a greater electrophilicity aid in the formation and reactions of the iodine–acetylene complex.

Summarized in Table II are total and individual organic product yields for the reactions of iodine with methane, ethane, ethene, and ethyne. Abstraction products could not be reported because of the previously mentioned experimental difficulties. In methane the only labeled products observed were by substitution modes. Ethane presents a two carbon system that should block addition. Any attempt by iodine to enjoin the carbon–carbon bond should result in rejection of the iodine or displacement of (substitution for) a methyl group. However, evidence[4] for the existence of the $[C_2H_6I^+]_{exc}$ complex followed by decomposition to CH_3I or collisional deexcitation with hydrogen expulsion to form C_2H_5I appears to be conclusive. The mechanism for formation of C_2H_3I remains unknown. The existence of a reaction complex $[C_2H_4I_2^+]$ which can decompose or stabilize by I or HI elimination has been postulated in ethene.[17] In this system there was experimental evidence to suggest that the formation of CH_3I was the result of ion–molecule (thermal) reactions. Our work on acetylene indicates similar products of decomposition and stabilization by the gain of hydrogen. Therefore, it is logical to postulate the formation of a reaction complex for iodine and acetylene.

High Pressure Gas and Condensed Phase. If the proposed reaction scheme proceeds as indicated in the last section, we should observe definite density (pressure) effects on the product distribution. Table III contains yield data for systems ranging from 1 atm, room temperature gas to those in the liquid phase near the freezing point. It was not possible to obtain a solid state sample due to fractional crystallization of the sample. It was also not possible to obtain data between 30 atm and room temperature liquid conditions due to the low critical temperature (35.5 °C) and high critical pressure (61.6 atm) of acetylene which can create an explosive hazard in the reactor.

Three characteristics of Table III are noteworthy: (1) the TOPY remains approximately constant from 1 to 30 atm; (2) the ΣC_2 COPY increases at the expense of the secondary addition and decomposition COPY values until the latter disappear; and (3) the vinyl iodide IOPY increases to a maximum and then decreases until it disappears. *At high pressures and liquid state conditions the IOPY, COPY, and TOPY values are experimentally identical.* The sole product observed is ethyl iodide, C_2H_5I.

Our proposed $[C_2H_2I^+]_{exc}$ reaction complex can be considered the activation step of a unimolecular decay reaction scheme.[32] However, the observance of C_3 and C_4 compounds suggests that the complex is not wholly unimolecular in nature in that $[C_2H_2I^+]_{exc}$ may undergo a secondary (bimolecular) reaction with another C_2H_2 molecule to form propyl and butyl iodides. Of interest are the data for reactions 5 and 6. Initially, both the formation of vinyl iodide and ethyl iodide increase with increasing density. Vinyl iodide reaches a maximum around 8×10^{-3} g cm^{-3} and then decreases and disappears. Vinyl iodide should increase with increasing pressure (as the number of collisions increases) since C_2H_3I is formed by stabilization of the secondary reaction intermediate $[C_2H_3I^+]_{exc}$ formed in reaction 4. At higher densities this stabilization mode competes unfavorably with hydrogen abstraction and stabilization to form ethyl iodide. Two factors need to be considered. First, the thermodynamically more stable product is ethyl iodide. It is reasonable to assume that the thermodynamically more stable product will be formed if energy barriers, molecular rearrangements, and other kinetic parameters do not forbid the reaction. Secondly, if caging reactions occur a reactive cage wall (C_2H_2) will supply the necessary hydrogen needed for saturation. The abstraction of hydrogen from acetylene to form vinyl and ethyl iodide appears to be endoergic and thus provides an additional deexcitation mode.

Figure 5 presents yield data as related to density. For purposes of convenience ΣC_1, ΣC_3, and ΣC_4 COPY's have been combined. TOPY values, when different from ΣC_2 COPY

TABLE II: Summary of Gas Phase Iodine Reactions with Selected Alkanes, Alkenes, and Alkynes

Reaction	TOPY, %	Products	IOPY	Reaction
$^{128}I + CH_4$[a]	5.4 ± 0.05	CH_3I	53.4	Substitution
		CH_3I_2	1.0	Substitution
$^{123}I + CH_4$[b]	51.8 ± 2.9			
$^{123}I + C_2H_6$[b]	2.5	CH_3I	~2.0	Decomposition
		C_2H_3I	<0.1	
		C_2H_5I	0.5	Addition
$^{128}I + C_2H_6$[c]	3.0			
$^{128}I + C_2H_4$[d]	18 ± 1	CH_3I	10.0%	Decomposition
		C_2H_3I	4.0%	Elimination
		C_2H_5I	4.0%	Addition
$^{128}I + C_2H_2$	14.9 ± 0.6	See Table I		

[a] See ref 15. [b] See ref 16. [c] A. A. Gordus and J. E. Willard, *J. Am. Chem. Soc.*, **79**, 4609 (1957). [d] See ref 17.

TABLE III: TOPY, COPY, and Selected IOPY Values in the Gas to Condensed Phase Transition

			COPY				IOPY	
ρ, g cm^{-3}	λ/σ	TOPY	ΣC_1	ΣC_2	ΣC_3	ΣC_4	C_2H_5I	C_2H_3I
0.001 (1 atm)	8.35	14.9 ± 0.6	1.19	9.70	2.71	1.30	9.30	0.40
0.004	5.26	15.2 ± 0.7	0.22	12.4	1.88	0.70	11.4	0.76
0.008	4.18	15.4 ± 0.6	0.14	14.0	0.40	0.80	12.4	1.59
0.010	3.88	15.4 ± 0.4	0.14	15.3			14.4	0.85
0.032 (30 atm)	2.62	16.2 ± 1.3		16.2			16.2	
0.388 (liq, 23 °C)	1.15	41.0 ± 1.3		41.0			41.0	
0.465 (liq, 0 °C)	1.08	49.0 ± 1.6		49.0			49.0	
0.615 (liq, −78 °C)	0.98	56.3 ± 7.7		56.3			56.3	

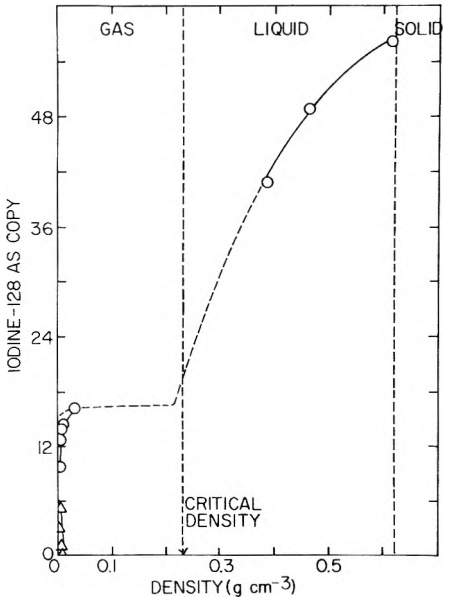

Figure 5. COPY as a function of density: ΣC_2 COPY (O), sum of other products COPY (Δ). Dashed (- - -) line from ρ = 0.032 to 0.388 g cm^{-3} interpolated via λ/σ data. Dashed line for ρ < 0.032 g cm^{-3} is TOPY behavior with density where different from ΣC_2 COPY.

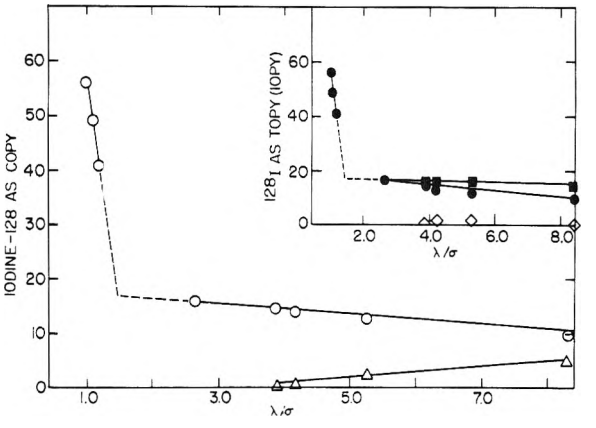

Figure 6. COPY as a function of λ/σ: ΣC_2 COPY (O), sum of other products COPY (Δ). Dashed (- - -) line represents computer interpolation of experimental data. (Insert) TOPY and selected IOPY's as a function of λ/σ: TOPY (■); C_2H_5I (●); C_2H_3I (◊). For $\lambda/\sigma \leq 2.62$ TOPY and C_2H_5I IOPY values are equivalent.

(<0.032 g cm^{-3}), are indicated by a dashed line. The dashed curve from 0.032 to 0.388 g cm^{-3} was interpolated using information obtained from the λ/σ plot (Figure 6). It is noteworthy that the curve obtained from COPY vs. density data is similar to that of Richardson and Wolfgang[2] and others.[3-6] Of further interest is the fact that the high density curvature is similar to that of ^{82}Br(IT) reactions in methyl halides[5] as opposed to the characteristic shape of bromine reactions activated by radiative neutron capture. The main difference in activation between ^{79}Br(n,γ)^{80}Br and ^{82}Br^{m}(IT)^{82}Br is that ^{82}Br is born with a higher positive charge and lower kinetic energy.[5] ^{128}I born by the (n,γ) process also possesses a lower kinetic energy and higher charge population than (n,γ) activated ^{80}Br.

Figure 6 presents the COPY data as a function of normalized intermolecular distance, λ/σ,[5] where λ represents the intermolecular distance between centers of spheroidal molecules of diameter σ. This suggests[28] a lowest value of λ/σ = 1.0; yet a value of λ/σ = 0.98 is observed. This discrepancy is minor and may be easily explained by the approximate nature of the

normalized intermolecular distance construct. One physical consideration is the nonspherical nature of acetylene. The value of σ (4.2 Å)[26] for acetylene is taken along the long molecular axis; however, molecular rotations may be restricted in low temperature, high density liquids near phase transitions.

The results depicted in Figure 6 are similar to those reported by Root[6] for the CF_3CH_3 and CF_3CH_2F systems with ^{18}F and to our previous work[5] with $^{80}Br(n,\gamma)$ and $^{82}Br(IT)$ with halomethanes. We note the intersection of two straight line segments at $\lambda/\sigma = 1.42$, the first segment exhibiting a minor rise with decreasing λ/σ, the second a sharp rise *indicating cage enhancement reactions of the iodine–acetylene complex*. In our work with halomethanes[5] we suggested the near horizontal segment to be indicative of molecular reactions and the angled segment of caging reactions. This is further supported by our current work, especially (see insert to Figure 6) in light of the variation of TOPY and the ethyl and vinyl iodide yield values as functions of λ/σ.

Based on our work with halomethanes,[5] we suggested the possible importance of the degradation and packing effects on cage radical reactions. These effects are not directly applicable to the iodide–acetylene system. The degradation effect is the ability of the solvent medium to deexcite translationally excited hot atoms or adducts by collision. The energy degradation factor (EDF)[29] for $^{128}I(n,\gamma)$ is 0.561 as compared to 0.993 for $^{80}Br(n,\gamma) + CH_3Br$. While it can be suggested that CH_3Br collisionally "cools" faster and is a better radical producer than C_2H_2, the differences among the condensed phase TOPY's are not that great; an alternate approach must be sought. The sole product in the condensed phase is C_2H_5I. This can only be produced by the abstraction of hydrogen from the cage wall, an endoergic process which aids in the cooling of the hot atom complex. The packing effect correlates molecular diameter with "holes" in the cage wall. While acetylene's molecular diameter (4.2 Å) compares favorably with that of CH_3Br (4.13 Å) two important differences are present. First, CH_3Br has a much larger EDF resulting in CH_3Br molecules being more difficult to dislocate, which would produce a "hole" in the cage wall. Secondly, C_2H_2 is spheroidal only when molecular rotations are excited. When molecular rotations are not excited, as near the freezing point, the molecules more closely resemble an ellipsoid, possessing both a long and short axis. As these molecules attempt to orient in a crystalline configuration, "holes" open along certain orientations.

Although λ/σ information provides insight into reactions in terms of molecular environment and other molecular parameters, the controversy in the literature among RRKM (molecular),[6] "caged" complex,[3] and radical cage reactions[4,5] as explanations of enhancement yields has not been resolved.

In their work with $^{18}F + CH_3F$, Richardson and Wolfgang[2] suggested that the enhanced product yields of $CH_3{}^{18}F$ and $CH_2F{}^{18}F$ were the result of radical cage reactions. They felt that in systems with small intermolecular distances any reaction complex would have to be stabilized within a period of vibration and therefore could not have previously existed (as a chemically bound entity). This does not invalidate the concept of collisional stabilization, rather it prevents its invocation to explain the appearance of new products in the condensed phase. One of the strong points of the radical cage reaction concept is *its ability to explain the emergence of new products in the condensed phase* that cannot be the result of simple molecular reaction. The new products are the results of the hot atom being "trapped" within the confines of a cage cell with radicals of its own creation. The hot atom after cooling can combine with these radicals to form products.

Unimolecular decay theory has been employed recently to investigate the nature of enhancement yields.[6,20] *The activated complex is envisioned as an energy sink of loosely coupled oscillators which interchange energy.* Although molecular rotations and reorientations are allowed to RRKM theory, unimolecular decay cannot explain products indicative of extensive scavenger reactions. Recently,[30–34] non-RRKM kinetic behavior has been found in several systems which indicate the failure of the random lifetime distribution.[35]

Halogen hot atom for halogen substitution reaction studies[3] of diastereomeric molecules as functions of phase and solvent have led to the suggestion of a "caged" complex. In this hypothesis an electronically excited intermediate is held together by the solvent for a time sufficient for reaction. The adduct formed from the hot atom and substrate constitute the sole occupants of the cage cell, thus bridging the idea of a complex with caging reactions. *The complex, however, need not be chemically bound as no interchange of internal energy is necessary.*

The iodine–acetylene system is unlike any other hot halogen system in that the number of observed products *decrease* rather than increase in the gas to condensed phase transition. In the high pressure region and liquid state, only one product, $C_2H_5{}^{128}I$, was observed. Our proposed reaction scheme suggests the formation of an electronically excited reactive intermediate, $[C_2H_2I^+]_{exc}$. *The gas to condensed phase transition data do not indicate any evidence for cage radical reactions. Therefore, the gas to condensed phase study should suggest whether a complex can cage and have behavior similar to that predicted for radical reactions.*

While it would be desirable to characterize the nature and lifetimes[36] of reaction complexes on a rigid mathematical basis employing the arguments presented by Richardson and Wolfgang[2] it is virtually impossible for the following reasons: (1) the distribution of the hot atom's translational energy into internal and translational modes of the complex is not known; (2) the intermolecular distance required in the collisional lifetime calculations is dependent on the microscopic density which *cannot* be assumed identical with the macroscopic density because of local perturbations and possible radical formation; (3) the unimolecular rate constants for RRKM kinetic lifetimes is experimentally unobtainable; and (4) the energy distribution function is non-Boltzmann in nature as a result of incomplete thermalization.

A "true" unimolecular complex requires $\geq 10^{-12}$ s to completely randomize internal energy.[37] Lifetimes of this magnitude require low internal energies and small collision numbers. These conditions require thermal or near-thermal systems at low to moderate pressures. An order of magnitude calculation of the collisional lifetime[36] in comparison with simple RRK kinetic lifetimes[38] indicates that the condensed phase iodine–acetylene reaction complex is *collisionally limited* and of the order of a vibrational period or less ($\sim 10^{-14}$ s). *We must conclude that an insufficient time is available to the complex for energy redistribution* and concede the possibility that the complex might not be chemically bound as a result of lack of vibrational modes. Although gas phase calculations appear to be of the same order of magnitude (10^{-13} to 10^{-12} s) or greater than RRK calculations, the lifetime cannot be ascribed to collisional or kinetic limitation because of large uncertainties in the calculations. In either case, *it is only possible to obtain sufficient time for energy redistribution at low pressures and low internal energies.*

We must conclude that except at low energies and pressures, unimolecular decay complexes do not play a significant role in product formation.

Analysis of our product yields as functions of density (pressure), intermolecular distance, and phase shows that a collapsing molecular environment decreases the decomposition and secondary addition modes by increasing stabilization as we would expect. In contrast to our halomethane study[5] the number of products has decreased in the gas (seven) to condensed (one) phase transition. Caging radical reactions suggests the opposite trend with an increase in the number of observed products with increasing density.

Our data suggest that in the iodine–acetylene system the enhancement yield *increase is due to the caging of the electronically excited complex*. It is our contention that unless systematic studies such as described elsewhere[5] are performed and consideration given to all reaction channels that can be observed involved in the hot atom reactions, we cannot on an a priori basis conclude that enhancement yields are primarily the result of a cage radical or caged complex reaction.

We feel that kinetic energy, positive charge, and electronic excitation energy of ^{128}I with subsequent electrophic attack on the acetylene π-bond system result in an excited complex with unimolecular (low pressure) and caged complex (high pressure) characteristics.

References and Notes

(1) This research was supported by the United States Energy Research and Development Administration Contract No. E(11-1)-1617. This is ERDA document No. C00-1617-42.
(2) A. E. Richardson and R. Wolfgang, *J. Am. Chem. Soc.*, **92**, 3480 (1970).
(3) H.-J. Machulla and G. Stöcklin, *J. Phys. Chem.*, **78**, 658 (1974).
(4) M. D. Loberg, K. A. Krohn, and M. J. Welch, *J. Am. Chem. Soc.*, **95**, 5596 (1973).
(5) M. E. Berg, W. M. Grauer, R. W. Helton, and E. P. Rack, *J. Phys. Chem.*, **79**, 1327 (1975).
(6) R. G. Manning and J. W. Root, *J. Phys. Chem.*, **79**, 1478 (1975).
(7) M. Yoong, Y. C. Pao, and E. P. Rack, *J. Phys. Chem.*, **76**, 2685 (1972).
(8) R. L. Williams and F. S. Rowland, *J. Am. Chem. Soc.*, **94**, 1047 (1972).
(9) The total organic product yield (TOPY) is the fraction of activity bound organically in the system. TOPY = OA/(OA + IA) × 100% where OA is the activity retained in the organic fraction of the extraction and IA is the activity in the inorganic fraction. Corrections for isotopic decay were made. Individual organic product yields (IOPY) represent the fraction of activity chemically bound in a specific organic substrate. Integration of the areas of radiochromatographic peaks, corrected for radioactive decay and normalized to the TOPY value, are used in the assignment of values. Combined organic product yields (COPY) are the summation of selected individual organic product yield values for quantitative and qualitative discussion, e.g., summation of individual organic products with a two carbon structure (ΣC_2 COPY).
(10) W. E. Rice and J. E. Willard, *J. Am. Chem. Soc.*, **75**, 6156 (1953).
(11) "International Critical Tables of Numerical Data, Physics, Chemistry and Technology", Vol. 3, National Research Council of the United States of America, 1933, p. 230.
(12) The critical values for acetylene are: T_c = 35.5 °C, P_c = 61.6 atm, ρ_c = 0.230 g cm^{-3}.
(13) At low temperature fractional crystallization may occur.
(14) T. A. Carlson and R. M. White, *J. Chem. Phys.*, **44**, 4510 (1966).
(15) E. P. Rack and A. A. Gordus, *J. Chem. Phys.*, **34**, 1855 (1961).
(16) M. D. Loberg and M. J. Welch, *J. Am. Chem. Soc.*, **95**, 1075 (1973).
(17) R. R. Pettijohn and E. P. Rack, *J. Phys. Chem.*, **76**, 3342 (1972).
(18) R. L. Ayres, O. C. Gadeken, and E. P. Rack, *J. Phys. Chem.*, **75**, 2880 (1971).
(19) R. L. Ayres, C. J. Michejda, and E. P. Rack, *J. Am. Chem. Soc.*, **93**, 1389 (1971).
(20) M. Kikuchi and L. B. Church, *Radiochim. Acta*, **19**, 128 (1973).
(21) A previous study (ref 17) could not observe directly $I^+(^1D_2)$ reaction with olefin since the first reaction $I^+ + I_2 \rightarrow I_2^+ + I$ results in an inorganic product not observed as TOPY.
(22) The exact nature of the further reactions are not known, however, the $\cdot CH^{128}I$ group appears to undergo endoergic hydrogen abstraction producing $CH_3{}^{128}I$ or $CH_2I^{128}I$. The expected further reaction, that of addition to acetylene, would lead, after hydrogen abstraction, to 1-iodopropane. This product was *not* observed under any sample conditions.
(23) The product may be 2-methyl-1-iodobutane. Because of approximately equal retention times the two possible products could not be resolved by the radiogas chromatograph.
(24) The distinction between addition to the iodo containing carbon and the hydro containing carbon is ignored in the reaction scheme. However, addition to the iodo side is preferred as evidenced by the small yield of *n*-butyl iodide and the absence of *n*-propyl iodide.
(25) Because of the paucity of thermodynamic data concerning iodine containing compounds, we report no probable heats of reaction. We are undertaking an ion cyclotron resonance study in an attempt to obtain suitable thermodynamic information.
(26) T. Smail, G. Miller, and F. S. Rowland, *J. Phys. Chem.*, **74**, 3464 (1970).
(27) R. A. Marcus, *J. Chem. Phys.*, **20**, 359 (1952).
(28) Two molecules of radii equal to $\sigma/2$ should have centers separated by $2(\sigma/2) = \sigma$. $\lambda/\sigma = \sigma/\sigma = 1$.
(29) EDF = $4M_HM_T/(M_H + M_T)^2$ where EDF is the energy degradation factor, M_H is the mass of the hot atom or complex and M_T is the mass of the solvent molecule.
(30) D. L. Bunker and W. L. Hase, *J. Chem. Phys.*, **59**, 4621 (1973).
(31) D. L. Bunker, *J. Chem. Phys.*, **57**, 332 (1972).
(32) C. T. Ting and F. S. Rowland, *J. Phys. Chem.*, **74**, 4080 (1970).
(33) J. D. Rynbrandt and B. S. Rabinovitch, *J. Chem. Phys.*, **54**, 2275 (1971).
(34) Y.-N. Tang and Y. Y. Su, *J. Chem. Phys.*, **57**, 4048 (1972).
(35) The random distribution of energy among oscillators is assumed and further, the complex decays randomly, governed only in bulk by first-order kinetics.
(36) Utilizing simple energy considerations it can be shown that the collisional lifetime (τ_c) is

$$\tau_c = \delta/(2\epsilon'/m)^{1/2}$$

where δ is the distance between molecules, ϵ' is the translational energy of the hot atom complex, and m is the mass of the complex. The collisional lifetime is the time between molecular collisions where each collision has been assumed to result in deactivation. RRKM theory states that the lifetime of any complex that obeys unimolecular kinetics is inversely related to the overall rate constant:

$$\tau_k = 1/k$$

$$k = \int_{\epsilon^*}^{\infty} k_a(\epsilon)\, P(\epsilon)\, d\epsilon/(1 + k_a(\epsilon)/Z[M])$$

where τ_k is the kinetic lifetime, k is the overall rate constant, $k_a(\epsilon)$ is the activation rate constant as a function of internal energy (ϵ), $P(\epsilon)$ is the energy distribution function, $Z[M]$ is the deactivation rate constant (equal to the product of the collision number and solvent concentration), and ϵ^* is the decomposition threshold energy.
(37) R. Wolfgang, *Adv. Chem. Res.*, **3**, 48 (1970).
(38) The RRK lifetime is

$$\tau = A\left(\frac{\epsilon - \epsilon^*}{\epsilon}\right)^{1-s}$$

where τ is the lifetime, A is the Arrhenius frequency factor, ϵ is the internal energy, ϵ^* is the decomposition threshold energy, and s is the effective number of oscillators.

Kinetic and Salt Effects of the Ethyloxalate–Hydroxide Ion Reaction

Roberto Zamboni,* Ambrogio Giacomelli, Francesco Malatesta,

Istituto di Chimica Analitica ed Elettrochimica, Università di Pisa, Pisa, Italy

and Antonio Indelli

Istituto di Tecnologie Chimiche Speciali, Università di Bologna, Bologna, Italy *(Received December 1, 1975)*

Publication costs assisted by the Consiglio Nationale delle Ricerche

The rate of the reaction of the ethyloxalate ion with hydroxide ion has been measured at eight different temperatures, using a potentiometric method, in the presence of twelve different salts. Where a direct comparison is possible, an agreement with published results within 4% was obtained, despite the difference in conditions (method and concentrations). The Olson–Simonson effect was shown to be predicted by a numerical integration of the Poisson–Boltzmann equation (IPBE). The effects of alkali metal sulfates and tri- and tetrametaphosphates, however, cannot be quantitatively predicted neither by IPBE nor by the Mayer theory in its simplest form (DHLL + B_2), using a single $\mathring{a}$ parameter, but only by DHLL + B_2 using two different $\mathring{a}$, which are the same for all the salts. Different methods give values of k_0, extrapolated at $I = 0$ for the alkali metal salts, which are in good agreement with each other, and fit very accurately an Arrhenius plot. Results for the alkaline earth metal ions require the additional assumption of ion pair formation, whereas results for the tetraalkylammonium ions cannot be predicted by any of the above theories or assumptions. It is concluded that nonelectrostatic effects are present, and this is confirmed by the values of $\Delta H^{\ddagger}$ and $\Delta S^{\ddagger}$. For Mg^{2+} inner-sphere interactions appear to be the most likely explanation, whereas for tetraalkylammonium ions the effects appear to be related to the structure-forming properties of these electrolytes.

Is it well known that elementary electrostatic theories, such as the Debye–Hückel theory, are inadequate to interpret the details of salt effects in reactions between ions, particularly when multivalent anions and/or cations or tetraalkylammonium salts are involved.[1-7] It has been shown qualitatively that the use of more sophisticated electrostatic theories can account for some of the most striking anomalies.[2-4] We considered it useful to make a careful study of a rather simple reaction in a variety of conditions in order to test the extent to which different theories can account for all the results, using as few adjustable parameters as possible. The reaction of ethyloxalate with hydroxide ion was chosen because it has already been studied with remarkable care,[3,5,6] so that a comparison with previous results is possible.

Experimental Section

Materials. Most of the chemicals were Erba RP. Sodium, potassium, magnesium, strontium, and barium nitrates were recrystallized three times from conductivity water and dried under vacuum. Potassium sulfate was recrystallized three times from conductivity water and then dried in a furnace at 350 °C. Sodium tri- and tetrametaphosphates were prepared and purified as described in preceding papers.[8]

Stock solutions of these salts were prepared by weighing, and the various concentrations were obtained by dilution. The tetraalkylammonium nitrates were prepared by adding to the corresponding bromides an amount of silver nitrate slightly lower than stoichiometric. The resulting solutions, after concentration under vacuum, were passed through an ion-exchange column filled with Dowex 50 resin in the nitrate form. The solutions were dried and the solid salts were dissolved in hot conductivity water and crystallized at low temperature. This was possible only for tetramethyl- and tetraethylammonium nitrates, while the *n*-tetrapropyl- and *n*-tetrabutylammonium nitrates, because of their high solubilities in water, were precipitated at low temperature from acetone and benzene, respectively. The solutions of tetraalkylammonium nitrates were standardized by passing them through an ion-exchange column filled with Dowex 50 in acid form and the effluents were titrated with 0.1 N NaOH using brom thymol blue as an indicator.

Potassium ethyloxalate was prepared by Nielsen's method[9] and crystallized from absolute ethanol. It was found to be 99.5% pure by complete hydrolysis and titration.

Kinetics. All the kinetic measurements were carried out at 4, 10, 15, 20, 25, 30, 35, and 40 °C, in thermostats which assured a temperature constancy of better than 0.005 °C.

A tenfold excess of potassium ethyloxalate was used, so that the reaction was pseudo-first order. The disappearance of OH^- was followed potentiometrically using a glass electrode Metrohm EA 121, which can be used without appreciable error up to a pH of 12. Since the reaction, even in the absence of added salts, did not involve a remarkable change in ionic strength, or in general of the ionic environment, the logarithm of $[OH^-]$ is a strictly linear function of the potential, with a Nernstian slope. This has been confirmed in preliminary runs using different additions of NaOH. In all the following runs the concentration of potassium ethyloxalate was 10^{-3} M and that of NaOH was 10^{-4} M. The electrode potential was measured and recorded using a Metrohm potentiograph E 436. A solution of potassium ethyloxalate was put in a quartz flask and freed from CO_2 by bubbling with pure nitrogen. After thermal equilibration the appropriate quantity of CO_2-free NaOH solutions was added with a microsyringe. Continuous stirring was maintained by means of a magnetic bar during all runs. The kinetic measurements were all repeated from two to four times.

Results

The rate constants at 25 °C, where a direct comparison is possible, agree with the results already published[3,6] within 4%, despite the different experimental method, and the different

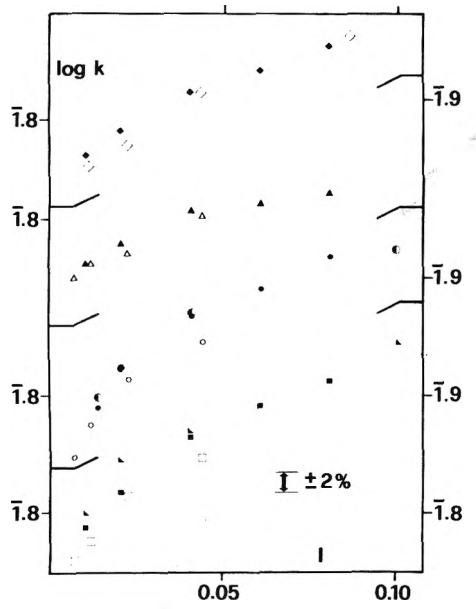

Figure 1. Values of log k for the reaction in the presence of $NaNO_3$ (squares), KNO_3 (circles), $Na_3P_3O_9$ (triangles), and $(CH_3)_4NNO_3$ (diamonds): filled symbols, present results; half-filled symbols, ref 6; open symbols, ref 3. Blank values of log k are $\bar{1}.716$ for $I = 0.001\ 10$ (present results), $\bar{1}.732$ for $I = 0.001\ 30$,[6] and $\bar{1}.717$ for $I = 0.001\ 67$.[3] Temperature, 25 °C.

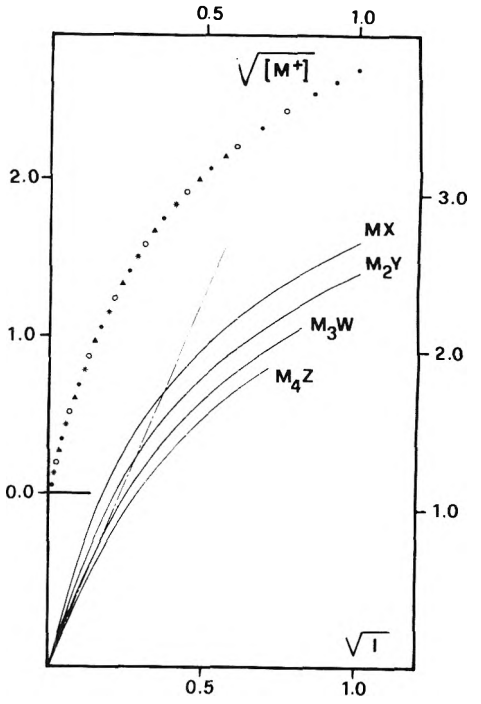

Figure 2. Natural logarithm of the ratio of the activity coefficients for the reaction $A^- + B^{2-} \rightleftharpoons C^{3-}$, in the presence of salts of different valence types, MX, M_2Y, M_3W, and M_4Z, calculated by means of IPBE for a distance of closest approach of 3.0 Å and plotted against $I^{1/2}$ (lower curves, lower and right scales) or against $[M^+]^{1/2}$ (upper and left scale; ●, ○, △, and • for the presence of MX, M_2Y, M_3W, and M_4Z, respectively): Dash-and-dot line, Debye–Hückel limiting slope; temperature, 25 °C.

reactant concentrations. This is shown in Figure 1, where some examples of the rate constants plotted against the square root of the ionic strength at 25 °C are reported. The agreement between our results in the presence of alkaline earth metal nitrates and the results of Hoppé and Prue[5] in the presence of the corresponding chlorides is somewhat poorer. This can probably be attributed to the conditions chosen by Hoppé and Prue (high concentration of reactants, in comparison with the added salts), and to their sampling technique, which was not well suited for high reaction rates.

In the presence of sodium or potassium the substitution of NO_3^- for ClO_4^- or Cl^- does not appear to have a remarkable influence. On the contrary, the tetraethylammonium nitrate shows an effect which is strikingly different from that of the corresponding perchlorate.[6] A lack of additivity of the action of the cation and the anion of the added salts has been observed in the persulfate iodide reaction: $KClO_4$ is as effective as KCl, whereas $NaClO_4$ is more effective than NaCl.[10] In the presence of multivalent anions SO_4^{2-}, $P_3O_9^{3-}$, or $P_4O_{12}^{4-}$, the well-known "Olson–Simonson effect"[7] is observed, that is the rate does not depend upon the ionic strength, but only upon the concentration of the cations. This is in agreement with what had been already reported.[3,6]

Alkaline earth cations have a large accelerating effect increasing in the order $Ba^{2+} < Sr^{2+} < Mg^{2+}$ at all temperatures. A summary of the results is reported in Tables I, II, and III, which give activation parameters for the reactions in the presence of different salts. These values were obtained from rate measurements at eight temperatures from 4 to 40 °C.

Discussion

One of the main features of the reaction between anions, that is, the Olson–Simonson effect, has been shown by Scatchard[2] to be in agreement with the prediction of the Mayer theory.[11] These results have been later confirmed for very high dilutions.[3,4] On the other hand, the Mayer theory, in the simple form called by Friedman DHLL + B_2,[12] fails to predict the activity coefficients and the molar enthalpies at $I > 0.01$.[13,14] The numerical integration of the Poisson–Boltzmann equation (IPBE) gives satisfactory results for the same problems up to $I = 0.1$.[13,14] Therefore we tried first of all to see whether IPBE is able to predict the Olson–Simonson effect.

The calculations, performed with the usual method,[13] have shown that for reactions between two anions, independently of the charge of the activated complex, from −2 to −7, the Olson–Simonson effect is predicted in a range of ionic strength and of distance of closest approach ($\mathring{a}$) much wider than for the Mayer theory. Figure 2 shows one example for a reaction between a univalent and a bivalent anion, for $\mathring{a} = 3.0$ Å. In contrast, the decrease in rate when increasing the charge of the ions of the same sign as that of the reactants for small $\mathring{a}$ (or for low values of the dielectric constant) is not predicted by IPBE. Such effect, which is opposite to the predictions of the Brønsted–Debye–Scatchard equation, has been some times observed experimentally,[14-16] and is predicted by the Mayer theory.[3,4] On the other hand, for very large values of $\mathring{a}$ (beyond 6 Å and much more for highly charged activated complexes) IPBE, as well as DHLL + B_2,[3,4] predicts a gradual disappearance of the Olson–Simonson effect and a dependence upon the ionic strength.

We conclude that the failure of the simple Debye–Hückel theory appears to be due mainly to the neglecting of the higher terms of the series development of the exponential, rather than to the well-known internal inconsistency of the Poisson–Boltzmann equation.[17]

Both IPBE and DHLL + B_2 predict the Olson–Simonson effect even in the presence of quadrivalent anions. This is not in agreement with our experimental data which show that in

TABLE I: $\Delta H^{\ddagger}$ (kJ mol^{-1}) and $\Delta S^{\ddagger}$ (J mol^{-1} deg^{-1}) for the Reaction in the Presence of Alkali Metal Salts[a]

$I^{1/2}$	$NaNO_3$	KNO_3	K_2SO_4	$Na_3P_3O_9$	$Na_4P_4O_{12}$
0.105 $\Delta H^{\ddagger}$	35.2 ± 0.2	35.7 ± 0.1	35.4 ± 0.4	35.3 ± 0.3	35.2 ± 0.2
$\Delta S^{\ddagger}$	−131.0 ± 0.4	−128.9 ± 0.4	−130.1 ± 1.3	−130.8 ± 1.0	−131.5 ± 0.8
0.145 $\Delta H^{\ddagger}$	35.2 ± 0.2	36.0 ± 0.1	35.8 ± 0.5	35.9 ± 0.3	35.8 ± 0.4
$\Delta S^{\ddagger}$	−130.2 ± 0.4	−127.3 ± 0.5	−128.4 ± 1.5	−128.4 ± 0.8	−129.2 ± 1.1
0.203 $\Delta H^{\ddagger}$	35.3 ± 0.2	36.6 ± 0.2	35.5 ± 0.2	35.0 ± 0.3	34.9 ± 0.3
$\Delta S^{\ddagger}$	−128.9 ± 0.6	−124.7 ± 0.5	−128.4 ± 0.8	−130.8 ± 0.7	−131.8 ± 0.9
0.247 $\Delta H^{\ddagger}$	36.0 ± 0.3	36.5 ± 0.2	35.2 ± 0.4	34.8 ± 0.3	34.3 ± 0.2
$\Delta S^{\ddagger}$	−125.9 ± 1.0	− 124.5 ± 0.5	−129.4 ± 1.1	−131.0 ± 0.9	−133.5 ± 0.7
0.285 $\Delta H^{\ddagger}$	37.3 ± 0.3	36.1 ± 0.2	35.3 ± 0.3	34.8 ± 0.3	34.2 ± 0.2
$\Delta S^{\ddagger}$	−121.1 ± 1.1	−125.2 ± 0.6	−128.6 ± 1.0	−130.6 ± 0.9	−133.8 ± 0.5

[a] The values of $\Delta H^{\ddagger}$ and $\Delta S^{\ddagger}$ for the reaction in absence of added salt ($I^{1/2}$ = 0.033) are 35.2 ± 0.4 and 132.1 ± 1.3, respectively.

TABLE II: $\Delta H^{\ddagger}$ (kJ mol^{-1}) and $\Delta S^{\ddagger}$ (J mol^{-1} deg^{-1}) for the Reaction in the Presence of Tetraalkylammonium Nitrates

$I^{1/2}$	$(CH_3)_4NNO_3$	$(C_2H_5)_4NNO_3$	$(n\text{-}C_3H_7)_4NNO_3$	$(n\text{-}C_4H_9)_4NNO_3$
0.105 $\Delta H^{\ddagger}$	35.3 ± 0.2	36.7 ± 0.4	37.3 ± 0.3	35.2 ± 0.3
$\Delta S^{\ddagger}$	−131.0 ± 0.5	−126.6 ± 1.2	−124.6 ± 0.8	−131.8 ± 1.0
0.145 $\Delta H^{\ddagger}$	36.2 ± 0.1	37.7 ± 0.4	37.5 ± 0.3	35.6 ± 0.3
$\Delta S^{\ddagger}$	−127.6 ± 0.4	−123.5 ± 1.2	−123.4 ± 0.7	−129.9 ± 0.9
0.203 $\Delta H^{\ddagger}$	36.1 ± 0.4	38.8 ± 0.2	38.0 ± 0.5	35.9 ± 0.3
$\Delta S^{\ddagger}$	−127.6 ± 1.1	−120.1 ± 0.5	−122.1 ± 1.4	−128.8 ± 0.9
0.247 $\Delta H^{\ddagger}$	35.2 ± 0.2	39.0 ± 0.2	38.3 ± 0.4	35.7 ± 0.6
$\Delta S^{\ddagger}$	−130.5 ± 0.4	−120.0 ± 0.5	−121.0 ± 1.4	−129.3 ± 2.1
0.285 $\Delta H^{\ddagger}$	34.9 ± 0.5	39.0 ± 0.3	38.5 ± 0.4	35.4 ± 0.6
$\Delta S^{\ddagger}$	−131.1 ± 1.5	−120.7 ± 0.8	−120.8 ± 1.4	−130.6 ± 1.8

TABLE III: $\Delta H^{\ddagger}$ (kJ mol^{-1}) and $\Delta S^{\ddagger}$ (J mol^{-1} deg^{-1}) for the Reaction in the Presence of Alkaline Earth Metal Salts

$I^{1/2}$	$Mg(NO_3)_2$	$Sr(NO_3)_2$	$Ba(NO_3)_2$
0.052 $\Delta H^{\ddagger}$	45.7 ± 0.2	38.7 ± 0.2	
$\Delta S^{\ddagger}$	−88.7 ± 0.5	−116.1 ± 0.5	
0.071 $\Delta H^{\ddagger}$	45.8 ± 0.4	39.0 ± 0.4	
$\Delta S^{\ddagger}$	−83.5 ± 1.4	−112.2 ± 1.1	
0.084 $\Delta H^{\ddagger}$	45.4 ± 0.3	39.2 ± 0.2	
$\Delta S^{\ddagger}$	−82.8 ± 0.8	−109.5 ± 0.4	
0.105 $\Delta H^{\ddagger}$	46.0 ± 0.4	40.6 ± 0.4	41.3 ± 0.4
$\Delta S^{\ddagger}$	−78.0 ± 1.3	−102.6 ± 1.3	−102.2 ± 1.3
0.145 $\Delta H^{\ddagger}$	45.1 ± 0.3	40.5 ± 0.5	42.1 ± 0.6
$\Delta S^{\ddagger}$	−78.3 ± 1.1	−100.1 ± 1.6	−96.8 ± 1.9
0.203 $\Delta H^{\ddagger}$	42.3 ± 0.2	40.5 ± 0.5	42.7 ± 0.8
$\Delta S^{\ddagger}$	−85.1 ± 0.7	−97.3 ± 1.6	−92.0 ± 2.5
0.247 $\Delta H^{\ddagger}$	39.4 ± 0.4	41.7 ± 0.5	42.7 ± 0.5
$\Delta S^{\ddagger}$	−94.0 ± 1.3	−91.6 ± 1.7	−90.7 ± 1.7
0.285 $\Delta H^{\ddagger}$	39.1 ± 0.6	40.5 ± 0.5	42.6 ± 0.3
$\Delta S^{\ddagger}$	−94.6 ± 1.8	−94.8 ± 1.5	−89.7 ± 0.8

the presence of $Na_4P_4O_{12}$ the rate is definitely smaller than in the presence of $NaNO_3$, at constant $[Na^+]$. A good agreement can instead be obtained by using DHLL + B_2 applied to a slightly different model, which involves two values of $\dot{a}$, one for the pairs of ions containing the activated complex and the other for all the other pairs of ions. For instance, in the case of alkali metal salts, assuming $\dot{a}$ = 3.7 for the first value and $\dot{a}$ = 3.0 for the second, a good quantitative agreement can be found for the reaction rate in the presence of $NaNO_3$, KNO_3, K_2SO_4, $Na_3P_3O_9$, and $Na_4P_4O_{12}$ at 25 °C (Figure 3).[18]

For other temperatures, the agreement is almost as good as at 25 °C for 15, 20, and 30 °C and deteriorates progressively both at higher and lower temperatures. Probably this is due to the oversimplifying assumption of constant $\dot{a}$'s. Even at 4 and 40 °C, however, the agreement is good enough to obtain a reliable extrapolation at zero ionic strength, using all results obtained with the five mentioned salts. The values of $\log k_0/T$ at 4, 10, 15, 20, 25, 30, 35, and 40 °C are respectively $\bar{4}.745 \pm 0.010$, $\bar{4}.889 \pm 0.007$, $\bar{3}.000 \pm 0.004$, $\bar{3}.111 \pm 0.005$, $\bar{3}.208 \pm 0.003$, $\bar{3}.313 \pm 0.005$, $\bar{3}.417 \pm 0.006$, and $\bar{3}.510 \pm 0.008$, and are a strictly linear function of $1/T$ with a standard deviation of ±0.003. The corresponding $\Delta H^{\ddagger}$ and $\Delta S^{\ddagger}$ values are 35.22 ± 0.07 kJ mol^{-1} and −132.7 ± 0.3 J mol^{-1} deg^{-1}, respectively.

Practically the same values of k_0 can be obtained using IPBE in the presence of $NaNO_3$, KNO_3, K_2SO_4, and $Na_3P_3O_9$, assuming $\dot{a}$ = 4.0 Å. A reasonable fit, giving again the same values of k_0, can also be obtained using the simple Brønsted–Debye–Scatchard equation if individual values of $\dot{a}$ are assumed for each different salt, namely, $\dot{a}$ = 3.0 for $NaNO_3$ and KNO_3, 5 Å for K_2SO_4, 7 Å for $Na_3P_3O_9$, and 15 Å for $Na_4P_4O_{12}$ (the fit in the last case is somewhat poorer). The latter treatment cannot be considered more than an empirical curve-fitting method, in our opinion, but it is reassuring that practically the same extrapolations are obtained.

In contrast, none of the three treatments succeeds in accounting for the rates obtained in the presence of tetraalkylammonium salts, particularly for the tetraethyl- and tetrapropylammonium nitrates. Since for 1–1 electrolytes the three theories give very similar results, the discrepancy must be attributed to the presence of nonelectrostatic effects.

A similar conclusion can be reached for the effects of the alkaline earth metal ions. Both DHLL + B_2 and IPBE predict a large accelerating effect of such cations, but neither succeeds in giving a quantitative agreement with the experimental values, no matter what average $\dot{a}$ is assumed for IPBE, or what combination of $\dot{a}$'s is assumed for DHLL + B_2. The results of the two treatments are remarkably different, though, so that, in principle, the possibility that a different type of electrostatic treatment gives a good results cannot be ruled out. However, further support for the existence of a nonelectrostatic effect will be given below.

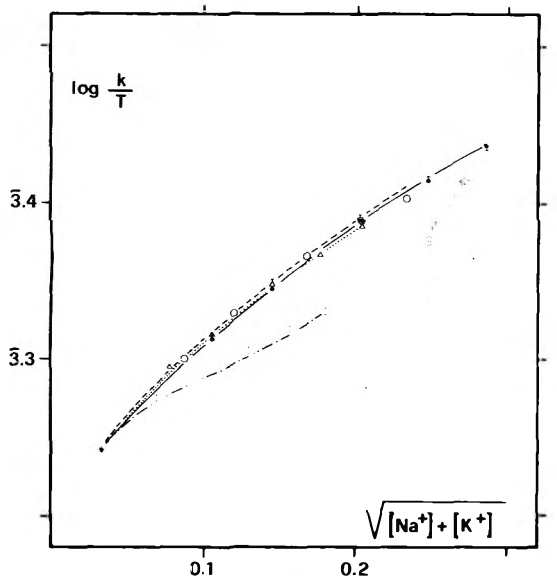

Figure 3. Values of log k/T as a function of the total cation's concentration in the blank solution (*) and in the presence of $NaNO_3$ (●), KNO_3 (+), K_2SO_4 (O), $Na_3P_3O_9$ (Δ), and $Na_4P_4O_{12}$ (□). As a comparison, DHLL + B_2 calculated curves for a model which assumes 3.7 Å as a distance of closest approach with the activated complex and 3.0 Å in all the other cases, by starting from log $k_0/T = \bar{3}.208$ for $I = 0$: continuous, dashed, dotted, and dash-and-dot lines for the presence of 1-1, 1-2, 1-3, and 1-4 electrolytes, respectively. Temperature, 25 °C.

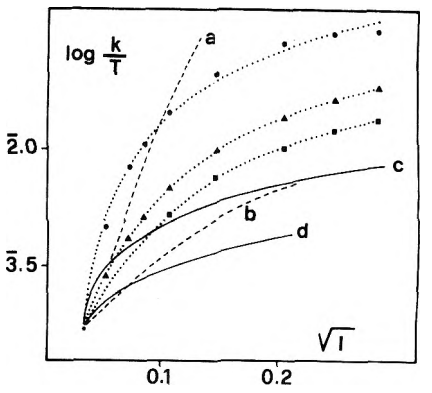

Figure 4. Values of log k/T from experimental measurements (* for the blank solution, ●, ▲, and ■ in the presence of $Mg(NO_3)_2$, $Sr(NO_3)_2$, and $Ba(NO_3)_2$, respectively) and comparison with calculated values: dashed lines, DHLL + B_2 previsions for $\mathring{a} = 2.5$ Å (curve a) and 3.0 Å (curve b); continuous lines, IPBE for $\mathring{a} = 2.0$ Å (curve c) and 2.6 Å (curve d); dotted lines, DHLL + B_2 with the assumption of different reaction paths (see text). Temperature, 25 °C.

A good agreement can be obtained using DHLL + B_2 and the assumption of different reaction paths, involving the association of the alkaline earth metal cations with the reactants (see Figure 4). One path could involve the ion pair MOH^+ and $Etox^-$, another OH^- and $MEtox^+$, and a third MOH^+ and $MEtox^+$. The reaction rate, v, was therefore calculated from

$$v = [OH^-][Etox^-]f_{-1}^2 \times \{k_0 f_{-2}^{-1} + k_1[M]f_{+2} + k_2[M]^2 f_{+2}\} \quad (1)$$

where $[OH^-]$, $[Etox^-]$, and $[M]$ are the concentrations of hydroxide, ethyloxalate, and alkaline earth metal ions calculated from the association constants, f_{+2}, f_{-1}, and f_{-2} are the DHLL + B_2 activity coefficients of a +2, −1, and −2 charged ion, and k_1 and k_2 are rate constants including the association constants of alkaline earth metal ion with OH^- (K') and with $Etox^-$ (K''), $k_1 = k_1'K' + k_1''K''$ and $k_2 = k_2'K'K''$. k_1 and k_2 were calculated by least squares with given values of $\mathring{a}$ (or $\mathring{a}$'s), K', and K''. A wide range of association constants and $\mathring{a}$ values leads to very similar fits to the experimental data, in spite the fact that very different values of k_1 and k_2 are obtained. No particular meaning can therefore be given to the various rate and association constants. Figure 4 shows the results of the calculation performed at 25 °C by assuming for $\mathring{a}$'s the same values as previously used for the alkali-metal ions case ($\mathring{a} = 3.7$ and 3.0 Å) and arbitrarily setting K'' equal to K'. To K' were attributed the values of 380, 6.6, and 4.35 M^{-1} for Mg^{2+}, Sr^{2+}, and Ba^{2+}, respectively,[19] a choice which also is rather arbitrary. The respective values of k_1 (M^{-2} s^{-1}) and k_2 (M^{-3} s^{-1}) are 3.91×10^3 and 1.32×10^6 for Mg^{2+}, 7.63×10^2 and 8.54×10^3 for Sr^{2+}, and 5.48×10^2 and 2.77×10^3 for Ba^{2+}, whereas k_0 has the previously extrapolated value of 0.482 M^{-1} s^{-1}. A similar treatment was adopted by Hoppé and Prue,[5] using the simple Brønsted-Debye-Scatchard equation. The fact that, even using DHLL + B_2, ionic association must be invoked suggests that inner-sphere interactions are involved.

A critical, although difficult, test for the existence of non-electrostatic effects is the dependence upon the concentration of the activation parameters.[17] The Brønsted-Debye-Scatchard equation predicts that an increase in the rate due to salt effects is accompanied by an increase in the activation enthalpy and an increase (eventually, a less negative value) of the activation entropy. This occurs because when increasing the temperature the product DT decreases, and in all cases this product appears in the denominator of the different equations expressing the logarithms of the activity coefficients. Therefore all electrostatic treatments should give the same trend. Not all the apparent exceptions have a clear meaning, because of the experimental errors. In the case of the alkali metal salts, for instance, this prediction cannot be considered unfulfilled.

In the case of the alkaline earth cations and particularly of Mg^{2+}, at very low concentration, up to 0.02 M, there is a continuous increase of the activation entropy, but from 0.02 onward the increase in the rate is entirely due to a decrease in $\Delta H^{\ddagger}$, $\Delta S^{\ddagger}$ becoming progressively more negative. Of course, if the ion pair assumption is considered as the explanation of the increase in the rate due to the magnesium salt, the activation parameters contain the enthalpy and entropy of formation of the ion pairs. However if the ion pairs were electrostatic in nature, the above rule for the comprehensive activation parameters should be obeyed in any case. This can be taken as another indication that Mg^{2+} forms inner-sphere compounds with the reactants or the activated complex.

Nonelectrostatic effects must be present in the case of tetraalkylammonium salts as well, and particularly for tetraethyl- and tetrapropylammonium salts, which at high concentration show consistently larger activation energies and less negative entropies than the alkali metal salts, despite the fact that the reaction rate is smaller. On the other hand, for the tetramethylammonium nitrate, there is apparently a slight decrease in $\Delta H^{\ddagger}$ and a slight decrease in $\Delta S^{\ddagger}$ when increasing the concentration. Finally for tetraethyl-, tetrapropyl-, and tetrabutylammonium nitrates the decrease in the rate at higher concentrations is accompanied by an increase in the activation energy. Although the experimental errors could invalidate some of these trends, it appears unlikely that they are not real. That these nonelectrostatic effects are due to the influence of these ions on the structure of the water is very likely. More specific effects, however, cannot be ruled out. The fact that the highest $\Delta H^{\ddagger}$ are observed for Et_4NNO_3 and for

n-Pr_4NNO_3 is perhaps related to the similarity in size with the leaving ethyl group.

References and Notes

(1) B. Perlmutter-Hayman, *Prog. React. Kinet.*, **6**, 240 (1971).
(2) G. Scatchard, *Natl. Bur. Stand. (U.S.), Circ.*, **No. 534**, 185 (1953).
(3) A. Indelli, *Gazz. Chim. Ital.*, **92**, 365 (1962).
(4) A. Indelli and R. De Santis, *J. Chem. Phys.*, **55**, 4811 (1971).
(5) J. I. Hoppe and J. E. Prue, *J. Chem. Soc.*, 1775 (1957).
(6) A. Indelli, V. Bartocci, F. Ferranti, and M. G. Lucarelli, *J. Chem. Phys.*, **44**, 2069 (1966); A. Indelli, *J. Phys. Chem.*, **65**, 972 (1961).
(7) A. R. Olson and T. R. Simonson, *J. Chem. Phys.*, **17**, 1167 (1949).
(8) A. Indelli, *Ann. Chim. (Rome)*, **43**, 845 (1953); **46**, 717 (1956); **47**, 586 (1957); T. Moeller, *Inorg. Synth.*, **5**, 98 (1957).
(9) R. F. Nielsen, *J. Am. Chem. Soc.*, **58**, 206 (1936).
(10) A. Indelli and J. E. Prue, *J. Chem. Soc.*, 107 (1959).
(11) J. E. Mayer, *J. Chem. Phys.*, **18**, 1426 (1950).
(12) J. C. Rasaiah and H. L. Friedmann, *J. Chem. Phys.*, **48**, 2742 (1968).
(13) A. Indelli and F. Malatesta, *Gazz. Chim. Ital.*, **103**, 421 (1973).
(14) A. Indelli and F. Malatesta, *Gazz. Chim. Ital.*, **103**, 435 (1973).
(15) R. M. Healy and M. L. Kilpatrich, *J. Am. Chem. Soc.*, **77**, 5258 (1955).
(16) *V. Carassiti, C. Dejak, and I. Mazzei, Ann. Chim. (Rome)*, **50**, 979 (1960).
(17) A. Indelli and E. S. Amis, *J. Am. Chem. Soc.*, **82**, 332 (1960).
(18) A rationalization of such model can be done by taking into account that the activated complex is a species intrinsically different from the other ions. It is not surprising therefore that its "radius" cannot be assumed to be identical with that of the other ions, even in a gross approximation which neglects the individual difference between "normal" ions. Obviously, no treatment of this kind can be made using IPBE.
(19) J. N. Butler, "Ionic Equilibrium. A Mathematical Approach", Addison-Wesly, Reading, Mass., *1964*, p 469.

Water Participation in Proton-Transfer Reactions of Glycine and Glycine Methyl Ester[1]

K. C. Chang and Ernest Grunwald*

Chemistry Department, Brandeis University, Waltham, Massachusetts 02154

(Received January 15, 1976)

NH-proton transfer reactions with water participation of glycine and methyl esters of glycine, alanine, and phenylalanine were studied by dynamic NMR methods. For glycine and its methyl ester, kinetic analysis (and comparison with total rates of NH-proton exchange due to Sheinblatt and Gutowsky) reveals that processes which are second order in substrate proceed partly with and partly without water participation. There is evidence for intramolecular proton transfer between the NH_3^+ and CO_2^- groups in glycine zwitterion, and for bifunctional proton transfer between the zwitterion and the uncharged amino acid. Rate constants are reported for proton transfer between ammonia and a series of carboxylic acids. A precise and convenient pulse sequence for NMR T_1 measurement is described.

The kinetics of NH_3-proton exchange of glycine in aqueous solution has been studied comprehensively by Sheinblatt and Gutowsky (SG).[2] These authors examined the CH_2-proton resonance and thus measured the *total* rate of NH-proton exchange. Because of the insight one can gain into solvation phenomena by studying proton exchange with water participation,[3] we now report a complimentary study of NH_3-to-HOH proton exchange. Total rates of NH_3-proton transfer between glycine and water have also been studied by ^{15}N NMR,[4,5] and by relaxation spectrometry.[6,7]

In the present work, exchange rates were deduced from measurements of $(1/T_2 - 1/T_1)$ of the H_2O NMR or, for fast exchange, of the collapsed H_2O–NH_3 NMR. The technique and rate calculations are familiar from previous publications.[8] Rate measurements were made at five glycine concentrations ranging from 0.04 to 0.20 M, and in the pH range 3.9–6.3. All in all, ~60 independent solutions were measured at 25 °C and subjected to kinetic analysis.

The kinetics is fully consistent with that established by SG. The rate law is shown as follows:

$$3/\tau_{NH} = k_A + k_B[R^{\pm}] + k_C[OH^-] + k_D[R^-] \qquad (1)$$

where τ_{NH} = mean time a proton resides on $-NH_3$ during one cycle of proton exchange between $R^{\pm}$ and water; $R^+ = H_3N^+CH_2CO_2H$; $R^{\pm} = H_3N^+CH_2CO_2^-$; $R^0 = H_2NCH_2CO_2H$; $R^- = H_2NCH_2CO_2^-$. The factor 3 allows for the fact that there are three NH protons per molecule of the reactant, $R^{\pm}$.

The new rate constants for proton exchange with water, and comparable rate constants reported by SG[2] for total NH-proton exchange, are listed in Table I. The ratio in each case measures the fraction f_W of reaction with water participation. These rate constants will now be discussed briefly.

k_A. As pointed out by SG, the major contribution to k_A is made by an intramolecular reaction, $R^{\pm} \rightleftarrows R^0$. Our rate constant is in good agreement with that of SG. Unfortunately, f_W is indeterminate in this case because the CO_2H proton in R^0 is in rapid exchange with water protons.[2,3]

k_B. Table I shows three possible reactions which might account for the observed kinetics. A fourth possibility, $2R^{\pm} \rightleftarrows 2R^0$, has a p$K$ of 10.8 and would be undetectably slow. Reactions III and IV, which yield $R^- + R^+$, involve just one functional group in each of the reactants, while the symmetrical process V involves two functional groups.

Reaction III involves the functional groups NH_3^+ and NH_2. Rate constants for such processes in the direction of negative $\Delta G°$ are rarely greater than 2×10^9 s^{-1} M^{-1}.[9,10] Thus a plausible upper limit to the contribution of III to k_B is estimated to be 100 s^{-1} M^{-1}. Reaction IV involves proton transfer between NH_3^+ and CO_2^-. Rate constants for the analogue of the reverse reaction have been measured[11,12] and are listed in Table II. The values are generally less than 10^9 s^{-1} M^{-1}, and a plausible upper limit to the contribution of IV to k_B is thus estimated to be 50 s^{-1} M^{-1}. Thus reaction V appears to make a significant contribution. Jencks and Hand[13] recently con-

TABLE I: Kinetic Results for NH-Proton Exchange of Glycine in Water at 25 °C

Term (eq 1)		Reaction	pK^a	Rate constant, s^{-1} or s^{-1} M^{-1} with H_2O	Rate constant, s^{-1} or s^{-1} M^{-1} Total (23 ± 1 °C)	f_W
k_A	(I)	$R^{\pm} \rightleftarrows R^- + H^+$ (k_a)	9.60	(10)[b]	(10)[b]	1.00
	(II)	$R^{\pm} \rightleftarrows R^0$ (k_{intra})	5.39	160 ± 20	170[c]	Indeterminate[f]
$k_B(R^{\pm})$	(III)	$R^{\pm} + R^0 \rightleftarrows R^- + R^+$	1.87			
	(IV)	$R^{\pm} + R^{\pm} \rightleftarrows R^- + R^+$	7.26	390 ± 100	640[c]	0.61 ± 0.16
	(V)	$R^{\pm} + R'^0 \rightleftarrows R^0 + R'^{\pm}$	0.00			
$k_C(OH^-)$	(VI)	$R^{\pm} + OH^- \rightleftarrows R^- + HOH$	−4.40	$(2.6 \pm 1.0) \times 10^{10}$	1.4×10^{10} [d] 1.9×10^{10} [e]	1.5 ± 0.6
$k_D(R^-)$	(VII)	$R^{\pm} + R'^- \rightleftarrows R^- + R'^{\pm}$	0.00	$(7.9 \pm 0.2) \times 10^7$	3.8×10^8 [c]	0.21 ± 0.01

[a] Based on data in ref 2 and 12. [b] k_{-a} for GME^+ was multiplied by a factor of 1.88 to allow for the effect of the negative charge, to give $k_{-a} = 4.1 \times 10^{10}$ s^{-1} M^{-1} for $R^- + H^+$. [c] Reference 2. [d] Reference 7. [e] Reference 6. [f] Because the CO_2H and water protons are in rapid exchange.

TABLE II: Rate Constants for Proton Transfer in the System $RCO_2H + NH_3 \rightleftarrows RCO_2^- + NH_4^+$ in Water at 25 °C[a]

RCO_2H	k_+, s^{-1} M^{-1}	k_-, s^{-1} M^{-1}
HCO_2H	8.0×10^8	2.5×10^3
CH_3CO_2H	6.5×10^8	2.1×10^4
$CH_3CH_2CO_2H$	4.7×10^8	2.0×10^4
$(CH_3)_3CCO_2H$	6.1×10^8	3.8×10^4

[a] Data of V. K. Anderson and E. Grunwald. Rate constants refer to total proton exchange.

sidered the formation of RCO_2^-·HO_2CR hydrogen-bonded complexes in aqueous solution and presented evidence that the association constant is 0.25 M^{-1} for HCO_2^-·HO_2CH. Accordingly, reaction V could be rationalized as bifunctional proton transfer within a hydrogen-bonded complex, as follows:

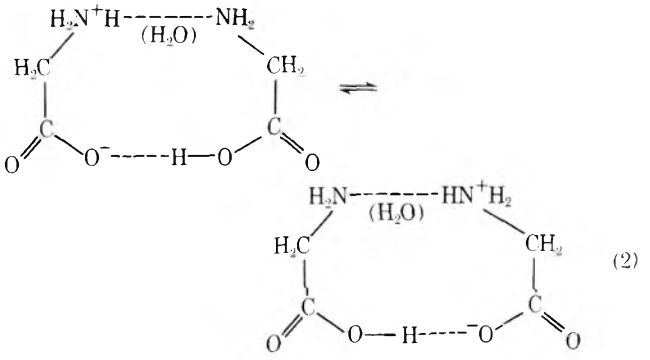

(2)

According to the upper-limit estimates for III and IV, the second-order rate constant for V should be between 490 and 640 s^{-1} M^{-1} total, and between 240 and 390 s^{-1} M^{-1} for reaction with water participation. On adopting a value of 0.25 for K_{assoc} of $R^{\pm}$ with R^0 and allowing for the equilibrium ratio of $R^0/R^{\pm}$, we obtain first-order rate constants k_V of (4–6) × 10^8 s^{-1} total and (2–4) × 10^8 s^{-1} with water participation. According to results presented elsewhere,[14] such values are not unreasonably high.

k_C, k_D. The rate constant for reaction of $R^{\pm}$ with hydroxide has been measured by relaxation spectrometry.[6,7] The NMR measurement of the corresponding rate constant k_C is experimentally difficult because reaction VI makes an appreciable contribution to $1/\tau$ only at such low $R^{\pm}$ concentrations that the exchange broadening is too small to be highly accurate. Within the experimental error, f_W for reaction VI could be unity. However, the fact that the actual value is >1, and that a control experiment for $CH_3NH_3^+$ (Table III) gives good agreement between NMR and relaxation results, leaves open the possibility that NH_2-proton exchange of R^- with water is significant. That is to say, at the higher pH's more than one NH_3^+ proton exchanges per cycle of reaction.

For reaction VII, f_W is accurately determined as 0.21 ± 0.01. Thus symmetrical proton exchange in this case proceeds largely by direct bimolecular reaction, without water participation. For the analogous symmetrical proton exchange of aliphatic amines, f_W is considerably <1 for primary amines, but not for secondary or tertiary amines.[3] Data for methylamine are included in Table III.

Esters of Amino Acids. NH_3^+ to HOH proton exchange was measured for the methyl esters of glycine (GME), alanine (AME), and phenylalanine (PAME) between pH 2 and 5. The kinetic results are reproduced satisfactorily by

$$3/\tau = k_a + k_D[MeO_2CCH_2NH_2] \quad (3)$$

Equation 3 involves fewer terms than (1) because analogues of reactions II–V do not exist for esters, and reaction VI is expected to be negligible compared to VII. The first-order rate constant is denoted by k_a to indicate that it represents acid dissociation, reaction I. For GME^+, rate constants for total reaction have been reported by SG.[2] f_W for k_a is essentially unity, as expected, while f_W for k_D is 0.33 ± 0.05, being appreciably less than unity. Values obtained for the rate constant k_{-a} for the reverse of acid dissociation ($-NH_2 + H^+$) are relatively insensitive to the nature of the amine ester, and are of the same magnitude, $\sim 10^{10}$ s^{-1} M^{-1}, as rate constants for proton addition to the CO_2^- group in amino acids.[15]

Experimental Section

Materials. Glycine, hydrochlorides of glycine methyl ester, DL-alanine methyl ester, and DL-phenylalanine methyl ester were purchased from Sigma Chemical Co. and were used without further purifications. Methylammonium chloride was purchased from Eastman Organic Chemical and was recrystallized twice from pure ethanol. Weighed chemicals were added to the freshly distilled water to make proper molar concentrations. HCl or NaOH was added to the solutions to adjust the pH to the desired values.

pH Measurements. A Fisher glass electrode together with a calomel reference electrode was used. A Corning digital 112 pH meter was calibrated by a Fisher buffer solution of pH 4, and the pH of the solutions was measured on the same scale.

p_cH ($-\log [H^+]$) for the solutions used in NMR measurements was calculated according to

TABLE III: Kinetic Results for NH-Proton Exchange in Water

Substrate	pK_a[a]	Rate constant, s^{-1} or s^{-1} M^{-1} Symbol	with H_2O (25 °C)	Total (23 ± 1 °C)	f_w
GME^+	7.59	k_a	570 ± 30	470[b]	1.2[c]
		$k_{-a} \times 10^{-10}$	2.2		
		$k_D \times 10^{-8}$	0.92 ± 0.13	2.8[b]	0.33 ± 0.05
AME^+	7.77	k_a	410 ± 30		
		$k_{-a} \times 10^{-10}$	2.4		
		$k_D \times 10^{-8}$	0.86 ± 0.10		
$PAME^+$	7.00	k_a	1600 ± 200		
		$k_{-a} \times 10^{-10}$	1.6		
		$k_D \times 10^{-8}$	0.39 ± 0.08		
$CH_3NH_3^+$	10.66	$k_D \times 10^{-8}$	7.4 ± 0.5		
			5.8[d]	10.2[d]	0.57
		$k_C \times 10^{-10}$	4.2 ± 0.4	3.7[e]	1[c]

[a] Reference 12. [b] Reference 2. [c] Unity, within the experimental error. [d] Reference 9. [e] M. Eigen, G. Maas, and G. Schwarz, *Z. Phys. Chem. (Frankfurt am Main)*, **74**, 319 (1971).

$$p_cH = pH + \log \gamma_{\pm} \quad (4)$$

$$\log \gamma_{\pm} = -0.509\sqrt{I}/(1 + \sqrt{I}) \quad (5)$$

where I is the ionic strength. $[OH^-]$ was then calculated from $K_W/([H^+]\gamma_{\pm}^2)$.

NMR Relaxation Times. Transverse (T_2) and longitudinal (T_1) relaxation times were measured using a modified Bruker Model SXP pulsed NMR spectrometer operating at 56.7 MHz. The modification consisted of (1) omitting the high-power radiofrequency amplifier, so that transmitter power was limited to 15 W; (2) installing a network of Kay Electric Co. Model 1/432 1-W attenuators, so that radiofrequency power supplied to the probe could be attenuated in successive steps of 0.3 (×2), 0.5 (×5), 1 (×3), and 2 (×2) db, followed by randomly switchable steps of 2, 3, 5, 10, and 20 (×2) db. The radiofrequency voltage supplied to the probe could be monitored with a Boonton Electronics Model 92 BD radiofrequency millivoltmeter; (3) using a Redfield pulse programmer,[16] built by Mr. W. J. Shea of Brandeis University; (4) interfacing the spectrometer with a Wang Model 700 programmable calculator, using an Adam-Smith Model 100 instrument interface. The modified spectrometer is particularly convenient for the measurement of proton T_1, T_2, and rotating-frame $T_{1\rho}$.

In the present work, T_2 of the H_2O, or exchange-averaged H_2O–NH_3 protons, was measured with better than 2% precision by the familiar Meiboom-Gill pulse sequence.[17] T_1 was measured by a convenient, and apparently novel, pulse sequence which begins with a 180° pulse and permits monitoring of the entire decay curve of the longitudinal magnetization in a single experiment. At chosen times, the magnetization is observed by (a) giving a +10° pulse and measuring the signal voltage V_a; (b) giving a −20° pulse and measuring V_b; (c) giving a +10° restoring pulse and measuring V_c. This sequence of observation pulses is repeated at convenient intervals (300–400 ms) until a total time of $\sim 6T_1$ has elapsed. A schematic diagram of the signal visible on the oscilloscope is shown in Figure 1.

During the observation periods (which are a small fraction of the total time) the longitudinal magnetization is reduced from $M_z(t)$ to $M_z(t)$ cos (10°), or $0.985M_z(t)$, while the observable transverse component is $M_z(t)$ sin (10°), or $0.174M_z(t)$. Thus the signal is proportional to $M_z(t)$, which is itself hardly perturbed by the measurement. Moreover, V_a, V_b, and V_c (see Figure 1) can be combined so as to give zero baseline and full compensation for any linear drift. Let s denote the signal (proportional to $M_z(t)$), b the baseline, and d the linear drift. Then $V_a = b + s$, $V_b = b - s + d$, and $V_c = b + 2d$. Hence $V_a - 2V_b + V_c = 3s$. In our experience, the monitoring of an entire decay curve, combined with the drift compensation, improves the precision of $1/T_1$ to better than 1%, and probably the absolute accuracy as well. The choice of the ±10° angle for the observation pulse is of course not critical; any precisely reproducible small angle θ will do.

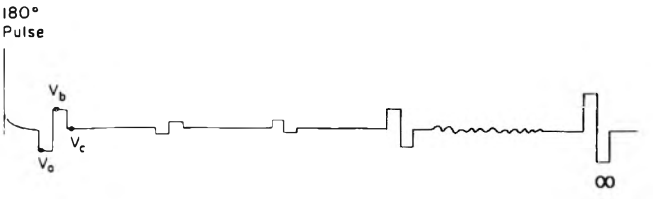

Figure 1. Schematic of signals observed in T_1 measurement. See text.

NMR Chemical Shifts. Values of $1/\tau$ were $<\delta$ at low pH and $>\delta$ at high pH, where δ denotes the NH-to-OH proton chemical shift (in radians/s). The exchange broadening therefore went through a maximum from which δ could be calculated.[8] Values of δ thus obtained led to the following NH-to-OH chemical shifts, in ppm at 25 °C: for glycine, 2.77 ± 0.08; for GME^+, 3.06 ± 0.08; for AME^+, 3.06 ± 0.08; for PMAE, 3.26 ± 0.08; for $MeNH_3^+$, 2.39 ± 0.08. (The NH protons are downfield.) In the case of glycine, we thought it worthwhile to confirm the chemical shift by direct measurement at 0.2 M concentration at pH 4, where NH_3 and OH protons still give separate (though exchange-broadened) resonances. Measurements were made on Refield's NMR spectrometer at 90 MHz,[16] using the Alexander pulse[16,18] to suppress the water resonance. The result was 2.89 ± 0.17 ppm, in adequate agreement with the result inferred from maximum exchange broadening. In the calculations of $1/\tau$,[8] values of δ based on exchange-broadening were used; the N^{14}–H spin–spin interaction was taken to be 340 s^{-1}.

References and Notes

(1) Work supported by the National Science Foundation.
(2) M. Sheinblatt and H. S. Gutowsky, *J. Am. Chem. Soc.*, **86**, 4814 (1964).
(3) E. Grunwald and D. Eustace in "Proton-Transfer Reactions", E. Caldin and V. Gold, Ed., Chapman and Hall, London, 1975, Chapter 4.
(4) R. A. Cooper, R. L. Lichter, and J. D. Roberts, *J. Am. Chem. Soc.*, **95**, 3724 (1973).
(5) T. K. Leipert and J. H. Noggle, *J. Am. Chem. Soc.*, **97**, 269 (1975).
(6) K. Applegate, L. J. Slutsky, and R. C. Parker, *J. Am. Chem. Soc.*, **90**, 6909 (1968).
(7) H. G. Busse and G. Maas, *Z. Phys. Chem. (Frankfurt am Main)*, **66**, 92 (1969).

(8) E. K. Ralph and E. Grunwald, *J. Am. Chem. Soc.*, **91**, 2422 (1969); E. Grunwald and E. Price, *ibid.*, **86**, 2965 (1964).
(9) E. Grunwald and A. Ku, *J. Am. Chem. Soc.*, **90**, 29 (1968).
(10) M. Eigen and L. DeMaeyer in "Technique of Organic Chemistry", S. L. Friess and A. Weissberger, Ed., Vol. 8, Part II, Interscience, New York, N.Y., 1963, p 1031.
(11) Results by V. K. Anderson and E. Grunwald, Brandeis University, 1974.
(12) Required pK_a values from D. D. Perrin in "Dissociation Constants of Organic Bases in Aqueous Solution", Butterworths, London, 1965.
(13) E. S. Hand and W. Jencks, *J. Am. Chem. Soc.*, **97**, 6221 (1975).
(14) E. Grunwald, K. C. Chang, P. S. Skipper, and V. K. Anderson, *J. Phys. Chem.*, following paper in this issue.
(15) S. Brun, J. E. Rassing, and E. Wyn-Jones, *Adv. Mol. Relaxation Processes*, **5**, 313 (1973).
(16) (a) A. G. Redfield and R. K. Gupta, *Adv. Magn. Resonance*, **5**, 81 (1971); (b) Y. Lange, E. K. Ralph, and A. G. Redfield, *Biochem. Biophys. Res. Commun.*, **62**, 891 (1975). Purchase of this NMR spectrometer was supported by an instrumentation grant from the National Science Foundation.
(17) S. Meiboom and D. Gill, *Rev. Sci. Instrum.*, **29**, 668 (1958).
(18) S. Alexander, *Rev. Sci. Instrum.*, **32**, 1066 (1961).

Kinetics of Bifunctional Proton Transfer. 2. Lysine and Cysteine in Aqueous Solutions[1]

Ernest Grunwald,* K. C. Chang, P. L. Skipper, and V. K. Anderson

Chemistry Department, Brandeis University, Waltham, Massachusetts 02154 *(Received January 15, 1976)*

From a kinetic analysis of proton exchange with water participation, measured by NMR, we report the following rate constants: For the conjugate base of lysine, $H_3N^+(CH_2)_4CHNH_2{\cdot}CO_2^- \rightleftarrows H_2N(CH_2)_4CHNH_3^+{\cdot}CO_2^-$, $k_f = 4.7 \times 10^6\ s^{-1}$, $k_r = 5.2 \times 10^7\ s^{-1}$; reaction takes place with an average number of 1.6 ± 0.5 water molecules. For the conjugate base of cysteine, $HSCH_2CHNH_2{\cdot}CO_2^- \rightleftarrows {}^-SCH_2CHNH_3^+CO_2^-$, reaction with water participation has $k_f \approx 2 \times 10^6\ s^{-1}$ and $k_r \approx 2 \times 10^6\ s^{-1}$. Reaction without water participation, according to ultrasonic relaxation data by Maas and Peters, has $k_f = 2.0 \times 10^8\ s^{-1}$ and $k_r = 1.6 \times 10^8\ s^{-1}$. The kinetic analysis also leads to approximate rate constants for bifunctional proton transfer between the α-NH_3^+ group and the CO_2^- group of these substrates, and to precise rate constants for bimolecular reaction. A kinetic analysis is also reported for *S*-methylcysteine. Chemical shifts at 25 °C (relative to H_2O, in dilute aqueous solution) are −2.85 ppm for the NH protons of lysine, and +2.94 ppm for the SH protons and −3.19 ppm for the NH protons of cysteine.

Bifunctional proton transfer by definition is a process in which one site in a molecule acts as a proton donor while another site acts as a proton acceptor.[2] In aqueous solution, kinetically first-order bifunctional proton transfer involving oxygen or nitrogen sites is often very fast, with rate constants well above $10^6\ s^{-1}$.[3,4] In some such reactions, e.g., *p*-aminobenzoic acid ⇄ *p*-ammoniumbenzoate zwitterion,[3] the proton donor and acceptor sites are so far apart in the molecule that the transfer cannot be simply an intramolecular proton shift; it must be inferred that water molecules participate.

In this series we are interested in defining steric requirements for bifunctional proton transfer, and how they affect solvent participation and reaction rate. Our kinetic analyses are based mostly on proton NMR. Dynamic NMR methods[5] are precise enough to unravel even complicated rate laws, and by examining the water resonance we obtain direct proof of participation by water molecules.[6] The experimental approach has been described in part 1.[4]

In this paper we examine the proton-transfer reactions of lysine and cysteine, with special emphasis on bifunctional proton transfer of the conjugate bases:

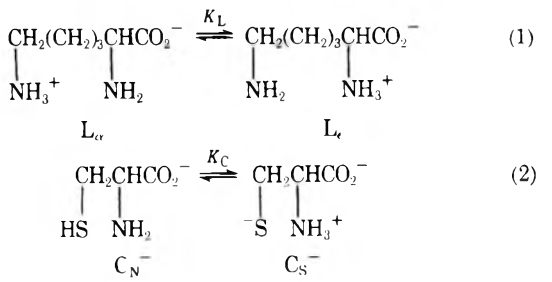

According to estimates made in the Appendix, $K_L = 0.089$ and $K_C = 1.3$. These values are near enough to unity so that bifunctional proton transfer could be fast in both directions, and thus be detectable by our methods. Reaction 1 is of interest because the donor and acceptor sites are separated by a long chain of five carbon atoms. Reaction 2 is of interest because one of the sites is a sulfur atom. According to a recent study by the ultrasonic relaxation method, the specific relaxation rate ($1/\tau'$) for (2) is $3.6 \times 10^8\ s^{-1}$.[7]

Results

Lysine. Formal acid dissociation constants are: $pK_1 = 2.18$; $pK_2 = 9.08$; $pK_3 = 10.51$.[8] Actual acid–base equilibria and microscopic pK values are summarized in Figure 1. NH-to-OH_2 proton exchange rates were measured in the pH range 3.4–7, in which lysine exists largely in the tripolar form L_z^+. Direct observation of the NH-proton resonance was possible at 90 MHz for ~0.02 M lysine in 20% D_2O–80% H_2O at 4 °C and pH 3.5.[1] A single resonance, 2.85 ± 0.06 ppm downfield from H_2O, of half-band width ~10 Hz was observed, indicating that direct exchange of α- and ϵ-NH_3 protons is fast enough to average out an expected ~0.4 ppm chemical-shift difference.[9a] In the absence of direct exchange, a broader resonance would be observed in which the two kinds of NH protons are probably resolved. In interpreting the NH-to-OH_2 exchange broadening, we did not assume that the two NH_3 groups exchange at equal rates, but we did assume that all NH protons have the same chemical shift. From the maximum broadening, that chemical shift was inferred to be 2.72 ± 0.08 ppm, in fair agreement with the direct measurement.[9b]

NH-to-OH_2 exchange broadening of the dominant water

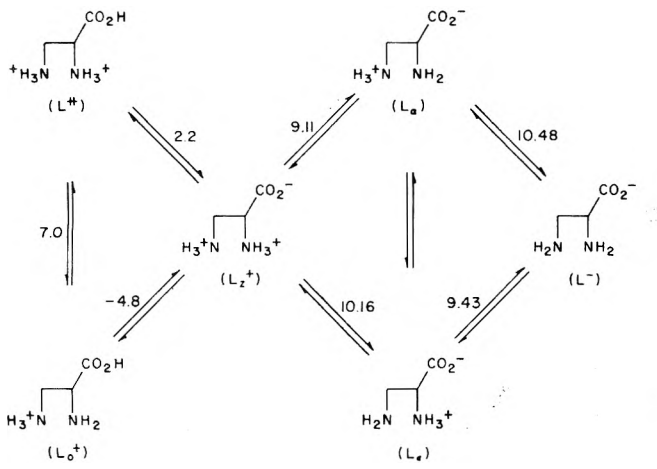

Figure 1. Acid dissociation equilibria for lysine. The indicated numbers are our estimates of microscopic pK values. (See Appendix.)

resonance was deduced from measurements of T_2 and T_1.[6] All in all, 70 independent solutions were measured at 25 °C, in which the lysine concentration ranged from 0.016 to 0.06 M. In the experimental pH range, the formal lysine concentration was justifiably set equal to $[L_z^+]$, and all other species in Figure 1 were treated as stoichiometrically and magnetically insignificant intermediates.

Bifunctional proton transfer according to (1) was included in the rate law according to the mechanism

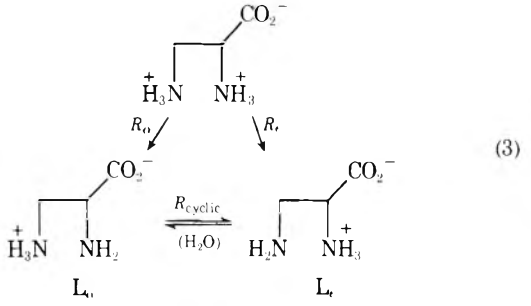

(3)

which R_α and R_ϵ denote the total rates of proton abstraction from the respective NH_3 groups, and R_{cyclic} denotes the rate of bifunctional proton transfer with water participation. At low pH, the lifetimes of L_α and L_ϵ are short and the probability of further exchange of NH protons with water protons owing to the bifunctional process is small, while at higher pH the probability becomes considerable.

Let p denote the probability that L_α will undergo bifunctional proton transfer during its lifetime, and let q denote the corresponding probability for L_ϵ. Because the system (3) is in dynamic equilibrium, $p \equiv R_{cyclic}/(R_{cyclic} + R_{-\alpha}) = R_{cyclic}/(R_{cyclic} + R_\alpha)$. Similarly, $q = R_{cyclic}/(R_{cyclic} + R_\epsilon)$. It can then be shown (see Appendix) that bifunctional proton transfer between L_α and L_ϵ contributes an additional term, $2R_{cyclic}(1 - [p + q]/[6 - 4pq])$, to the rate of NH-to-$OH_2$ proton exchange.

Two limiting cases of this term are of interest. When $R_{cyclic} \gg R_\alpha, R_\epsilon$, the term reduces to 5 $(R_\alpha + R_\epsilon)$, i.e., proton removal from L_z^+ is rate determining. When $R_{cyclic} < R_\alpha, R_\epsilon$, the term reduces to $2R_{cyclic}$. It will be clear from rate constants to be presented (Table I) that the second case applies here, so that rate constants for bifunctional proton transfer can be deduced.

To derive the complete rate law for NH-to-OH_2 proton exchange, let R_{NH} denote the total rate, $R_{NW,\alpha}$ and $R_{NW,\epsilon}$ the contributions due to reaction of L_z^+ with water participation

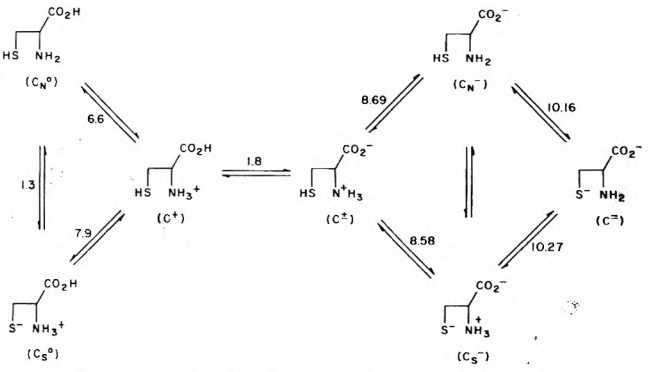

Figure 2. Acid dissociation equilibria for cysteine. The indicated numbers are estimates of microscopic pK values. (See Appendix.)

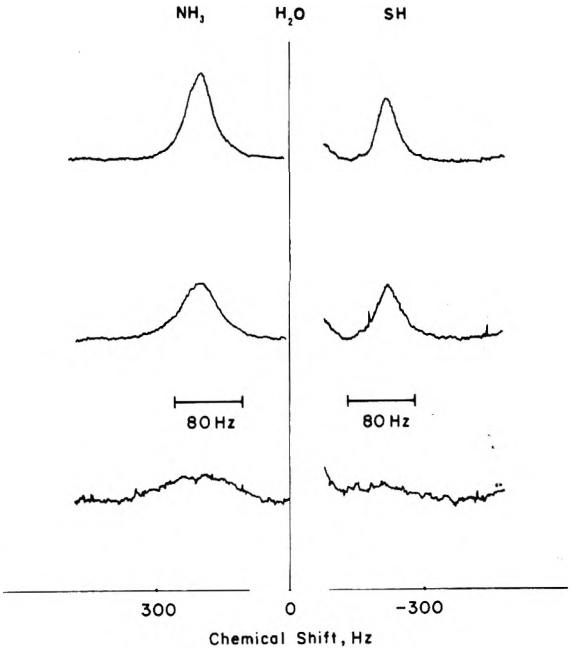

Figure 3. Tracings of actual NH_3 and SH proton resonances of cysteine at 90 MHz in 80% H_2O–D_2O at 1.5 °C as a function of pH. (Note the breaks in the abscissa.) Half-bandwidths are as follows: pH, NH_3 (Hz), SH (Hz), 3.373, 37, 30; 4.959, 52, 36; 5.491, 130, 80; the chemical shifts of the β-CH_2 and α-CH protons in $C^\pm$ are −1.08 and −2.20 ppm (downfield), respectively, with respect to the SH protons.

at the sites indicated, and $2R_{cyclic}(1 - [p + q]/[6 - 4pq]) \approx 2R_{cyclic}$ the contribution owing to bifunctional proton transfer $(L_\alpha \rightleftarrows L_\epsilon)$ with water participation:

$$R_{NH} = R_{NW,\alpha} + R_{NW,\epsilon} + 2R_{cyclic} \quad (4)$$

We then represent $R_{NW,\alpha}$ and $R_{NW,\epsilon}$ by rate laws of the same form that have been shown to fit the data for glycine[6] and which, it turns out, also fit the present data.

$$R_{NW,\alpha} + R_{NW,\epsilon} = (k_A + k_B[L_z^+] + k_C[OH^-] + k_D[L_\alpha + L_\epsilon])[L_z^+] \quad (5)$$

In (5), $k_A = k_A^\alpha + k_A^\epsilon$, $k_B = k_B^\alpha + k_B^\epsilon$, and so on.

Recalling that $1/\tau_{NH} = R_{NH}/(6[L_z^+])$, and writing $R_{cyclic} = k_{cyclic}[L_\alpha + L_\epsilon] = (k_{cyclic}K_2/K_W)[L_z^+][OH^-]$, we obtain the final rate law:

$$6/\tau_{NH} = k_A + k_B[L_z^+] + (k_C + [k_{cyclic}K_2/K_W])[OH^-] + k_D[L_\alpha + L_\epsilon] \quad (6)$$

In testing eq 6, k_A and k_B were obtained by fitting the data at pH 3.4–4, and the other two kinetic constants were obtained by fitting the rest of the data. The fit was satisfactory; results are listed in Table I. In order to separate $k_{cyclic}K_W/K_z$ from k_C, we assumed that $k_C = 6 \times 10^{10}$ s^{-1} M^{-1}, which is the sum of k_C for glycine and $CH_3NH_3^+$.[10] On that basis, k_C accounts for about ⅓ of the observed kinetic constant, so that k_{cyclic} can be deduced with an accuracy within 20%. The result is included in Table I.

In order to check on these results and determine the number of water molecules that participate in the bifunctional process, we also measured the rate of proton exchange among water molecules in ^{17}O-enriched water. These measurements were made in the pH range 7.5–9 where the residual water broadening from NH-to-OH_2 exchange is predictably small. The results of 18 experiments, in which the lysine concentration varied from 0.008 to 0.19 M, were reproduced by the following rate law:

$$1/\tau_W = 2.7 \times 10^9[H^+] + 2.25 \times 10^9[OH^-] + \frac{1.8 \times 10^8}{110}[L_z^+][L_\alpha + L_\epsilon] + \frac{7.8 \times 10^6}{110}[L_\alpha + L_\epsilon] \quad (7)$$

The first two terms on the right in (7) represent proton exchange catalyzed by H^+ and OH^-, respectively.[11] The kinetic constant for the H^+-catalyzed exchange was taken from Meiboom;[11] that for the OH^--catalyzed exchange was obtained by adjustment to our data and may be compared with literature values centered around 1.9×10^9 s^{-1} M^{-1}.[11-13] The remaining two kinetic constants refer to reactions involving lysine species and are compared in Table I with corresponding kinetic constants in the rate law for $1/\tau_{NH}$. The ratio, n, measures the average number of water molecules that participate in the given process. For the bifunctional process measured by k_{cyclic}, $n = 1.6 \pm 0.5$.

Cysteine. Formal acid dissociation constants are $pK_1 = 1.8$, $pK_2 = 8.33$, $pK_3 = 10.52$.[14] Actual acid–base equilibria and microscopic pK values are summarized in Figure 2. The figure also defines the abbreviations we shall use for the various species.

In interpreting the NMR results, we accepted Maas and Peters' interpretation of their ultrasonic relaxation data[7] that bifunctional proton transfer according to (2) proceeds with $1/\tau' = 3.6 \times 10^8$ s^{-1}. Our own kinetic measurements with ^{17}O-enriched water (to be reported below) indicate that bifunctional proton transfer with water participation proceeds with $1/\tau \sim 1 \times 10^6$ s^{-1}; thus the process measured by Maas and Peters would be a simple intramolecular proton shift. In our experiments, at pH 4–7, the conjugate bases C_N^- and C_S^- may be treated as stoichiometrically and magnetically insignificant intermediates. Nevertheless, the mean lifetimes of C_N^- and C_S^- are long enough relative to τ' to justify the assumption of complete scrambling of NH and SH protons in these intermediates.

At pH <5 and temperatures below ~10 °C we were able to observe the resonances of the NH_3 and SH protons as separate signals. Tracings, showing the broadening of typical signals with increasing pH, are shown in Figure 3.[1] Here and in the following, negative values denote *downfield* chemical shifts. At 1.5 °C, chemical shifts (relative to H_2O) are −2.94 ppm for NH_3 and +3.20 ppm for SH in $C^\pm$; and −3.49 ppm for NH_3 and +2.92 ppm for SH in C^+. The temperature coefficients of these chemical shifts are essentially those of water, the latter being +0.0103 ppm/°C.[15] Thus at 25 °C, chemical shifts are estimated to be −3.19 ppm for NH_3 and +2.94 for SH in $C^\pm$. The observation of separate signals for NH_3 and SH protons indicates that direct proton transfer between these groups in $C^\pm$ under the stated conditions is relatively slow. However, this is not inconsistent with rapid scrambling of protons in the conjugate bases C^-; it merely indicates that the rate-determining step for the latter, the removal of a proton from $C^\pm$, is relatively slow.

TABLE I: Kinetic Analysis for Proton Exchange of Lysine in Water at 25 °C

Kinetic constant	Experimental result		n
	From τ_{NH}	From τ_W	
k_A, s^{-1}	190 ± 20		
k_B, s^{-1} M^{-1}	1300 ± 300		
$(k_C K_W/K_z) + k_{cyclic}$, s^{-1}	(5.0 ± 0.4) × 10^6	(7.8 ± 2) × 10^6	1.56 ± 0.4
k_D, s^{-1} M^{-1}	(1.4 ± 0.1) × 10^8	(1.8 ± 0.2) × 10^8	1.27 ± 0.2
k_C, s^{-1} M^{-1}	(6 × 10^{10})[a]	(6 × 10^{10})[a]	
k_{cyclic}, s^{-1}	(4.3 ± 0.5) × 10^6	(7.1 × 10^6)	1.6 ± 0.5

[a] Assumed value is the sum of k_C from τ_{NH} for glycine and $CH_3NH_3^+$. The number of water molecules, n, participating in base dissociation is assumed to be 1.

At 25 °C, measurements of exchange broadening of the water resonance indicate that the rate of direct NH_3–SH proton exchange increases with pH. Thus, as shown in Figure 4, the maximum exchange broadening, which occurs at ca. pH 5.5, is distinctly smaller than expected for separate signals and has the characteristic value expected for the average chemical shift of all four protons. A clear distinction is possible because the NH_3 and SH chemical shifts (relative to H_2O) have opposite signs (Figure 3).

In this connection it is useful to introduce an adaptation of Meiboom's approximate method of *effective* chemical shifts[11] to the present problem. Let λ denote the relaxation time for direct exchange of NH and SH protons, let τ_{NH} and τ_{SH} denote the respective relaxation times for exchange of NH and SH protons with water, and let τ denote the overall relaxation time, given by

$$\frac{1}{\tau} = \frac{3}{4}\frac{1}{\tau_{NH}} + \frac{1}{4}\frac{1}{\tau_{SH}} \quad (8)$$

The exchange broadening of the water resonance is then given by

$$T_2^{-1} - T_1^{-1} = \frac{p_{NH}}{\tau_{NH}} \frac{\delta_{NH,eff}^2}{\delta_{NH,eff}^2 + \left(\frac{1}{\tau_{NH}}\right)^2} + \frac{p_{SH}}{\tau_{SH}} \frac{\delta_{SH,eff}^2}{\delta_{SH,eff}^2 + \left(\frac{1}{\tau_{SH}}\right)^2} \quad (9)$$

in which the *effective* chemical shifts are functions of *real* chemical shifts, λ and τ, according to

$$\delta_{NH,eff} = \langle\delta\rangle + (\delta_{NH} - \langle\delta\rangle)(\lambda/[\lambda + \tau]) \quad (10a)$$

$$\delta_{SH,eff} = \langle\delta\rangle + (\delta_{SH} - \langle\delta\rangle)(\lambda/[\lambda + \tau]) \quad (10b)$$

$$\langle\delta\rangle = (3\delta_{NH} + \delta_{SH})/4 \quad (10c)$$

Because δ_{NH} and δ_{SH} are of opposite sign, eq 10 show that direct NH–SH proton exchange will cause both effective

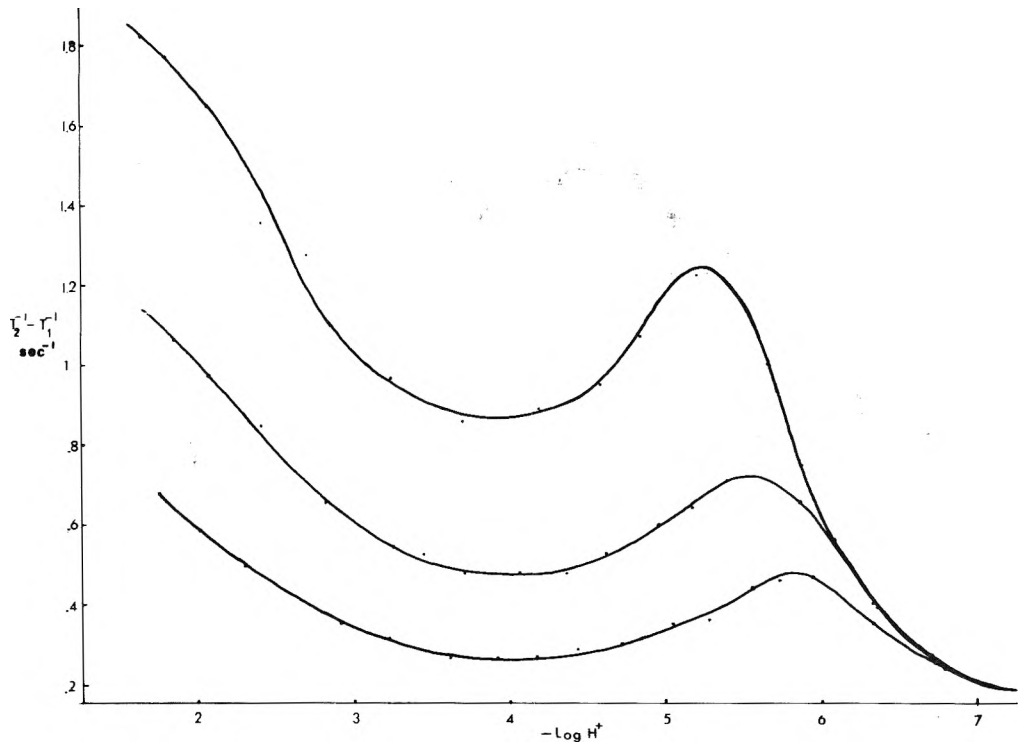

Figure 4. Exchange broadening of the water proton resonance for aqueous cysteine at 25 °C. Cysteine concentrations are (top to bottom) 0.103, 0.061, 0.035 M. Maximum broadenings at pH 5–6 indicate effective averaging of NH and SH proton chemical shifts. The greater broadenings observed at low pH indicate that averaging is ineffective.

chemical shifts to be smaller than actual chemical shifts, and thus reduce the magnitude of the exchange broadening.

In deriving a rate law for proton exchange, we recognize three distinct proton exchange rates: (1) R_{NW} for NH-to-OH_2 proton exchange; (2) R_{SW} for SH-to-OH_2 exchange; (3) $R_{SN} = R_{NS}$ for direct SH-to-NH exchange. These rates have direct contributions ($R_{\alpha W}$, $R_{\beta W}$, $R_{\alpha\beta}$) from the primary processes ($C^{\pm} \rightarrow C_N^-$ and $C^{\pm} \rightarrow C_S^-$), and further contributions from bifunctional proton transfer, $C_N^- \rightleftarrows C_S^-$, of the conjugate bases.

By analogy with glycine, we shall write the following rate laws (11) and (12) for the rates $R_{\alpha W}$ and $R_{\beta W}$ of the primary processes with water. (Kinetic terms of the form $k_B[C^{\pm}]$ are not required and will be omitted.)

$$R_{\alpha W}/[C^{\pm}] = k_A^{NH} + k_C^{NH}[OH^-] + k_D^{NH}[C_N^- + C_S^-] \quad (11)$$

$$R_{\beta W}/[C^{\pm}] = k_A^{SH} + k_C^{SH}[OH^-] + k_D^{SH}[C_N^- + C_S^-] \quad (12)$$

For $R_{\alpha\beta}$ we visualize the reaction in

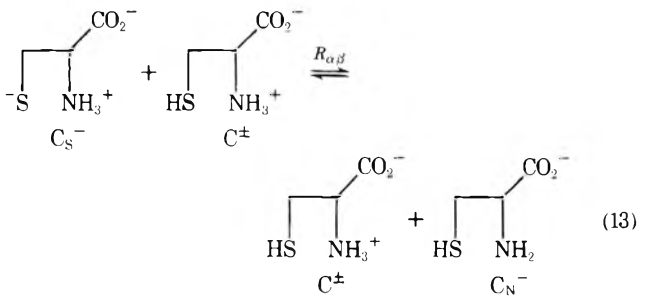

(13)

hence the rate-law

$$R_{\alpha\beta} = k_{SN}[C^{\pm}][C_S^- + C_N^-] \quad (14)$$

in which k_{SN} is a *formal* rate constant. We further define total rates of primary reaction $R_\alpha = R_{\alpha W} + R_{\alpha\beta}$, and $R_\beta = R_{\beta W} + R_{\alpha\beta}$. We assume complete scrambling of NH and SH protons in the conjugate base ($C_N^- + C_S^-$) and let p denote the probability that a scrambled proton will exchange with a water proton during the lifetime of the conjugate base. As in the case of lysine, we let R_{cyclic} denote the rate of bifunctional proton transfer with water participation in the conjugate base, and define the rate constant k_{cyclic} according to

$$R_{cyclic} = k_{cyclic}[C_S^- + C_N^-] \quad (15)$$

On that basis, eq 16–18 are derived in the Appendix; $p = R_{cyclic}/(R_\alpha + R_\beta + R_{cyclic})$.

$$R_{NW} = R_{\alpha W} + p(2R_\alpha + 3R_\beta)/(3 - 2p) \quad (16)$$

$$R_{SW} = R_{\beta W} + pR_\alpha/(3 - 2p) \quad (17)$$

TABLE II: Results of Kinetic Analysis for Proton Exchange of Cysteine and *S*-Methylcysteine in Water at 25 °C

Kinetic constant[a]	Cysteine[b]		*S*-Methylcysteine[c]
	NH	SH	
k_A, s^{-1}	800 ± 100	100 ± 50	500 ± 100
$10^{-10}k_C$, s^{-1} M^{-1}	2.5 (E)[d]	1.4 (E)[d]	2.5 (E)[c]
$10^{-6}k_D$, s^{-1} M^{-1}	7.4 ± 2	0.5 (s)[e]	28 ± 4
k_{cyclic}, s^{-1}	1×10^6 (s)[e]		
k_{SN}, s^{-1} M^{-1}	1.2×10^6 (s)[e]		

[a] Defined in eq 11, 12, 14, and 15. All kinetic constants except k_{SN} refer to proton exchange with water. k_{SN} refers to reaction 13. [b] Rate law assumes rapid proton scrambling owing to reaction 2 without water participation. If such proton transfer were in fact negligible, the data could be reproduced with comparable error of fit and the following kinetic constants: $k_{SN} = 7.3 \times 10^7$ s^{-1} M^{-1}; $k_D^{NH} = 1.3 \times 10^7$ s^{-1} M^{-1}; other constants remain unchanged. [c] Chemical shift of NH_3 in *S*-methylcysteine zwitterion relative to H_2O is −3.18 ppm at 25 °C. [d] Estimated by analogy with glycine[6] for NH and phenol[3] for SH. [e] Semiquantitative; correct with respect to magnitude only.

TABLE III: Microscopic Constants for Bifunctional Proton Transfer Reactions of Amino Acids in Water at 25 °C

Reaction	K_{eq}	k_f, s^{-1}	k_r, s^{-1}	Remarks
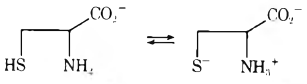	1.3	2.0×10^8 2.3×10^6	1.6×10^8 1.8×10^6	Total rate Rate with H_2O
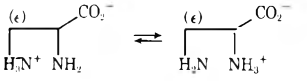	0.089	4.7×10^6	5.2×10^7	Rate with H_2O $n = 1.6 \pm 0.5$
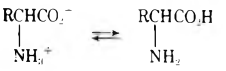				
(a) Glycine	4.1×10^{-6}	1.7×10^2	4.1×10^7	Total rate
(b) Cysteine	1.6×10^{-5}	7.0×10^2	4.4×10^7	Total rate
(c) *S*-Methylcysteine	2.0×10^{-5}	4.3×10^2	2.1×10^7	Total rate
(d) Lysine	1.6×10^{-5}	1.5×10^2	0.9×10^7	Total rate

$$R_{NS} = R_{SN} = R_{\alpha\beta} + \frac{(1-p)}{(3-2p)}(2R_\alpha + 3R_\beta)\frac{R_\alpha}{(R_\alpha + R_\beta)} \quad (18)$$

Finally, the relaxation times required to calculate the exchange broadening are given in

$$\frac{1}{\tau_{NH}} = \frac{R_{NW}}{3[C^\pm]}, \frac{1}{\tau_{SH}} = \frac{R_{SW}}{[C^\pm]},$$
$$\frac{1}{\lambda} = \frac{R_{NS}}{3[C^\pm]} + \frac{R_{SN}}{[C^\pm]} = \frac{4}{3}\frac{R_{NS}}{[C^\pm]} \quad (19)$$

The kinetic scheme 11–19 involves eight rate constants, which is an unrealistically large number. The number was therefore reduced by (a) measuring $k_\alpha^{NH} + k_a^{SH}$ in separate experiments at lower pH; (b) measuring k_{cyclic} in separate experiments in ^{17}O-enriched water; (c) estimating the relatively unimportant rate constants k_C^{NH} and k_C^{SH} by analogy with glycine[6] and phenol,[3] respectively. The remaining four parameters were obtained by least-squares adjustment of data for 27 independent solutions. Final results are summarized in Table II. Comparative kinetic results were also obtained for *S*-methylcysteine and are included in Table II. As shown in the table, some of the rate constants are accurate enough to warrant the listing of standard errors; others are only semiquantitative. The fit of the experimental exchange broadenings is about 5%, about as good as for glycine.[6]

We wish to stress that the rate law adopted for fitting the data is not unique. In assuming proton scrambling in the conjugate base, we rely on Maas and Peters' necessarily indirect evidence from relaxation spectroscopy.[7] An alternative model without proton scrambling fits equally well; see Table II, footnote b. Any of the semiquantitative rate constants in Table II could be omitted without serious deterioration of the overall fit.

Discussion

We shall limit this discussion to bifunctional proton transfer of amino acids. Microscopic constants obtained in this and previous work[6,7] are listed in Table III. For reaction in the direction of decreasing standard free energy, rate constants for *total* reaction are high, 10^7 s^{-1} or greater in every case. The table covers a considerable range of functional groups and structures. Especially remarkable are the results for lysine, where the functional groups are separated by five carbon atoms and reaction proceeds with participation of an average of 1.6 water molecules. Another example of fast intramolecular proton transfer, probably of long range, is provided by glutathione, where Maas and Peters found a relaxation time of 1.6×10^{-8} s.[7]

Rate constants for the interconversion of α-amino acids with their zwitterions were obtained by correction of formal rate constants k_A for acid dissociation, as described previously,[6] and are listed in Table III. We cannot tell whether the bifunctional process proceeds with water participation, because the CO_2H protons in the amino acid are in rapid exchange with the water protons of the solvent.[17] Molecular models do not provide a clue, because the insertion of a water molecule between the NH_3^+ and CO_2^- groups does not obviously relieve hydrogen-bond strain. In the case of lysine, the rate constant may also contain a small contribution from proton exchange with the ε-amino group. In the case of cysteine, k_A^{SH} is somewhat greater than might have been expected for acid dissociation ($k_a^{SH} \approx 50$ s^{-1} if $k_{-a} \approx 2 \times 10^{10}$ s^{-1} M^{-1}), suggesting that there is some bifunctional proton transfer from SH to CO_2^-. Related evidence for bifunctional proton transfer between sulfur and oxygen atoms in $HSCH_2CH_2OH$ has been reported by Kreevoy, Sappenfield, and Schwabacher.[16]

Experimental Section

Materials, Solutions, and pH Measurements. Reagent grade L-lysine hydrochloride, L-cysteine, and *S*-methyl-L-cysteine were purchased from Sigma Chemical Co. and were used without further purification. ^{17}O-enriched water was purchased from Miles Laboratories and was vacuum distilled twice. Weighed chemicals, as well as ^{17}O-enriched water in the τ_W experiments, were added to freshly distilled water to make proper molar concentrations and ^{17}O contents. Techniques of pH measurement have been reported.[7]

NMR Measurements. Instrumentation and techniques for the measurements of longitudinal (T_1) and transverse (T_2) relaxation times of the dominant (OH_2 or coalesced OH + NH + SH) proton NMR line have been reported previously.[6] Calculation of exchange rates from these measurements were described previously,[18] except that the longitudinal (T^I) relaxation time of ^{17}O was taken to be 0.0044 s.[11]

Appendix

Microscopic pK_a Values. Values listed in Figures 1 and 2 are based essentially on ref 8 and 14. The following remarks explain the selections.

Lysine. We adopted the average of reported p*K* values at 25 °C and an ionic strength of 0.1 M. We used an estimated p*K* of 0.32 unit for $L_\alpha + L_\epsilon \rightleftarrows L^- + L_z^+$, as suggested by Hermann and Lemke,[8] to allow for the acid-strengthening effect of the α-NH_3^+ electrical charge. These assumptions are sufficient to evaluate all p*K* values to the right of L_z^+ in Figure 1. pK_a for $L^{2+} \rightleftarrows L_z^+$ is essentially pK_1. pK_a for $L^{2+} \rightleftarrows L^0$ was estimated from the pK_a of the methyl ester.

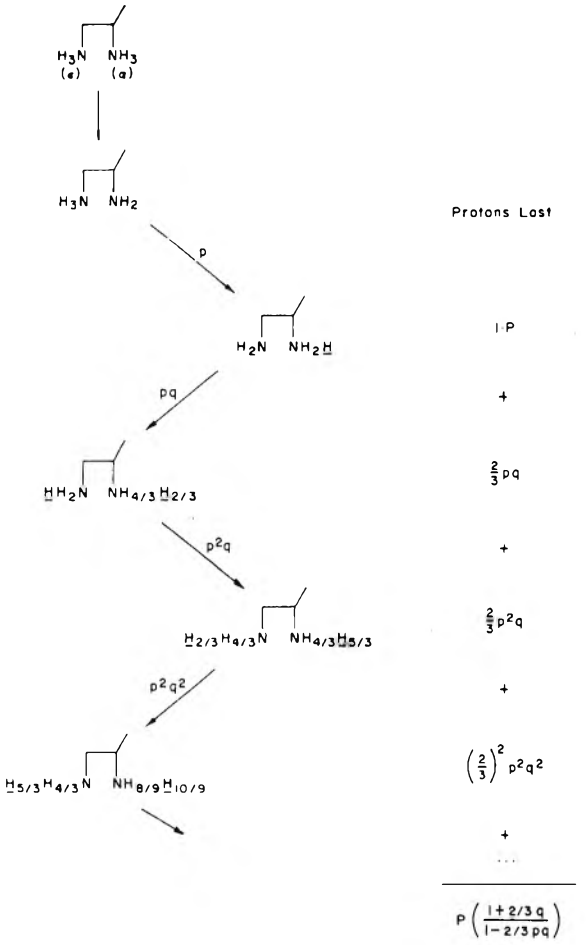

Figure 5. Probability of bifunctional proton transfer with water participation in the conjugate base of lysine.

Cysteine. On the basis of data for *S*-methylcysteine, *S*-ethylcysteine, and cysteine betaine,[14,19] K for $[C_S^-]/[C_N^-] = 1.3$. This value was then combined with $pK_2 = 8.33$ and $pK_3 = 10.52$ to obtain the pK_a values to the right of $C^{\pm}$ in Figure 2. pK_a for $C^+ \rightleftarrows C^{\pm}$ is essentially pK_1. pK_a for $C^+ \rightleftarrows C_N^0$ was estimated from the pK_a for cysteine methyl and ethyl esters.[14] pK_a for $C^+ \rightleftarrows C_S^0$ was estimated from the pK_a for $C^{\pm} \rightleftarrows C_S^-$ and an estimate of 0.7 pK unit for the acid-weakening effect of the CO_2^--group negative charge.

Rate Law for Lysine. In this section we wish to derive the contribution to R_{NH} due to bifunctional proton transfer ($L_\alpha \rightleftarrows L_\epsilon$) with water participation. We shall neglect bifunctional proton transfer without water participation because it makes no contribution to the NMR exchange broadening (we see only a single NH-proton resonance; see previous text).

Figure 5 shows a scheme for calculating the number of protons lost during the lifetime of the conjugate base. In Figure 5, the initial step is removal of the N_α proton, and the rate of proton exchange triggered by this process is therefore $R_\alpha p(3 + 2q)/(3 - 2pq)$. Removal of the N_ϵ proton analogously triggers proton exchange in the conjugate base with a rate of $R_\epsilon q(3 + 2p)/(3 - 2pq)$. To obtain a simple expression involving R_{cyclic}, we apply the definitions of p and q to obtain: $R_\alpha p = R_{cyclic}(1 - p)$; $R_\epsilon q = R_{cyclic}(1 - q)$. Thus the total contribution to R_{NH} due to bifunctional proton transfer is given by

$$R_{cyclic}[(1 - p)(3 + 2q) + (1 - q)(3 + 2p)]/(3 - 2pq) \qquad (20)$$

which reduces to the expression given in the text.

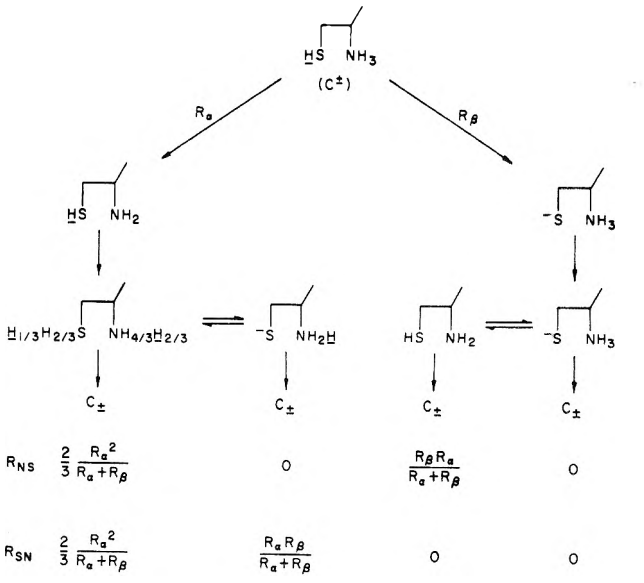

Figure 6. Effect of scrambling in the conjugate base of cysteine on R_{NS} and R_{SN}.

Rate Law for Cysteine. In this section we wish to consider the effect of proton scrambling in the conjugate base of cysteine on the rates of proton exchange. Initially we shall neglect bifunctional proton transfer ($C_N^- \rightleftarrows C_S^-$) with water participation; i.e., $p = 0$. Figure 6 then shows how proton scrambling enhances the rates, R_{NS} and R_{SN}, of direct proton transfer between NH and SH sites. By adding $R_{\alpha\beta}$ to the rate terms given in Figure 6, and recalling that $p = 0$, we obtain (18) at once.

When the reaction mechanism is expanded to include bifunctional proton transfer with water participation in the conjugate base, a rate law can be derived by applying the general method of Figure 5. Because of the rapid proton scrambling, the conjugate base may be treated as a single species for this purpose, and the probability of reaction with water participation during its lifetime may be expressed by a single variable, p. This leads to eq 16–18. We shall not give details.

References and Notes

(1) Work supported by a grant from the National Science Foundation. Purchase of the NMR spectrometer assisted by an instrumentation grant from the NSF.
(2) C. G. Swain and J. F. Brown, Jr., *J. Am. Chem. Soc.*, **74**, 2538 (1952); P. R. Rony, *ibid.*, **91**, 6090 (1969); P. R. Rony and R. O. Neff, *ibid.*, **95**, 2896 (1973); R. D. Gandour, G. M. Maggiora, and R. L. Schowen, *ibid.*, **96**, 6967 (1974).
(3) M. Eigen and L. DeMaeyer in "Investigation of Rates and Mechanism of Reactions", S. L. Friess, E. S. Lewis, and A. Weissberger, Ed., Wiley-Interscience, New York, N.Y., 1963.
(4) E. Grunwald and D. W. Fong, *J. Am. Chem. Soc.*, **94**, 7371 (1972); part 1 of this series.
(5) L. M. Jackman and F. A. Cotton, Ed., "Dynamic Nuclear Magnetic Resonance", Academic Press, New York, N.Y., 1975.
(6) K.-C. Chang and E. Grunwald, *J. Phys. Chem.*, preceding paper in this issue.
(7) G. Maas and F. Peters, *Angew. Chem., Int. Edit. Engl.*, **11**, 428 (1972).
(8) M. H. T. Nyberg and M. Cefola, *Arch. Biochem. Biophys.*, **111**, 327 (1965); R. W. Hay and P. J. Morris, *J. Chem. Soc., Perkin Trans. 2*, 1021 (1972); P. Hermann and K. Lemke, *Hoppe-Seyler's Z. Physiol. Chem.*, **349**, 390 (1968).
(9) (a) Chemical shifts of NH_3^+ protons of glycine and of $CH_3NH_3^+$ differ by 0.38 ppm; (b) At pH 3.5, several percent of the dissolved lysine exists in the form L^{2+}.
(10) k_c for $L_\epsilon + OH^-$ is somewhat smaller than k_c for $CH_3NH_3^+ + OH^-$. H. G. Busse and G. Maass, *Z. Phys. Chem. (Frankfurt am Main)*, **66**, 92 (1969).
(11) S. Meiboom, *J. Chem. Phys.*, **34**, 375 (1961).
(12) A. Lowenstein anc A. Szöke, *J. Am. Chem. Soc.*, **84**, 1151 (1962); Z. Luz and S. Meiboom, *ibid.*, **86**, 4768 (1964).

(13) Part of the ~20% discrepancy between values reported for this important kinetic constant from various laboratories may be due to differences in ionic strength correction.
(14) L. R. Ryklan and C. L. A. Schmidt, *Arch. Biochem.*, **5**, 89 (1944); W. Stricks and I. M. Kolthoff, *J. Am. Chem. Soc.*, **73**, 4569 (1951); D. D. Perrin, "Dissociation Constants of Organic Bases in Aqueous Solution", Butterworths, London, 1965.
(15) D. R. Cogley, M. Falk, J. N. Butler, and E. Grunwald, *J. Phys. Chem.*, **76**, 855 (1972).
(16) M. M. Kreevoy, D. S. Sappenfield, and W. Schwabacher, *J. Phys. Chem.*, **69**, 2287 (1965).
(17) Z. Luz and S. Meiboom, *J. Am. Chem. Soc.*, **85**, 3923 (1963).
(18) D. Rosenthal and E. Grunwald, *J. Am. Chem. Soc.*, **94**, 5956 (1972).
(19) M. A. Grafius and J. B. Neilands, *J. Am. Chem. Soc.*, **77**, 3389 (1955).

The Role of H_2O^- and D_2O^- in Competitive Electron Trapping by the Matrix and by Cadmium(II) in Sodium Perchlorate Aqueous Glasses

Cz. Stradowski[1] and William H. Hamill*

Department of Chemistry and Radiation Laboratory,[2] University of Notre Dame, Notre Dame, Indiana 46556
(Received December 15, 1975)

Publication costs assisted by the U.S. Energy Research and Development Administration

Aqueous glasses of 8 M $NaClO_4$ containing 0–0.15 M $Cd(ClO_4)_2$ in H_2O and D_2O have been pulse irradiated at 77–160 K. Yields of matrix-trapped electrons (e_t^-) and of Cd^+ obey simple Stern–Volmer type kinetics with no evidence of recombination of e_t^- or conversion to Cd^+ in the dark at $>10^{-8}$ s. Electron trapping by Cd^{2+} is more efficient in D_2O than in H_2O and the initial yield of e_t^- in D_2O is much greater than in H_2O. Isotope effects appear to be a consequence of relatively inefficient electron localization prior to hydration in D_2O, for which there is direct evidence. Optical bleaching of e_t^- at 400 nm and 77 K following ^{60}Co irradiation converts e_t^- to Cd^+ with progressively diminishing quantum yield ϕ, no loss of electrons by recombination, and $\phi(D_2O) = 1.7\phi(H_2O)$ throughout. The trapped charge pair are presumed to be free after dipole relaxation, but the photoelectron is Coulombically bound to the trapping site by oriented dipoles. The electron is expected to return to this site if it is not trapped by Cd^{2+}. For small $[Cd^{2+}]$, prolonged optical bleaching selects a population of electrons characterized by local $[Cd^{2+}]$ much less than the average and steadily decreasing quantum yields.

Introduction

The dynamics of localization of dry electrons in polar media has not been examined theoretically, but it is expected to depend on long-range collective polarizations and on localized defects arising from statistical fluctuations.[3]

Dry electron (e^-) scavenging by Cd^{2+} in aqueous solutions can be distinguished from that for hydrated electrons (e_{aq}^-) by adding large concentrations of acid to remove the latter selectively.[4] The 100-eV yield, $G(Cd^+)$, was greater in D_2O than in H_2O.[5] Localization of an electron at a defect site entails dissipation of the binding energy to the lattice, presumably by vibrational excitation. Efficient coupling is provided by compound ion states, H_2O^- and D_2O^-. Sanche and Schulz concluded from their failure to resolve the resonance of H_2O^- that the autoionization width was greater than 1 eV.[6] The resonance has been found in the solid state.[7] Both H_2O and D_2O thin-film solids at 77 K under slow electron impact have resonances at ~0.6 eV. Prompt autoionization of H_2O^- and D_2O^- may compete with vibrational excitation and thus introduce an isotope effect.

The work reported here describes a further effort to examine the role of the lattice in dry-electron localization and subsequent solvation for 8 M $NaClO_4$ in H_2O and D_2O glasses in competition with scavenging by Cd^{2+}. Yields of both e_t^- and of Cd^+ were measured from 77 to 150 K. The relative quantum yields of bleaching e_t^- with added Cd^{2+} in H_2O and D_2O provided information for isotope effects in the process of delocalization.

Experimental Section

Pulse irradiations were performed with a linear accelerator providing ~8 MeV electrons for 10-ns pulses and doses of ~5 krads. Samples in Spectrosil cells were immersed in liquid nitrogen or the temperature was manually controlled ($\gtrsim$ 100 K) by flowing cooled nitrogen gas through the dewar container. Some experiments were performed with ^{60}Co irradiation at 77 K by conventional methods.

Optical bleaching experiments were performed using the monochromatic light beam of a Cary 14R spectrophotometer. The accuracy of these measurements was somewhat limited by cracked glasses.

$NaClO_4$ was obtained from the G. F. Smith Chemical Co., $Cd(ClO_4)_2$ from ICN Pharmaceuticals, Inc. Water was triply distilled. Heavy water was used as received from Merck Sharp and Dohme.

Results

All samples contained 8 M $NaClO_4$ and 0–0.15 M $Cd(ClO_4)_2$ which permitted observation of both the e_t^- band at 540 nm and the Cd^+ band at 300 nm. These bands were quite stable under the conditions of both pulsed and ^{60}Co irradiations. Typical oscilloscope traces are shown in Figure 1 for 0.05 M

Cd^{2+} in D_2O for e_t^- (upper) and Cd^+ (lower). Much faster sweep rates also showed no evidence for conversion of e_t^- to Cd^+. In ^{60}Co-irradiated glasses at 77 K, as well, both bands were stable to ~50 min except under photobleaching conditions. Miller has also observed no change in these bands for 8 M $NaClO_4$ in methanol at ~100 K during the interval ~10^{-3} to ~10 s.[8]

If all Cd^+ and e_t^- arise from a common precursor, the dry electron, the results may conform to a simple competition described by the following when there is no competing process

$$G(Cd^+) = G^0(e^-)(1 + \nu_2/\nu_1[Cd^{2+}]^{-1}) \quad (1)$$

where $G^0(e^-)$ is the primary yield of dry electrons and ν_1 and ν_2 are the efficiencies of trapping e^- by Cd^{2+} and localization by the matrix. A test of this simple model for H_2O and D_2O at 77 K by pulse radiolysis, corrected for e_t^- absorption at 300 nm, appears in Figure 2. The efficiency for trapping e^- by Cd^{2+}, given by ν_1/ν_2, is greater in D_2O than in H_2O. The concentration of Cd^{2+} required for $G(Cd^+) = 0.37G^0(e^-)$ was 0.22 M in H_2O and 0.16 M in D_2O.

The dependence of $G(e_t^-)$ on $[Cd^{2+}]$ is described by

$$G(e_t^-) = G^0(e^-)(1 + \nu_1[Cd^{2+}]/\nu_2')^{-1} \quad (2)$$

where $\nu_2' = \alpha\nu_2$, $1 - \alpha$ is the probability of recombination and the results appear in Figure 3. The efficiency is 34% greater in D_2O. These results are collected in Table I for comparison with earlier data for isotope effects at ~290 K.[5]

The yields of e_t^- in pulse-irradiated Cd^{2+}-free glasses depend on temperature, being greater in D_2O, as shown in Figure 4. Higher yields in D_2O were also observed for ^{60}Co irradiations.

The dependence of the ratio of optical densities $OD(Cd^+)/OD(e_t^-)$ on temperature appears in Figure 5 for 25, 50, and 100 mM Cd^{2+}. The data at 77 K were obtained by ^{60}Co irradiation. If the empirical Arrhenius equation is applicable ΔE_{act} is in the range 0.1–0.3 kcal/mol for ν_1/ν_2, depending upon the weight assigned to the data at 77 K. Since optical spectra commonly change somewhat with temperature, there is no clear evidence for activation, particularly at >100 K.

Photobleaching of e_t^- at 400 nm in ^{60}Co-irradiated H_2O and D_2O glasses with 0.025 M Cd^{2+}, both at 77 K, was monitored at 540 and 400 nm. There was negligible bleaching during measurements of OD. The results in Figure 6 show that bleaching is more efficient in D_2O than in H_2O. Within the uncertainty caused by cracked glasses in measuring transmitted light intensities before and after irradiation, the effects are similar at 400 and 540 nm. The concomitant increases in $OD(Cd^+)$ at 300 nm are shown in Figure 7. The two sets of results obey the relation $OD(e_t^-) + \alpha OD(Cd^+) = \beta$, where α and β are constants, within an average deviation of ~0.01 units of OD. The transfer efficiency is the same for H_2O and D_2O throughout, and is probably unity.

Discussion

Miller has observed transfer of matrix-trapped electrons to various electron acceptors in aqueous 6 M NaOH at ≥77 K.[9] $G(e_t^-)$ decreased roughly linearly with log t from 10^{-8} to 10^2 s and approached zero. A tenfold increase in acceptor concentration decreased the lifetime of e_t^- about 10^6. The mechanism was attributed to quantum mechanical tunneling.

The system used in the present work behaves quite differently. At 77 K, G (e_t^-) does not decrease in the range 10^{-8} to 10^3 s and a sixfold change in $[Cd^{2+}]$ alters $OD(e_t^-)$ only at $t < 10^{-8}$ s. There is no evidence that e_t^- is converted to Cd^+ at $t < 10^{-8}$ s and comparison with the NaOH glass excludes dy-

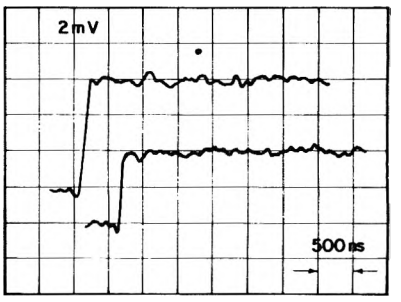

Figure 1. Oscilloscope traces for 8 M $NaClO_4$ with 0.05 M $Cd(ClO_4)_2$ in D_2O at 180 K for e_t^- at 540 nm (above) and Cd^+ at 300 nm (below).

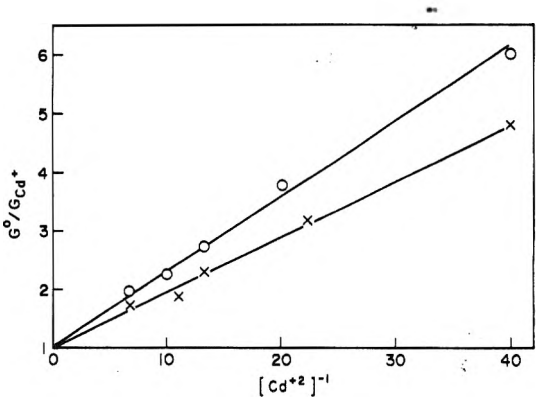

Figure 2. The normalized reciprocal yield of Cd^+, measured at 300 nm, vs. $[Cd^{2+}]^{-1}$ in 8 M $NaClO_4$ at 77 K in H_2O (O) and D_2O (X), from eq 1.

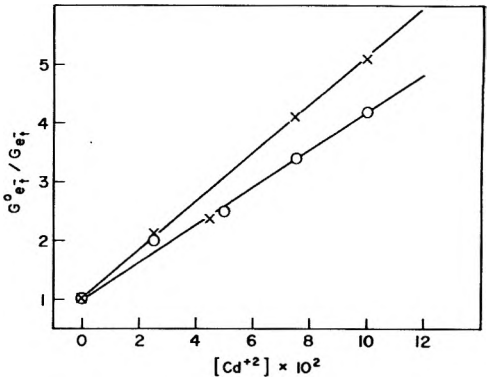

Figure 3. The normalized reciprocal yield of e_t^- vs. $[Cd^{+2}]$, measured at 532 nm for D_2O and 540 nm for H_2O, in 8 M $NaClO_4$ at 77 K, from eq 2.

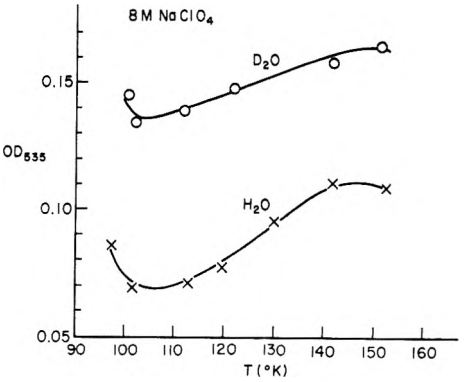

Figure 4. The dependence of OD_{535} for e_t^- on irradiation temperature in 8 M $NaClO_4$ in (X) H_2O and (O) D_2O.

TABLE I: A Summary of Results for the Relative Yields of e_t^- and Cd^+ in 8 M $NaClO_4$ Glasses in H_2O and D_2O

System	Transient	ν_1/ν_2 H_2O	ν_1/ν_2 D_2O	Isotope effect, %
4 M $HClO_4$ and Cd^{2+}, 290 K[a]	Cd^+	2.87	4.25	47
8 M $NaClO_4$ and Cd^{2+}, 77 K[b]	Cd^+	7.8[c]	10.4[c]	33
8 M $NaClO_4$ and Cd^{2+}, 77 K[b]	e_t^-	30.9[d]	41.2[d]	34

[a] From ref 5. [b] For $G_{Cd^+} = 0.37G^0$, $[Cd^{2+}]_{0.37}$ is 0.22 in H_2O and 0.16 in D_2O for these glasses at 77 K. [c] From eq 1. [d] From eq 2.

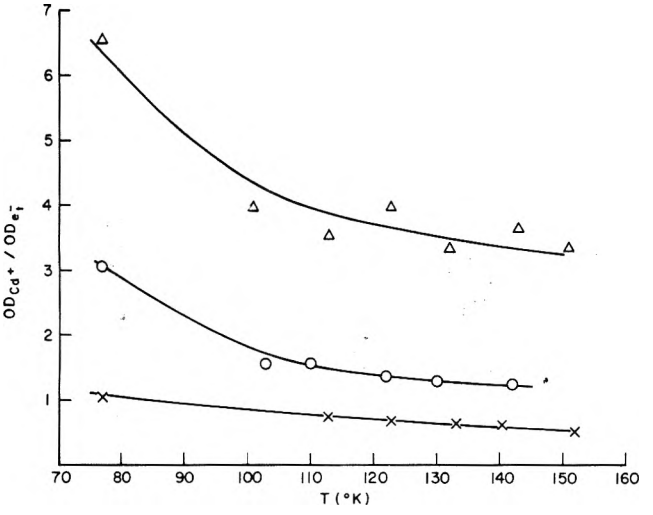

Figure 5. The optical density ratio for Cd^+ and e_t^- vs. irradiation temperature for (×) 25, (O) 50, and (Δ) 100 mM $Cd(ClO_4)_2$ in H_2O. Data for 77 K were obtained following ^{60}Co irradiation, all others by pulse irradiation.

namic similarities. If all e_t^- are comprised within a single continuous distribution, failure to detect $e_t^- + Cd^{2+} \rightarrow Cd^+$ over a range of 10^{11} in time excludes this mechanism for $t < 10^{-8}$ s except for contact pairs, both for hopping and for tunneling. Consequently, all Cd^+ can be attributed to dry-electron scavenging by Cd^{2+}. This is consistent with eq 1 and Figure 2. Similarly, eq 2 and Figure 3 describe yields of e_t^- resulting exclusively from dry-electron precursors. The data summarized in Table I show that ν_1/ν_2' for e_t^- is four times greater than ν_1/ν_2 for Cd^+, both in H_2O and D_2O. By eq 1 and 2, this is interpreted as $(1 - \alpha) = 0.75$, the probability of recombination of the localized electron prior to relaxation.

It is notable that $(\nu_1/\nu_2)_{D_2O}/(\nu_1/\nu_2)_{H_2O}$ for $G(Cd^+)$ vs. $[Cd^{2+}]$ is approximately the same in 8 M $NaClO_4$ at 77 K and in 4 M $HClO_4$ at ~300 K,[5] and no activation is involved. It has been proposed that the isotope effect in liquid solutions resides almost entirely in ν_2, the frequency of localization of e^-. Also, it involves transferring to the lattice the binding energy of e^- at the trapping site as a vibrational excitation, probably through formation of H_2O^- or D_2O^-.[5] An isotope effect in ν_2 could arise from the very fast autoionization, with $\Delta E > 1$ eV,[5] which competes with vibrational excitation. The slower vibrations of D_2O could produce a smaller cross section to form the transient ion. Such an effect has been observed for the resonances of H_2O^- and D_2O^-.

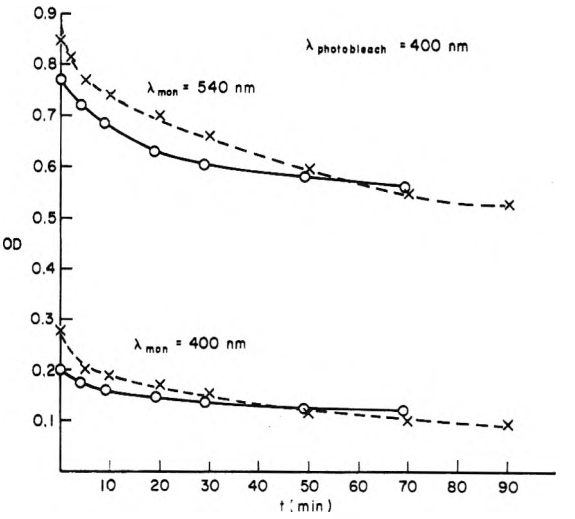

Figure 6. Photobleaching at 400 nm of e_t^- at 77 K for 8 M $NaClO_4$ with 25 mM $Cd(ClO_4)_2$ in (O) H_2O and (×) D_2O. The OD was monitored at 400 and 540 nm.

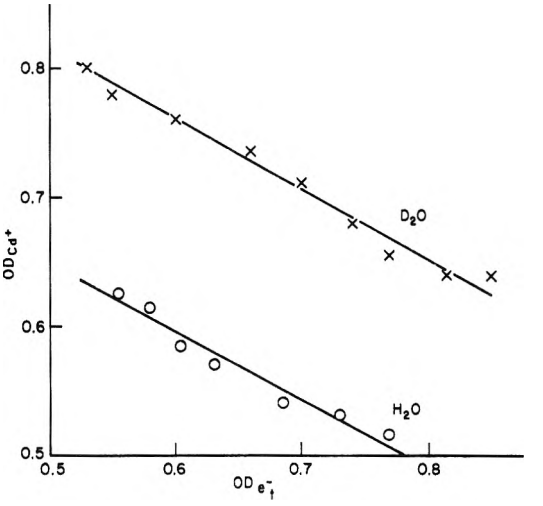

Figure 7. The OD_{Cd^+} at 300 nm vs. $OD_{e_t^-}$ at 540 nm for the same experiment as Figure 6.

There is a large cross section near resonance for H_2O^-, and an appreciably smaller cross section for D_2O^-, measured by retarding potential analysis of very low energy electrons back scattered from thin ice films at 77 K. Results of Hiraoka[7] and Huang[10] are summarized in Figure 8. Both resonances appear at ~0.6 eV (cf. Figure 24 of ref 7). Their amplitudes are expressed as the ratio of the area under the loss peak to the area under the elastic peak from curves for dI_b/dV_r vs. V_r of the back-scattered current and the retarding potential.[7] The ordinate in Figure 8 depends both on the cross section and on the probability for the inelastically scattered electron to escape from the film to vacuum. Since these films have bulk electron affinities χ of ~1.0 eV, relatively few inelastically scattered slow electrons can reach vacuum. The threshold is ~1.6 eV, in rough agreement with Figure 8. The zero of energy is the bottom of the conduction band. If $\chi_{H_2O} = \chi_{D_2O}$ and the probability of escape to vacuum depends only on the electron energy and χ, then the ratio of ordinates in Figure 8 provides a rough measure of the relative inelastic cross sections.

The larger yields of e_t^- in D_2O, Figure 4, may be a consequence of the smaller cross section for D_2O^-. Trapping in the matrix competes with prompt recombination since $G(e_t^-)$ in

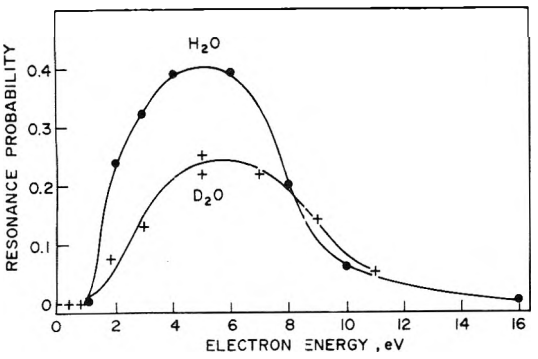

Figure 8. The normalized yields of inelastically back-scattered electrons for H_2O^- and D_2O^- resonances at ~0.6 eV at various electron energies.

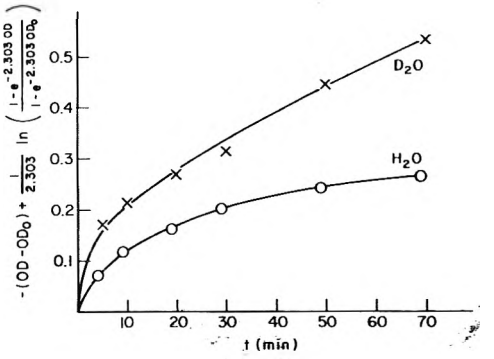

Figure 9. The time-dependent quantum efficiency for bleaching e_t^- at 77 K and 400 nm according to eq 4. The results are those of Figure 5 for (O) H_2O and (X) D_2O.

the H_2O glass is ~1.8.[11] A small percentage change in recombination produces a threefold change in $G(e_t^-)$. The electron energy goes negative at a larger charge-pair radius in D_2O, consistent with a greater probability of trapping. The large yield of free electrons in neopentane is associated with a negligible cross section for $C_5H_{12}^-$.[7]

Prompt Coulombic recombination of the localized electron, prior to relaxation, involves the high-frequency dielectric constant. No comparable electron transfer to Cd^{2+} can occur, excepting nearest neighbors, because it is fully screened.

These considerations imply that recombining electrons may have very short ranges, but this is contrary to the small value of C_{37} for Cd^{2+}. The remaining possibility is a large range for H_2O^+ in its electronically conducting state. This mechanism decreases $G^0(e^-)$ by removing Cd^+ and e_t^- indiscriminately. $G(e_t^-)$ would be greater in D_2O because localization to form D_3O^+ is slower.[12]

Following the regime of prompt recombination the self-trapped positive holes are screened by dipole relaxation and the probability of further recombination is greatly decreased.

There was no appreciable change in the spectrum of e_t^- during photobleaching. The OD's at 400 and 540 nm in Figure 6 cannot be compared by simple scaling because cells acquired some frost while transferring between dewar containers and base lines are not comparable before and after irradiation. Nevertheless OD_{400} vs. OD_{540} is linear, implying $(OD_{400} + \Delta_1)/(OD_{540} + \Delta_2)$ is constant for unknown shifts Δ and a single trapped species is implied throughout optical bleaching. In alkaline glasses there are at least two distinguishable species of e_t^-.[13]

The decay of e_t^- and growth of Cd^+ in Figures 6 and 7 during photobleaching can plausibly be attributed to quantitative electron transfer. While the photoejected electron is in the conducting state it is dry and cannot react with $H_3O_{aq}^+$, unlike alkaline glasses.[13]

The efficiency of photobleaching should be described by

$$-dn/dt = \Delta I_a = \phi I_0[1 - \exp(-2.3OD)] \quad (3)$$

$$\frac{-\phi I_0 \epsilon l t}{VN} = OD_0 - OD - 0.43 \ln\left[\frac{1 - \exp(-2.30D)}{1 - \exp(-2.30D)}\right] \quad (4)$$

where the number of electrons bleached, n, depends on the quantum yield, ϕ, the absorbed light intensity, I_a, and the extinction coefficient, ϵ. The results of Figure 6 for e_t^- at 400 nm are presented in Figure 9 according to eq 4. The quantum yield of photobleaching decreases strongly with progressive bleaching, but $\phi_{D_2O} = 1.7\phi_{H_2O}$ for given t over the entire range and neither is unity initially. Consequently, the inefficiency changes throughout in D_2O as in H_2O for the same stage of photobleaching.

Since Cd^{2+} is an efficient trap for e^-, the photoelectron has a fairly limited range if the process involves direct ionization of e_t^- as proposed for alkaline glasses.[13] The electron vacancy has an effective charge of about +1, the electron range is small at 77 K, and the electron can be retrapped at the original unrelaxed site or by Cd^{2+}. When the former occurs the local $[Cd^{2+}]$ is, on the average, less than the bulk concentration. After repeated photoionizations the surviving population of e_t^- is a selected group, relative to its environment, with a small quantum yield for bleaching. A comparable mechanism may apply to solute-free systems where recombination occurs efficiently, e.g., O^- in NaOH glasses.[13] The local environment now depends on charge separation and repeated photoionization produces a surviving population with larger-than-average separation.

Photoelectrons in $NaClO_4$ glass appear to be "free" with respect to recombination, but they must still be Coulombically bound to the polarized trapping site. It is quite plausible that they can reoccupy the same site. It is improbable that the excited electron is in a stationary state in the disordered solid. For Coulombic retrapping the electron must excite lattice vibrations while it is still being strongly scattered. During this process it may be trapped by Cd^{2+}. Possibly ~40% more scattering events are required in D_2O than in H_2O. Since $\phi_{D_2O} = 1.7\phi_{H_2O}$ it may be that some energy is dissipated by excitation of hindered rotations with $h\omega_{H_2O} = 2h\omega_{D_2O}$.

The possibility that e_t^- is H_2O^-, or D_2O^-, deserves serious consideration. These species have been observed by Rusch and Seidel[14] as substitutional impurity centers in the KCl lattice. They were fully characterized by ESR, ENDOR, optical, and electrooptical investigations. The zero-field optical spectrum at 4 K consists of peaks at 2.09 and 2.40 eV with a long vibrational tail, the envelope resembling that for e_t^- and e_{aq}^-. The hydration energy of KCl closely matches the lattice energy and hydrated H_2O^- must be considered. It offers an attractive alternative to $e_{aq}^- + e_{aq}^- \rightarrow H_2$.

Acknowledgment. The authors are indebted to J. L. Magee and P. K. Funabashi for many stimulating discussions.

References and Notes

(1) On leave of absence from the Institute of Radiation Chemistry, Technical University, Lodz, Wroblewskiego 15, Poland.
(2) The Radiation Laboratory of the University of Notre Dame is operated under contract with the U.S. Energy Research and Development Administration.

This is ERDA Document No. COO-38-1029.
(3) P. M. Rentzepis, R. P. Jones, and J. Jortner, *J. Chem. Phys.*, **59**, 766 (1973).
(4) K. Y. Lam and J. W. Hunt, *Int. J. Radiat. Phys. Chem.*, **7**, 317 (1975).
(5) Cz. Stradowski and W. H. Hamill, *J. Phys. Chem.*, **80**, 1054 (1976).
(6) L. Sanche and G. J. Schultz, *J. Chem. Phys.*, **58**, 474 (1972).
(7) K. Hiraoka and W. H. Hamill, *J. Chem. Phys.*, **57**, 3870 (1972).
(8) J. R. Miller, private communication.
(9) J. R. Miller, *J. Phys. Chem.*, **79**, 1070 (1975).
(10) T. Huang, unpublished work.
(11) B. G. Ershov and A. K. Pikaev, *Radiat. Res. Rev.*, **2**, 1 (1971).
(12) H. Ogura and W. H. Hamill, *J. Phys. Chem.*, **77**, 2952 (1973); K. J. Kim, work in progress.
(13) H. Hase and L. Kevan, *J. Chem. Phys.*, **54**, 908 (1971).
(14) W. Rusch and H. Seidel, *Phys. Status Solidi*, 501 (b) **63**, 183 (1974).

Radiolytic and Photolytic Production and Decay of Radicals in Adamantane and Solutions of 2-Methyltetrahydrofuran, 2-Methyltetrahydrothiophene, and Tetrahydrothiophene in Adamantane. Conformation Equilibrium of the 2-Methyltetrahydrothiophene Radical[1,2]

G. Charles Dismukes and John E. Willard*

Department of Chemistry, University of Wisconsin, Madison, Wisconsin 53706 *(Received January 19, 1976)*

Publication costs assisted by the U.S. Energy Research and Development Administration

The radicals produced by γ radiolysis of adamantane and adamantane containing 2-methyltetrahydrofuran (MTHF), 2-methyltetrahydrothiophene (MTHT), and tetrahydrothiophene (THT) have been investigated for the purpose of obtaining a better understanding of radical reactions in the adamantane matrix and of clarifying the identity of the radical formed by γ irradiation of pure glassy MTHF. Thermal and photochemical changes in the identity of the radicals produced by γ irradiation of pure adamantane can be induced at 77 K. If solutes are present the adamantyl radicals formed at 77 K are quantitatively replaced by solute radicals on warming, apparently as a result of diffusion of solute molecules to the adamantyl radical centers followed by abstraction of an H atom. For the solutes MTHT, MTHT, and THT, the radicals form only by H abstraction from carbon atoms adjacent to the heteroatom. MTHT forms only the secondary α radical; MTHF forms both the secondary and tertiary α radicals. MTHT radicals in adamantane decay by second-order kinetics with a rate constant of $\sim$0.17 M^{-1} s^{-1} at 295 K. The tertiary and secondary MTHF radicals decay by first-order kinetics with half-lives of $\sim$1.5 and 3.4 min, respectively, at $\sim$245 K, accompanied by growth of new radicals. The evidence suggests a unimolecular ring opening followed by H atom abstraction from the matrix. Reversible changes in the ESR spectrum of the MTHT radical in adamantane indicate that the axial methyl conformation is favored relative to the equatorial at 77 K, and that the enthalpy and entropy differences for the two conformations are 1.7 kcal mol^{-1} and -4.2 cal deg^{-1}, respectively. Analyses of the ESR spectra of the MTHF radicals in adamantane as a function of temperature indicate that the ESR spectrum of the matrix radical in γ-irradiated glassy MTHF is attributable to the tertiary α radical.

Introduction

The polycyclic hydrocarbon adamantane (I) has been extensively used[3] as a matrix for the ESR examination of radicals produced from solutes by radiolysis and photolysis. It offers several advantages over isolation of the radicals in the low temperature matrices of the parent compounds of the radicals. These include freer rotation of the radicals (and hence better resolved spectra) and the possibility of studying the radicals on a convenient time scale over a wide temperature range without excessive decay due to softening of the matrix. Also, in some cases, solute radicals of interest are produced which cannot be formed by irradiation of the solute compound in the pure state. We have determined the ESR spectra of the radicals produced in adamantane samples containing 2-methyltetrahydrofuran (MTHF, II), 2-methyltetrahydrothiophene (MTHT, III), and tetrahydrothiophene (IV) to assist in the interpretation of the broad spectra of trapped intermediates produced by γ irradiation of the neat glassy states of MTHF[4] and MTHT. Observations have also been made on: (1) the effects of temperature and photolysis on the radicals formed by γ irradiation of adamantane without solutes; (2) the mechanisms by which solute radicals are formed by adamantyl radicals; (3) the decay kinetics of the radicals, and the temperature dependence of the axial-

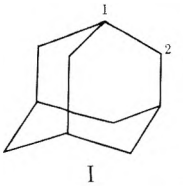

I

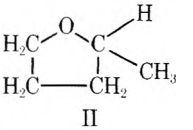

II

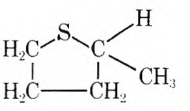

III

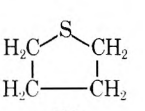

IV

equatorial equilibrium of the secondary α-MTHT radical in adamantane. These studies contribute to the understanding of the adamantane isolation technique for radical investigations. This is part of a broader investigation of the nature, yields, and decay mechanisms of trapped intermediates produced by the γ radiolysis glassy and polycrystalline organic matrices.[5]

Experimental Section

Reagents and Sample Preparation. Adamantane from Aldrich Chemical Co. was recrystallized from cyclohexane which had been passed through a 150-cm column of freshly activated silica gel. For the ESR experiments on neat adamantane the crystals were then dried in air, sublimed twice under vacuum, and sealed in the Suprasil tubes while still under vacuum. For a few experiments the recrystallization from cyclohexane was preceded by stirring with activated charcoal and filtration. These gave the same results.

Adamantane containing a few mole percent of MTHT, MTHF, or THT was prepared by crystallization of the purified adamantane from its saturated solutions in MTHT, MTHF, and THT. These solvents were purified by fractional distillation and, for MTHF, by more thorough methods.[2] The concentration of the MTHT in the adamantane was determined by dissolving a weighed sample of the crystals in purified 3-methylpentane and measuring the absorbance due to the MTHT at a wavelength where its extinction coefficient is known.[2] The polycrystalline adamantane–solute samples were prepared for ESR analysis by placing a 2–3 cm height in a 2 or 3 mm i.d. Suprasil or Kel-F tube, evacuating at 200 K to $<10^{-5}$ Torr, and sealing. Polycrystalline samples for spectrophotometric analysis were prepared by compression to 1-cm diameter semitransparent disks of <1 mm thickness in a pellet press. These were not degassed.

MTHT was synthesized[6] from 1,4-dibromopentane and sodium sulfide and purified by fractional distillation, degassed, and stored over activated type 3A molecular sieve in a glass bulb with a Teflon stopcock. It had a boiling point of 132 ± 1 °C in agreement with literature reports.[7] The absorption spectra from 200 to 400 nm and from 15 to 30 μ and the mass spectrum were identical with those previously reported.[8] Both gas chromatography, using a Carbowax 1540 on Chromosorb P column with thermal conductivity detection, and thin-layer chromatography on silica gel with hexane as the solvent showed only one component present. The proton NMR spectrum at 60 MHz was consistent with that expected for MTHT by comparison with the spectra of MTHF and THT.

MTHF from Aldrich Chemical Co. contained as impurities, water, 2-methylfuran, methyldihydrofurans, and 1% hydroquinone stabilizer. Refluxing for 3 days under bubbling N_2 partially removed the more volatile impurities. Passage through a column of freshly activated alumina followed by fractional distillation through a column of stainless steel helices removed the remaining impurities detected by gas chromatographic and spectrophotometric analyses.

γ Irradiations. γ Irradiations were made with a ^{60}Co source, with the samples under liquid nitrogen, unless otherwise indicated. Dose rates were determined by Fricke dosimetry.[2] For the sample positions, and over the period of this work, they ranged from $\sim 3 \times 10^{18}$ to 1×10^{19} eV g^{-1} min^{-1}.

Optical and ESR Absorption Measurements. Optical absorption spectra were determined with a Cary 14R spectrophotometer. Pellets of adamantane for optical analysis were held between two quartz plates in the sample compartment.

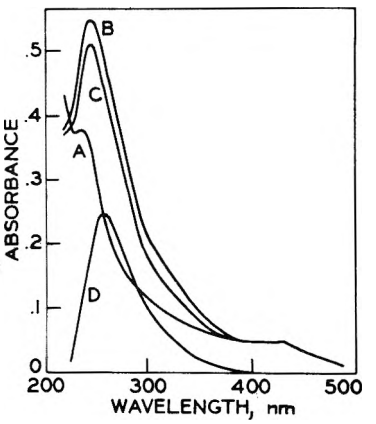

Figure 1. Optical absorption induced by γ radiolysis of an adamantane pellet at room temperature. The pellet thickness was ~1 mm: (A) before radiolysis; (B) 7 min after a 10-min radiolysis to $\sim 8 \times 10^{19}$ eV g^{-1}; (C) same as B except 22 h later; (D) optical absorption induced by the radiolysis, obtained by subtraction of curve A from curve B.

Light scattering in the opaque pellets limited measurements to wavelengths above 215 nm. Neutral density screens were used to offset the light attenuation by the sample.

ESR measurements were made in the X-band with a Varian E-15 or 4502 spectrometer using 100-kHz field modulation and a V-4531 cavity. The temperatures of measurement were 77 K, maintained by liquid nitrogen, or ≥83 K maintained by a Varian variable temperature controller. A copper–constantan thermocouple adjacent to the sensitive region of the sample, with a digital thermocouple meter for readout, was used for monitoring the temperature when the variable temperature device was used. Microwave powers were measured with a Hewlett-Packard 431-C power meter. Double integration of the first derivative ESR signals was performed with a Tracor Northern electronic integrator/signal averager. The g factors were determined from the positions of the centers of the radical spectra relative to the high-field line at $g = 2.0009$[9] in the spectrum of the γ-irradiated silica sample cells.

Results

γ-Irradiated Pure Adamantane. Optical Spectra. γ irradiation of pure adamantane pellets induces optical absorption peaking at 260 nm, which decays over hours, as illustrated in Figure 1. The difference between the spectrum before irradiation (curve A) and that at the end of irradiation (curve B) is plotted as curve D. We tentatively ascribe this absorption to 2-adamantyl radicals, in accordance with ESR signal assignments discussed in a later section.

ESR Spectra. γ irradiation at 77 K of purified degassed adamantane or adamantane containing 2 mol % of MTHF, MTHT, or THT produced a species which gave a structureless ESR singlet of 28-G line width (ΔH_{pp}, peak-to-peak width of the first-derivative spectrum) at low microwave powers. In the sections that follow, we discuss the changes in this signal with standing or photolysis of the sample at 77 K and on warming. For convenient reference, some of these are summarized in Table I.

The 28-G singlet shows the onset of saturation at microwave powers above a few microwatts (Figure 2). A paramagnetic species produced by γ irradiation of the Suprasil tube is responsible for the signal at S in the figure. This silica signal is broadened by the large modulation amplitude used. Above 10 mW the 28-G singlet is no longer observable and a much weaker 18-G singlet is revealed.

When a γ-irradiated sample giving the ESR signal of Fig-

TABLE I: Suggested Assignment of Sequential Reactions Initiated by γ Irradiation at 77 K and Warming of Adamantane, Adamantane–MTHF, and Adamantane–MTHT

Adamantane	Adamantane + MTHF	Adamantane + MTHT
γ irradiation at 77 K	γ irradiation at 77 K	γ irradiation at 77 K
↓	↓	↓
28-G ΔH_{pp} ESR singlet (2-adamantyl radical)	28-G ΔH_{pp} ESR singlet (2-adamantyl radical)	28-G ΔH_{pp} ESR singlet (2-adamantyl radical)
↓	↓	↓
Standing at 77 K or 254-nm exposure	Warming to > 180 K	Warming to > 180 K
↓	↓	↓
Unassigned five-line spectrum	H abstraction by 2-A· forming *sec*- and *tert*-α-MTHF·	H abstraction by 2-A· forming *sec*-α-MTHT· which undergo reversible conformation change. They disappear by bimolecular combination.
↓	↓	
Warming to 208 K	MTHF ring rupture giving radicals which abstract H from A forming 1-adamantyl radical	
↓		
Partially resolved ESR doublet (2-adamantyl radical)		

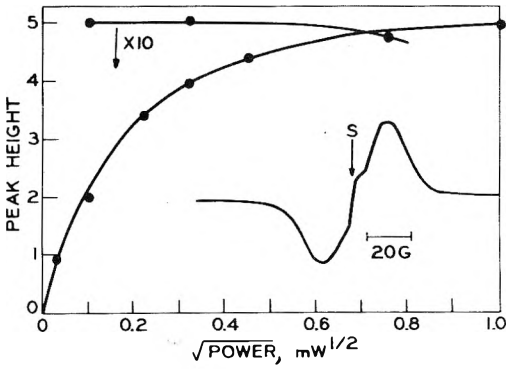

Figure 2. ESR spectrum and power saturation curve of the 28-G singlet signal from γ-irradiated adamantane at 77 K. The first-derivative peak height was used in the measurement of the saturation behavior. The data shown for the upper curve are an extension of the saturation measurements above 1 mW. Dose, 4.9×10^{19} eV g^{-1}; S, position of the Suprasil signal. The spectrometer settings for the spectrum shown are microwave power, 0.001 mW; gain, 800; modulation amplitude, 6.3 G; recorder sensitivity, 1 V.

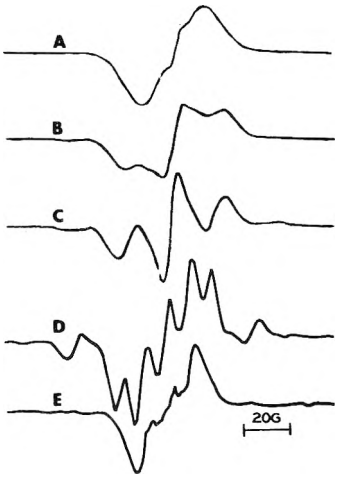

Figure 3. ESR spectra of adamantane γ irradiated at 77 K: (A) at 77 K 5 min after 10-min irradiation; (B) at 77 K 2 h after irradiation; (C) at 77 K after 30-s photolysis with 254-nm light of a sample of type A or B; (D) after warming type C sample to 206 K; (E) after warming type A or D sample to 256 K. (A,B,C) dose, 4.9×10^{19} eV g^{-1}; power, 0.001 mW; modulation amplitude, 6.3 G; gain, 800; recorder, 1 V. (D,E) dose, 5×10^{18} eV g^{-1}; microwave power, 2 mW; modulation amplitude, 2.5 G; gains, 2000 and 4000; recorder, 1 V. S indicates signal induced in the Suprasil sample cell.

ures 2 and 3A is allowed to stand at 77 K, the signal changes to that of Figure 3C with intermediate stages such as Figure 3B. During the 2 h between recording the spectra of Figure 3A and 3B, the radical concentration decreased by 9% as determined from the double integrals of the first-derivative spectra. Photolysis with ~80 mW cm^{-2} of 254-nm light (from a Vycor spiral low-pressure Hg lamp) for 30 s immediately after irradiation caused the complete change from the spectrum of Figure 3A to 3C with no loss of radical concentration. An additional 6-min photolysis produced an 8% decrease in concentration with no further enhancement of resolution. The five-line spectra produced by standing in the dark at 77 K and by 254-nm exposure are identical, with a 21.2 ± 0.3 G spacing between adjacent lines at 1 μW and relative areas of the peaks of ~0.6:4.9:8.7:4.6:1.0. Neither 633-nm (2 mW cm^{-2}) or 365 nm (5 mW cm^{-2}) light produced any change in either the 28-G singlet or the five-line spectrum during several minutes exposure. Adamantane has negligible absorption at each of the photolysis wavelengths tested.

When either a sample giving the 28-G singlet or one giving the five-line spectrum is warmed, the spectrum changes to the poorly resolved doublet shown in Figure 3E, having a coupling constant of ~21 G but retaining the 28-G peak to peak separation of the outer halves of each hyperfine peak, in coincidence with the width of the 28-G singlet observed immediately after irradiation at 77 K. Since controlled warm-up experiments with repeated ESR scans were not done on samples warmed immediately after irradiation (before development of the five-line spectrum), it is not known whether the spectral change from Figure 3A to 3E involved an intermediate stage of conversion to the five-line spectrum. During further warming after appearance of the unresolved doublet, the radical concentration decreases steadily. In samples which have had a high dose (>10^{20} eV g^{-1}), the decrease in total concentration is accompanied by a growth of a new eight- or nine-line signal with overall width of ~160 G. It appears to be the spectrum of a species formed by reaction of the 2-adamantyl radical (believed to give the spectra of Figures 3A and 3E, as discussed later) with a product of the γ irradiation.

A photolyzed sample of γ-irradiated adamantane which gave the five-line spectrum of Figure 3C was warmed from 77 K by increments of 20 to 30 K. At ~145 K two new lines separated by ~21 G, one on each side of the central line of the five-line spectrum, appeared and increased with increasing

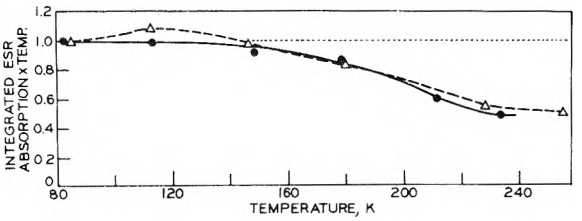

Figure 4. Total radical concentration during warm-up from 77 K of γ-irradiated adamantane (△) and adamantane containing 2 mol % MTHT (●) following irradiation at 77 K to 4.4×10^{19} eV g^{-1}. Microwave power 0.001 mW. The integrated ESR absorption areas were multiplied by the temperature to correct for the change in Boltzmann distribution of spins.

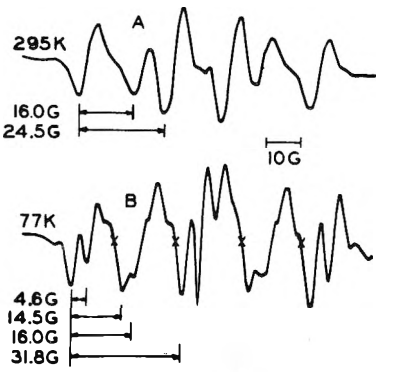

Figure 5. (A) ESR spectra of an adamantane–THT sample γ irradiated at 295 K or at 77 K and then warmed to room temperature before measuring. The room temperature spectrum consists of a doublet of 16.0 G and a triplet of 24.5-G splitting. (B) The spectrum at 77 K: four doublet couplings of 4.6, 14.5, 16.0, and 31.8 G are observed: dose, 5.6×10^{19} eV g^{-1}; microwave power, 200 mW; modulation amplitude, 0.5 G; gain, 2000; recorder, 1 V. The 77 K spectrum is partially saturated and the 295 K spectrum is unsaturated.

temperature as the lines of the five-line spectrum decreased. A spectrum taken at 206 K (Figure 3D) indicates both radicals and the line narrowing which occurs as the temperature is increased. Below the adamantane phase transition[10] from the tetragonal crystalline form to the disordered cubic form at 208 K the intensity of the spectrum at each temperature of observation remained constant for at least several minutes. Above the phase transition there was a continual decrease in the five-line spectrum relative to the two-line spectrum and a decrease in the total radical concentration. When a sample which has been warmed to above the phase transition is cooled to temperatures below the transition, the spectrum does not revert to its earlier form but radical decay slows to a rate which is imperceptible over several minutes. Typically the total radical concentration at 255 K was half of the original concentration at 77 K, for warm-up in increments of 30 K over 45 min (Figure 4).

The g factors of the original 28-G singlet, the five-line spectrum, and the 21-G doublet produced on warming are all 2.0061 ± 0.0003.

The radiation G value for species which gives the 28-G singlet has not been measured for pure adamantane but we have obtained a value of 1.8 ± 0.7 at 77 K in adamantane containing ~2% MTHT, using double integration of the ESR signals and a G value for trapped electrons in MTHF[4] glass of 2.6 as the standard. Other results of the present work imply that the initial G at 77 K of the species produced from adamantane is not significantly affected by the MTHT solute.

Search for Trapped H Atoms. Two samples of purified degassed adamantane were γ irradiated to doses of 1×10^{19} and 4.4×10^{19} eV g^{-1}, respectively, in sealed Kel-F tubes which, unlike fused silica, do not give an H atom signal on irradiation. ESR measurements at 77 K began 10 min after irradiation at 77 K. No H atom signal could be observed in either sample at 0.001, 0.10, 1.0, or 100 mW. The absence of trapped H atoms is in agreement with a previous report.[11]

γ-Irradiated Adamantane Containing Solutes. Conversion of Adamantyl Radicals to Solute Radicals. When a 2 mol % solution of MTHF, MTHT, or THT in adamantane at 77 K is γ irradiated, the initial ESR signal is indistinguishable from the 28-G singlet (Figure 3A) obtained from pure adamantane. On warming the sample to room temperature this signal changes to the signal of the solute radical and this is not converted to the matrix radical spectrum on cooling the sample to 77 K. An adamantane–MTHT sample stored in the dark at 77 K for 12 days following γ irradiation at 77 K showed partial replacement of the adamantyl signal by a signal due to MTHT radicals. When the total radical concentration in samples of pure adamantane and adamantane containing MTHF or MTHT is monitored as the samples are gradually warmed following irradiation at 77 K, very little conversion of adamantyl to solute radicals occurs at ≤180 K unless several hours pass. Solute radicals appear more rapidly at higher temperatures still below the adamantane phase transition at 208 K, with more rapid conversion occurring at and above 208 K. Cooling back to below 208 K does not reverse the changes in spectral shape caused by the warming, but slows their rate. Figure 4 shows the total radical concentration (arbitrary scale) as a function of temperature for a sample of pure adamantane and a sample of adamantane containing MTHT. The coincidence of the two curves through temperatures where complete conversion of adamantyl radicals to MTHT radicals occurs in the mixed system indicates that an MTHT radical replaces every adamantyl radical which would not have promptly decayed in the absence of MTHT. The 50% decrease in radical concentration in the neat adamantane in the temperature range of ~140–230 K is plausibly attributed to intraspur reactions similar to those in glassy hydrocarbon samples.[12] Extensive diffusion seems precluded by the reported activation energy of 36 kcal mol^{-1} for diffusion of adamantane molecules in adamantane.[13] A decay mechanism involving migration of the radical center by H atom exchange between an adamantane radical and a molecule[3a,11] has been suggested but no evidence exists for this mechanism.

ESR Spectra of THT Radicals at 295 and 77 K. When adamantane containing a few mole percent THT is γ irradiated at 295 K (or at 77 K and warmed to 295 K), it gives the ESR spectrum of Figure 5A, which is different from any spectrum observed from pure adamantane. This six-line spectrum consists of a doublet splitting of 16 G and a triplet splitting of 24.5 G with a first-derivative line width of 5.5 G. The peak height ratios are nearly 1:1 for the doublet and 1:2:1 for the triplet. The hyperfine pattern is only consistent with the radical formed by abstraction of a hydrogen atom from a position α to the sulfur atom of the THT molecule. This agrees with the exclusive abstraction of α H atoms from THT[14] and straight chain alkyl sulfides[15] by peroxy radicals. The couplings reported in the THT work were $a_\alpha = 16.9$ G (doublet), $a_\beta = 26.1$ G (triplet), and $a_\gamma = 2.2$ G (triplet) at 295 K.

The broad (5.5 G) line width of the spectrum of Figure 5A implies unresolved hyperfine structure and/or exchange broadening due to conformational equilibrium of the ring rotamer structures. The equivalence of the two β proton couplings indicates that ring pseudorotation equilibrium is rapid relative to the difference in frequences of the β protons in their limiting configurations. When the sample temperature

is lowered to 77 K, the spectrum undergoes a reversible change to that of Figure 5B, indicating that the rate of conformational change has decreased. At 77 K the line widths narrow and a new doublet coupling of 4.6 G is revealed which is most obvious from the outer two lines of Figure 5B. The inner lines show additional changes from the 295 K spectrum due to the nonequivalence of the β H atoms at this temperature. The five major groupings of lines at 77 K, separated by the X marks on Figure 5B, have an integrated ratio of 1:2:2:2:1, to the nearest integer, corresponding to a total of eight hyperfine substates, in agreement with the finding at room temperature. The hyperfine pattern at 77 K can be resolved into doublet splittings of 31.8, 16.0, 14.5, and 4.6 G. The α proton coupling in the THT radical is expected to be insensitive to temperature relative to the β protons, which are expected to show nonequivalent coupling at 77 K due to slow exchange of the ring conformations indicated by

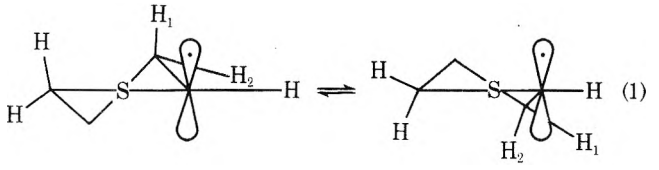

(1)

The doublet coupling of 16.0 G which does not change with temperature must be due to the α proton. The β couplings are then 14.5 and 31.8 G. As expected, these are sensitive to temperature. The spectrum appears complex because of the fortuitous near degeneracies resulting from $a_\alpha \simeq a_{\beta_1}$ and $2a_\alpha \simeq a_{\beta_2}$. The doublet coupling of 4.6 G appears to be due to one of the γ-hydrogen atoms adjacent to the sulfur atom. This coupling is absent in the ESR spectrum of the secondary α-MTHT radical in adamantane (V), in which a methyl group is present in place of one of the H atoms of the THT γ position adjacent to the sulfur atom (discussed below). The methyl group in the MTHT radical may occupy an axial or an equatorial site on the γ-carbon adjacent to the sulfur atom for the equilibrium analogous to that illustrated for THT in eq 1. However, at 77 K where this equilibrium is slow the axial methyl conformation in the MTHT radical must be predominant, since only then will the remaining γ-hydrogen atom be in the plane of the ring, and hence in an unfavorable position for coupling with the spin density on the adjacent sulfur atom. The sulfur atom bears about 25% of the spin density according to estimates made from the β proton coupling.[2,14] The axial γ-hydrogen atom is positioned in a nearly eclipsed conformation with the orbital on the sulfur atom bearing the spin density and so would be predicted to produce a larger splitting than the equatorial hydrogen atom. At room temperature where ring equilibrium is rapid, the γ coupling in THT should become a triplet of coupling constant approximately one-half that observed for the axial H atom in the frozen conformation, i.e., ~2.3 G. This structure was not resolved in the room temperature spectrum of the THT radical in adamantane, although the large 5.5 G line width for transitions not involving the exchanging β H atoms implied the existence of this unresolved coupling. A 2.2-G triplet splitting has been observed for the γ protons in this radical produced in aqueous solutions at room temperature.[14] An alternative explanation for the large γ-hydrogen atom coupling involving a "through space" interaction with the unpaired electron[16] is not supported by the data.

ESR Spectra of MTHT Radicals at 295 and 77 K. Like the THT solid solutions in adamantane, MTHT solutions γ irradiated at room temperature or γ irradiated at 77 K and

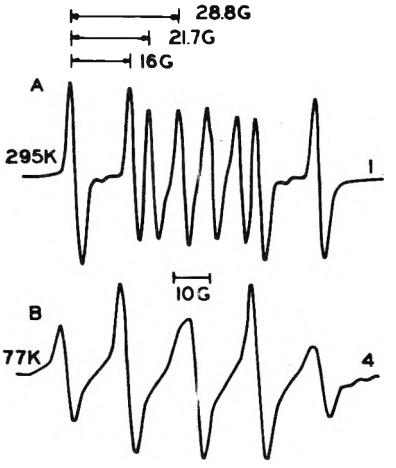

Figure 6. ESR spectra of adamantane–MTHT: (A) determined at 295 K following γ irradiation at 77 or 295 K; (B) determined at 77 K. The spectra change reversibly between (A) and (B) on temperature cycling. The coupling constants at 295 K are a_α = 16.0, a_{β_1} = 21.7, and a_{β_2} = 28.8 G. Dose, 5.6 × 10^{19} eV g^{-1}; microwave power, 0.2 mW; modulation amplitude, 0.4 G; gain setting × 10^{-3} given at right of each spectrum; recorder, 1 V.

warmed to room temperature give an ESR signal attributable only to solute radicals (Figure 6A). This signal changes reversibly on cooling to 77 K (Figure 6B), indicating a slowing down of the rate of pseudorotation of the conformational isomers. The room temperature spectrum which consists of eight lines of equal intensity is consistent with coupling to three unequivalent protons. The coupling constants are a_α = 16.2 G, a_{β_1} = 22.1 G, and a_{β_2} = 28.7 G at 303 K. The g factor is 2.0047. The spectrum is consistent with the secondary α radical:

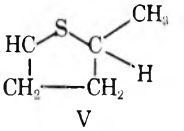

V

and there is no evidence for the presence of the tertiary α radical. The line width at 303 K of 2.5–2.6 G is much narrower than for the THT radical. The broad line width for the latter was attributable partly to unresolved hyperfine splitting due to the hydrogen atoms α to the sulfur in the γ position relative to the radical site. No such splitting is observed for MTHT radicals, from 77 to 303 K. As discussed above for the THT radical, this requires that the most stable (i.e., low temperature) conformation of the MTHT radical must be the axial methyl conformation. This is opposite to the usual preference displayed by substituted five- and six-membered ring compounds and some cyclic π radicals[16b] for the equatorial conformation indicating the significant influence which spin delocalization with the adjacent sulfur atom has on determining the most favored conformation in MTHT.

The line width for the MTHT radical spectrum at room temperature is due principally to dipolar interactions with hydrogen atoms on neighboring adamantane molecules. Some of the lines show additional broadening due to the β protons exchanging their positions upon ring flipping, analogous to that found in THT. Unlike the THT radical, however, the MTHT radical conformations are of unequal energy. At 77 K the lowest energy conformation exists in by far the largest relative amount. The ESR spectrum at 77 K consists of five lines of relative integrated intensities 1:2:2:2:1 (Figure 6B). This pattern is due to the three nonequivalent protons with

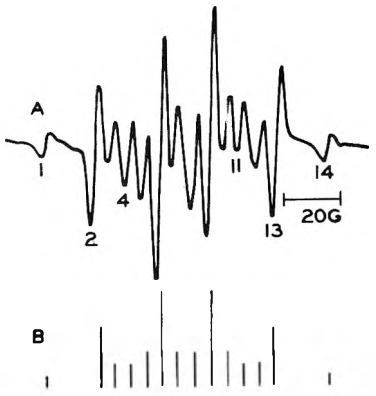

Figure 7. (A) ESR spectrum of a γ-irradiated adamantane–MTHF sample immediately following warm-up from 77 to 233 K. Dose at 77 K, 3.2 × 10^{19} eV g^{-1}; microwave power, 100 mW; modulation amplitude, 0.5 G; gain, 2500; recorder, 1 V. (B) Theoretical ESR spectrum of a 1:2 ratio of the tertiary to secondary α-MTHF radicals. The coupling constants used for the tertiary radical are $a(CH_3)$ = 18 G and $a(CH_2)$ = 24 G, and for the secondary radical are a_α = 12 G, a_{β_1} = 24 G, and a_{β_2} = 30 G. The ESR g values are assumed equal.

coupling constants $a_\alpha \simeq a_{\beta_1} \simeq 17$ G and $a_{\beta_2} \simeq 34$ G. No γ splitting is observed. The temperature dependence of the β-proton couplings from 303 to 77 K for MTHT radicals in adamantane is described in a later section and implies an activation energy for ring inversion of several kilocalories per mole.

ESR Spectra of MTHF Radicals and Radicals Produced During Their Decay. γ irradiation of adamantane containing MTHF at 77 K produces the adamantyl radical signal (Figure 3A). When the sample is warmed to 233 K and the spectrum is taken immediately, the signal of Figure 7A is observed, which is in close agreement with the predicted spectrum of Figure 7B for a 2:1 mixture of secondary to tertiary α-MTHF radicals having identical g values. The theoretical spectra of the two radicals are shown individually in Figure 8C and 8D, it being assumed that conformational exchange is rapid at the temperatures in question. The coupling constants noted in the figure legends are similar to those found for the α-THF radical.[17] If the sample is allowed to stand at 233 K for ~10 min or more following the conversion to MTHF radicals, or is warmed, changes in the spectrum occur which indicate that: (1) two MTHF radicals are present, one of which decays faster than the other; (2) at least two new radicals are generated in the decay of the MTHF radicals, during which there is also a decrease in total spin concentration. Figure 8A shows the spectrum recorded at 273 K, 10 min after rapid warming from 77 K at which time all of the more rapidly decaying MTHF radical (the tertiary α radical, see below) is gone. Figure 8B is the spectrum after nearly all the MTHF radicals had decayed, taken on a sample which warmed slowly after emptying the liquid nitrogen from the dewar. The rapid decay of both MTHF radicals (which, as shown in a later section, follows first-order kinetics) and the replacement by new radicals during their decay is in sharp contrast to the relatively slow second-order decay (also discussed below) of MTHT radicals, which occurs without concurrent formation of new radicals. The decay kinetics of THT radicals were not measured but it was observed that these radicals decay without the production of new radicals.

The predicted secondary α radical spectrum of Figure 8C agrees well with the spectrum of the slower decaying component of the Figure 7A spectrum, part of which is still present in the spectrum of Figure 8A. The g values for the two initial

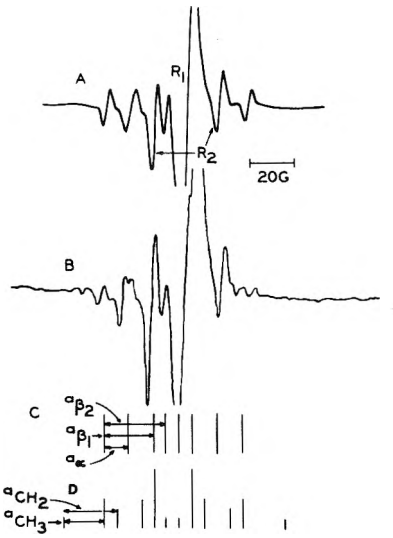

Figure 8. (A) ESR spectrum of a γ-irradiated adamantane–MTHF sample after complete decay of the outer pair of hyperfine lines (due to the tertiary α radical). Spectrum A was recorded at 273 K, 10 min after warming from 77 K. Two new radicals, R_1 and R_2, grow in as the original MTHF radicals decay. (B) ESR spectrum ~25 min after complete conversion of the adamantyl radicals to solute radicals during slow warm-up. Dose at 77 K, 3.2 × 10^{19} eV g^{-1}; modulation amplitude, 0.5 G; gain, 1600; recorder, 1 V; microwave power, 100 mW. (C) Theoretical spectrum of the secondary α-MTHF radical with a_α = 12 G, a_{β_1} = 24 G, and a_{β_2} = 30 G. (D) Theoretical spectrum of the tertiary α-MTHF radical with $a(CH_3)$ = 18 G and $a(CH_2)$ = 24 G.

MTHF radicals were nearly identical at 2.0040 ± 0.0003. R_1 and R_2 of Figure 8 indicate lines of the new radicals which grow as the original MTHF radicals decay. As discussed later, the intense signal of R_1, which continues to grow with continuing decay of the original radicals, is probably due to the 1-adamantyl radical, which may be produced by H abstraction from a bridgehead site by an alkyl-like radical which is formed when one of the original MTHF radicals undergoes ring opening. The R_1 signal is a singlet of line width of 6.5 G, in good agreement with the 6.6-G peak-to-peak width observed for the envelope of the hyperfine structure for the 1-adamantyl radical in solution.[18] The center of the R_1 spectrum, at g = 2.0009 ± 0.0003, is 3.7-G upfield from the center of the MTHF radical spectra, and ~9-G upfield from the center of the doublet spectrum of 20.7-G coupling (likely the 2-adamantyl radical) produced in γ-irradiated adamantane. A lower g value is expected for the 1-adamantyl radical than the 2-adamantyl radical since the former is presumably a σ-type radical and these are known to have low g values.[19] The R_2 signal, which represents a much lower concentration than R_1, may be from one or more radicals. The g values of both radicals R_1 and R_2 are lower than that of either MTHF radical. This is consistent with the suggestion to be discussed below that ring opening of the MTHF radicals occurs forming radicals in which the unpaired electron is no longer on an atom adjacent to an oxygen atom, thus decreasing the g value.

Decay of MTHT Radicals. The MTHT radicals produced on warm-up from 77 K to room temperature of a sample of γ-irradiated 2% MTHT in adamantane decay by second-order kinetics (Figure 9) as determined by ESR measurements using either the peak heights or double integrals of the ESR spectra of the type of Figure 6A. No new radicals are produced during the decay. The ESR measurements at 295 K were begun within 1 min of the start of warm-up from 77 K. At all γ doses studied (1.0 × 10^{19} to 5.6 × 10^{19} eV g^{-1}), the initial half-lives are in the range of 8.3–1.5 h. The rate constant was

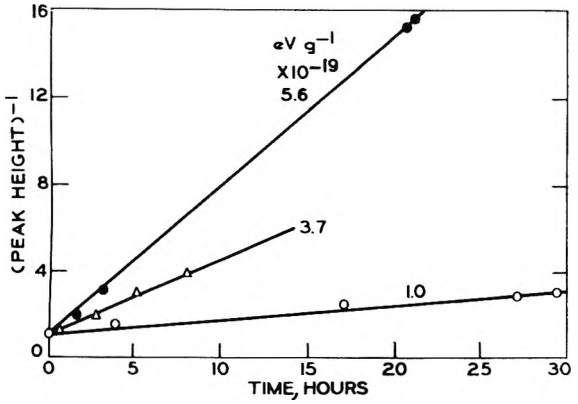

Figure 9. Second-order plots of the decay of MTHT radicals in adamantane at 295 K following γ irradiation to different doses at 77 K. Plots are normalized at time = 0.

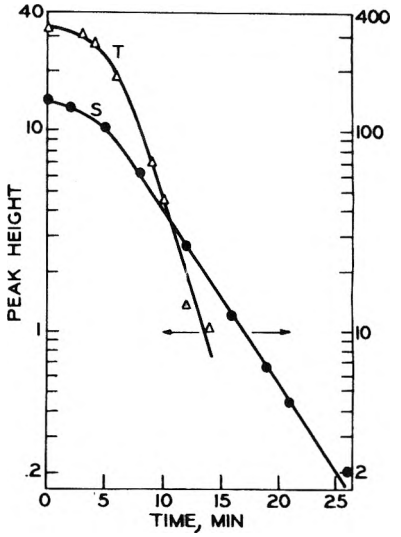

Figure 10. Decay of tertiary (T) and secondary (S) MTHF radicals in an adamantane–MTHF sample γ irradiated at 77 K and allowed to warm by emptying the liquid nitrogen from the dewar. Solute radicals are produced as the adamantyl radicals decay, and reach a maximum concentration shown at early times in this figure (~235 K) following which only decaying solute radicals are present. The major portion of the decay occurred at 245 ± 5 K. The radical concentration was monitored by ESR peak heights as discussed in the text.

~0.17 M^{-1} s^{-1}. For this calculation the initial concentration of MTHT radicals, $[R]_0$, has been estimated from the initial concentration of adamantyl radicals and the ~50% conversion of adamantyl radicals to solute radicals on warming (Figure 4).

Decay of MTHF Radicals. Data are available from a single but highly informative exploratory experiment on the decay rates of the two MTHF radicals produced by warm-up of γ-irradiated adamantane–MTHF solutions. The decay rate of the tertiary radical was monitored by the decrease in height of the unobscured outer peak of the spectrum of Figure 7A, while the relatively intense adjacent line was used to follow the secondary radical. Since the intensity of the latter line is made up of three degenerate substates from the tertiary radical to one from the secondary, the relative secondary radical concentration was obtained by subtracting three time the height of the outer peak (nondegenerate) from the height of the second peak. Upon complete decay of the faster decaying tertiary α radical, the peak height of the secondary radical from this composite peak was the same as the peak height of other nondegenerate hyperfine lines. This method avoided using lines from the interior part of the spectrum where overlapping of adjacent lines is serious.

The sample was allowed to warm slowly from 77 K in an ESR dewar from which the liquid nitrogen had been emptied. The solute radicals started to grow within a few minutes and reached their maximum concentration between 230 and 240 K. After complete conversion of the adamantyl radicals to solute radicals, the radicals decayed with first-order kinetics (Figure 10), with rate constants of 7.7×10^{-3} s^{-1} for the tertiary and 3.4×10^{-3} s^{-1} for the secondary. Although the exact temperature range within which the decays of Figure 10 occurred was not measured, it may be estimated with confidence that >50% of the decay represented by the straight line portions of the two decay curves occurred between 240 and 250 K and that the temperature of the sample at the 26 min point of Figure 10 was less, and perhaps much less, than 270 K.

The initial relative yield of the tertiary (T) and secondary (S) α MTHF radicals does not vary with different rates of warm-up following irradiation at 77 K. The mean relative yield of $[T] = (0.3 \pm 0.15)[S]$ was obtained from four separate measurements using two different sets of peak heights. The wide error limits (variation between extremes) reflect the somewhat different estimates of the relative yields given by the two methods. Considering the faster decay of the tertiary radical, this estimated initial relative yield is probably slightly low as a result of decay in the short time (~1 min) necessary for warm-up and scanning of the spectrum after warm-up.

Radicals Produced by Photolysis of MTHT in Adamantane. Exposure of samples of ~2% MTHT in adamantane at 300 K to 254-nm light (~80 mW cm^{-2}) in the center of a spiral Vycor low-pressure Hg lamp generated secondary α-MTHT radicals (with spectra identical with that of Figure 6A). MTHT absorbs at 254 nm while the absorption by adamantane is negligible. The concentration of radicals produced in a 2-min photolysis was the same as that produced when a sample which had received a γ dose of 1.6×10^{19} eV g^{-1} at 77 K was warmed to 300 K. Photolysis of gaseous[20a] and solid neat alkyl sulfides[20b] produces C–S bond rupture as the primary process. Thus primary C–H bond rupture on absorption of a photon by the MTHT in adamantane seems improbable. If C–S bond rupture occurs, the biradicals formed must rapidly abstract H from MTHT molecules upon diffusive encounters, or abstraction must occur through a sequence of reactions involving the adamantane. Either process would be too fast at 300 K for conventional ESR detection.

Decay of the radicals formed by photolysis of MTHT in adamantane does not follow a simple kinetic order. Second-order plots ($1/[R]$ vs. t) rise relatively rapidly at the onset and approach straight line character after ~70% decay. Presumably this reflects spatially nonhomogeneous radical production resulting from greater absorption of light near the surface of the semiopaque polycrystalline samples than in the interior.

Discussion

Radicals Produced in Pure Adamantane. At least six groups[11,21-25] have reported ESR spectra of radicals produced by x- or γ-ray irradiation of adamantane without added solutes. No two of the groups have found exactly the same spectra. Both the 1-adamantyl and 2-adamantyl radicals have been postulated as responsible for the observed signals. Only two groups have indicated the radiation dose used and one the microwave power. Only one has prepared the adamantane by sublimation under vacuum, as was done in the present work.

None has made observations on the effects of time and photolysis at 77 K on the radical spectra.

The paramagnetic species which may conceivably be produced by γ irradiation of adamantane are 1-adamantyl radical, 2-adamantyl radical, anion radicals, cation radicals, radicals produced by rupture of C–C bonds in adamantane or by subsequent isomerization of such radicals, trapped electrons, and radicals produced from impurities present before γ irradiation or produced by the irradiation.

The 1-adamantyl radical in solution displays a 6.6-G coupling to six equivalent β protons, with further splittings from the remaining protons resolved.[18] The envelope of these hyperfine splittings is a singlet of 6.6-G line width (ΔH_{pp}). In a polycrystalline sample an unresolved singlet of this line width can be expected since broadening due to dipolar interactions causes coalescence of neighboring hyperfine components. Little hyperfine anisotropy is expected for this radical since there are no α protons. The g anisotropy is also expected to be small. The 2-adamantyl radical would be expected to show a doublet splitting due to the single α proton. If the radical anion were formed, with the unpaired electron in the center of the adamantane cage, the electron might be expected to participate in electron exchange with the bonding electrons of the four bridgehead C–H bonds through interaction with the backsides of these orbitals, giving rise to a five-line spectrum. The radical cation can be visualized likewise as having the unpaired electron shared equally between the backsides of the four bridgehead C–H bonds. Such rear-orbital interactions are known to give unusually large long-range coupling.[16,18] Physically trapped electrons in hydrocarbon glasses produce an ESR singlet of 3–4-G line width.[5b] The expected nature of the spectra of the four radicals which might ensue from C–C bond rupture in γ-irradiated adamantane has been discussed;[2] they do not coincide with the observations reported here.

The most plausible assignment for the singlet of 28-G ΔH_{pp} and 80-G total width (Figures 2 and 3) observed at 77 K, and the poorly resolved doublet (a = 20.7 G) of the same width and g value to which it converts on warming, seems to be the 2-adamantyl radical, the doublet character being obscured at 77 K by line broadening.

It has been reported that at 77 K irradiated adamantane yields "a typical powder spectrum with peak-to-peak separation of ~43 G and a semiresolved doublet splitting",[11] an "unresolved broad singlet" [21b] and a broad singlet envelope ~80 G in breadth of ~25-G ΔH_{pp} with superimposed hyperfine components.[24] In the first work cited[11] the ΔH_{pp} is greater than that of Figures 2 and 3A, but is reported to narrow on warming with the doublet splitting becoming resolved with a_H^α = 20.5 G at 239 K. This 239 K spectrum is in close agreement in total width and line splitting with that of Figure 3E and has been assigned by the authors to the 2-adamantyl radical. The envelope of the spectrum of Hyfantis and Ling[24] at 77 K which they assign to the 1-adamantyl radical is very similar to Figures 2 and 3A save for the superimposed fine structure. The assignment appears questionable since the envelope of hyperfine lines for the 1-adamantyl radical has been shown to be a singlet of only 6.6-G line width.[18] We have observed a singlet of 6.6-G ΔH_{pp} (Figure 8A) in γ-irradiated adamantane containing MTHF where, as discussed in a later section, 1-adamantyl radicals appear to be formed by hydrogen abstraction by radicals resulting from MTHF radical decay. The spectrum of Figure 2 was obtained from adamantane samples which had received γ doses of 4.9×10^{19} or 1×10^{19} eV g^{-1} and were measured at a microwave power of 10^{-3} mW. The measurements of Hyfantis and Ling were made with a dose of ~10^{18} eV g^{-1} and an undesignated power. Figure 2 shows that the 28-G singlet (produced with a radiation yield of G = ~1.8) begins to saturate at low powers. At powers >10 mW the spectrum of a radical presumably due to a trace impurity obliterates the 28-G singlet. The evidence suggests that this may be the cyclohexyl radical formed by H abstraction from a small amount of solvent not removed during purification.

As far as we are aware, the thermal and photochemical changes at 77 K of radicals produced by γ irradiation of adamantane (Figure 3) have not previously been noted. We do not have a consistently satisfactory assignment for the five-line spectrum of Figure 3C. The radical anion of adamantane with the electron in the cage would give a five-line spectrum but could not be a conversion product of the 28-G singlet species if the latter is the 2-adamantyl radical, and could not convert to the doublet attributed to the 2-adamantyl radical on warming, as it is observed to do (Figure 3A–E). Further, the anion seems to be eliminated by the absence of bleaching by 633- and 365-nm light, in contrast to the bleaching of the trapped electron signal in organic glasses.[5] Although rupture of C–C bonds by 254-nm light might occur, this process seems to be ruled out since the spectral changes occur thermally at 77 K as well as photochemically. Further, if thermal rupture of the 2-adamantyl radical occurred at 77 K, it would not be plausible for the radical to re-form on warming. These evaluations suggest that perhaps the 28-G singlet observed at 77 K may not represent the same species as the doublet observed after warming, but we are not aware of a plausible alternative.

Selective Formation of α-MTHF and α-MTHT Radicals. γ irradiation of 2% solutions of MTHF or MTHT in adamantane yields adamantyl radicals with which solute molecules react when the samples are warmed to form exclusively α radicals. Both the secondary and tertiary α radicals are formed from MTHF and only the secondary from MTHT. The number of secondary α MTHF radicals is some 2 to 5 times the number of tertiary radicals, indicating that abstraction from MTHF at these two sites does not show high selectivity. Presumably the slightly lower bond energies of the α C–H bonds than the β C–H bonds and in the case of the MTHT of the secondary α than of the tertiary α are responsible for the selectivity. (The α C–H bond energy in THF is 92 ± 2 kcal mol^{-1} while the C–H bond energy in cyclopentane is 95 ± 1 kcal mol^{-1}.) The lower bond energy for the α-H atoms probably arises from the electron-donating influence of the adjacent heteroatom which stabilizes the resulting electron deficient radical center. Spin delocalization can account for the formation of both α radicals of MTHF and the single MTHT radical.[26] For MTHT only the secondary α radical forms, presumably because formation of the tertiary α radical is inhibited by the relatively greater electrostatic repulsion that would occur between the electron-rich methyl group and the slightly negative trigonal center (due to the approximate 25% spin delocalization from the S). Since spin delocalization in the α MTHF radical is considerably lower (12%), such repulsive interactions are of less importance, and so the directing effect of the methyl group is decreased. This is supported by the data which show the secondary radical to be favored by a minimum of two to one over the tertiary α MTHF radical (this lower limit would indicate a totally nonpreferential abstraction at the two α sites).

MTHT Conformational Equilibrium. The ESR spectra of both the THT and MTHT radicals are temperature dependent because of the temperature sensitive equilibrium

between the axial (A) and equatorial (B) conformations of the type indicated in eq 1. If the rate of exchange between the two forms is much faster than the difference in frequencies for the hyperfine interactions of the two β protons in their limiting conformations, then only a single average hyperfine coupling giving a triplet signal is found. If the rate is much slower than this difference, two distinct couplings occur and a pair of doublets results. The enthalpy and entropy differences of the two conformations of MTHT can be obtained from the available data, since the position of the hyperfine lines for exchanging hydrogen nuclei reflects the equilibrium ratio of the two conformations. The observed hyperfine splitting constant (hfsc) for a particular proton, a_{obsd}^{H}, is the time average of two limiting values a_E^H and a_A^H,[16b] hence the probability (f_e) of the radical existing in conformation E is

$$f_e = \frac{a_{obsd}^{H} - a_A^H}{a_E^H - a_A^H}$$

The equilibrium constant for the equatorial–axial equilibrium is then $K = f_a/f_e$, where $f_a = 1 - f_e$. The values for the hfsc, f_a, and K as a function of temperature are given in Table II. A plot of log K vs. $1/T$ shows a linear relationship from which ΔH and ΔS in the relationship $-RT \ln K = \Delta H - T\Delta S$ can be evaluated. The enthalpy and entropy differences between the equatorial and axial configurations of MTHT are $H_E - H_A = 1.7$ kcal mol^{-1} and $S_E - S_A = -4.2$ cal deg^{-1}. These are typical of the values for similar unsymmetrical cyclic radicals.[16b] The conformation with the methyl group axial is the more stable, and the predominant form at low temperatures in contrast to the majority of five- and six-membered cyclic molecules and some radicals.[16]

The activation energies for the conformational exchange in MTHT must be on the order of several kilocalories per mole, since even at room temperature (RT = 0.6 kcal mol^{-1}) the exchange is sufficiently slow that separate hfsc are observed for hydrogen nuclei in axial and equatorial sites. This is in qualitative agreement with the energy barrier to internal rotation about the C–S bond for the trigonal carbon in $\cdot CH_2SC(CH_3)_3$ (6.3 kcal mol^{-1}).[14] The spin delocalization between the trigonal carbon and sulfur accounts for the fairly large barrier. The barriers between the conformations of the symmetric radicals of cyclopentane (C_5H_9) and THF (α-C_4H_7O) in adamantane[3c] are 2.8 and 2.4 kcal mol^{-1}. These compare with 2.8 kcal mol^{-1} for the barriers in the stable molecules of cyclopentane[27] and THT[28] in the gas phase. It is plausible that the barriers for the A $\rightleftarrows$ E exchange in the MTHT molecule are similar to that for the THT molecule. However, it is not apparent that the barriers for the MTHT molecule and radical will be similar, since the spin delocalization in the radical can significantly affect the barrier height. Both a twist and an envelope (S at the apex) configuration, each having its own conformational equilibrium, can be formulated. However, the envelope configuration is unlikely for the MTHT radical, since the delocalization will favor a planar geometry between the trigonal carbon and sulfur. The barriers in cyclic radicals like THT and MTHT may then involve ring equilibrium between conformations of the twist configuration (see eq 1), which does not involve the loss of planarity at the sulfur atom. If there is a change from the envelope to the twist configuration in going from the molecule to the radical, this may account for the observed preference for the axial conformation of the MTHT radical at low temperatures.

Mechanism of Solute Radical Formation. Adamantyl radicals formed by γ irradiation at 77 K of adamantane containing a solute are completely converted to solute radicals in the time required to warm to room temperature and begin ESR measurement (~1–2 min). Because diffusion of adamantane is very slow (E_A for self-diffusion = 36 kcal mol^{-1}),[13] and because the decay of solute radicals is slow compared to the rate of radical formation, intermolecular H atom transfer from adamantane molecules to adamantyl radicals has been proposed[3a,11] to explain the rapid migration of radical centers to solute molecules where abstraction can occur giving the solute radical. The results of the present work do not require postulation of this mechanism. They are consistent with the conclusion that the solute radicals form when a diffusing solute molecule in the ~2% solution encounters a nonmigrating adamantyl radical. It may be assumed that the rate of diffusion of MTHT molecules is the same as that of MTHT radicals for which the rate constant (k) for combination at 295 K, reported in a previous section, is 0.17 M^{-1} s^{-1}. Assuming a high probability for reaction on each encounter of an MTHT molecule with an adamantyl radical (A·), the rate of solute radical formation may be estimated as $d[MTHT\cdot]/dt = k[A\cdot][MTHT] = 4 \times 10^{-5}$ M s^{-1} at 295 K for an A· concentration of 1.2×10^{-3} M and [MTHT] = 0.2 M. At this rate essentially all the MTHT radicals that could be formed by abstraction reactions by A· would be formed in the 1–2-min period between warming of an irradiated sample from 77 K to room temperature and the initiation of ESR measurement.

TABLE II: MTHT Radical Proton Coupling Constants[a] and Axial–Equatorial Equilibrium Constant as a Function of Temperature

Temp, K	1000/T	a_α	a_{β_1}	a_{β_2}	f_e[b]	K[c]
303	3.30	16.1$_5$	22.1	28.7	0.313	2.19
293	3.41	15.9$_5$	21.7	28.8	0.306	2.27
273	3.66	15.9	21.0	29.5	0.266	2.76
253	3.95	16.0	20.5	30.3	0.220	3.55
223	4.48	16.3	19.7	31.5	0.150	5.67
213	4.69	16.5$_5$	19.5	31.8	0.133	6.52
203	4.93	16.6	19.2	32.3	0.104	8.62
77	13.0	16.8	16.8	34.1	~0	

[a] In gauss. [b] $f_e = (a_{obsd}^H - a_A^H)/(a_E^H - a_A^H)$. [c] $K = f_a/f_e$, $f_e = 1 - f_a$.

Mechanism of Decay of MTHT and MTHF Radicals. The data of Figure 9, showing second-order decay of MTHT radicals in adamantane at 295 K, together with the observation that no new radicals grow during the decay, indicate that the radicals are removed by reaction with each other upon encounter by diffusion, the rate constant being 0.17 M^{-1} s^{-1}, as estimated in the Results section. Assuming reaction on every encounter, the diffusion coefficient (D) obtained from the relation $k = 3 \times 10^{-22}$ cm^3 molecule^{-1} s^{-1} $= 4\pi d2D$ is 2×10^{-16} cm^2 s^{-1}, if the diameter (d) of the radical is taken as 5 Å.

The first-order decays (Figure 10) of the secondary α-MTHF and tertiary α-MTHF radicals require either a unimolecular decomposition mechanism or a pseudo-first-order abstraction from the adamantane matrix molecules. It seems improbable, although not impossible, that the original MTHF radicals abstract from the bridgehead position of adamantane to give the 1-adamantyl radical believed to be responsible for the R_1 signal of Figure 8. If this occurs, the tertiary α-MTHF radicals abstract more readily than the secondary α-MTHF radicals, and in contrast to MTHT radicals which do not abstract.

The most plausible mechanism to explain the first-order decay, the two different rate constants, the growth of the 1-adamantyl radical and much smaller growth of a second rad-

ical (R_2) (Figure 8) seems to involve unimolecular ring opening by each of the two MTHF radicals:

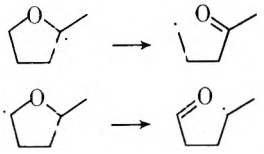

(2)

(3)

followed by abstraction of H from adamantane by the alkyl-like radical to give the 1-adamantyl radical. An analogous ring opening has been observed for the radical of the cyclic ether 1,3-dioxolane.[29] Radical R_2 of Figure 8 which has an overall width of ~30 G may be similar to the radical on the right side of (2) or of (3) above but with the radical center on the C atom adjacent to the carbonyl group. Such radicals formed in adamantane by other methods have spectral widths similar to R_2.[30]

The MTHF Radical in γ-Irradiated MTHF Glass. The ESR spectrum of radicals in γ-irradiated MTHF glass (Figure 11) has been assigned to the tertiary α radical.[4a,b] The spectra of the α-MTHF radicals in adamantane (Figures 7 and 8) support this assignment. The 104-G width of the spectrum from the glass precludes the possibility that the secondary radical (66 G width at 273 K) can be responsible for the entire spectrum. Evidence that the secondary α radical is not formed in the glass is given by the total lack of similarity between the radical spectrum from the glass, and the spectrum of a 3:1 ratio of secondary to tertiary α-MTHF radicals, produced by cooling the sample of Figure 7 to 77 K after sufficient decay of the tertiary radical to produce this ratio. The theoretical spectrum of the tertiary α radical at 77 K, where ring conformational equilibration is slow, is shown in Figure 11B. At this temperature the β proton couplings becomes nonequivalent since pseudorotation is slow, although the sum of the β couplings should remain nearly constant with temperature.

$$a(\beta)_{\text{isotropic}} \simeq \tfrac{1}{2}[a(\beta_1) + a(\beta_2)]_{77\text{ K}} = 24\text{ G}$$

The theoretical spectrum in Figure 11 fits the experimental spectrum when the β couplings are 16 and 33 G, while the more freely rotating methyl group retains its room temperature coupling of 18 G. The seven groups of lines in the theoretical spectrum have relative integrated intensities of 1:4:7:8:7:4:1. The large peak height of the central line in the experimental spectrum is expected for the choice of couplings used in the theoretical spectrum, which shows a closer spacing of the component hyperfine lines in the central line group than for other groups of lines. The intensities and couplings agree well with the experimental spectrum.

Simulated spectra based on high temperature coupling constants, assuming no temperature dependence of the β proton couplings, have led to the conclusion that neither secondary nor tertiary radicals alone nor their mixture can account for the ESR spectrum of γ-irradiated MTHF glass.[25] However, the temperature dependence of the β proton couplings in MTHT glass (Figure 6, where the slowness of radical decay allows study of the temperature dependence of the couplings) indicates that such dependence must be considered in MTHF. When it, and the additional evidence given above, are taken into account, the results strongly support assignment of the spectrum to the tertiary radical.

Unique Features of Adamantane as a Reaction Medium. Polycrystalline adamantane ($C_{10}H_{16}$) melts at 268 °C when warmed in a sealed tube but sublimes readily in the air at room temperature; its melting point contrasts with that of *n*-decane ($C_{10}H_{22}$) (−30 °C) and that of the smaller symmetric molecule

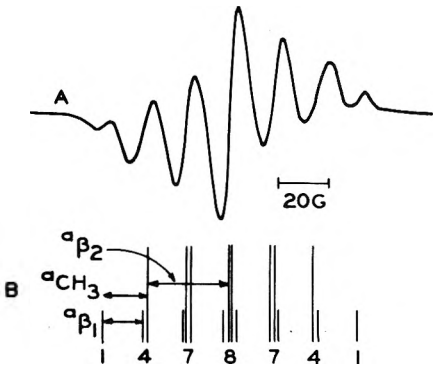

Figure 11. (A) ESR spectrum of MTHF glass γ irradiated at 77 K and exhaustively bleached with light >400 nm to remove trapped electrons: dose, 2.3 × 10^{19} eV g^{-1}; microwave power, 0.20 mW; modulation amplitude, 0.5 G; gain, 2400; recorder, 1 V. (B) Theoretical ESR spectrum of the tertiary α radical of MTHF at low temperature where ring equilibrium is slow. The coupling constants used are $a(CH_3)$ = 18 G, $a(H_{\beta_1})$ = 16 G, and $a(H_{\beta_2})$ = 33 G. The theoretical relative intensities are shown below the groups of lines.

neopentane (C_5H_{12}, −20 °C). The calculated density changes from 1.18 g cm^{-3} for the tetragonal crystalline form below the phase transition temperature of 208 K to 1.08 for the disordered cubic form at 295 K[10] and contrasts with the 0.73 g cm^{-3} density of liquid *n*-decane at 295 K.

The second-order decay of MTHT radicals in adamantane occurs readily at 295 K (0.5 of the melting point) whereas readily measurable decay of matrix radicals in their parent crystals in general does not occur below ~0.8 of the melting point. The MTHT radical decay at 295 K occurs much faster than the decay of 3-methylpentyl radicals in glassy 3MP at 77 K[12] (k = 0.17 M^{-1} s^{-1} as compared to 2.4 × 10^{-6} M^{-1} s^{-1}) even though the density of the latter is only 0.85 g cm^{-3} as compared to the 1.08 g cm^{-3} for adamantane at 295 K. The decay of matrix radicals in polycrystalline *n*-decane ($d \simeq 0.86$) at 77 K is undetectable over many hours.[31]

Acknowledgments. We wish to thank L. Kevan and A. C. Ling for providing us with a copy of their recent results[25] prior to publication and to thank S. F. Nelsen for helpful discussions.

References and Notes

(1) This work has been supported in part by the U.S. Atomic Energy Commission under Contract No. AT(11-1)-1715 and by the W. F. Vilas Trust of the University of Wisconsin.
(2) Additional details of the work are given in the Ph.D. Thesis of G. C. Dismukes, University of Wisconsin—Madison, 1975.
(3) For examples and references see: (a) M. E. Manzuk, D. L. Winters, G. J. Hyfantis, and A. C. Ling, *Int. J. Radiat. Biol.*, **26**, 51 (1974); (b) D. E. Wood and R. E. Lloyd, *J. Chem. Phys.*, **53**, 3932 (1970); (c) A. P. Kuleshov and V. I. Trofimov, *Zh. Struk. Khim.*, **14**, 926 (1973).
(4) (a) D. R. Smith and J. J. Pieroni, *Can. J. Chem.*, **43**, 876 (1965); (b) F. S. Dainton and G. A. Salmon, *J. Chem. Soc. A*, **285**, 319 (1965); (c) D. P. Lin and L. Kevan, *J. Chem. Phys.*, **55**, 2629 (1971).
(5) For examples and references see: (a) J. E. Willard, *Int. J. Radiat. Phys. Chem.*, **6**, 325 (1974); (b) J. E. Willard, *J. Phys. Chem.*, **79**, 2966 (1975).
(6) J. K. Lawson, W. K. Easley, and W. S. Wagner, *Org. Syn.*, **36**, 89 (1963).
(7) (a) J. v. Braun, *Ber. Dtsch. Chem. Ges.*, **43**, 3223 (1911); (b) R. Bordwell, *J. Org. Chem.*, **23**, 636 (1958).
(8) Spectral data on selected compounds from the catalogs of the American Petroleum Institute, Project 44.
(9) J. G. Castle, D. W. Feldman, D. G. Klemens, and R. A. Weeks, *Phys. Rev. B*, **130**, 577 (1963).
(10) C. E. Nordman and D. L. Schmitkons, *Acta Crystallogr.*, **18**, 764 (1965).
(11) J. R. Ferrell, G. R. Holdren, R. V. Lloyd, and D. E. Wood, *Chem. Phys. Lett.*, **9**, 343 (1971).
(12) M. A. Neiss and J. E. Willard, *J. Phys. Chem.*, 79, 783 (1975).
(13) H. A. Resing, N. T. Corke, and J. N. Sherwood, *Phys. Rev. Lett.*, **20**, 1227 (1968).
(14) I. Biddles, A. Hudson, and J. T. Wiffen, *Tetrahedron*, **28**, 867 (1972).

(15) J. Q. Adams, *J. Am. Chem. Soc.*, **92**, 4535 (1970).
(16) (a) G. A. Russell, *Science*, **161**, 423 (1968); (b) G. A. Russell, G. R. Underwood, and D. C. Lini, *J. Am. Chem. Soc.*, **89**, 6636 (1967).
(17) J. K. S. Wan, *Adv. Photochem.*, **9**, 1 (1974).
(18) P. J. Krusic, T. A. Rettig, and P. v. R. Schleyer, *J. Am. Chem. Soc.*, **94**, 995 (1972).
(19) P. J. Krusic and T. A. Rettig, *J. Am. Chem. Soc.*, **92**, 721 (1970).
(20) (a) J. G. Calvert and J. N. Pitts, "Photochemistry", Wiley, New York, N.Y., 1966; (b) P. S. H. Bolman, I. SaFarik, D. A. Stiles, W. J. R. Tyerman, and O. P. Strausz, *Can. J. Chem.*, **48**, 3872 (1970).
(21) (a) D. R. Gee, L. Fabes, and J. K. S. Wan, *Chem. Phys. Lett.*, **7**, 311 (1970); (b) W. G. Filby and K. Gunther, *Chem. Phys. Lett.*, **14**, 1440 (1972); (c) L. Bonnazola and R. Marx, *Chem. Phys. Lett.*, **8**, 413 (1971).
(22) R. V. Lloyd and M. T. Rogers, *Chem. Phys. Lett.*, **17**, 428 (1972).
(23) G. J. Hyfantis and A. C. Ling, *Can. J. Chem.*, **52**, 1206 (1974).
(24) G. J. Hyfantis and A. C. Ling, *Chem. Phys. Lett.*, **24**, 335 (1974).
(25) A. C. Ling and L. Kevan, *J. Phys. Chem.*, **80**, 592 (1976).
(26) For a discussion of the spin delocalization in MTHT and MTHF and references, see ref 2.
(27) K. S. Pitzer and W. E. Donath, *J. Am. Chem. Soc.*, **81**, 3213 (1959).
(28) W. N. Hubbard, H. L. Finke, D. W. Scott, J. P. McCullough, C. Katz, M. E. Gross, J. F. Messerly, R. E. Pennington, and G. Wadington, *J. Am. Chem. Soc.*, **74**, 6025 (1952).
(29) V. I. Trofimov and I. I. Chkeidze, *Dokl. Akad. Nauk, SSSR*, **198**, 354 (1971). English translation p 411.
(30) D. M. Camaioni, H. F. Walter, J. E. Jordan, and D. W. Pratt, *J. Am. Chem. Soc.*, **95**, 7978 (1973).
(31) H. Fenrick and J. E. Willard, unpublished results.

Spectroscopic Study on Aggregate Ion Radicals of Naphthalene and Pyrene in γ-Irradiated Alkane Glasses

Akira Kira,* Masashi Imamura,

The Institute of Physical and Chemical Research, Wako, Saitama 351, Japan

and Tadamasa Shida

Department of Chemistry, Faculty of Science, Kyoto University, Kyoto 606, Japan *(Received December 19, 1975)*

Publication costs assisted by The Institute of Physical and Chemical Research

Rigid solutions of naphthalene or pyrene in mixed alkane matrices at 77 K were γ irradiated and optical measurements were carried out for samples under controlled warming. Two new species, unrelaxed dimer cations and probably tetramer cations of the solutes, were found. It is presumed that the unrelaxed dimer cation is produced upon the capture of migrating positive holes in the alkane matrix by the preexisting neutral dimer molecule of the solutes and holds the conformation of the neutral dimer. Thus, the unrelaxed dimer cation differs from the known dimer cation whose conformation is relaxed in a thermal equilibrium. The absorption maxima of characteristic bands of the unrelaxed dimer cations of naphthalene and pyrene are situated at about 2100 and 1600 nm, respectively. The tetramer cation is formed upon softening of the irradiated sample by a reaction between the relaxed dimer cation and the neutral dimer molecules. The tetramer cation is characterized by the absorption at 1450 nm for naphthalene and the one at 1900 nm for pyrene. Although explicit spectral evidence was not obtained, the formation of dimer anions was also indicated by the concentration dependence of the formation of the monomer anions.

Introduction

Hamill and co-workers pioneered the use of organic matrices at 77 K for the spectroscopic study of ionic processes induced by γ irradiation.[1] The rigidity of the frozen solution ensures the preservation of reactive ionic intermediates and enables the spectroscopic measurement of otherwise elusive species. Ionic processes occurring in matrices such as methyltetrahydrofuran and *sec*-butyl chloride appear to be amazingly simple because in most cases absorption spectra in the near-ir through near-uv region are exclusively attributable to the monomer anions and cations of solute molecules.[2,3] Irradiation of a number of organic compounds in these matrices has provided comprehensive spectral data on ion radicals.[3,4]

The rigidity, however, prevents the study of the dynamic behavior of the ion radicals. Thus, controlled warming of irradiated rigid solution and softer matrices has been used for the study of diffusion-induced reactions of the ion radicals and the effect of rigidity on their optical spectra.[5-9] Badger and Brocklehurst measured the spectra of dimer cations resulting from the diffusion in soft or softened matrices.[5,6] Bühler and Funk have recently reported the dependence of the charge resonance energy on rigidity.[7]

However, it has been repeatedly experienced that warming the sample leads to cracking which interferes with the measurement of subtle changes in the spectrum. Using properly chosen matrices which do not suffer cracking we have studied the dynamic aspect of frozen intermediates. In this paper we present the results for naphthalene and pyrene in matrices of mixed alkanes. It was found that the matrices provide new species, a transient "unrelaxed" dimer cation and a tetramer cation.

Experimental Section

Methylcyclohexane (MCH) and 3-methylpentane (MP) from Tokyo Kasei Co. were distilled and passed through a silica gel column. Zone-refined naphthalene from Tokyo Kasei Co. was used as received. Pyrene from the same source was purified chromatographically. The aromatic hydrocarbons were dissolved in a 3:1 (by volume) mixture of MCH and MP.

The solution in a 1.5–1.7-mm thick Suprasil cell was degassed, unless otherwise stated, and the frozen solution was γ irradiated with a dose rate of 3×10^{18} eV/g min^{-1} at 77 K. The optical change induced by irradiation and by subsequent warming was measured using a Cary 14 spectrophotometer. The warming was effected by raising the cell above the level of the liquid nitrogen for a limited period. The sample was intermittently cooled to 77 K to record the spectrum change at each step of warming. The glassy sample was not cracked by the warming and cooling procedure.

Results

Naphthalene. The absorption spectra immediately after irradiation of 15 and 49 mM naphthalene in the MCH–MP matrix are shown by bold curves in Figures 1a and 1b. The peaks and shoulders marked with S^+ and S^- in the region 600–900 nm coincide with the known bands of monomeric cations and anions of naphthalene.[3] Addition of triethylamine, a known positive hole scavenger, at 1–3 vol % removed the peaks denoted with S^+. Nitromethane (1%) and *sec*-butyl chloride (1%), which are known to scavenge electrons, suppressed the absorption indicated by S^-. The effect of the scavengers confirms the assignment of the peaks. Besides these bands the spectra in bold curves exhibit a hitherto unknown peak at about 2100 nm.

The optical density for the S^+ and S^- bands decreased with an increase in the solute concentration as seen in Figure 1. Figure 2a shows the initial optical densities at 700 nm (for S^+) and at 850 nm (for S^-) as a function of solute concentration. Since the absorption at 700 nm comprises a considerable amount of the S^- absorption, corrections were made to extract the net S^+ absorption by referring to the spectra of S^- at each concentration.[10] The broken curve in Figure 2a corresponds to the corrected S^+ absorption. Figure 2a demonstrates that the intensity of the 2100-nm band also increases with solute concentration. Careful measurements revealed that the wavelength of the absorption maximum gradually shifted from 2050 to 2150 nm as the concentration was varied from 15 to 77 mM. The 2100-nm band disappeared when triethylamine (1–3%) was added, and was not removed by addition of nitromethane or *sec*-butyl chloride (1%). The scavenger effect indicates that the 2100-nm band is due to a cationic species. In the softer 3MP glass the corresponding band appeared at 1900 nm. It is emphasized that, although the band is associated with a cationic species, it was not observed either in butyl chloride or in a Freon mixture which is the established matrix for the production of a monomer cation of the solute.[3] Addition of more than 20 vol % of butyl chloride and analogous compounds to alkane matrices also eliminated this band. Thus, the appearance of the cationic species absorbing at about 1900 nm to about 2150 nm is peculiar to the alkane matrices.

Warming the irradiated sample in the alkane matrices caused the spectral change shown by broken and dotted curves in Figure 1. The spectra in the broken curve were recorded when the intensity of the 1040-nm band attained its maximum. Likewise, the dotted curves correspond to the step of the maximum development of the 1450-nm band. The bands at 1040 and 580 nm have been assigned to the naphthalene dimer cation, S_2^+ by previous workers.[5,6c] The 1450-nm band accompanying a weak band near 570 nm was first observed in the present work. Figure 3 shows detailed changes in the spectrum. The numbers indicate consecutive warming steps. The 2100-nm band assigned to the new cationic species shifts gradually toward shorter wavelengths as warming proceeds.

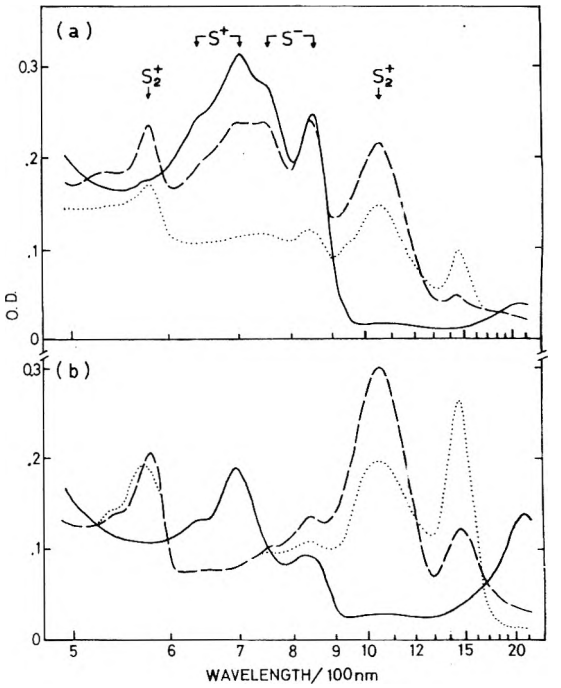

Figure 1. Absorption spectra in 15 (a) and 49 mM (b) naphthalene solutions in the MCH–MP matrix irradiated with a dose of 9×10^{19} eV/g: immediately after irradiation (bold curves), after warming by which the intensity at 1040 nm was maximized (broken curves), and after further warming which maximized the absorption at 1450 nm (dotted curves).

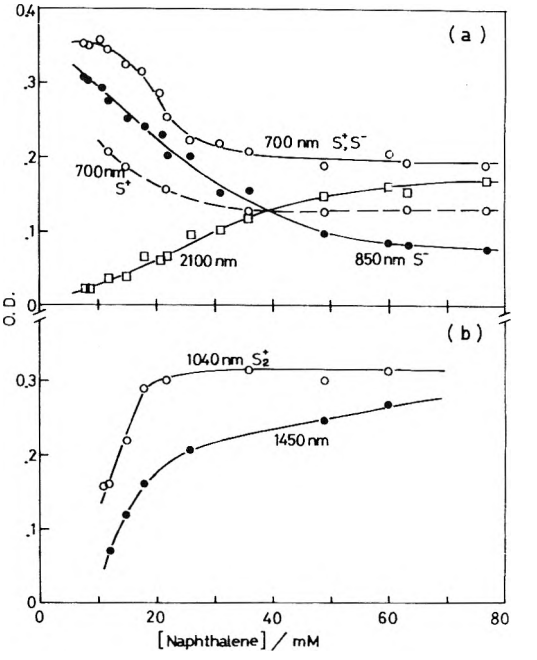

Figure 2. The concentration dependence of the relative yield of ionic species produced by irradiation (a) and by subsequent warming (b). Naphthalene solutions in the MCH–MP matrix were irradiated with a dose of 9×10^{19} eV/g. See text for the two curves for 700 nm in (a).

Curves 3 and 4 resemble the spectrum measured for a solution in 3MP at 77 K which is slightly softer than the solution in MCH–MP at the same temperature. The intensity at 1040 nm increases with the concomitant shift of the band initially at 2150 nm. The 1450-nm band begins to increase at step 5. After step 6 the absorption at 1040 nm diminishes but absorption at 1450 nm still grows. Exessive warming removes all the

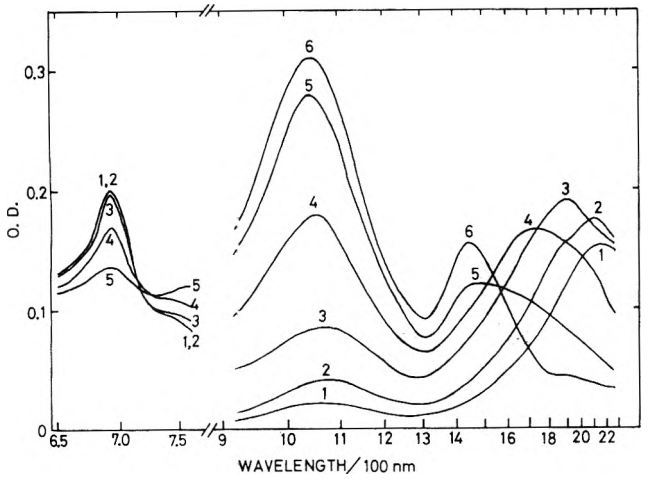

Figure 3. The detailed thermal change in a 60 mM naphthalene solution in the MCH–MP matrix irradiated with a dose of 9 × 10^{19} eV/g. The number indicates the warming consecutive steps.

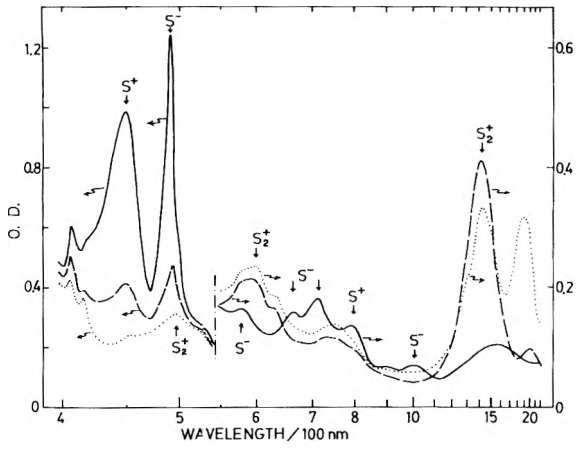

Figure 4. The absorption spectra in a 39 mM pyrene solution in the MCH–MP matrix irradiated with a dose of 4.5 × 10^{19} eV/g : immediately after irradiation (bold curve), after warming (broken curve); and after further warming (dotted curve).

bands including the most persisting one at 1450 nm. The decrease in the absorption of S^+ at 700 nm and the increase in the absorption of S_2^+ at 1040 nm are not complementary as shown in Figure 3. The maximum optical densities at 1040 and 1450 nm attained by warming are shown as a function of the solute concentration in Figure 2b. The correction for the overlap of the bands was not made.

Warming the irradiated solutions in the alkane matrices induced luminescence. Weak greenish yellow emission was observed at an early stage of warming, and was followed by whitish blue emission. The emission terminated with the disappearance of the 1450-nm band. When the irradiated solution was photobleached at 77 K with light longer than λ 480 nm, the anionic bands were removed, but cationic bands remained with their intensity reduced. On warming the photobleached solution the remaining cationic band eventually changed to the 1450-nm band. The appearance of the 1450-nm band was not affected by addition of 1% nitromethane. Thus, it appears that any anionic species is not involved in the formation of the species giving the 1450-nm band.

Pyrene. Experiments for pyrene solutions in MCH–MP were carried out without deaeration since a preliminary test showed that dissolved air did not affect the intrinsic feature of the results.

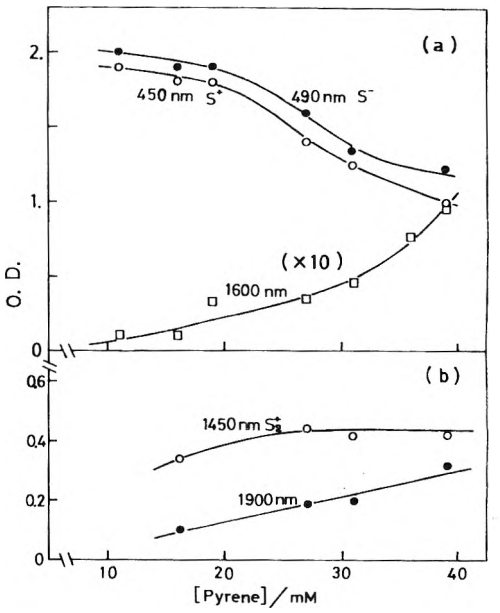

Figure 5. The concentration dependence of the relative yield of ionic species produced by irradiation (a) and by subsequent warming (b). Pyrene solutions in the MCH–MP matrix were irradiated with a dose of 4.5 × 10^{19} eV/g.

As in the naphthalene solutions, pyrene solutions immediately after irradiation also exhibited a hitherto unknown band at 1600 nm in addition to the known bands of monomer ions[3] as shown by the solid curve in Figure 4. Subtle spectral changes (corresponding to the shift of the 2100-nm band in Figure 3) of the 1600-nm band on warming could not be recorded for pyrene because of the overlap of the bands of S_2^+ with a peak at 1420 nm. The spectral change induced by warming is analogous to that for naphthalene. The 1600-nm band and the bands of S^+ were first replaced by the band of the dimer cation at 1420 nm[6c] shown by a broken curve, which was substituted upon further warming by a new band at 1900 nm in the dotted curve in Figure 4. Figure 5 shows the concentration dependence of the yields of the pyrene ions and two new species absorbing at 1600 and 1900 nm.

Discussion

The spectral change observed in the present experiments are summarized as follows:

Naphthalene

$$S \longrightarrow \begin{matrix} S^+(700\text{ nm}) \longrightarrow S_2^+(1040\text{ nm}) \longrightarrow B(1450\text{ nm}) \\ A(2100\text{ nm}) \longrightarrow \\ S^-(850\text{ nm}) \end{matrix}$$

Pyrene

$$S \longrightarrow \begin{matrix} S^+(450\text{ nm}) \longrightarrow S_2^+(1420\text{ nm}) \longrightarrow B(1900\text{ nm}) \\ A(1600\text{ nm}) \longrightarrow \\ S^-(490\text{ nm}) \end{matrix}$$

Symbol A denotes the new species appearing immediately after irradiation. Symbol B represents another new species appearing in a later stage of controlled warming. Both A and B are cationic, and most likely related to aggregate ions of the solute molecule as suggested by the concentration dependence of their formation. So far, only dimer cations have been studied in some detail. Badger and Brocklehurst employed

an isopentane–butyl chloride matrix to find new absorption bands attributable to the dimer cation of benzene, naphthalene, and others.[5,6] Pulse radiolytic studies have proved the formation of dimer cations in equilibrium with the monomer cation.[11,12]

The result that species A and B were found only in the alkane matrices suggests that formation of A and B depends critically on the properties of the matrix. Alkane matrices are generally known to freeze solute molecules partly as aggregates composed of two or more molecules. Ferguson first found the dimerization of perylene in isopentane–MCH glass,[13] and similar examples have been reported.[13–16] Such dimerization has not been observed in matrices other than alkanes.

If both monomeric and dimeric solute molecules are frozen in the alkane matrices, the positive hole in the matrix, M^+, produced by irradiation will be competitively scavenged by the monomer and dimer which are in equilibrium as shown by eq 4.

$$M \xrightarrow{\gamma} M^+ + e^- \quad (1)$$

$$M^+ + S \rightarrow S^+ \quad (2)$$

$$M^+ + (S_2) \rightarrow (S_2)^+ \quad (3)$$

$$S + S \rightleftharpoons (S_2) \quad (4)$$

The parenthesized dimer cation in reaction 3 indicates that its conformation is the same as that of the frozen neutral dimer molecule, (S_2). The ion, $(S_2)^+$, may not be equal to the relaxed dimer cation, S_2^+, which is in the most favorable conformation for the ion in a thermal equilibrium.

If the mechanism represented by reactions 2–4 is correct, the ratio of the yield of $(S_2)^+$ to that of S^+ will increase with solute concentration. The observed behavior of species A is consistently accounted for by assigning it to the unrelaxed dimer cation, $(S_2)^+$; it is formed initially on irradiation, favored in concentrated solutions, and different from the known relaxed dimer cation absorbing at 1040 nm for naphthalene and at 1420 nm for pyrene. The thermally induced gradual shift of the band assigned to A is considered to correspond to the following sequence:

$$(S_2)^+ \rightarrow \text{intermediate conformations} \rightarrow S_2^+ \quad (5)$$

All dimer cations thus far reported in the literature are regarded as the relaxed ones. Figure 3 shows that in spite of the increase in the (relaxed) dimer cation at an early stage of warming the monomer cation does not decrease appreciably until the stage of curve 3. This result is understood by eq 5, i.e., the unrelaxed dimer cation supplies the relaxed dimer cation. The relaxed dimer cation can also be produced from the monomer cation by

$$S^+ + S \rightarrow S_2^+ \quad (6)$$

Reaction 6 is the usual process for the formation of a dimer cation in rigid solutions and fluid solutions in other solvents,[5,6,11,12] but reaction 5 prevails in concentrated solutions in the alkane matrices where the unrelaxed dimer cation predominates. The slight shift of the 2100-nm band for naphthalene with concentration might be due to the involvement of aggregates (S_n), with n larger than 2, which produce ions $(S_n)^+$.

Species B appears on prolonged warming at the expense of the relaxed dimer cation. The yield of species B relative to that of the relaxed dimer cation increased with solute concentration as shown in Figures 2b and 5b. The result indicates that species B results from a reaction of the dimer cation with neutral solute molecules. Taking into account the fact that in concentrated solutions equilibrium 4 shifts to the right in favor of the dimeric solute molecules, we consider that species B may be a tetramer cation formed by

$$S_2^+ + (S_2) \rightarrow S_4^+ \quad (7)$$

Our unpublished results show that in matrices of alkyl halides or Freon mixtures neither the unrelaxed dimer cation nor the proposed tetramer cation is produced. The appearance of these two cations is, therefore, specific to the alkane matrices. The prerequisite for reaction 7, i.e., the existence of neutral dimer molecules, is also peculiar to the alkane matrix. The whitish blue emission observed at later stages of warming is considered to be due to charge neutralization which competes with reactions 6 and 7.

In the low concentration region the yield of the monomer anion of electron-scavenging solutes increases with the increase of the concentration as Gallivan and Hamill showed for biphenyl in 3MP matrix.[17] However, in the present study of concentrated solutions a reverse concentration dependence was found as seen in Figures 2a and 5a. The reactions

$$e^- + S \rightarrow S^- \quad (8)$$

$$e^- + (S_2) \rightarrow (S_2)^- \quad (9)$$

similar to 2 and 3 for cations, together with equilibrium 4, account for the concentration dependence of the yield of the monomer anion in the high concentration region. However, no definite band attributable to either $(S_2)^-$ or S_2^- presumably formed by warming was detected in the region 320–2200 nm even when the cationic bands were removed by triethylamine in order to record the subtle change in the anion spectrum. Attempts to produce dimer anions of aromatic hydrocarbons have not been successful except for the anthracene dimer anion derived from the anthracene photodimer.[8] The present results suggest that the dimer anions of naphthlene and pyrene are produced by reaction 9 but do not absorb appreciably in the above described region. The charge resonance bands[5,18,19] of the dimer anions may be located at wavelengths longer than 2200 nm and beyond the limit of our measurements.

References and Notes

(1) W. H. Hamill, "Radical Ions", E. T. Kaiser and L. Kevan, Ed., Interscience, New York, N.Y., 1968.
(2) In this report a cation and an anion radical will be called simply a cation and an anion, respectively.
(3) T. Shida and S. Iwata, *J. Am. Chem. Soc.*, **95**, 3473 (1973).
(4) T. Shida and S. Iwata, *J. Phys. Chem.*, **75**, 2591 (1971); T. Shida, S. Iwata, and M. Imamura, *ibid.*, **78**, 741 (1974).
(5) B. Badger, B. Brocklehurst, and R. D. Russel, *Chem. Phys. Lett.*, **1**, 122 (1967).
(6) (a) B. Badger and B. Brocklehurst, *Trans. Faraday Soc.*, **65**, 2576, (1969); (b) **65**, 2582 (1969); (c) **65**, 2588 (1969).
(7) R. E. Bühler and W. Funk, *J. Phys. Chem.*, **79**, 2098 (1975).
(8) T. Shida and S. Iwata, *J. Chem. Phys.*, **56**, 2858 (1972).
(9) T. Shida, Y. Takahashi, H. Hatano, and M. Imamura *Chem. Phys. Lett.*, **33**, 491 (1975).
(10) The spectral shape of S^- of naphthalene changes slightly with the naphthalene concentration.
(11) A. Kira, S. Arai, and M. Imamura, *J. Phys. Chem.*, **76**, 1119 (1972); *J. Chem. Phys.*, **54**, 4890 (1971); S. Arai, A. Kira, and M. Imamura, *ibid.*, **56**, 1777 (1972).
(12) M. A. J. Rodgers, *Chem. Phys. Lett.*, **9**, 107 (1971); *J. Chem. Soc., Faraday Trans. 1*, **68**, 1278 (1972).
(13) J. Ferguson, *J. Chem. Phys.*, **44**, 2677 (1966); E. A. Chandross, J. Ferguson, and E. G. Macrae, *ibid.*, **45**, 3546 (1966).
(14) J. A. Katul and A. B. Zahlan, *J. Chem. Phys.*, **47**, 1012 (1967).
(15) D. N. de Vries, R. P. H. Pettschnick, and G. J. Hoytink, *J. Chem. Phys.*, **54**, 2723 (1971).
(16) F. Dupuy, M. Martinaud, G. Nouchi, and J-M. Turlet, *J. Chim. Phys.*, **69**, 614, 617 (1972); G. Fournie, F. Dupuy, M. Martinaud, G. Nouchi, and J-M. Turlet, *Chem. Phys. Lett.*, **16**, 332 (1972).
(17) J. B. Gallivan and W. H. Hamill, *J. Chem. Phys.*, **44**, 1279 (1966).
(18) B. Badger and B. Brocklehurst, *Nature (London)*, **219**, 263 (1968).
(19) A. Ishitani and S. Nagakura, *Mol. Phys.*, **12**, 1 (1967).

A Qualitative Failure of Electrostatic Theories of Salting In. The Enthalpy of Interaction of Glycine and Sodium Chloride in Water

John W. Larson* and Darrell G. Morrison

Department of Chemistry, Marshall University, Huntington, West Virginia 25701 *(Received May 29, 1975; Revised Manuscript Received March 15, 1976)*

The enthalpy of interaction between NaCl and glycine in an aqueous medium has been determined calorimetrically. For the reactions NaCl(ag) = NaCl(ideal, 1 M Gly) or Gly(aq) = Gly(ideal, 1 M NaCl) the enthalpy has been determined as $\Delta H_s^\circ = -211$ cal/mol. This value differs qualitatively from the value predicted from Kirkwood's and others theories, even though these same theories have given a relatively good quantitative description of the free energy of interaction.

Introduction

Amino acids, peptides, and proteins are extremely polar, even when their net charge is zero. These molecules exist predominately as zwitter or dipolar ions at their isoelectric point. The interactions between these important molecules and ions have therefore been extensively studied, both experimentally and theoretically.[1-3]

Experimentally, the focus of the work has been on the free energy of interaction. The majority of this work involves the influence of an electrolyte on the solubility of amino acids, peptides, or proteins, that is, salting in (or out).[2,4] Activity coefficients of dilute aqueous solutions of amino acid–electrolye mixtures have also been determined[2,5,6] from which the free energy of interaction can be calculated.

A variety of theories have been proposed to account for these experimental results,[3,7] the most widely applied being those of Kirkwood. These theories have enjoyed considerable quantitative success in that, for example, the dipole moments of simple amino acids and peptides calculated via them are in good agreement with those obtained from either dielectric constant measurements or structural consideration.[3]

In this paper, we report the experimental measurement of the enthalpy of interaction between NaCl and glycine. Originally our intention was to use this experimental method as an alternative way of obtaining information about solvated dipolar ions via Kirkwood's theories. The results reported here however indicate that these theories do *not* account for the enthalpy of interaction, either quantitatively or qualtitatively. The eventual explanation of this failure should prove to be of considerable interest and importance.

Experimental Section

The calorimeter used has been described previously.[8] Several modifications have been made. A 100-l. water bath is used instead of the aluminum block bath. The thermometer circuit consists of two 1000-ohm thermistors connected in two arms of a transposed Maier bridge.[9] A Leeds and Northrup K-4 potentiometer and dc null detector were used to measure the bridge potentials. Temperature differences could be measured to ±0.000 05 °C under normal operating conditions. All calorimetric data were obtained with 300 ml of solution in the dewar at 25.0 ± 0.1 °C. Electrical calibration of the calorimeter preceded and succeeded each run.

Certified ACS sodium chloride was obtained from Fisher Scientific Co. When used as a part of the solvent system in the first set of runs, it was used without further purification. In the second set of runs, when used as the solute it was recrystallized from water.

Glycine (ammonia free) was obtained from Eastman Kodak Co. and used without further purification. Samples from two different lots were used and gave identical results.

Solutions of $NaCl{\cdot}16.69H_2O$ and $Gly{\cdot}18.86H_2O$ were made up by weight. Samples of about 6 g were taken from these solutions and weighed accurately into thin walled glass bulbs of 6 to 12 ml capacity. Sample entry was effected by breaking the bulb.

Results

Method 1. Enthalpies of "solution" of $Gly{\cdot}18.86H_2O$ and H_2O into 0, 0.25, 0.5, 0.75, and 1 M NaCl were determined calorimetrically. These results are reported in Table I and correspond to

$$Gly \cdot 18.86H_2O = Gly^{\pm}(a \text{ M NaCl}) + 18.86 \cdot H_2O(a \text{ M NaCl}) \quad \Delta H_1(a) \quad (1)$$

and

$$18.86 \cdot H_2O = 18.86 \cdot H_2O(a \text{ M NaCl}) \quad \Delta H_2(a) \quad (2)$$

The uncertainties reported are average deviations.

The enthalpy of dilution of glycine from the final concentration of our measurements (0.05 M) to infinite dilution is small (+5 cal/mol). We could not measure this accurately and therefore corrected the measured heats by using the literature values for the heats of dilution in water,[10] assuming these are not appreciably affected by the concentration of NaCl. Because of the small amount of H_2O used as a solute compared to the amount of solution, we apply no correction to $\Delta H_2(a)$. The enthalpies for reactions 1 and 2 at infinite dilution, $\Delta H_1^*(a)$ and $\Delta H_2^*(a)$, are reported in Table II.

The enthalpy of transfer of glycine, $\Delta H_3^*(a)$, from water to a NaCl solution

$$Gly^{\pm}(\infty, \text{aq}) = Gly^{\pm}(\infty, a \text{ M NaCl}) \quad (3)$$

may be calculated by the equation

$$\Delta H_3^*(a) = \Delta H_1^*(a) - \Delta H_2^*(a) - \Delta H_1^*(0) + \Delta H_2^*(0) \quad (4)$$

These values are reported in Table II. Finally, we define an enthalpy, ΔH_5°, as the limit of $H_3^*(a)/a$ as a approaches 0. This is the value of the enthalpy of the reaction

$$Gly(\infty, \text{aq}) = Gly(\infty, \text{ideal 1 M NaCl}) \quad (5)$$

TABLE I: Enthalpies of Solution of Gly·18.86H_2O

a M NaCl	No. of runs	Final Gly, M	$\Delta H_1(a)$, cal/mol	No. of runs	$\Delta H_2(a)$, cal/mol
0	3	0.048	+188 ± 3		0
0.25	2	0.051	+134 ± 2	3	−1 ± 0.5
0.5	2	0.046	+86 ± 1	2	+8 ± 1
0.75	2	0.046	+46 ± 1	2	+28 ± 1
1.0	2	0.049	+25 ± 1	2	+57 ± 2

TABLE II: Enthalpy of Interaction (Method 1)

a	$\Delta H_1^*(a)$, cal/mol	$\Delta H_2^*(2)$, cal/mol	$\Delta H_3^*(a)$, cal/mol	$\Delta H_3^*(a)/a$, cal/mol
0	+192	0		
0.25	+138	−1	−53	−212
0.5	+90	+8	−110	−220
0.75	+50	+28	−170	−227
1.0	+29	+57	−220	−220

TABLE III: Enthalpies of Solution of NaCl·16.69H_2O

a M Gly	No. of runs	Final NaCl, M	$\Delta H_6(a)$, cal/mol	No. of runs	$\Delta H_7(2)$, cal/mol
0	3	0.057	+412 ± 4		0
0.25	2	0.052	+361 ± 2	2	−0.2 ± 0.5
0.50	3	0.052	+315 ± 2	2	−2 ± 1
1.0	3	0.046	+260 ± 5	3	+18 ± 2

TABLE IV: Enthalpy of Interaction (Method 2)

a	$\Delta H_6^*(a)$	$\Delta H_7^*(a)$	$\Delta H_8^*(a)$	$\Delta H_{11}^*(a)$	$(\Delta H_8^* - \Delta H_{11}^*)/a$
0	+338	0			
0.25	+289	−0.2	−49	2	−204
0.50	+243	−2	−93	4	−194
1.0	+183	+18	−173	9	−182

It is directly related to the temperature derivative of the interaction coefficient, k_s, as determined by either isopiestic vapor pressure measurements, freezing point depression data, or approximately by salting in coefficients.

Linear extrapolation of our data gives a value of $\Delta H_5° = -212 \pm 10$ cal/mol.

Method 2. Enthalpies of "solution" of NaCl·16.69H_2O into 0, 0.25, 0.5, and 1.0 M glycine were determined. Equation analogous to eq 1–5 may be written as

$$NaCl \cdot 16.69H_2O = NaCl(a \text{ M Gly}) + 16.69H_2O(a \text{ M Gly}) \quad (6)$$

$$16.69H_2O = 16.69H_2O(a \text{ M Gly}) \quad (7)$$

$$NaCl(\infty, aq) = NaCl(\infty, a \text{ M Gly}) \quad (8)$$

$$\Delta H_8^*(a) = \Delta H_6^*(a) - \Delta H_7^*(a) - \Delta H_6^*(0) + \Delta H_7^*(0) \quad (9)$$

$$NaCl(\infty, aq) = NaCl(\infty, \text{ideal 1 M Gly}) \quad (10)$$

The results reported in Tables III and IV were calculated in a manner similar to that in method 1. The heat of dilution of NaCl from the final concentration of our measurements (0.05 M) at infinite dilution is not small (75 cal/mol in H_2O) and could be appreciably affected by the glycine. Using the Debye–Hückel theory and the temperature dependence of the dielectric constant of aqueous glycine solutions,[11] we calculate that the heats of dilution of NaCl in the glycine solutions are within 5% of those in aqueous solution. Heats of dilution of aqueous NaCl solutions[12] were therefore used for all solution.

In method 2, the intermolecular proton transfer reaction

$$2GlyH = GlyH_2^+ + Gly^- \quad (11)$$

must be considered. Using the acid ionization constants of glycine,[1] the enthalpies of ionization,[13] and estimated activity coefficients, a straightforward calculation leads to the result that in 1 M Gly, the introduction of 0.05 M NaCl causes a shift from 0.019% ionic glycine to 0.024%. Because of the large amount of glycine present and the large ΔH_{11}, this small change results in ΔH_6 about 9 cal larger than if reaction 11 had not occurred. This effect is subtracted from ΔH_8 in determining ΔH_{10}.

A value of $H_{10} = -210 \pm 10$ cal/mol is obtained.

Accuracy. $\Delta H_1^*(0)$ and $\Delta H_6^*(0)$ are in excellent agreement with the literature values[10,11] of 192 and 334 cal/mol, respectively.

ΔH_5 and ΔH_{10} should be equal to each other by the Gibbs–Duhem equation and are within experimental error. The enthalpy of interaction corresponding to either reaction 5 or 10 is $\Delta H_s = -211 \pm 10$ cal/mol. No previous determination of this quantity has been reported.

The interaction coefficient, k_s, has been determined at 0 and 25 °C.[2,6] It is related to the thermodynamics of reactions 5 and 10 by the relationships

$$\Delta G_s° = -2.303RTk_s \quad (12)$$

$$\Delta G_s° = \Delta H_s° - T\Delta S_s° \quad (13)$$

$$\Delta H_s° = -2.303RT_1T_2\Delta k_s/\Delta T \quad (14)$$

Use of eq 14 (the integral form of the van't Hoff equation assuming $\Delta C_p = 0$) allows calculation of a value of $\Delta H_s = -2330$ cal/mol from the interaction coefficient data. It should be noted however that the uncertainty in this quantity is large and that there is a very large concentration dependence as indicated by a calculated value of $\Delta H_3(1) = -370$ cal/mol using the same data.

Thermochemical Calculations. The interaction coefficient reported by Schrier and Robinson is used in conjunction with our enthalpy and eq 12 and 13 to obtain the experimental quantities reported in Table V.

Discussion

From purely electrostatic considerations, Kirkwood has derived the equation

$$k_s = \frac{2\pi z^2 e^2}{2303DkT\mathbf{a}}\left(\frac{3\mu^2}{2DkT} - \alpha(\rho)\bar{V}\right) \quad (15)$$

Assuming the same parameters as Schrier and Robinson (μ = 13.5 D, $\bar{V}$ = 51 cm^3, **a** = 4.2 Å, $\alpha(\rho)$ = 1.29) and D = 78.54 and d ln D/dT = 4.579 × 10^{-3},[14] values of k_s, $\Delta G_s°$, $\Delta H_s°$, and $\Delta S_s°$ are calculated using eq 15 and eq 12–14. These results are included in Table V.

Similar results are obtained with the Debye–McAulay theory[7]

$$k_s = \left(\frac{ze}{D}\right)^2 \frac{\delta}{\mathbf{a}kT} \quad (16)$$

that forms the basis of many more elaborate theories. In calculating the values reported in Table V, the dielectric incre-

TABLE V: Thermodynamics of Interaction between Sodium Chloride and Glycine

	k_s	$\Delta G_s°$, cal/mol	$\Delta H_s°$, cal/mol	$\Delta S_s°$, cal mol^{-1} deg^{-1}
Exptl	0.127	−173	−211	−0.13
Kirkwood	0.156	−214	+195	+1.38
Debye–McAulay	0.218	−295	−30 to +330	+1.81 to +0.8

ment, δ, was taken as 22.7,[11,15] $d\delta/dT = 0.052$[15] to 0.14,[11] and **a** = 4.2 Å.

Even though these theories account rather well for the free energy of interaction, neither theory even qualitatively accounts for the enthalpy of interaction. Although one would not expect good agreement in a complex system, a qualitative breakdown in the results calculated for the system studied in this work is surprising.

A resolution of this anomaly is not readily apparent. For example, an additional term has been introduced in eq 15 by Schrier and Robinson to account for the salting out of the nonpolar portion of the nonelectrolyte (in the case of glycine it is just the CH_2 group). Assuming the contributions to this term are additive, a value for the enthalpy associated with this term can be estimated from literature values for the heat of solution of HCl in aqueous methanol,[16] ethanol,[16] and ethylene glycol[17] or NaCl in aqueous ethanol[15] and hydrogen peroxide.[18] The values obtained for the enthalpy of interaction between these electrolytes and the CH_2 group are +203 and +153 cal/mol, respectively. Thus applying this "correction" would result in an even larger discrepancy.

More experimental data on similar systems are needed before an explanation of this anomaly can be offered.

Acknowledgments. The authors wish to thank the Marshall University Foundation for financial support.

References and Notes

(1) J. T. Edsall and J. Wyman, "Biophysical Chemistry", Vol. 1, Academic Press, New York, N.Y., 1958.
(2) E. J. Cohn and J. T. Edsall, "Proteins, Amino Acids and Peptides", Reinhold, New York, N.Y., 1943.
(3) J. G. Kirkwood, E. J. Cohn, and J. T. Edsall, in ref 2; J. G. Kirkwood, *J. Chem. Phys.*, **2**, 351 (1934); *Chem. Rev.*, **19**, 275 (1936).
(4) E. J. Cohn, *Chem. Rev.*, **19**, 241 (1936).
(5) G. Scatchard and S. S. Prentiss, *J. Biol. Chem.*, **246**, 2870 (1971).
(6) E. E. Schrier and R. A. Robinson, *J. Biol. Chem.*, **246**, 2870 (1971).
(7) P. Debye and J. McAulay, *Phys. Z.*, **26**, 22 (1925).
(8) R. N. Goldberg and L. G. Hepler, *J. Phys. Chem.*, **72**, 4654 (1968).
(9) W. F. O'Hara, C. H. Wu, and L. G. Hepler, *J. Chem. Educ.*, **38**, 512 (1961).
(10) D. D. Wagman, W. H. Evans, V. B. Parker, I. Halow, S. M. Bailey, and R. H. Schuum, *Natl. Bur. Stand. Techn. Note* **No. 270-3** (1968).
(11) F. E. Linquist and C. L. A. Schmidt, *C. R. Trav. Lab. Carlsberg*, **22**, 307 (1938).
(12) V. B. Parker, *Natl. Stand. Ref. Data Ser., Natl. Bur. Stand.*, **No. 2** (1965).
(13) J. W. Larson and L. G. Hepler, "Heats and Entropies of Ionization" in "Solute-Solvent Interactions", C. D. Ritchie and J. F. Coetzee, Ed., Marcel Dekker, New York, N.Y., 1969.
(14) H. S. Harned and B. B. Owen, "The Physical Chemistry of Electrolytic Solutions", Reinhold, New York, N.Y., 1958.
(15) J. T. Edsall and J. Wyman, Jr., *J. Am. Chem. Soc.*, **57**, 1964 (1935).
(16) G. Bertrand, F. Millero, C. Wu, and L. Hepler, *J. Phys. Chem.*, **70**, 699 (1966).
(17) J. H. Stern and J. M. Nobilione, *J. Phys. Chem.*, **72**, 3937 (1968).
(18) J. H. Stern and W. R. Bottenberg, *J. Phys. Chem.*, **75**, 2229 (1971).

Metal Ion Association in Alcohol Solutions. 7. Neodymium Nitrate in Water and Aqueous Methanol

Herbert B. Silber* and John Fowler

Division of Earth and Physical Sciences, The University of Texas at San Antonio, San Antonio, Texas 78285 and Department of Chemistry, University of Maryland Baltimore Country, Baltimore, Maryland 21228 *(Received November 25, 1974; Revised Manuscript Received September 17, 1975)*

Publication costs assisted by the Petroleum Research Fund

Ultrasonic absorption measurements on 0.200 M $Nd(NO_3)_3$ solutions as a function of water composition indicate the existence of at least two relaxations. The results are interpreted in terms of an equilibrium between two forms of inner-sphere complexes in aqueous methanol. The extension of these measurements to aqueous solution confirms the existence of both inner- and outer-sphere complexes in water. The rate constant for the formation of the inner-sphere $NdNO^{2+}$ complex in water at 25 °C is $(1.5 \pm 0.2) \times 10^8$ s^{-1}.

We have applied the ultrasonic relaxation technique as a spectroscopic and kinetic probe to examine cation interactions with solvent and ligand molecules in aqueous methanol solutions.[1-5] A problem of particular interest has been that of the environment surrounding lanthanide cations, since different coordination number species have been postulated for the light and heavy rare earths, coupled to a region between Nd and Dy where an equilibrium between the two forms of solvated cations has been used to explain experimental ob-

* Address correspondence to this author at the Division of Earth and Physical Sciences, The University of Texas at San Antonio, San Antonio, Tex. 78285.

servations.[6] Because of the relatively large volume change observed for the formation of inner-sphere complexes in lanthanide systems, the ultrasonic relaxation technique easily discriminates between inner- and outer-sphere ion pairs in solution. By switching solvents from water to aqueous methanol the concentrations of both types of complexes are increased and any coordination number change which is induced upon complexation would be enhanced and would be observable as an increase in the excess absorption maximum, μ_{max}, which is proportional to the concentrations of reacting species times the square of the volume change upon reaction.

In an earlier ultrasonic relaxation study in water utilizing the rare earth nitrates, an abnormally high μ_{max} was observed for outer-sphere complexation with neodymium relative to the heavy lanthanides, and this was attributed a solvation number change equilibrium reaction.[7] The kinetic data were interpreted in terms of the multistep complexation mechanism:[8]

$$\underset{\text{step I}}{Ln^{3+}(aq) + NO_3^-(aq) = Ln^{3+}(H_2O)_yNO_3^-} \underset{\text{step II}}{= Ln^{3+}(H_2O)_xNO_3^-} \underset{\text{step III}}{= LnNO_3^{2+}(aq)} \quad (1)$$

Step I represents the diffusion-controlled formation of an outer-sphere complex and the rate constant for this step can be evaluated by the Debye–Smoluchowski[9] and the Eigen[10] equations. Solvent is lost from the anion inner solvation shell to form a second outer-sphere complex in step II. Step III, the slow step, involves the loss of solvent from the cation solvation shell followed by cation–ligand bond formation. The relaxation corresponding to step I is expected to occur near 500 MHz and has not been detected in any lanthanide system. Therefore, the first two steps of reaction 1 are generally combined:

$$\underset{\text{step 12}}{Ln^{3+}(aq) + NO_3^-(aq) \underset{k_{21}}{\overset{k_{12}}{\rightleftharpoons}} Ln^{3+}(H_2O)_xNO_3^-} \underset{\text{step III}}{\overset{k_{34}}{\underset{k_{43}}{\rightleftharpoons}} LnNO_3^{2+}(aq)} \quad (2)$$

For all of the cations studied (Nd, Gd, Dy, and Er) the results were interpreted in terms of both inner- and outer-sphere ion pairs even for those solutions where the existence of a high-frequency relaxation attributable to outer-sphere complexes was ambiguous. These solutions were composed of $Ln(NO_3)_3$ and excess nitrate added in the form of $NaNO_3$. This analysis, in terms of two types of complexes present, is consistent with the observations of optical spectroscopic measurements,[11,12] ^{17}O NMR data,[13] ^1H NMR data,[14] and ultrasonic measurements on stoichiometric concentrations of the rare earth nitrate salts in water.[15-17] This investigation on $Nd(NO_3)_3$ in aqueous methanol was undertaken in an effort to determine if the unusual high frequency relaxation could be characterized, and in addition to provide a comparison for different rare earth nitrates in aqueous methanol.

Experimental Section

The stoichiometry of the neodymium nitrate (American Potash and Chemical Corp.) was established to be $Nd(NO_3)_3 \cdot 4.7H_2O$ by ion exchange.[18] Stock solutions were made in methanol and water by weight. The methanol was distilled from a solution of methanol plus magnesium metal. The concentrations of all solutions were 0.200 M $Nd(NO_3)_3$ for the spectroscopic study as a function of water mole fraction, X_{H_2O}. The kinetic investigations were carried out with different salt concentrations in a solvent system containing 50% water by final volume, corresponding to $X_{H_2O} = 0.68$. All experimental temperatures were at 25 °C. All calculations were carried out on a Wang 700 programmable calculator.

The ultrasonic relaxation apparatus and technique employed were similar to those described earlier.[7] For a system undergoing chemical relaxation, the measured sound absorption, α/f^2, fits a standard curve defined by

$$\alpha/f^2 = B + \sum_i \left[\frac{A_i}{1 + (f/f_{R_i})^2}\right] \quad (3)$$

where f is the frequency, f_{R_i} is the relaxation frequency of each independent chemical relaxation step, A_i is the amplitude of each relaxation, and B is the experimental background characteristic of the solvent medium. The difference between the solution absorbance and that of the solvent is described in terms of the excess absorbance, μ, defined as:

$$\mu = (\alpha/f^2 - B)fc \quad (4)$$

where c is the sound velocity in the solution.

Results

An excess absorption occurs within the frequency range of 10–190 MHz for the 0.200 M $Nd(NO_3)_3$ solutions in water and in aqueous methanol.[19] The absorption data can be calculated in terms of either a single or a double relaxation process as shown in Table I. For 0.200 M Nd(III) solutions the calculated single relaxation values of B increase with increasing water content to a maximum of 50.2×10^{-17} Np cm^{-1} s^2 at $X_{H_2O} = 0.48$ and then decrease to 27.5×10^{-17} Np cm^{-1} s^2 in water. In 50% aqueous methanol solutions, the calculated single relaxation values of B increase with increasing concentration to 80.9×10^{-17} Np cm^{-1} s^2 for a 0.50 M salt solution. In aqueous solution B is known to be between 21.5 and 22.4×10^{-17} Np cm^{-1} s^2 from high frequency measurements on lanthanide salts.[20] For aqueous methanol alone the observed solvent background is $(25 \pm 2) \times 10^{-17}$ Np cm^{-1} s^2, a result which has also been obtained when $NaClO_4$ is added.[1,21] As in aqueous solution and in the previous papers in this series, the existence of an abnormally high B value indicates that at least one additional relaxation process is present within the experimental frequency range. Therefore, we believe that the data calculated in terms of a double relaxation computer program are the correct interpretation.

The two relaxations can be identified with the two reaction steps in reaction 2, analogous to the results in water for the nitrates[7,15,16] and to other lanthanide salt systems in aqueous methanol.[1-5] The high frequency relaxation corresponds to the formation of the outer-sphere complex and the low frequency one to the formation of the inner-sphere $NdNO_3^{2+}$ complex. Figure 1 shows typical data for $Nd(NO_3)_3$ in aqueous alcohol. After resolution into two relaxations, the $Nd(NO_3)_3$ solutions possess a systematic deviation of the experimental data at frequencies above 110 MHz, a feature not characteristic of any of our earlier aqueous methanol systems.[1-5] One interpretation of this result is that the difference corresponds to the start of a third relaxation appearing at high frequency. Although measurements at much higher frequencies are necessary to confirm the true existence of a third relaxation, its presence is certainly consistent with the observations on plus-two metal ion complexation systems in water.[22,23]

The excess absorption maximum, μ_{max}, is defined as:

$$2\mu_{max} = f_{R_i}A_ic \quad (5)$$

TABLE I: Relaxation Data at 25 °C for 0.200 M $Nd(NO_3)_3$ in Aqueous Methanol

A. Single Relaxation Calculation

X_{H_2O}	A^a	f_R	B^a
0.03	503.9 ± 32.3	9.7 ± 0.5	39.5 ± 1.1
0.06	460.0 ± 29.0	11.5 ± 0.7	37.8 ± 1.7
0.20	753.1 ± 36.1	10.4 ± 0.4	42.2 ± 1.2
0.35	577.1 ± 22.0	13.3 ± 0.5	45.5 ± 1.8
0.48	367.9 ± 13.6	18.0 ± 0.8	50.2 ± 2.2
0.59	283.2 ± 6.7	24.9 ± 0.9	48.4 ± 2.0
0.68	254.0 ± 5.9	31.2 ± 1.3	39.9 ± 3.0
0.83	241.8 ± 3.8	37.6 ± 1.2	34.2 ± 2.2
0.95	198.6 ± 2.2	52.5 ± 1.3	27.5 ± 1.9
1.00	169.9 ± 1.2	59.1 ± 1.3	27.5 ± 2.2

B. Double Relaxation Calculation[b]

X_{H_2O}	A_{12}^a	$f_{R_{12}}$, MHz	A_{III}^a	$f_{R_{III}}$, MHz	$\mu_{max_{12}}{}^c$	$\mu_{max_{III}}{}^c$
0.03	22.0 ± 2.6	150.5 ± 28.3	582.1 ± 49.9	8.4 ± 0.6	18.3 ± 5.6	26.9 ± 4.2
0.06	18.1 ± 4.9	167.8 ± 81.4	484.4 ± 41.2	10.7 ± 1.0	17.2 ± 13.0	29.3 ± 5.1
0.20	31.6 ± 3.0	123.0 ± 14.7	883.7 ± 45.1	8.8 ± 0.4	24.1 ± 5.2	47.9 ± 4.6
0.35	31.1 ± 5.0	162.3 ± 41.0	608.2 ± 27.5	12.2 ± 0.7	32.3 ± 13.4	47.3 ± 4.8
0.48	65.1 ± 5.5	98.9 ± 7.8	419.3 ± 18.1	12.4 ± 0.8	44.4 ± 7.3	35.8 ± 3.8
0.59	68.1 ± 5.6	100.6 ± 6.8	274.0 ± 4.7	17.9 ± 0.8	50.8 ± 7.6	36.4 ± 2.3
0.68	121.6 ± 12.6	64.3 ± 4.1	207.5 ± 8.6	14.8 ± 1.9	60.1 ± 10.1	23.6 ± 4.0
0.83	141.2 ± 24.8	58.8 ± 4.9	134.9 ± 18.3	19.4 ± 3.8	65.6 ± 17.0	20.7 ± 6.9
0.95	158.3 ± 18.3	65.4 ± 3.6	58.2 ± 15.2	22.4 ± 6.7	79.9 ± 13.8	10.1 ± 5.6
1.00	152.5 ± 7.2	70.0 ± 2.0	36.8 ± 4.4	16.9 ± 5.8	79.9 ± 6.1	4.7 ± 2.2

[a] Units, 10^{17} Np cm^{-1} s^2. [b] $B = 25.0 \times 10^{-17}$ Np cm^{-1} s^2 except in the solutions with $X_{H_2O} = 0.95$ and greater where $B = 21.7 \times 10^{-17}$ Np cm^{-1} s^2. [c] Units, 10^4 Np.

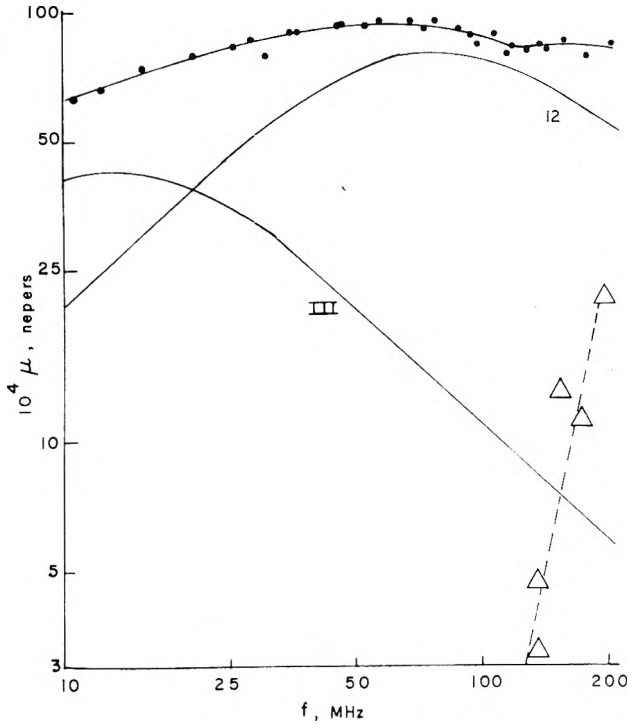

Figure 1. The excess absorption for 0.300 M $Nd(NO_3)_3$ in aqueous methanol. The triangles represent the difference between the measured and calculated absorption assuming only two relaxations are present, indicating the possible existence of a third relaxation.

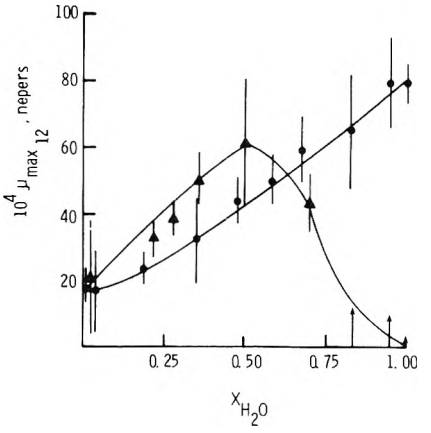

Figure 2. The excess absorption maxima corresponding to outer-sphere ion pair formation in aqueous methanol solutions of erbium and neodymium nitrates. The vertical arrows at high water mole fractions for erbium are an estimate because the relaxation amplitude is too low to be resolved by our relaxation program: (▲) 0.22 M $Er(NO_3)_3$; (●) 0.200 M $Nd(NO_3)_3$.

The variation in μ_{max} with water mole fraction is shown in Figures 2 and 3 for the high and low frequency relaxations, respectively. The data for $Er(NO_3)_3$ in aqueous methanol are also plotted in the figures. The analysis of these two figures will be used to explain the behavior of the rare earth nitrates in water and aqueous methanol.

The relaxation data for different concentration $Nd(NO_3)_3$ solutions in 50% aqueous methanol, shown in Table II, indicate that the relaxation frequency errors are larger than the variation of f_R with concentration. This difficulty is partially caused by the closeness of both the high and low relaxation frequencies (approximately 70 and 15 MHz). To obtain a successful separation usually requires that the two frequencies be separated by at least a decade, a condition which was fulfilled in the other aqueous methanol studies.[2,3] Furthermore, systematic errors are present in this study due to the possible

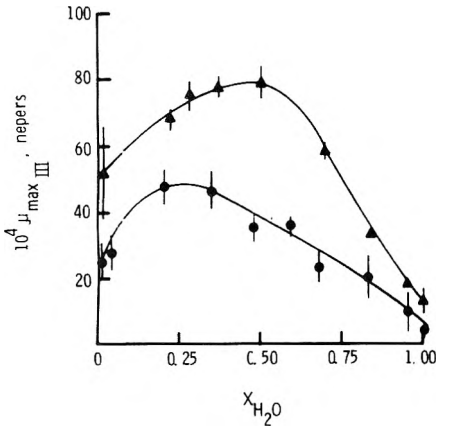

Figure 3. The excess absorption maxima corresponding to inner-sphere ion pair formation in aqueous methanol solutions of erbium and neodymium nitrates: (▲) 0.22 M $Er(NO_3)_3$; (●) 0.200 M $Nd(NO_3)_3$.

TABLE II: Relaxation Data at 25 °C for $Nd(NO_3)_3$ in 50% Aqueous Methanol (X_{H_2O} = 0.68)[a]

c, M	A_{12}[b]	$f_{R_{12}}$, MHz	A_{III}[b]	$f_{R_{III}}$, MHz
0.100	73.8 ± 8.8	70.9 ± 5.5	126.8 ± 7.0	14.9 ± 2.4
0.200	121.6 ± 12.6	64.3 ± 4.1	207.5 ± 8.6	14.8 ± 1.9
0.300	133.1 ± 9.8	79.3 ± 4.5	420.2 ± 16.0	13.4 ± 1.0
0.400	119.9 ± 7.2	100.2 ± 5.2	541.5 ± 7.9	16.4 ± 0.6
0.500	154.5 ± 8.5	98.7 ± 4.8	760.5 ± 13.8	14.7 ± 0.5

[a] Double relaxation calculation, $B = 25 \times 10^{-17}$ Np cm^{-1} s^2. [b] units, 10^{17} Np cm^{-1} s^2.

existence of the third relaxation at still higher frequencies. Under these conditions, further kinetic analysis in 50% aqueous methanol is impossible.

Discussion

The first question to be answered is whether these effects reflect specific neodymium nitrate–solvent interactions or whether the salt causes a solvent–solvent interaction for the aqueous methanol solutions similar to that observed in the absence of salt for the higher alcohols.[21] Aqueous alcohol solutions have the same sound absorption in the presence or absence of $NaClO_4$, a nonassociating salt.[2,3] At water mole fractions greater than 0.6, $Ca(ClO_4)_2$ possesses a single high frequency relaxation attributed to outer-sphere ion pair formation[4] and $Mg(ClO_4)_2$ appears to have no excess absorption, although at lower water mole faactions outer-sphere complexation is detected.[24] The corresponding erbium perchlorate salt, $Er(ClO_4)_3$, possesses two relaxations, attributed to both outer- and inner-sphere complex formation.[3] If there is an electrostatic interaction between the salt and solvent to cause the solvent ordering, then the data in terms of ionic charge are consistent with this argument. However, the weaker interaction observed when the small Mg(II) ion is compared to the larger Ca(II) ion is inconsistent with this thesis. Major ultrasonic absorption differences are observed in aqueous methanol for the erbium nitrates, chlorides, and perchlorates.[1-5] Since these anions all have a single negative charge, one would expect the same effect upon solvent–solvent interactions if specific salt effects are ignored. These changes as a function of ligand parallel the optical spectroscopic changes observed in the spectral lines characteristic of lanthanide cations in water and in aqueous alcohols.[25] Therefore, we believe that ultrasonic differences must be attributed to specific cation–ligand solvation effects.

The variation in μ_{max} for inner-sphere complex formation, shown in Figure 3, is similar to that for $Er(NO_3)_3$. The data can best be explained in terms of the coupling of an additional reaction step to step III. As in the case of $Er(NO_3)_3$,[1] we believe the additional step to be an equilibrium between two forms of solvated Nd(III) ion. This means that the solvation number of the inner-sphere complex in water is different from that observed for the inner-sphere complex in methanol. The observation that the maximum in μ_{max} occurs at different water mole fractions for the two rare earth ions is reasonable, since it has previously been demonstrated that the solvation number changes in aqueous methanol are a function of the solvated cation plus the ligand.

The excess absorption maximum is greater for the $ErNO_3^{2+}$ than for the $NdNO_3^{2+}$ complex at all solvent compositions. A quantitative explanation for this observation may be made by calculating the parameters contributing to μ_{max} for the erbium and neodymium nitrates. The complex formation constants for $NdNO_3^{2+}$ formation is 17[15] and for $ErNO_3^{2+}$ the maximum value is 7.5.[7] If the same outer-sphere association constant is assumed for both salts, the volume change attributed to step III of reaction 2, ΔV_{III}, can be determined using the equations derived earlier.[7] ΔV_{III} is calculated to be 2.7 and 4.7 cm^3/mol for the neodymium and erbium nitrate solutions in water, respectively. These results are similar to earlier studies where ΔV_{III} equals 3.5 cm^3/mol for $NdNO_3^{2+}$,[7] 3.4 cm^3/mol for $CeNO_3^{2+}$,[26] and 4.2 cm^3/mol for $EuNO_3^{2+}$.[26] At all water mole fractions, μ_{max} is a factor of 1.5–2 greater for Er than for Nd, consistent with the calculated ΔV_{III} in water. The observation that ΔV_{III} is greater for the heavy rare earths than for the light ones may be a reflection of the different geometries surrounding these cations.

As the water content of the 0.20 M $Nd(NO_3)_3$ solutions increases, the relaxation frequencies corresponding to inner-sphere ion pair formation tend to increase, although the closeness of the double relaxation frequencies causes scatter in the results. For step III, the relaxation frequency is related to the solution concentration by

$$\tau_{III}^{-1} = 2\pi f_{R_{III}} = k_{43} + k_{34}\phi(c) \tag{6}$$

where

$$\phi(c) = \theta(c)/(\theta(c) + K_{12}^{-1}) \tag{7}$$

$$\theta(c) = \pi_\gamma \left[[Nd^{3+}] + [NO_3^-] \left(1 + \frac{\partial \ln \pi_\gamma}{\partial \ln [Nd^{3+}]} \right) \right] \tag{8}$$

$$K_c = \frac{[NdNO_3^{2+}]}{[Nd^{3+}][NO_3^-]} \frac{\gamma_{NdNO_3^{2+}}}{\gamma_{Nd^{3+}}\gamma_{NO_3^-}} = \frac{[NdNO_3^{2+}]}{[Nd^{3+}][NO_3^-]} \frac{1}{\pi_\gamma} \tag{9}$$

$$K_c = K_{12}(1 + K_{III}) \tag{10}$$

Even in aqueous rare earth solutions, π_γ cannot be accurately obtained. In aqueous methanol we have measured the complex formation in terms of concentration and we use a simplified form of eq 8:

$$\theta(c) = [Nd^{3+}] + [NO_3^-] \tag{11}$$

Although K_c has not been measured in aqueous methanol for $NdNO_3^{2+}$, a 10-fold increase in K_c has been estimated for $ErCl^{2+}$ association in going from water to 50% aqueous methanol.[2] Calculations utilizing eq 11 result in only an 11% change in $\theta(c)$ as K_c is increased 10-fold from the water value. Further increases in K_c result in the limiting value of $\theta(c)$ = 0.4, which corresponds to the excess nitrate concentration

after stoichiometric amounts of the 1:1 complex are formed. Thus $\theta(c)$ is relatively insensitive to water mole fraction changes for constant concentration lanthanide salt solutions. Although there is no a priori reason why K_{12} should be independent of solvent composition in aqueous methanol solutions, direct evidence exists for this in $MnSO_4$ association.[22] Experimental K_{12} values for lanthanide association with minus-one anions in water and aqueous methanol are essentially constant, and therefore we assume that K_{12} is insensitive to water–methanol composition. The net result is that $\phi(c)$ shows only a small variation with methanol content for 0.200 M $Nd(NO_3)_3$ solutions and the variation of relaxation frequency with solvent composition must be explained in terms of the variations in the rate constants with composition.

Bear and Lin investigated the relaxation kinetics of metal ion complexation with murexide in 50% aqueous ethanol and they compared the results to earlier aqueous studies.[27] Although a 5-fold increase in the complex formation rate constant was found for a d-type transition metal element such as Ni(II), essentially no change in this rate constant was observed for lanthanide systems. However, the dissociation rate constant was decreased in the aqueous alcohol leading to the increased stability of complexes. This same effect has been noted in our earlier lanthanide studies in aqueous methanol.[1-3] Thus, as water is added to 0.200 M $Nd(NO_3)_3$ solutions, f_R is expected to increase due to an increasing k_{43}, even though both k_{34} and $\phi(c)$ are essentially constant. The absence of a large decrease in $f_{R_{III}}$ in the region of low water content indicates that the bisnitrato complex is not formed with Nd or Er, whereas the bis complex is stable with $ErCl_3$,[2] $Er(ClO_4)_3$,[3] and $Gd(ClO_4)_3$.[5]

The analysis of Figure 2 for the formation of outer-sphere complexes for the Nd and Er system is extremely interesting. As water is added to the Nd solutions there is continual increase in $\mu_{max_{12}}$, which can be interpreted in terms of an increase in the concentration of outer-sphere complex or an increase in ΔV_{12}. For the reaction between a lanthanide salt and a plus-one anion, K_{12} has been determined to be 2.9 for $Nd(NO_3)_3$ in water, 3.3 and 3.7 for $ErCl_3$ in aqueous methanol containing 1.5 and 2.9% water, respectively,[2] and 0.9 to 1.6 for $Er(ClO_3)$ in 50% aqueous methanol.[3] The near constancy of K_{12}, independent of the nature of the univalent ligand and the solvent composition, argues against the 4-fold increase in $\mu_{max_{12}}$ arising simply from an increased concentration of outer-sphere complex. This suggests that in the $Nd(NO_3)_3$ system there is an increased ΔV_{12} with increasing water composition. This is analogous to the effect observed in step III except that the additional process coupled to the formation of the outer-sphere complexes continues to increase in importance as water is added and is not absent even in water. As was postulated in the $Er(NO_3)_3$ case where a maximum in $\mu_{max_{12}}$ was observed, this process probably involves either a loosening of the bound solvent molecules in the outer-sphere complex or perhaps a second decrease in solvation number.[1] This process decreases in importance for $Er(NO_3)_3$ in the high water compositions resulting in a large decrease in $\mu_{max_{12}}$. At very high water content, the amplitude of the high frequency relaxation is so low that the solutions appear to have only one relaxation present with a B value slightly higher than in pure water. In water, this abnormally large excess absorption for step 12 is observed only for Nd and is also attributed to a solvation number change.

During the course of this study, Hemmes published an ultrasonic investigation of $Y(NO_3)_3$ association in water in which only a single relaxation was observed and was assigned to only a single type of complex.[28] Hemmes attributed the high frequency relaxation in our earlier study[7] to the formation of a bis complex, a hypothesis which can be eliminated by the results of this study. We believe that the yttrium results parallel the erbium system and in water no solvation number change is associated with outer-sphere complexation between Y(III) and nitrate. Thus, only a single relaxation in water would be observed corresponding to the formation of the inner-sphere complex. We believe outer-sphere complexes are present in the solution, but ΔV_{12} is so small that the excess absorbance for this step disappears. If the $Y(NO_3)_3$ study is extended to aqueous methanol, we are confident that outer-sphere complexation would be detected in the region of high water content.

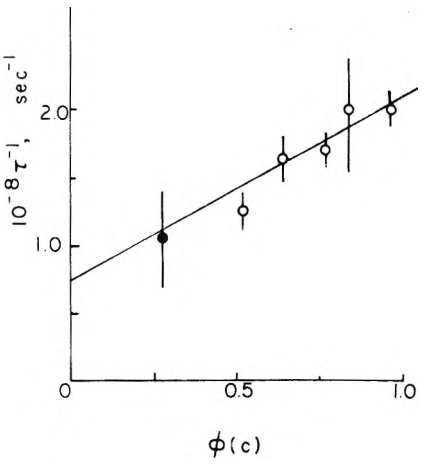

Figure 4. Relaxation data for the kinetic evaluation of the inner-sphere rate constants in water at 25 °C.

Hemmes[28] attributes bis complex formation to the large excess of ligand used in our aqueous study. The present data for 0.200 M $Nd(NO_3)_3$ in water are calculated by eq 6–9 and combined with the earlier results in Figure 4, based upon the assumption that reaction 2 holds. If the proposed mechanism is wrong, the point in the absence of excess nitrate would not fit the same line as those where the bis complex is formed. The new values of the rate constants for inner-sphere complexes are: $k_{34} = (1.5 \pm 0.2) \times 10^8\ s^{-1}$ and $k_{43} = (6 \pm 1) \times 10^7\ s^{-1}$, and these are within experimental error of the earlier results of $k_{34} = (1.8 \pm 0.3) \times 10^8\ s^{-1}$ and $k_{43} = (4 \pm 3) \times 10^7\ s^{-1}$.[7] Both sets of results cannot be considered exact since the relaxation expressions are treated separately for the high and low frequency relaxations, due to the relatively large errors in determining the high frequency relaxation parameters. Although the absolute values of the rate constants cannot be obtained, comparisons across the lanthanide series can still be made.

Further confirmation of the absence of bis complexation comes from Figure 2. If the high frequency peak corresponds to bis complex formation, its amplitude would decrease as water is added to the system due to destabilization of this complex, and this is not observed. Thus, in water and in aqueous methanol, the data can be best explained in terms of the formation of the 1:1 complex predominating, both as inner- and outer-sphere species.

Acknowledgment. Acknowledgment is made to the donors of the Petroleum Research Fund, administered by the American Chemical Society, for support of this research.

References and Notes

(1) J. Reidler and H. B. Silber, *J. Inorg. Nucl. Chem.*, **36**, 175 (1974).
(2) J. Reidler and H. B. Silber, *J. Chem. Soc., Chem. Commun.*, 354 (1973);

J. Phys. Chem., **78**, 424 (1974).
(3) H. B. Silber, *J. Phys. Chem.*, **78**, 1940 (1974).
(4) H. B. Silber, *FEBS Lett.*, **41**, 303 (1974).
(5) H. B. Silber, *Proc. 11th Rare Earth Res. Conf.*, **II**, 901 (1974).
(6) F. H. Spedding, M. J. Pikal, and B. O. Ayers, *J. Phys. Chem.*, **70**, 2440 (1966).
(7) H. B. Silber, N. Scheinin, G. Atkinsor, and J. J. Grecsek, *J. Chem. Soc., Faraday Trans. 1*, **68**, 1200 (1972).
(8) H. Diebler and M. Eigen, *Z. Phys. Chem. (Frankfurt am Main)*, **20**, 299 (1959); M. Eigen and K. Tamm, *Z. Electrochem.*, **66**, 93, 107 (1962).
(9) P. Debye, *Trans. Electrochem. Soc.*, **82**, 265 (1942).
(10) M. Eigen, *Z. Phys. Chem. (Frankfurt am Main)*, **1**, 176 (1954).
(11) G. R. Choppin, D. E. Henrie, and K. Buijs, *Inorg. Chem.*, **5**, 1743 (1966).
(12) K. Bukietynska and G. R. Choppin, *J. Chem. Phys.*, **52**, 2975 (1970).
(13) I. Abrahamer and Y. Marcus, *Inorg. Chem.*, **6**, 2103 (1967); J. Reuben and D. Fiat, *J. Chem. Phys.*, **51**, 4909 (1969).
(14) A. Fratiello, V. Kubo, S. Peak, B. Sanchez, and R. E. Schuster, *Inorg. Chem.*, **10**, 2552 (1971).
(15) R. Garnsey and D. W. Ebdon, *J. Am. Chem. Soc.*, **91**, 50 (1969).
(16) D. P. Fay, D. Litchinsky, and N. Purdie, *J. Phys. Chem.*, **73**, 544 (1969).
(17) G. S. Darbari, F. Fittipaldi, S. Petrucci, and P. Hemmes, *Acustica*, **25**, 125 (1970).
(18) H. B. Silber, *J. Chem. Educ.*, **50**, 720 (1973).
(19) A copy of the ultrasonic absorption data can be obtained by writing the principal author.
(20) K. Fritsch, C. J. Montrose, J. L. Hunter, and J. F. Dill, *J. Chem. Phys.*, **52**, 2242 (1970).
(21) C. J. Burton, *J. Acoust. Soc. Am.*, **20**, 186 (1948); L. R. O. Storey, *Proc. Phys. Soc., Sect. B.*, **65**, 943 (1952).
(22) G. Atkinson and S. Petrucci, *J. Phys. Chem.*, **70**, 3122 (1966); G. Atkinson and S. K. Kor, *ibid.*, **69**, 128 (1965); **71**, 673 (1967).
(23) A. Bechtler and K. G. Breitschwerdt, *Ber. Bunsenges. Phys. Chem.*, **70**, 1177 (1966); A. Bechtler, K. G. Breitschwerdt, and K. Tamm, *J. Chem. Phys.*, **52**, 2975 (1970).
(24) H. B. Silber, *Proc. 11th Rare Earth Res. Conf.*, **II**, 723 (1974).
(25) S. Freed, S. I. Weissman, F. E. Fortress, and H. F. Jacobson, *J. Chem. Phys.*, **7**, 824 (1939).
(26) T. G. Spiro, A. Revesz, and J. Lee, *J. Am. Chem. Soc.*, **90**, 4000 (1968).
(27) J. L. Bear and C. T. Lin, *J. Inorg. Nucl. Chem.*, **34**, 2368 (1972).
(28) H. C. Wang and P. Hemmes, *J. Phys. Chem.*, **78**, 261 (1974).

The Two-Step Equilibrium Reaction of 2-Substituted 4,6-Diamino-*s*-triazine with Formaldehyde

Tatsuo Tashiro* and Masayoshi Oiwa

Research Institute for Polymers and Textiles, Sawatari, Kanagawa-ku, Yokohama 221, Japan and Department of Applied Chemistry, Faculty of Engineering, Kansai University, Senriyama, Suita-shi, Osaka 565, Japan *(Received November 14, 1975)*

The reaction of amino groups of 2-substituted 4,6-diamino-*s*-triazine (I) with formaldehyde is an equilibrium reaction, and the equilibrium state is expresed by: $-NH_2 + CH_2O \rightleftharpoons -NHCH_2OH$ (K_1); $-NHCH_2OH + CH_2O \rightleftharpoons -N(CH_2OH)_2$ (K_2). This paper describes a method to determine the equilibrium constants K_1 and K_2 of the two reactions. K_1 and K_2 values have been determined for 2-methoxy- (MT), 2-isopropoxy- (iPT), 2-methyl- (acetoguanamine, AG), 2-diethylamino- (*N,N*-bis(ethyl)melamine, BEM), and 2-guanidinyl-4,6-diamino-*s*-triazines (guanylmelamine, GM). The apparent equilibrium constant K has been calculated using the K_1 and K_2 values determined by this method (K_{calcd}). The K_{calcd} were in good agreement with the observed values, K_{obsd}. The theory also agreed well with experimental data in other points and the validity of the proposed method has been proved. The van't Hoff's isochore was observed for iPT, and the heats of reaction were −4.96 for K_1 and −5.08 kcal/mol for K_2.

Introduction

The melamine or 2-substituted 4,6-diamino-*s*-triazine (I) undergoes an equilibrium reaction with formaldehyde as follows:

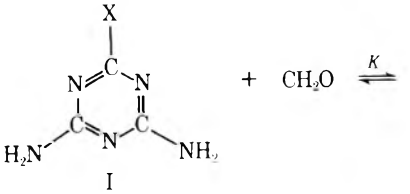

I

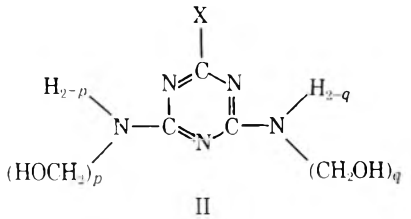

II

* Address correspondence to this author at the Research Institute for polymers and textiles.

The apparent equilibrium constant K, which is calculated from the simple equilibrium equation

$$K = [II]/[I][CH_2O]$$

varies with the concentration of reactants. In the reaction of formaldehyde with the amino groups of melamine or I, $-NHCH_2OH$ groups are produced first. Formaldehyde reacts further with these groups to form $-N(CH_2OH)_2$ groups. The change of the K value with the concentrations of reactants is considered attributable to the fact that this two-step reaction is dealt with by use of a simple equilibrium equation. Actually, in the reaction of acetoguanamine with formaldehyde, large differences have been observed among the individual equilibrium constants for the formation of mono-, di-, tri-, and tetramethylol compounds.[1] (Detailed discussion will be described later.)

This study has been carried out to obtain definite equilibrium constants, which are not influenced by the concentrations of reactants, eliminating the difficulty of determining the individual equilibrium constants for each meth-

TABLE I: x_e and K of the Reaction of 2-Methoxy-4,6-diamino-s-triazine (MT) with Formaldehyde [a]

f, M	x_e, M	$(f - x_e)$, M	$(4m - x_e)$, M	K_{obsd}, M^{-1}	K_{calcd}, M^{-1}	$(1/f_e - K)$, M^{-1}	K/f_e, M^{-2}
0.050	0.0263	0.0237	0.1737	6.39	6.43	35.80	269.6
0.100	0.0475	0.0525	0.1525	5.93	6.02	13.11	113.0
0.150	0.0651	0.0849	0.1349	5.68	5.67	6.10	66.90
0.200	0.0797	0.1203	0.1203	5.51	5.39	2.80	46.05
0.300	0.0999	0.2011	0.1001	4.96	4.97	0.013	24.66
0.400	0.1143	0.2857	0.0857	4.67	4.70	−1.17	16.35
0.500	0.1266	0.3734	0.0734	4.62	4.51	−1.94	12.37
0.690	0.1369	0.5531	0.0631	3.92	4.27	−2.11	7.09
1.00	0.1561	0.8439	0.0439	4.21	4.07	−3.13	4.99

$K_1 = 13.8\ M^{-1}$, $K_2 = 1.79\ M^{-1}$

[a] [MT] = 0.050 M, 30 ± 0.1 °C.

ylol compound. This paper describes a method to determine the equilibrium constants K_1 and K_2 of the two reactions of the amino groups of I with formaldehyde, i.e., $-NHCH_2OH$ and $-N(CH_2OH)_2$ groups formation reactions, from the equilibrium concentration of formaldehyde.

The apparent equilibrium constants (K) of the reactions of I with formaldehyde were calculated using K_1 and K_2 values determined by this method. The calculated apparent equilibrium constants (K_{calcd}) were compared with the observed values (K_{obsd}) and the validity of the method was examined.

Equations for the Determination of Equilibrium Constants K_1 and K_2

The equilibrium state for the reaction of amino groups of I with formaldehyde is expressed by

$$-NH_2 + CH_2O \overset{K_1}{\rightleftharpoons} -NHCH_2OH \quad (1)$$

$$-NHCH_2OH + CH_2O \overset{K_2}{\rightleftharpoons} -N(CH_2OH)_2 \quad (2)$$

The concentrations of $-NHCH_2OH$ and $-N(CH_2OH)_2$ groups at equilibrium are given by

$$[-NHCH_2OH] = K_1[-NH_2][CH_2O] \quad (3)$$

$$[-N(CH_2OH)_2] = K_2[-NHCH_2OH][CH_2O] = K_1K_2[-NH_2][CH_2O]^2 \quad (4)$$

The concentrations of reacted amino groups and formaldehyde are expressed by

$$[-NH_2]_0 - [-NH_2] = [-NHCH_2OH] + [-N(CH_2OH)_2] \quad (5)$$

$$[CH_2O]_0 - [CH_2O] = [-NHCH_2OH] + 2[-N(CH_2OH)_2] \quad (6)$$

where $[-NH_2]_0$ and $[CH_2O]_0$ are the initial concentrations of amino groups and formaldehyde. Elimination of $[-N(CH_2OH)_2]$ and $[-NHCH_2OH]$ terms from eq 5 and 6 leads to

$$2([-NH_2]_0 - [-NH_2]) - ([CH_2O]_0 - [CH_2O]) = [-NHCH_2OH] = K_1[-NH_2][CH_2O] \quad (7)$$

$$([CH_2O]_0 - [CH_2O]) - ([-NH_2]_0 - [-NH_2]) = [-N(CH_2OH)_2] = K_1K_2[-NH_2][CH_2O]^2 \quad (8)$$

Rearranging eq 7 and 8 gives

$$2[-NH_2]_0 - [CH_2O]_0 + [CH_2O] = (2 + K_1[CH_2O])[-NH_2] \quad (9)$$

$$[CH_2O]_0 - [-NH_2]_0 - [CH_2O] = (K_1K_2[CH_2O]^2 - 1)[-NH_2] \quad (10)$$

In order to eliminate the $[-NH_2]$ term, dividing eq 9 by eq 10 leads to eq 12 via eq 11.

$$K_1(2K_2[CH_2O] + 1)[-NH_2]_0[CH_2O] = ([CH_2O]_0 - [CH_2O])(1 + K_1[CH_2O] + K_1K_2[CH_2O]^2) \quad (11)$$

$$[CH_2O]_0 - [CH_2O] = \frac{K_1[CH_2O] + 2K_1K_2[CH_2O]^2}{1 + K_1[CH_2O] + K_1K_2[CH_2O]^2}[-NH_2]_0 \quad (12)$$

When x_e and f_e denote respectively the concentrations of combined and unreacted free formaldehyde at equilibrium state (M), $[CH_2O]_0 - [CH_2O]$ is replaced by x_e. Calculating $2[-NH_2]_0 -$ eq 12 leads to

$$2[-NH_2]_0 - x_e = \frac{2 + K_1f_e}{1 + K_1f_e + K_1K_2f_e^2}[-NH_2]_0 \quad (13)$$

Substituting the $[-NH_2]_0$ term in eq 12 into eq 13 gives

$$2[-NH_2]_0 - x_e = \frac{2 + K_1f_e}{K_1f_e + 2K_1K_2f_e^2}x_e \quad (14)$$

The apparent equilibrium constant K is expressed by

$$K = \frac{x_e}{(2[-NH_2]_0 - x_e)(f - x_e)} \quad (15)$$

where f is taken as the initial concentration of formaldehyde (M). As I has two amino groups, 4 mol of formaldehyde at maximum can combine with I, i.e., the ability of an $-NH_2$ group to combine with formaldehyde is 2. Therefore, if $2[-NH_2]_0$, the concentration of functional groups of I, is represented by $4m$ (m, the initial concentration of I, M)

$$K = \frac{x_e}{(4m - x_e)(f - x_e)} \quad (= K_{obsd}) \quad (15')$$

Since $f - x_e$ is f_e, introduction of eq 14 into eq 15 yields

$$K = \frac{K_1(1 + 2K_2f_e)}{2 + K_1f_e} \quad (= K_{calcd}) \quad (16)$$

Thus, the apparent equilibrium constant is a function of the formaldehyde concentration at the equilibrium state, i.e., it depends on f_e. Further, rearrangement of eq 16 leads to

$$\frac{K}{f_e} = \frac{K_1}{2}\left(\frac{1}{f_e} - K\right) + K_1K_2 \quad (17)$$

Here, we can expect a linear relationship between K/f_e and $1/f_e - K$. The f_e values can be measured at the equilibrium

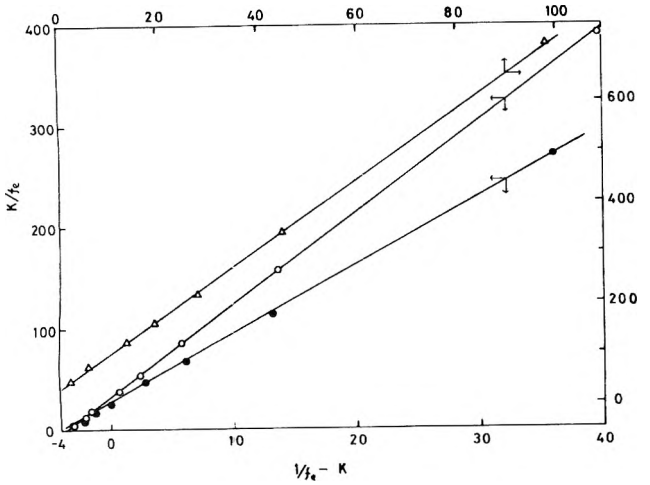

Figure 1. Correlations between K/f_e and $1/f_e - K$ for the reactions of 2-methoxy-, 2-isopropoxy-4,6-diamino-*s*-triazines, and *N,N*-bis(ethyl)melamine with formaldehyde at 30, 25, and 30 ± 0.1 °C: (●) MT, [MT] = 0.050 M, the molar ratios of $[CH_2O]/[MT]$ = 1–20; (○) iPT, [iPT] = 0.050 M, the molar ratios of $[CH_2O]/[iPT]$ = 1–20; (△) BEM, [BEM] = 0.0125 M, the molar ratios of $[CH_2O]/[BEM]$ = 1–12.

states in the reactions of formaldehyde of various concentrations with I of constant concentrations and K values can be calculated from eq 15′. The values of K_1 and K_2 can be determined from the slope and the intercept of the plotted line, which can be calculated from the several values of K/f_e and $1/f_e - K$ by the least-squares method.

When $4m = f$, eq 15′ = eq 16, i.e.

$$K = \frac{f - f_e}{f_e^2} = \frac{K_1(1 + 2K_2 f_e)}{2 + K_1 f_e}$$

leads to

$$2K_1K_2f_e^3 + 2K_1f_e^2 - (K_1f - 2)f_e - 2f = 0 \qquad (18)$$

Insertion of $f_e/f = z$ into eq 18 and rearrangement gives

$$z^3 + \frac{z^2}{K_2 f} - \frac{K_1 f - 2}{2K_1K_2f^2}z - \frac{1}{K_1K_2f^2} = 0 \qquad (19)$$

As K_1 and K_2 can be determined by the method described above and f is known, z can be obtained by solving this cubic equation. Thereafter, K is computable from

$$Kf = (1 - z)/z^2 \qquad (20)$$

Experimental Section

Materials. The 2-substituted 4,6-diamino-*s*-triazines (I's) used were 2-methoxy- (MT), 2-isopropoxy- (iPT), and 2-diethylamino-4,6-diamino-*s*-triazines (*N,N*-bis(ethyl)-melamine, BEM). These compounds were synthesized from cyanuric chloride using the method described by Controulis et al.[2] and Thurston et al.[3] MT was recrystallized from dioxane, mp 229–230 °C, iPT from water, mp 170–171 °C, and BEM from isopropyl alcohol, mp 167–169 °C. As for formaldehyde, the best grade formalin of Wako Junyaku Co. was used.

Reaction of I with Formaldehyde and Measurement of Free Formaldehyde. As a general procedure, 0.3529 g (0.0025 mol) of MT was dissolved in 20–40 ml of distilled water in a measuring flask. To this were added 0.5 ml of 0.1 N sodium hydroxide and diluted, neutralized formalin containing formaldehyde of 1–20 molar ratios to MT. The reaction solution was dipped in a thermostat bath regulated

TABLE II: x_e and K of the Reaction of 2-Isopropoxy-4,6-diamino-*s*-triazine with Formaldehyde [a]

f, M	x_e, M	K_{obsd}, M^{-1}	K_{calcd}, M^{-1}	$(1/f_e - K)$, M^{-1}	K/f_e, M^{-2}
0.050	0.0291	8.15	8.18	39.70	389.95
0.100	0.0524	7.46	7.40	13.55	156.72
0.150	0.0703	6.80	6.75	5.75	85.64
0.200	0.0839	6.22	6.24	2.39	53.57
0.250	0.0944	5.75	5.84	0.68	36.95
0.400	0.1184	5.15	5.11	−1.60	18.29
0.500	0.1273	4.70	4.82	−2.02	12.61
1.00	0.1555	4.14	4.20	−2.96	4.90

$K_1 = 18.1\ M^{-1}$, $K_2 = 1.78\ M^{-1}$

[a] [iPT] = 0.050 M, 25 ± 0.1 °C.

TABLE III: x_e and K of the Reaction of *N,N*-Bis(ethyl)melamine with Formaldehyde [a]

f, M	x_e, M	K_{obsd}, M^{-1}	K_{calcd}, M^{-1}	$(1/f_e - K)$, M^{-1}	K/f_e, M^{-2}
0.0125	0.003 01	6.75	6.75	98.62	711.28
0.0250	0.005 64	6.57	6.62	45.08	339.36
0.0375	0.007 91	6.35	6.50	27.45	214.60
0.0500	0.010 11	6.35	6.39	18.72	159.19
0.0625	0.012 03	6.28	6.29	13.53	124.43
0.100	0.017 11	6.28	6.04	5.78	75.76
0.150	0.021 42	5.83	5.79	1.95	45.36

$K_1 = 13.8\ M^{-1}$, $K_2 = 2.27\ M^{-1}$

[a] [BEM] = 0.0125 M, 30 ± 0.1 °C.

TABLE IV: x_e and K of the Reaction of Acetoguanamine with Formaldehyde [a]

f, M	x_e, M	K_{obsd}, M^{-1}	K_{calcd}, M^{-1}	$(1/f_e - K)$, M^{-1}	K/f_e, M^{-2}
0.0618	0.0330	5.54	5.56	29.18	192.36
0.120	0.0588	5.30	5.17	11.04	86.60
0.180	0.0774	4.64	4.80	5.11	45.24
0.275	0.1026	4.33	4.38	1.47	25.12
0.361	0.1206	4.20	4.11	−0.04	17.47
0.596	0.1488	3.65	3.66	−1.41	8.16

$K_1 = 12.1\ M^{-1}$, $K_2 = 1.39\ M^{-1}$

[a] [AG] = 0.060 M, 20 ± 0.5 °C, pH 7.6.

TABLE V: x_e and K of the Reaction of Guanylmelamine with Formaldehyde [a]

f, M	x_e, M	K_{obsd}, M^{-1}	K_{calcd}, M^{-1}	$(1/f_e - K)$, M^{-1}	K/f_e, M^{-2}
0.101	0.059	4.12	4.16	19.69	98.10
0.202	0.110	4.12	3.90	6.75	44.78
0.303	0.146	3.66	3.67	2.71	23.31
0.404	0.181	3.71	3.50	0.77	16.64
0.505	0.203	3.41	3.36	−0.10	11.29
0.708	0.238	3.13	3.16	−1.00	6.66
1.011	0.274	2.95	2.99	−1.59	4.00
2.022	0.319	2.31	2.76	−1.72	1.36

$K_1 = 8.93\ M^{-1}$, $K_2 = 1.29\ M^{-1}$

[a] [GM] = 0.10 M, 40 ± 0.1 °C, pH 7.2.

to operating temperature, and was made up to 50 ml at this temperature. The reaction solution became pH 10.2–10.3 by this procedure. When the reaction attained equilibrium, the pH value had decreased to 8.5–8.0. Free formaldehyde concentration was measured by the sulfite method modified by Kurabayashi et al.[4] An appropriate amount of sample containing ca. 1 mmol of formaldehyde was pipetted into a 100-ml beaker containing 5–24 ml of ice-cold distilled water acidified by hydrochloric acid and the final volume was made to 25 ml. The solution was adjusted to pH 9.33–9.35 by adding 0.1 N sodium hydroxide. Into this was poured immediately 20 ml of 0.1 N HCl–0.5 N Na_2SO_3 solution and the excess hydrochloric acid was titrated with 0.1 N sodium hydroxide to pH 9.35 which was determined experimentally. Iodometry was used for titrating of the sum of both methylol groups and unreacted free formaldehyde. In the iodometry, an aliquot containing ca. 0.1 mmol of total methylol and free formaldehyde was poured into 5 ml of 10% sodium hydroxide, and immediately 20 ml of 0.1 N iodine solution was added. Then, 5 ml of 10% hydrochloric acid was added after 15 min, and thereafter the excess iodine was titrated with 0.1 N sodium thiosulfate.

Results

Determination of K_1, K_2, and K for the Hydroxymethylation of Several I's. K_1, K_2, and K for MT. The reaction solutions with 1–20 molar ratios of formaldehyde to 0.050 M of MT were prepared and allowed to stand at 30 ± 0.1 °C. After attaining equilibria, the reaction solutions were titrated by the modified sulfite method and iodometry, and the measured x_e and f_e values are listed in Table I. The formaldehyde concentration of each reaction solution evaluated by iodometry was in accord with the initial concentration of added formaldehyde within experimental error. The analytical data suggest that no methylene and dimethylene ether groups were formed during the reaction process. The values of $1/f_e - K$ and K/f_e were calculated (Table I) and the plot of the K/f_e vs. $1/f_e - K$ gave a straight line (Figure 1). The values of K_1 and K_2 were determined from the slope and the intercept. They are listed in Table I. The values of K_{calcd} (Table I) were computed by inserting the values of K_1 and K_2 into eq 16. The values of K_{obsd} were in good agreement with K_{calcd} except for the value at f = 0.069 M. This disagreement will be probably ascribable to titration error.

K_1, K_2, and K for iPT. The reactions were carried out similarly to MT. The measured x_e's are listed in Table II. The plot of K/f_e vs. $1/f_e - K$ gave a straight line (Figure 1) and K_1 and K_2 were determined as 18.1 and 1.78 M^{-1}, respectively. Also the values of K_{obsd} were in fairly good agreement with the K_{calcd} (Table II).

K_1, K_2, and K for BEM. As the solubility of BEM is small compared with MT and iPT, the reaction was carried out under the condition of m = 0.0125, f/m molar ratio = 1–12, and at 30 °C. The K/f_e and $1/f_e - K$ values were calculated from the measured x_e's (Table III). The plot of K/f_e vs. $1/f_e - K$ gave a straight line (Figure 1), and K_1 and K_2 were 13.8 and 2.27 M^{-1}, respectively. The K_{obsd} values were in good agreement with the K_{calcd} (Table III).

K_1, K_2, and K for AG. These values were determined from the data measured by Morimoto[5] (Table IV). Plot of K/f_e vs $1/f_e - K$ gave a straight line (Figure 2) and K_1 and K_2 were determined to be 12.1 and 1.39 M^{-1}, respectively. The K_{obsd} values were in fairly good agreement with the K_{calcd}.

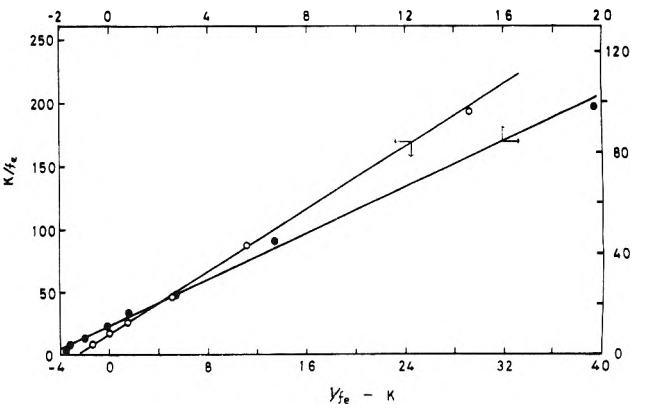

Figure 2. Correlations between K/f_e and $1/f_e - k$ for the reactions of acetoguanamine and guanylmelamine with formaldehyde at 20 ± 0.5 and 40 ± 0.05 °C: (O) AG, [AG] = 0.060 M, the molar ratios of $[CH_2O]/[AG]$ = 1–10; (●) GM, [GM] = 0.10 M, the molar ratios of $[CH_2O]/[GM]$ = 1–20.

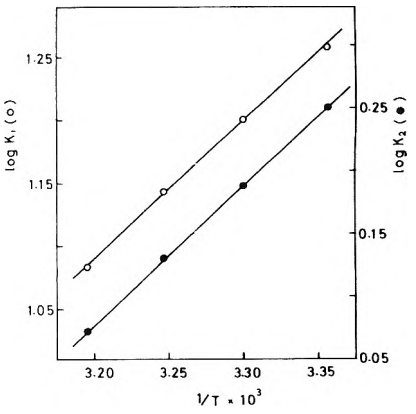

Figure 3. The van't Hoff's isochore for the reaction of 2-isopropoxy-4,6-diamino-s-triazine with formaldehyde at 25–40 °C.

K_1, K_2, and K for GM. These values were determined from the data measured by Kurabayashi et al.[4] (Table V). The correlation between K/f_e and $1/f_e - K$ showed good linearity (Figure 2), and the K_1 and K_2 values were 8.93 and 1.29 M^{-1}, respectively. The K_{obsd} values were in fair agreement with the K_{calcd} except for f = 2.022 M, of which disagreement will be attributable to experimental error.

From the K_1 and K_2 values determined here, it became clear that the K_2 values were small compared with the K_1, and about 1/6 to 1/10 of the K_1.

Effect of Temperature on K_1 and K_2. The K_1 and K_2 values of the reaction of iPT with formaldehyde were determined at 25–40 °C. Table VI lists the values of x_e, K_{obsd}, K_1, K_2, and K_{calcd} at each temperature. The K_{obsd} values were in good agreement with the K_{calcd}, and a good linear correlation was observed between K/f_e and $1/f_e - K$ at each temperature.

Figure 3 illustrates the van't Hoff's isochore, which gives straight lines with almost equal slope. The heats of reaction were calculated as −4.96 for K_1 and −5.08 kcal/mol for K_2.

K Values for the Reaction at $4m = f$. The values of z and k at $4m = f$ were calculated from eq 19 and 20 (Table VII). The calculated K values were consistent with the K_{obsd}. Further, the values of z and K at $4m = f$ = 0.40 M were calculated by using the K_1 and K_2 values determined at m = 0.050 M for iPT (Table VIII). Although slightly larger differences were observed between the calculated K values and the K_{obsd}, the calculated K values were approximately

TABLE VI: x_e and K of the Reaction of 2-Isopropoxy-4,6-diamino-s-triazine with Formaldehyde at 30, 35 and 40 °C [a]

	30 °C			35 °C			40 °C		
f, M	x_e, M	K_{obsd}, M^{-1}	K_{calcd}, M^{-1}	x_e, M	K_{obsd}, M^{-1}	K_{calcd}, M^{-1}	x_e, M	K_{obsd}, M^{-1}	K_{calcd} M^{-1}
0.050	0.0277	7.21	7.22	0.0262	6.33	6.35	0.0246	5.52	5.56
0.10	0.0499	6.63	6.57	0.0474	5.90	5.81	0.0447	5.20	5.38
0.15	0.0671	6.09	6.02	0.0639	5.45	5.36	0.0601	4.78	4.75
0.20	0.0804	5.62	5.59	0.0767	5.05	4.99	0.0729	4.51	4.45
0.25				0.0870	4.72	4.69	0.0832	4.27	4.20
0.30	0.0987	4.84	4.97						
0.40	0.1144	4.68	4.58	0.1078	4.00	4.10	0.1038	3.64	3.68
0.50	0.1242	4.36	4.32	0.1172	3.70	3.86	0.1125	3.32	3.46
0.70	0.1353	3.70	3.98						
1.00	0.1514	3.67	3.73	0.1463	3.19	3.31	0.1403	2.73	2.96
		K_1 = 15.9 M^{-1} K_2 = 1.54 M^{-1}			K_1 = 13.9 M^{-1} K_2 = 1.35 M^{-1}			K_1 = 12.1 M^{-1} K_2 = 1.18 M^{-1}	

[a] [iPT] = [illegible] 0.050 M.

TABLE VII: Comparison of K_{obsd} with K_{calcd} Calculated from Eq 19 and 20 at $4m = f$ for I's

I	f, M	x_e, M	K_{obsd}, M^{-1}	z	K_{calcd}, M^{-1}
MT	0.20	0.079 7	5.51	0.606	5.36
BEM	0.050	0.010 11	6.35	0.797	6.39
AG	0.24			0.604	4.52
GM	0.404	0.181	3.71	0.559	3.53

in agreement with the K_{obsd}. The calculated K values were consistent with the K_{obsd} at $4m = f = 0.20$ M.

Discussion

In this experiment, we calculated the equilibrium constants without taking the activity coefficient of formaldehyde (γ) into consideration. In calculating the γ value on the basis of the partial pressure of formaldehyde solution,[6] the following values were obtained:

Concn, %	3.88	3.89	3.95	4.46	7.93	7.95	7.98	8.00
γ	0.976	0.988	0.957	0.990	0.951	0.949	0.964	0.943

From these results, the γ values are presumed about 0.98 at 1 M formaldehyde solution and about 0.96 at 2. Therefore, the activity coefficient correction can be neglected at the concentration of formaldehyde used in this experiment.

Taking into account the reaction scheme shown by Gordon et al.[7] for the hydroxymethylation of melamine, the hydroxymethylation of I can be illustrated by

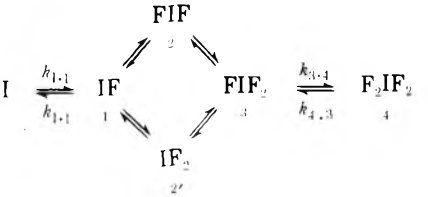

where I denotes 2-X-4,6-diamino-s-triazine, F_1, monomethylol, F_2, dimethylol as the following examples show:

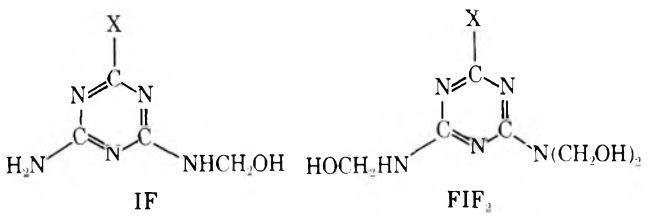

If the individual equilibrium constants of all reaction steps are expressed on the basis of the concentration of functional groups, they are given by following equations.

$$K_{1\text{-}1} = \frac{k_{1\text{-}1}}{k_{1\text{-}1}} = \frac{[\mathrm{IF}]}{4[\mathrm{I}][\mathrm{CH_2O}]}$$

$$K_{1\text{-}2} = \frac{k_{1\text{-}2}}{k_{2\text{-}1}} = \frac{[\mathrm{FIF}]}{3[\mathrm{IF}][\mathrm{CH_2O}]}$$

$$K_{2\text{-}3} = \frac{k_{2\text{-}3}}{k_{3\text{-}2}} = \frac{[\mathrm{FIF_2}]}{2[\mathrm{FIF}][\mathrm{CH_2O}]}$$

$$K_{1\text{-}2'} = \frac{k_{1\text{-}2'}}{k_{2'\text{-}1}} = \frac{[\mathrm{IF_2}]}{3[\mathrm{IF}][\mathrm{CH_2O}]}$$

$$K_{2'\text{-}3} = \frac{k_{2'\text{-}3}}{k_{3\text{-}2'}} = \frac{[\mathrm{FIF_2}]}{2[\mathrm{IF_2}][\mathrm{CH_2O}]}$$

$$K_{3\text{-}4} = \frac{k_{3\text{-}4}}{k_{4\text{-}3}} = \frac{[\mathrm{F_2IF_2}]}{[\mathrm{FIF_2}][\mathrm{CH_2O}]}$$

Ideally speaking, it is necessary to determine these individual constants. For AG, the determination was actually tried by Uragami and Oiwa.[8] No compound of the IF_2 type had been observed by means of paper chromatography, and mono-, di-, tri-, and tetramethylol AG were synthesized and isolated.[8] The $K_{1\text{-}1}$, $K_{1\text{-}2}$, $K_{2\text{-}3}$, and $K_{3\text{-}4}$ values were determined by measuring the equilibrium concentrations of formaldehyde in the hydroxymethylations of AG, mono-, di-, and trimethylol AG, by measuring those of the cleavages of the methylol AG's, and by calculating the ratios of the rate constant of the formation of methylol AG to the one of the cleavage of methylol AG.[1] Table IX shows two examples of them.

Judging from their studies, however, it is difficult to isolate the each methylol compound and determine these individual equilibrium constants. Therefore, we determined K_1 and K_2 by assuming eq 1 and 2: these values were comparatively easily obtained.

Taking AG for an example, the K_1 and K_2 values obtained by our method are now examined. The reactivity of $-NH_2$ groups to formaldehyde is about twice as large in AG as in other of monomethylol compound.[1] The reactivity of a secondary amino hydrogen atom in a $-NHCH_2OH$ group is smaller than the amino hydrogens of an $-NH_2$ group in monomethylol compound. The reactivity is larger in dimethylol compound than in trimethylol. Accordingly, the K_1 determined here is a value which contains on the aver-

TABLE VIII: Comparison of K_{obsd} with K_{calcd} Calculated from Eq 19 and 20 for iPT

	$4m = f = 0.20$				$4m = f = 0.40$			
T, °C	x_e, M	K_{obsd}, M^{-1}	K_{calcd}, M^{-1}	z	x_e, M	K_{obsd}, M^{-1}	K_{calcd}, M^{-1}	z
25	0.0839	6.22	6.24	0.580	0.2072	5.57	5.54	0.483
30	0.0804	5.62	5.59	0.599	0.2050	5.39	4.89	0.501
35	0.0767	5.05	5.05	0.619	0.1951	4.65	4.44	0.520
40	0.0729	4.51	4.45	0.638	0.1890	4.24	3.97	0.539

TABLE IX: Equilibrium Constants (M^{-1}) for the Formation of each Methylol AG at 20 °C

		$K_{I\text{-}1}$	$K_{1\text{-}2}$	$K_{2\text{-}3}$	$K_{3\text{-}4}$
pH 7	Obsd[a]	111	38.5	5.26	2.00
	Calcd[b]	112	38.2	6.16	2.44
pH 8	Obsd[a]	125	33.3	5.56	1.96
	Calcd[b]	104	30.3	5.27	1.85

[a] Estimated from the equilibrium concentration of CH_2O. [b] Calculated from the ratios of $K_{I\text{-}1}/K_{I\text{-}I}$, etc.

age the reactivity of $-NH_2$ groups for AG and the reduced reactivity of an $-NH_2$ group for monomethylol AG. The K_2 is a value which contains on the average the reactivity of each secondary amine hydrogen atom of two $-NHCH_2OH$ groups of dimethylol AG and the reduced reactivity of a $-NHCH_2OH$ group in trimethylol AG.

Uragami and Oiwa[1] determined the $K_{I\text{-}1}$, $K_{1\text{-}2}$, $K_{2\text{-}3}$, and $K_{3\text{-}4}$ for AG on the basis of molecular concentration. We converted them to the basis of the concentration of functional groups, and obtained $K_{I\text{-}1} = 26.0$, $K_{1\text{-}2} = 10.1$, $K_{2\text{-}3} = 2.64$, and $K_{3\text{-}4} = 1.85$ (from the values of $k_{I\text{-}1}/k_{I\text{-}I}$, etc.) at pH 8.

Calculating the averages of $K_{I\text{-}1}$ and $K_{1\text{-}2}$ as well as $K_{2\text{-}3}$ and $K_{3\text{-}4}$, we obtain $(K_{I\text{-}1} + K_{1\text{-}2})/2 = 18.0$, $(K_{I\text{-}1}K_{1\text{-}2})^{1/2} = 16.2$, $(K_{2\text{-}3} + K_{3\text{-}4})/2 = 2.24$, and $(K_{2\text{-}3}K_{3\text{-}4})^{1/2} = 2.21$. These average values differ from the K_1 and K_2 values. The differences will be partly ascribable to the measured values of the two workers. The difference between the K_1 and the average value of $K_{I\text{-}1}$ and $K_{1\text{-}2}$ can be explained by a consideration that K_1 may also contain in part the reactivity of a $-NHCH_2OH$ group in dimethylol AG. However, the difference concerning the K_2 and the average value remains inexplicable.

Strictly speaking, the K_1 and K_2 values are not the equilibrium constants of eq 1 and 2. However, K_1 and K_2 are the definite values which are not influenced by the concentrations of reactants. Since the K_{obsd} in the reaction of $4m = f$ can be determined by the use of the K_1 and K_2 values, K_1 and K_2 are applicable to a wider range of concentration than the K_{obsd} determined from the ordinary equilibrium equation; the K_{obsd} value varies with the concentrations of I and formaldehyde. Therefore, the practical utility value of the K_1 and K_2 is much superior.

Conclusions

We proposed a method to determine K_1 and K_2 for the formation of $-NHCH_2OH$ and $-N(CH_2OH)_2$ groups in the hydroxymethylation of I. The K_1 and K_2 values of five kinds of I's were determined by the method, and the K_{obsd} values were in good agreement with the K_{calcd}'s, which were calculated by the use of K_1 and K_2. A good linear correlation was observed between K/f_e and $1/f_e - K$. Further, in the case of $4m = f$, the K_{obsd} values were in accord with the K values calculated from eq 19 and 20. Thus, the results proved the validity of the proposed method for the determination of K_1 and K_2.

Acknowledgment. The authors thank Dr. Y. Shimura at this Institute for his encouragement and reading the manuscript.

References and Notes

(1) T. Uragami and M. Oiwa, *Kogyo Kagaku Zasshi*, **73**, 611, 616 (1970).
(2) J. Controulis and C. K. Banks, *J. Am. Chem. Soc.*, **67**, 1946 (1945).
(3) J. T. Thurston, J. R. Dudley, D. W Kaiser, et al., *J. Am. Chem. Soc.*, **73**, 2981, 2984. 2986 (1951).
(4) M. Kurabayashi, K. yanagiya, and I. Shibuya, *Nippon Kagaku Zasshi*, **87**, 270 (1966).
(5) G. Morimoto, *Nippon Kagaku Zasshi*, **87**, 794 (1966).
(6) J. F. Walker, *ACS Monogr.*, 95 (1953); E. L. Piret and M. W. Hall, *Ind. Eng. Chem.*, **40**, 661 (1948).
(7) M. Gordon, A. Halliwell, and T. Wi son, *J. Polym. Sci.*, **10**, 1153 (1966).
(8) T. Uragami and M. Oiwa, Presented at 18th Meeting of Thermo-setting Resin, Preprint p 106 (1968); *Bull. Chem. Soc. Jpn.*, **42**, 2426 (1969).

On the Conformational State of Surfactants in the Solid State and in Micellar Form. A Laser-Excited Raman Scattering Study

K. Kalyanasundaram and J. K. Thomas*

Department of Chemistry and Radiation Laboratory,[1] University of Notre Dame, Notre Dame, Indiana 46556 *(Received January 8, 1976)*

Publication costs assisted by the U.S. Energy Research and Development Administration

The Raman spectra of a series of cationic, anionic, and nonionic surfactants have been examined as pure solids or liquids, and in aqueous micellar solutions. The spectra show that cationic surfactants such as hexadecyltrimethylammonium bromide (CTAB), dodecylammonium chloride (DAC), and decyltrimethylammonium bromide (DeTAB), along with anionic surfactants such as sodium laurate (NaL) and sodium lauryl sulfate (NaLS) exist in all-trans structures in the crystalline state. Aqueous micellar solution of these surfactants show additional Raman lines which correspond to a liquidlike nature of the micellar core. Raman spectral studies indicate that the ethylene oxide chains in nonionic surfactant such as Igepal CO-880 and Brij 35 assume dihedral helical structures. Nonionic liquid surfactants with shorter ethylene oxide chains such as Triton X-100 and Igepal CO-630 have a major part of the ethylene oxide chain in an open coil form. No significant differences are observed in Brij 35 in H_2O. However, micellization of Igepal CO-630 shows spectra which indicate a partial ordering of the ethylene oxide chains. The phase changes associated with the electrolyte-induced sphere–rod transition in micellar systems have also been examined by Raman spectroscopy. These studies show a greater ordering of the hydrocarbon chain in the rod-shaped compared to the sphere-shaped aggregates.

Introduction

A renewed interest has arisen recently in the study of micellar assemblies.[2-4] Several aspects of the structural and dynamical properties of micellar assemblies such as, the parameters which characterize a micelle, nature of the micellar core, charge on the Stern-layer and counterions binding to it, permeability of the micelle with respect to various species, kinetic aspects of the micellar association equilibria, etc., have been investigated. Of immediate interest is information on the micellar core. It is argued[5] that the interior or core of micelles must be "liquidlike". (This is based on thermodynamic analysis, on observations that micelles can solubilize a wide variety of hydrophobic organic solutes, and on the ability of surfactants to form mixed micelles.) Strong experimental evidence on the liquidlike core comes from studies of fluorescence depolarization of aromatic probes solubilized selectively in the micellar core. The measured microviscosities of the order of 30 cP agree well with similar values obtained in pure (homogeneous) hydrocarbon liquids.[6] Quite recently the measurement of carbon-13 spin–lattice relaxation times[7] for various carbon atoms that form the backbone of the hydrocarbon chains show that the fluidity of the micellar core is probably restricted to a few carbon atoms toward the end of the hydrocarbon chain in the micellar core. Further investigations on these aspects of the micelle are necessary at this point, viz., on the conformational state of the hydrocarbon chain in the micelle core and also studies on the influence, if any, of external additives solubilized in the micellar core on the hydrocarbon chain conformation. Laser Raman spectroscopy is an ideal technique for the study of conformations of molecules, especially in aqueous solutions.

In the first part of the paper, Raman spectra of several cationic, anionic, and nonionic surfactants have been examined as pure solids or liquids and also in aqueous solutions. In aqueous media, above a certain critical micelle concentration (cmc), the surfactants aggregate together to form spherical micelles. Assignment of the various peaks in these spectra leads to (further) direct evidence for the liquidlike nature of the micellar core. In the second part, the influence of external additives on the micellar core is examined. In particular the phase changes associated with the electrolyte-induced sphere–rod transition in micellar systems have been investigated. These studies provide significant information on the conformational state of the hydrocarbon chains in the solid state and how they are affected following micellization.

Experimental Section

The laser-excited Raman spectra reported in this study were recorded on a Spex Ramalog laser-Raman spectrometer system equipped with a Spectra-Physics Model 164 Ar ion laser and a photon counting system. Typically the laser was operated to give about 200 mW power (for pure solid and liquid samples) and about 700 mW power (for aqueous solutions) of the 5145-Å green line on the sample. The samples were contained in 1-mm melting point capillaries and the scattered light was collected at 90° to the incoming laser light and analyzed in a Spex dual-grating monochromator. The spectra were run with approximately 200-μm slit width corresponding to $\simeq$4-cm^{-1} band width. Hence the accuracy in the reported frequencies is estimated to be $\pm$2 cm^{-1}. None of the spectra reported in this work are polarized. No interference filters were used in this work.

All surfactants used in this study were of purum grade and were recrystallized several times in ethanol–ether mixtures before recording the spectra. No significant differences, however, were observed in the solid spectra of the samples used before and after crystallization. All spectra reported were recorded at room temperature (25 °C). All electrolytes and additive used were also of AR grade.

Results and Discussion

(1) *Laser-Excited Raman Spectra in Pure and Micellar Form.* (a) *Cationic Surfactants in the Solid State.* The

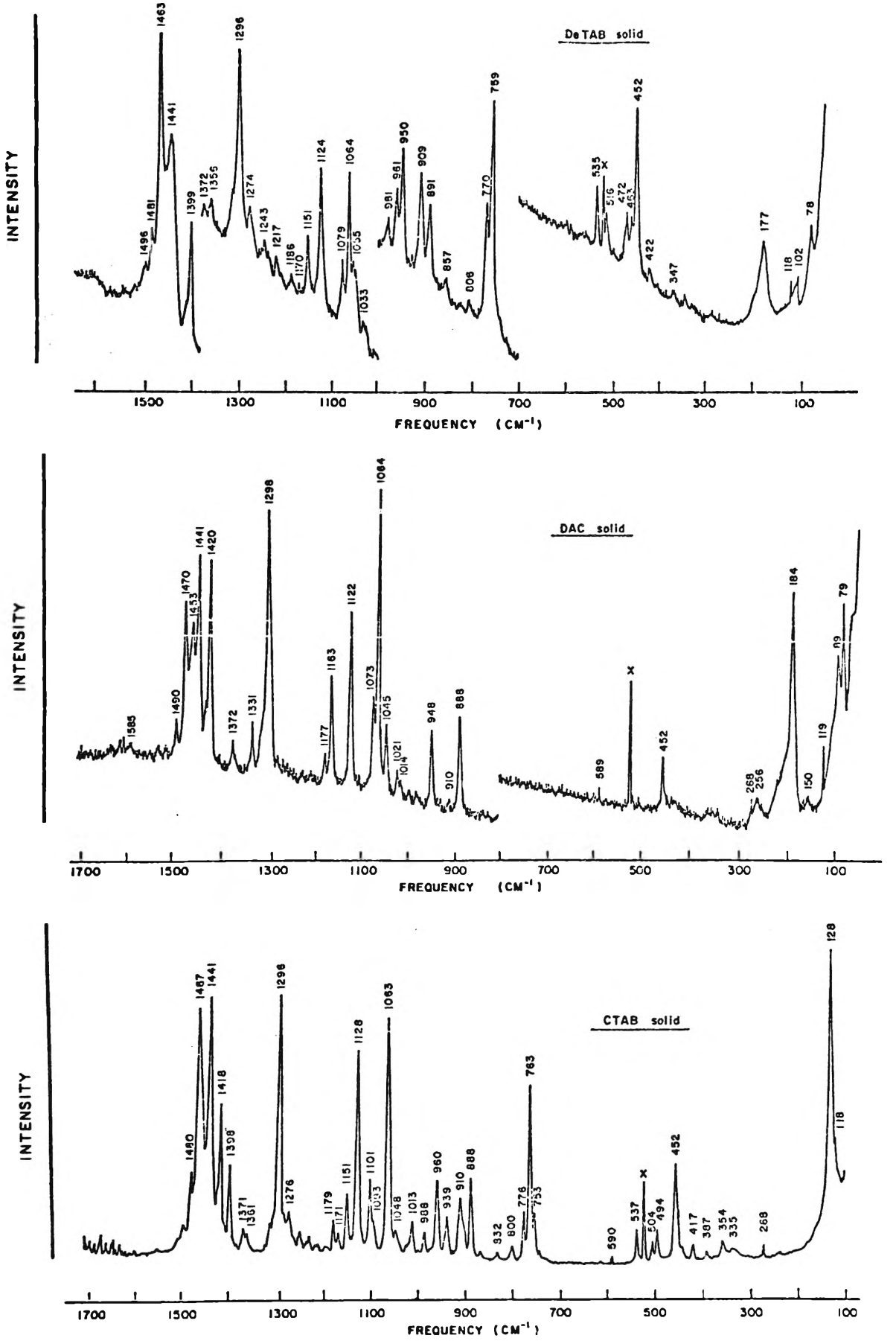

Figure 1. Raman spectra (up to 1700 cm^{-1}) of the crystalline surfactant solids hexadecyltrimethylammonium bromide (CTAB), dodecylammonium chloride (DAC), and decyltrimethylammonium bromide (DeTAB).

TABLE I: Raman Frequencies for the Cationic Surfactant Solids CTAB, DAC, and DeTAB

CTAB	Hexadecane[a]	DAC	Dodecane[a]	DeTAB	Decane[a]	Tentative assignments
128	150	184	194	177	231	
		256				
		268				
452		452		452		Longitudinal accordion modes
				463		
494				472		
504				506		
537				535		
753						
763				759		CH_3 rock from $N^+(CH_3)_3$ group
776				770		
800				806		
888	883	888	892	891	886	CH_3 rock (terminal methyl)
910		910		909		$C-N^+$ stretch
939		948		950		
960				961		CH_2 rock
988				988		
1013		1014		1033		
1048		1045		1055		CH_2 twist, crystalline
1063	1053	1064	1061	1064	1060	C–C sym stretch + CH_2 wag
1093		1073		1079		C–C stretch, crystalline
1101						
1128	1135	1122	1136	1124	1136	C–C asym stretch + CH_2 wag
1151		1163		1151		from (TG_mT) with m large
						CH_2 rock
1179		1177		1186		
1212					1217	
1229		1224				CH_2 wag, crystalline
1241		1240		1243		
1276				1274		
1296	1295	1298	1297	1296	1295	CH_2 twist
		1331		1356		CH_2 wag
1371		1372		1372		$C-CH_3$ sym bending
1398				1399		C–H sym bend from $N(CH_3)_3$ group
1418		1420				$-CH_2$ bend
1441	1442	1442	1441	1441	1447	$-CH_2$ bend
1467	1471	1453	1462	1463	1475	$-CH_2$ bend, crystalline
1480		1470				$-CH_2$ bend
2849	2846	2848	2845	2851	2843	C–H sym stretch of $-CH_2^-$
2857		2857		2858		
2882	2878	2882	2879	2883	2877	C–H sym stretch of CH_3^-
2889		2888				
2904		2902		2906		
2914		2914				
2933	2934	2932	2933	2933	2935	C–H asym stretch of $-CH_2^-$
2944		2950		2943		
2972	2963	2973	2964	2965	2964	C–H asym stretch of CH_3^-
2981		2981		2982		C–H sym stretch of $CH_2-N^+(CH_3)_3$ group

[a] Data taken from ref 12.

Raman spectra of the typical cationic surfactants hexadecyltrimethylammonium bromide (CTAB), dodecylammonium chloride (DAC), and decyltrimethylammonium bromide (DeTAB) in the crystalline solid state are shown in Figure 1. The observed Raman frequencies (100–1700-, 2800–3000-cm^{-1} regions) along with their tentative assignments are summarized in Table I. These assignments are based on a comparative analysis of the spectra of a wide series of surfactants of different chain length and of different head groups and on the basis of the earlier assignments made on the ir and Raman spectra for n-paraffin solids and liquids.[8] For the purpose of comparison we have also included in this table data for solid n-hexadecane, dodecane, and n-decane.

Chain conformations of solid and liquid long-chain hydrocarbons have been examined already[8–10] by ir and Raman spectroscopy. Several regions in the Raman spectra are sensitive to conformational changes. The 1000–1200-cm^{-1} region corresponds to the skeletal C–C stretching vibration in which the alternate carbon atoms move in the opposite direction. For an extended chain with all-trans structures, there are two intense bands in this region: one at 1064 ± 2 cm^{-1} and the other around 1130 cm^{-1}. These bands have been assigned to the symmetric or in-phase C–C stretching and the asymmetric C–C stretching, respectively. In addition, there is another additional band at 1075–1100 cm^{-1} arising from all-trans crystalline structure vibrations. In molten polyethylene and in liquid hydrocarbons a broad intense band centered around 1090 cm^{-1} is observed in addition to much weaker bands at 1064 and 1130 cm^{-1}. The collapse of the symmetric and antisymmetric C–C stretching into a central spectral maximum implies that an ordered crystalline and extended all-trans chain becomes kinked with the concomitant appearance of a wide distribution of structures which include several gauche rotations. The acoustical mode vibrations due to the presence

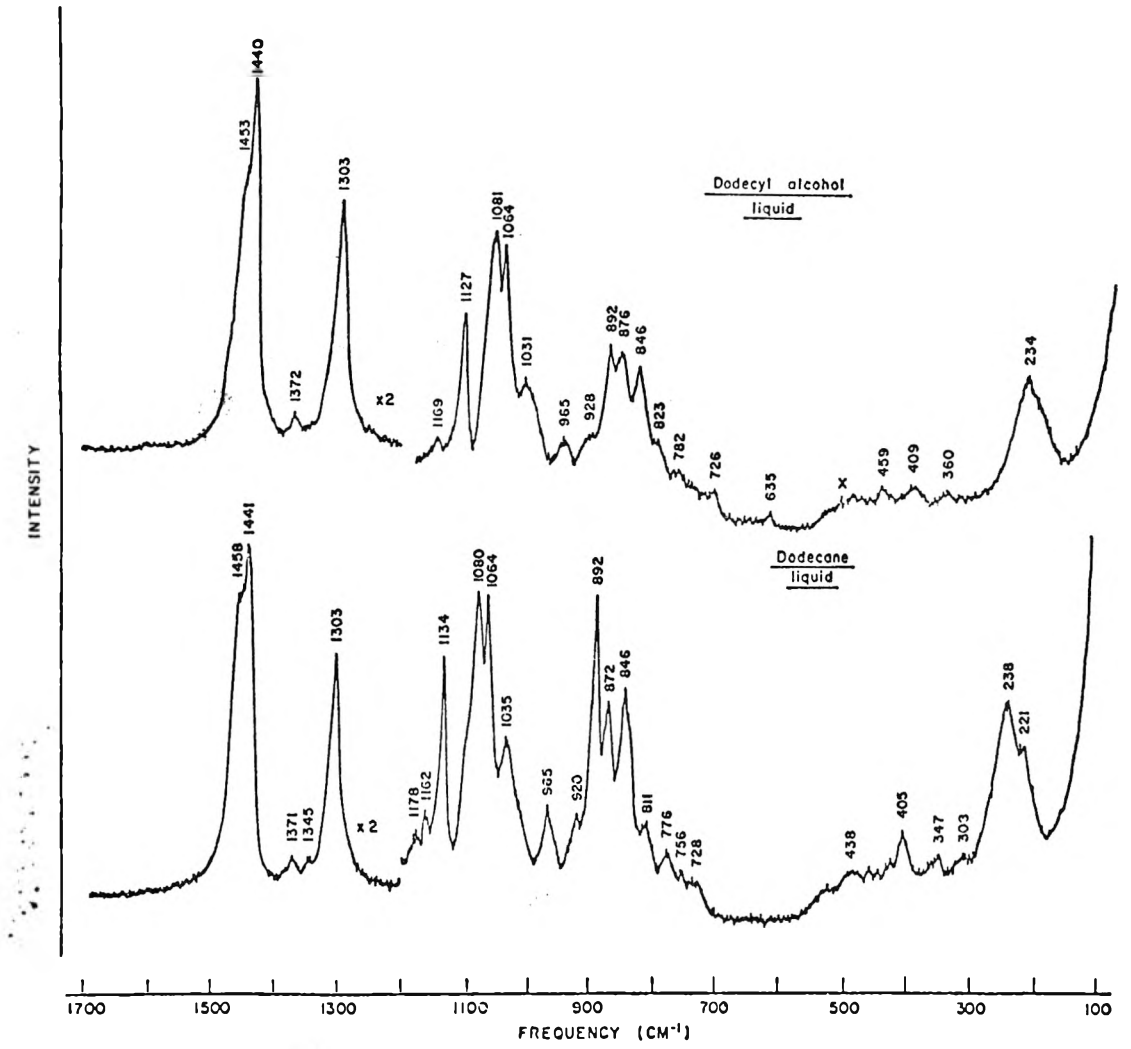

Figure 2. Raman spectra (up to 1700 cm^{-1}) of the hydrocarbon liquids dodecane and dodecyl alcohol.

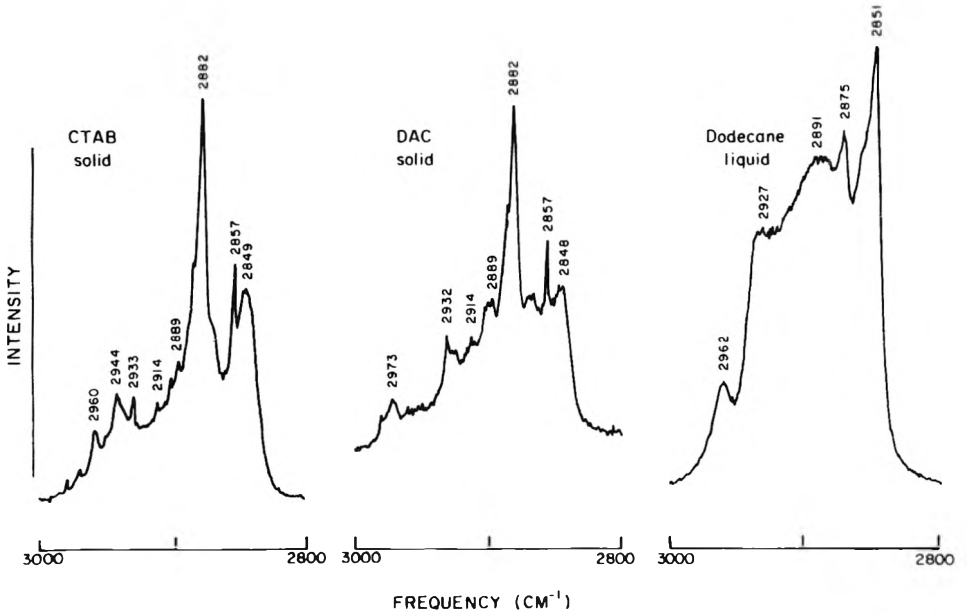

Figure 3. Raman spectra (2800–3000-cm^{-1} region) for CTAB solid, DAC solid, and dodecane liquid.

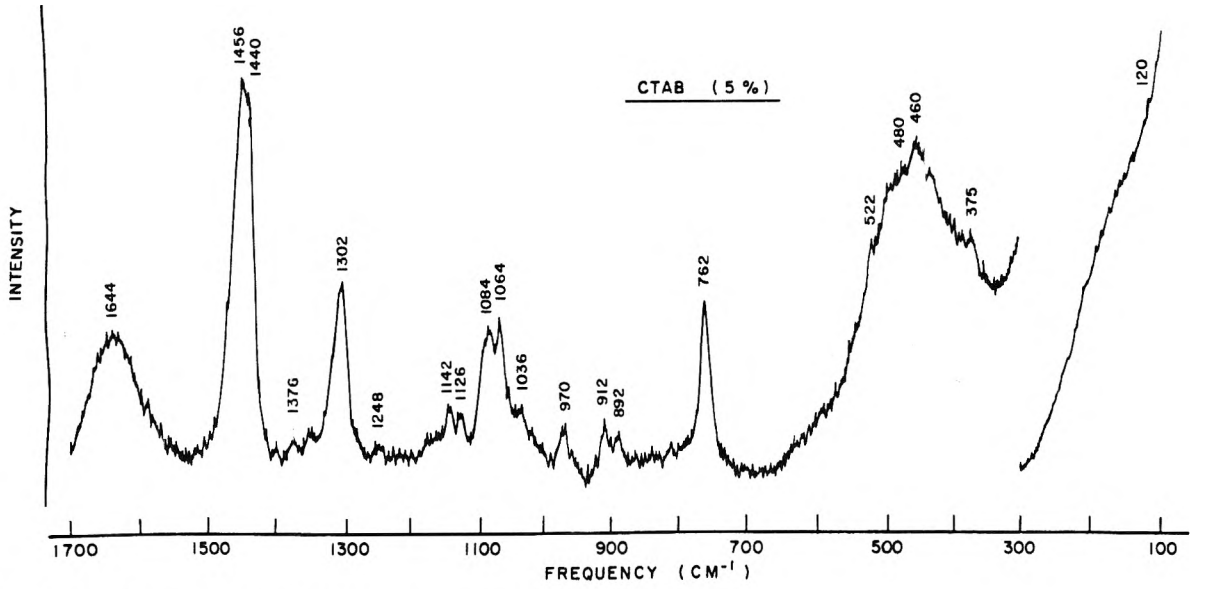

Figure 4. Raman spectrum for a 5% (0.1375 M) micellar solution of CTAB in H_2O.

of random gauche isomers also give rise to a broad band around 230 cm^{-1} (cf. Figure 2). In the C–H stretching region, in the crystalline state the peak around 2880 cm^{-1} due to the symmetric stretch of the CH_3 group is more intense than the symmetric stretch of the CH_2 group at 2850 cm^{-1}. These bands assume equal intensities or even $I_{2880} < I_{2850}$ when several gauche isomers are present.

The Raman spectra of the cationic surfactants CTAB, DAC, and DeTAB, presented in Figure 1, all indicate the existence of an all-trans extended chain structure. All three spectra show intense bands at 1064 and 1124 cm^{-1} (due to C–C symmetric stretching in an all-trans structure), and a weak band around 1100 cm^{-1}. The longitudinal accordion motions of the hydrocarbon chains lead to the peaks at 128 cm^{-1} in CTAB, 184 cm^{-1} in DAC, and 177 cm^{-1} in DeTAB, respectively. The peak at 1296 ± 2 cm^{-1} and the resolved fine-structure band around 1450 cm^{-1} arise from the methylene twisting and bending modes, respectively. Another salient feature of all three spectra is the occurrence of peaks at constant frequencies of 452, 888, and 960 cm^{-1} having their origin in the C–N stretching, CH_3 rocking, and $-CH_2$ rocking modes, respectively. As the hydrocarbon chain length increases from 10 carbons in DeTAB to 16 in CTAB, the spectrum becomes more and more complex due to the several additional combinatorial vibrational modes of the hydrocarbon chain.

Returning now to Figure 2, which represents the Raman spectra of the pure hydrocarbon liquids dodecane and dodecyl alcohol, one observes two significant differences. As mentioned earlier, the presence of several gauche rotational isomers in these liquids gives rise to new bands at frequencies of about 1080 ± 2 cm^{-1} and a broad band around 235 cm^{-1}. The peak at 1080 cm^{-1}, due to random liquidlike configurations, has been used earlier to study phase transition in phospholipid dispersions.[10]

Further evidence for an extended chain conformation in solid cationic surfactants derives from the nature of the Raman spectrum in the 2800–3000-cm^{-1} region. The solid state spectra for CTAB, and liquid dodecane, in this region are presented in Figure 3. It is seen that in liquid dodecane the symmetric CH_2 group vibration (at 2851 cm^{-1}) is more intense than the methyl symmetric vibration (at 2882 cm^{-1}) and the asymmetric vibration of the CH_2 group (at 2927 cm^{-1}). The reverse situation, however, prevails in solid CTAB and DAC. In a rigid crystalline structure, the CH_3 symmetric vibrations are well defined and hence the peaks at 2882 cm^{-1} are more intense.

(b) *Cationic Surfactants in Micellar Form.* In aqueous solutions of about 0.1 M, the cationic surfactants CTAB and DAC aggregate together to form "spherical" micelles. For CTAB Figure 4 represents the Raman spectrum of a 5% (0.1375 M) aqueous solution of this surfactant. The critical micelle concentration of CTAB is 9.2×10^{-4} M and hence contributions from monomeric surfactants are <1% and can be safely assumed to be negligible. This situation is also true for all the surfactants examined in micellar form in this study. Micellization of the surfactant in water leads to a simplification of the Raman spectrum. In Figure 4 a new intense band at 1084 cm^{-1} is noted which indicates that the hydrocarbon chains in the micellar core remain "fluid" (kinked) with several gauche isomers present. In contrast to the spectra of liquid hexadecane or molten polymethylenes in this region, the bands at 1064 cm^{-1} (due to C–C symmetrical stretching) and at 1126 cm^{-1} (due to C–C asymmetrical stretching) are still present showing that a significant length of the hydrocarbon chain remains in an all-trans form. In the low frequency region (<500 cm^{-1}), the water scatter background tends to obscure any well-defined spectral structure. However, it is still possible to observe a broad intense band around 460 cm^{-1} and a diffuse band at ca. 150 cm^{-1} due to random gauche configurations.

In *n*-paraffins, it is suggested that as the random character of the hydrocarbon chain increases (either by an increase in chain length or by a phase change, viz., the melting of a solid to the liquid state) and that the accordion motions shift to higher frequencies. Mizushima and Simanouti[12] have calculated the skeletal deformational frequencies for *n*-paraffin solids in the extended form (all-trans) to be around 432 (n = 4), 402 (n = 5), and 369 cm^{-1} (n = 6). Indeed these frequencies have been observed in the spectra of *n*-paraffins. The presence of a broad band in the 350–520-cm^{-1} region in the micellized CTAB implies that this band should have its origin in the carbon atoms of the hydrocarbon chain that are removed four–six CH_2 units from the polar head group. The polar head

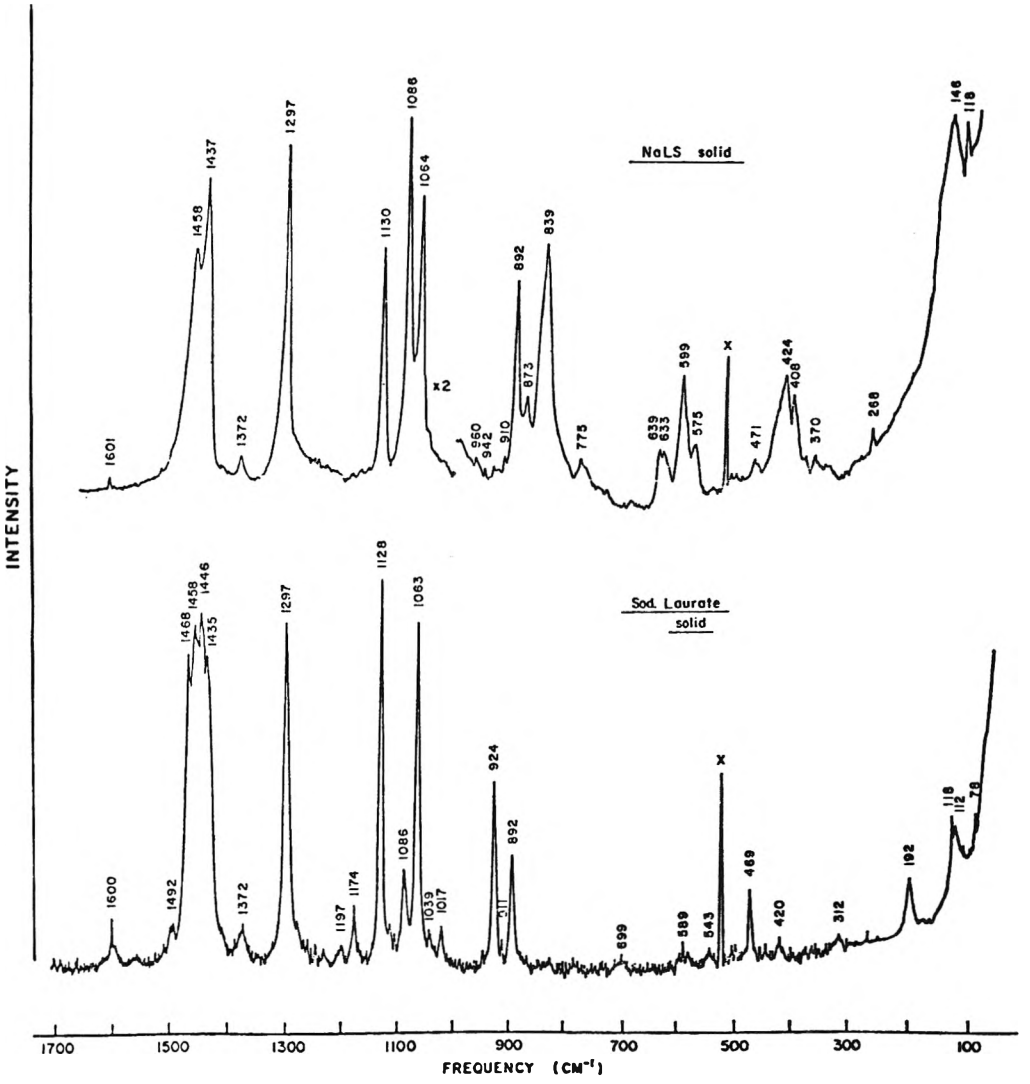

Figure 5. Raman spectra (up to 1700 cm^{-1}) for the crystalline solids sodium laurate (NaL) and sodium lauryl sulfate (NaLS).

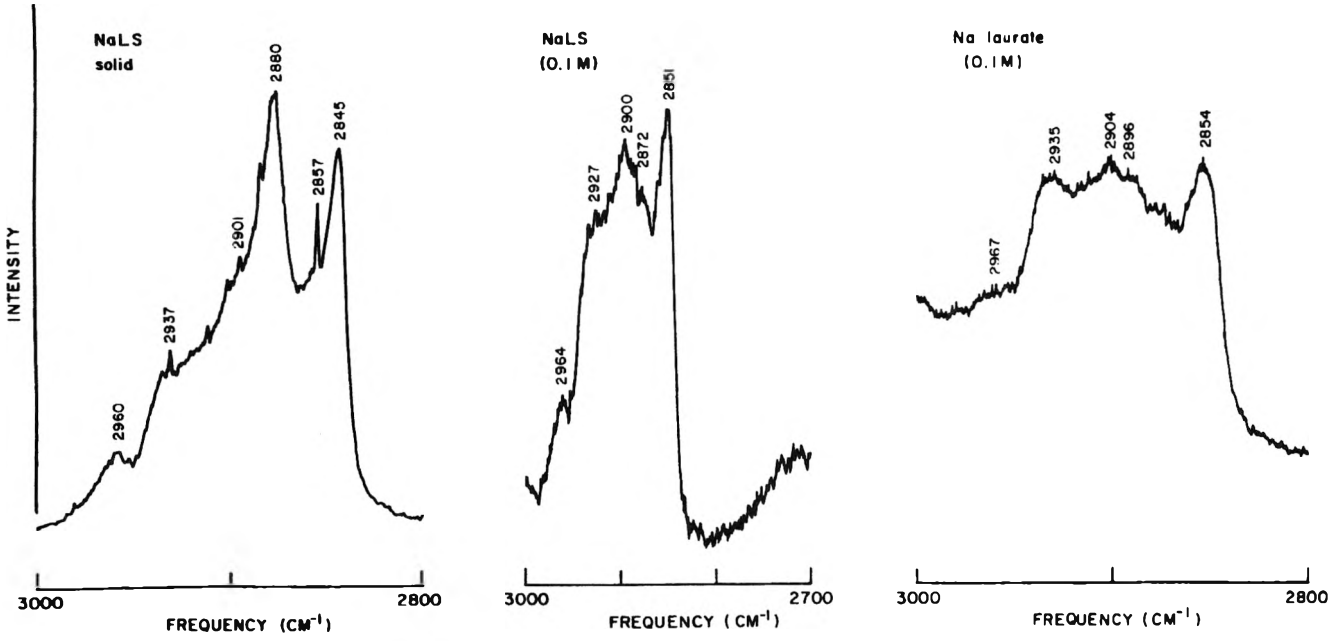

Figure 6. Raman spectra (2800–3000-cm^{-1} region) for NaLS solid along with those of micellar solutions of NaLS (0.1 M) and NaL (0.1 M).

groups are anchored in the Stern-layer of the micelle. Hence the motion of the hydrocarbon chain subsequent to the head group is considerably restricted.

The identification of exact location of the chain kinking, i.e., the positions of the carbon atoms involved in the formation of "gauche" isomers, requires a complete vibrational analysis similar to those performed by Snyder et al.[8] For short chain hydrocarbons, ($n < 8$) the Raman frequencies and intensities are calculated for various configurations of the hydrocarbon chain, viz., those with two, three, or four gauche isomers. The most probable configurations are then identified by comparison of the calculated spectra to those observed experimentally. Unfortunately for long-chain surfactants where the number of C atoms is greater than eight, the calculations become prohibitively complex. The experimental task of identifying and observing each of the numerous Raman frequencies is also difficult. In a qualitative sense the Raman spectral data presented above confirm the presence of gauche isomers (fluidity). The data also indicate that the molecular motions of the hydrocarbon chains are *not* as random as observed in pure hydrocarbon liquids such as hexadecane or molten polymethylene.

The above picture for the conformational state of hydrocarbon chains in the micellar core agrees well with the carbon-13 spin–lattice relaxation data.[7] In micellar solutions of 0.2 M DAC the carbon-13 T_1 values for backbone carbons range from 0.34 to 0.50 s. These data indicate that about eight carbon atoms adjacent to the polar head group are in a rigid structure. The T_1 values, however, show a sharp increase to 2 s for the remaining carbon atoms (three carbons in DAC) at the end of the chains. This T_1 value is comparable to those observed for the various carbon atoms in *n*-paraffin liquids.[13] It is suggested that the gauche isomers which contribute to the 1081-cm^{-1} band in the laser-Raman spectrum should arise from the liquidlike structures associated with the carbon atoms toward the end of the chains. The presence of gauche isomers is also indicated by the increased intensities of the methyl and methylene wagging modes of gauche isomers in the 890-cm^{-1} spectral region (compare Figures 2 and 4).

(c) *Crystalline Anionic Surfactants.* The laser-Raman spectra of two representative anionic surfactants, sodium lauryl sulfate (NaLS), and sodium laurate (NaL), in the crystalline state are presented in Figure 5. A similarity is observed on comparing the NaL spectrum to the spectra of the cationic surfactants (Figure 1). The spectrum of NaLS, however, seems to show some apparent anomalies. The sodium laurate spectrum exhibits features characteristic of an extended all-trans chain, viz., (a) intense C–C symmetric and antisymmetric stretching modes at 1063 and 1128 cm^{-1}, (b) a rather sharp and intense methylene twists peak at 1296 cm^{-1}, and (c) and intense CH_2 wagging mode frequencies characteristic of trans structures at 592 and 924 cm^{-1}. These features were also observed in cationic solids CTAB and DAC.

Sodium lauryl sulfate is one of the few surfactants which has been studied extensively by a variety of physicochemical techniques. Hence a detailed study of its laser-Raman spectrum was made. It is possible by a comparison of the solid state spectrum of a series of sodium alkyl sulfates [$CH_3(CH_2)_n$-SO_4Na with n = 4, 6, 8, 10, 12, 16] to assign the various peaks in the Raman spectrum of solid NaLS. As in other long chain hydrocarbon solids, NaLS shows C–C symmetric and antisymmetric stretching frequencies at 1064 and 1130 cm^{-1}. In all sodium alkyl sulfates, the symmetric stretching of SO_3 appears as a strong band around 1080 cm^{-1}. (In NaLS this band appears at 1086 cm^{-1}.) In addition to the Raman frequencies arising from the hydrocarbon chain, Raman frequencies due to the sulfate head group appear: (a) RO–SO_3 stretch at 839 cm^{-1}, (b) symmetric and antisymmetric deformation modes at 575 and 633 cm^{-1}, and (c) SO_3 rocking at 408 cm^{-1}. In *n*-paraffins Raman spectra are characterized by (a) a broad intense peak at 1086 cm^{-1}, (b) a broad band in the 830–900-cm^{-1} region, and (c) a broad band in the 600–650-cm^{-1} region. These imply the presence of extensive gauche forms of the hydrocarbon chains. The appearance of Raman frequencies in these regions due to the sulfate head group[14] obviates clear cut answers on this point. However, the presence of an extended chain with all-trans structures is indicated by several features: (i) presence of sharp intense bands at 1064 and 1130 cm^{-1} due to C–C stretching; (ii) a sharp peak at 1297 cm^{-1} as in CTAB and DAC solids and unlike the rather broad peak at 1303 cm^{-1} in hydrocarbon liquids; (iii) the appearance of the accordion mode frequency at 146 cm^{-1}. The corresponding frequencies for DAC solid and dodecane liquid are 184 and 278 cm^{-1}, respectively. With increasing amounts of gauche isomers, the accordion frequencies shift to higher frequencies; (iv) the nature of the Raman spectrum in the C–H stretching region 2800–3000 cm^{-1} (Figure 6). The features of this spectrum resemble that of extended chain solids, e.g., CTAB and DAC, as compared to that of liquid dodecane.

(d) *Anionic Surfactants in Micellar Forms.* The laser-Raman spectrum of a 0.1 M aqueous micellar solution of NaLS is presented in Figure 7. The 1000–1200- and 2800–3000-cm^{-1} regions for micellar NaLS and NaL are specifically compared in Figures 6 and 8. As in the case of cationic surfactants micellization of the surfactant leads to changes in the chain configurations. A predominance of gauche rotomers is observed. This is quite apparent in the case of sodium laurate micelles. The sodium laurate micelles appear to be more fluidlike, as the intensity of the 1081-cm^{-1} peak is greater than the 1065- and 1123-cm^{-1} peaks. In the case of NaLS, micellization leads to a considerable reduction in the intensity of the 1084-cm^{-1} peak (it appears as a shoulder in the 1063-cm^{-1} peak). In addition there are broad bands around the 828- and 300–500-cm^{-1} regions, respectively. The spectral features of the 2800–3000-cm^{-1} region are also in accord with the picture of a micelle with a fluid core. A change in conformation for NaLS following interactions with lysozyme has been noted recently by Lord et al.[15] Presumably the significant drop in the intensity of the 1086-cm^{-1} peak is due to a freezing of the sulfate head group in the electrical double layer of the micelle.

(e) *Raman Spectra of Pure Nonionic Surfactants.* In addition to examining the Raman spectra of cationic and anionic surfactants, we have also investigated the Raman spectra of a series of nonionic surfactants. In particular we have examined Igepal CO-630, Igepal CO-880, Triton X-100, and Brij

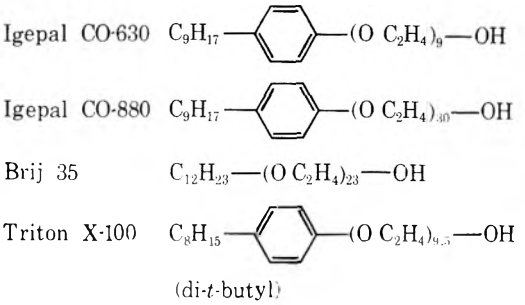

35. The lower members of these polyoxygenated surfactants are viscous liquids at room temperature (25 °C), while the higher member Igepal CO-880 is a waxy solid. Raman spectra

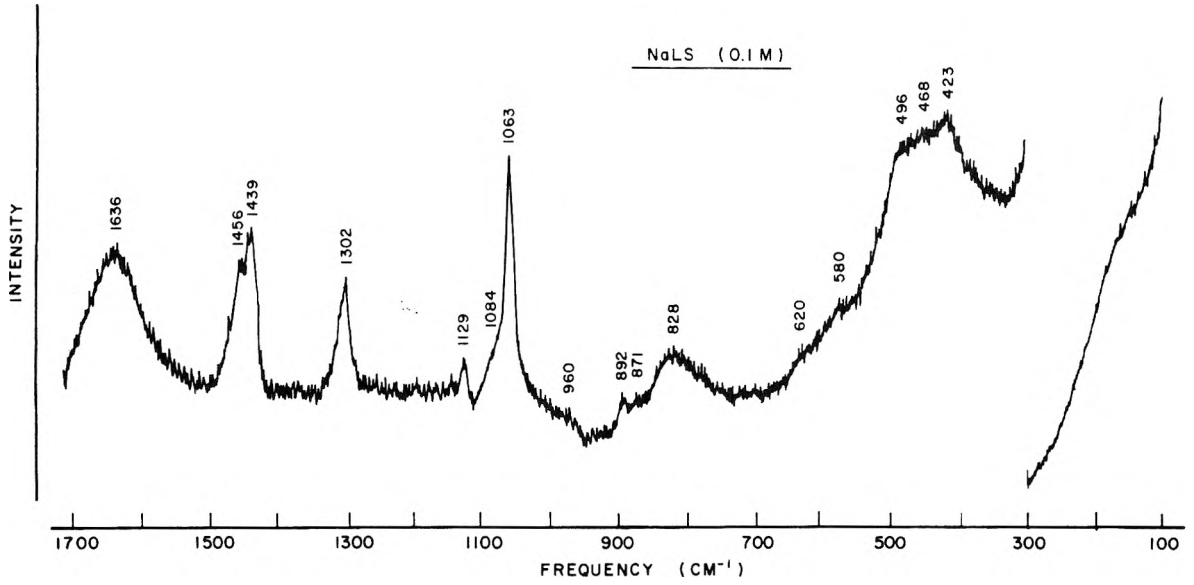

Figure 7. Raman spectrum of 0.1 M micellar solution of NaLS in H_2O.

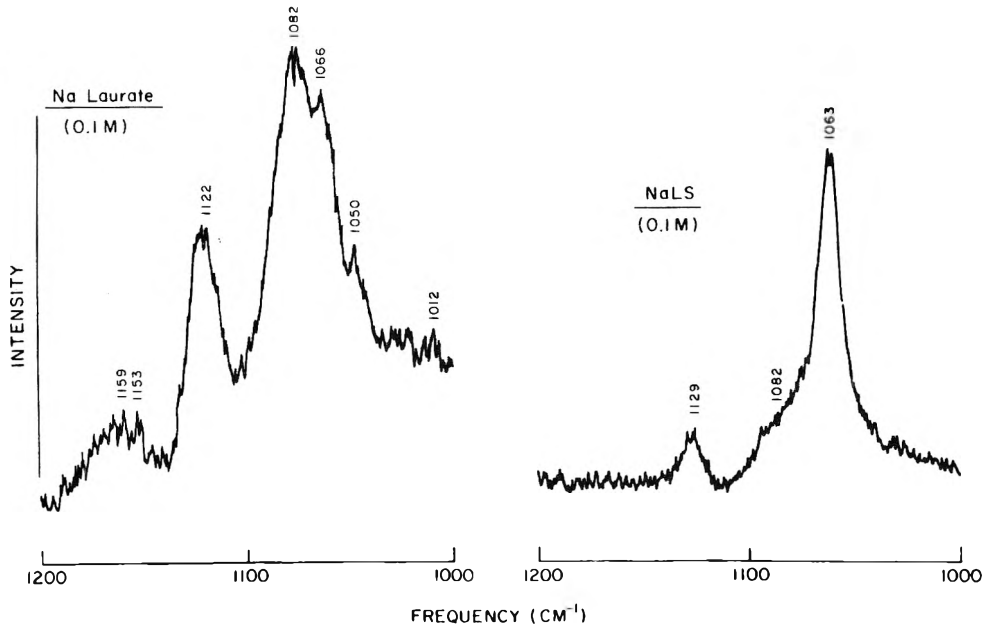

Figure 8. Raman spectra (1000–1200-cm^{-1} region) for 0.1 M micellar solution of NaLS and NaL in H_2O.

for Triton X-100 and Igepal CO-630 liquids and Brij 35 and Igepal CO-880 as solids are presented in Figures 9 and 10. The Raman spectra of nonionic surfactants give information on the nature of hydrocarbon core of these micelles. In addition information on the configuration of the ethylene oxide chain is also obtained. Both "zig-zag" and "meander" models for the oxyethylene group have been discussed in the literature.[16] The first model refers to ethylene oxide configurations which are "fully extended" chains in the paliside layer on the exterior of the micelle. In the second model the ethylene oxides assume helical coil forms which twist and wind in the paliside layer from the hydrophobic center to the micellar surface.

Several interesting conclusions can be drawn from examination of the Raman spectra presented in Figures 9 and 10. The Raman spectra in Figures 9 and 10 look entirely different from those of long chain fatty acids, but resemble more those of polyethylene glycols[17] (PEG). This is to be expected as the hydrocarbon part of the nonionic surfactants examined here are either short or highly branched. The Raman frequencies arising from the alkane chains overlap with those arising from the polyxyethylene chains. In short the Raman spectra are dominated by vibrations arising from the polyoxyethylene chain, thereby facilitating a direct observation of the conformational state of the hydrophilic part of the micelles formed by these nonionic amphiphiles. In the series Igepal CO-630, Brij 35, and Igepal Co-880, the ethylene oxide (EO) unit increases from 9 to 30. Examination of the Raman spectra show drastic changes from Igepal CO-630 to Igepal Co-880. Brij 35, occupying an intermediate position, shows a spectrum which is an overlap of the spectra of the shorter chain CO-630 and longer chain CO-880.

As mentioned earlier, the Raman spectrum of solid Igepal CO-880 strongly resembles that of solid polyethylene glycol (PEG). Table II summarizes the observed Raman frequencies

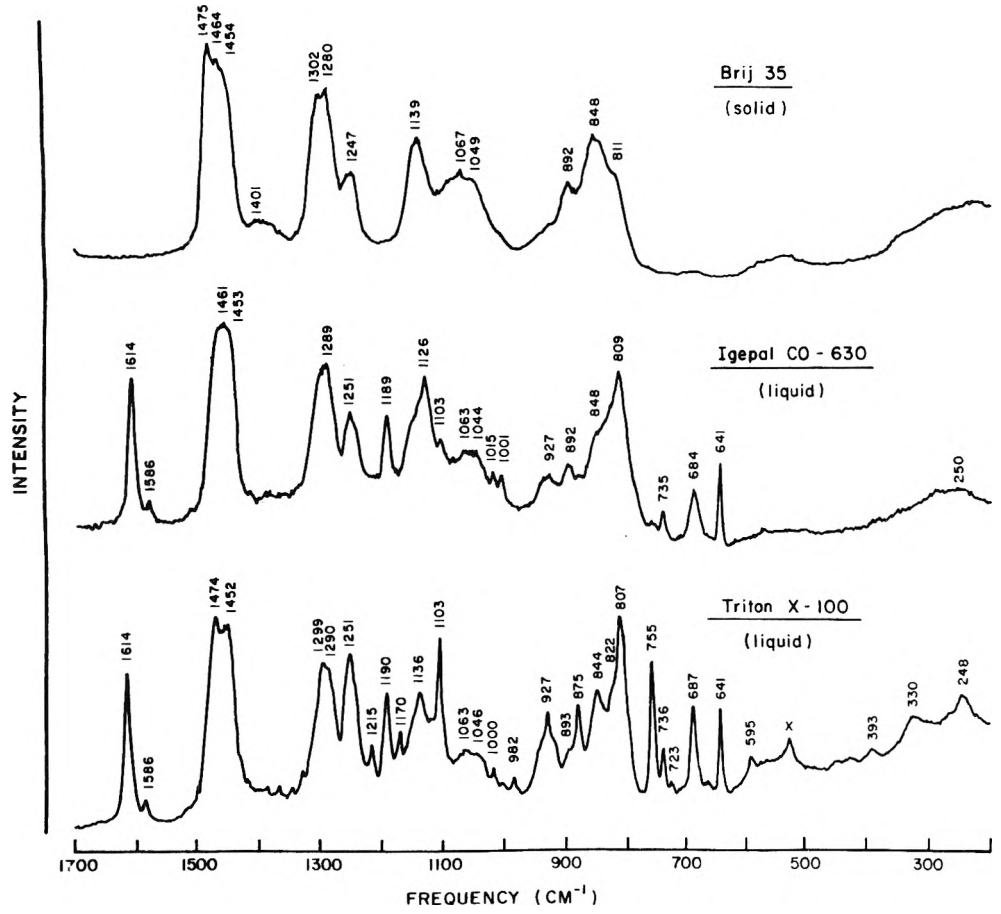

Figure 9. Raman spectra for the nonionic surfactants Triton X-100 liquid, Igepal CO-630 liquid, and Brij 35 waxy solid.

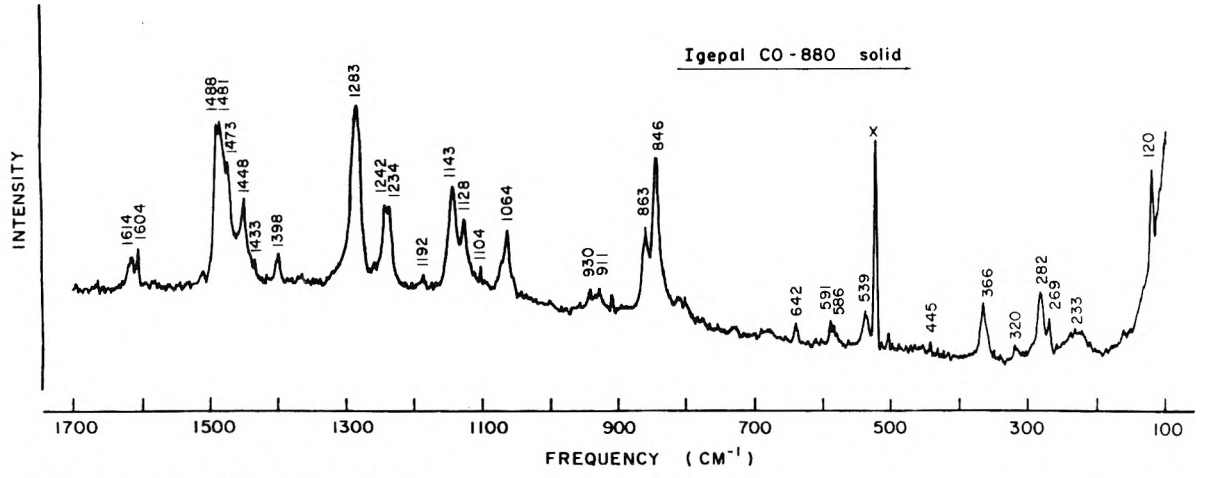

Figure 10. Raman spectrum of Igepal CO-880 solid.

together with their intensities for comparison with solid PEG. The conformational states of the ethylene oxide unit in solid PEG, molten PEG, and PEG in aqueous solution have been examined earlier by Koenig and Argood.[17] Combined (x-ray analysis, ir, NMR, and Raman) studies of PEG have established that PEG has a helical conformation in the crystalline solid with the seven chemical units (CH_2–CH_2–O) and two turns in a repeat distance of 19.3 Å. Furthermore the PEG has a dihedral symmetry (i.e., the chain possesses two kinds of twofold axis: one passing through the oxygen atom and the other bisecting the C–C bond). The PEG repeating unit has a TGT (T = trans, G = gauche) conformation of the CH_2–O–CH_2–CH_2–O sequence. The dihedral helical conformation is characterized by typical Raman lines and will be discussed below. The striking similarities between the Raman spectra of the 30 (EO) unit nonionic surfactant Igepal CO-880 and that of PEG solid indicate that the long ethylene oxide unit has a helical structure with the dihedral symmetry in the surfactant. However, as the length of the ethylene oxide decreases from 30 EO units to 9 in Igepal CO-630 (the latter is a viscous liquid at room temperature), the helical conformation is no longer preferred. A disordered structure prevails

TABLE II: Raman Frequencies for Igepal CO-880 Solid along with Those of Polyethylene Glycol (PEG) Solid

PEG solid[a]	Igepal CO-800 solid	Tentative assignments
537 s	538 w	(OCC) bending
583	586 w	
	591 w	
	643 w	
	777 vw	
811 w	806 vw	Amorphous (from disordered structures)
846 vs	846 vs	CH_2 rock
860 m	863 m	CH_2, C=O rock
	911 m	
936 vm	929 w	Amorphous (from disordered structures)
947 w	945 w	CH_2 C=O rock
1065 m	1065 m	C–O stretch, CH_2 rock
1073 sh	1078 sh	
1125 m	1128 m	C–C stretch, CH_2 wag
1142 s	1143 s	C–O stretch
1232 m	1232 m	CH_2 twist
1237 w	1242 m	
1283 vs	1283 vs	
1286 w		
1376 w	1367 w	CH_2 wag, C–C stretch
1396	1399 mw	
1448 m	1448 m	CH_2 scissoring
1471 sh	1473 sh	
1481 s	1481 s	CH_2 scissoring
1486 s	1488 s	

[a] Data taken from ref 17: s = strong, w = weak, m = medium, sh = shoulder, vw = very weak.

which includes the presence of several rotational isomers. Table III presents a comparison of the Raman frequencies for liquid Igepal CO-630 and Triton to that of molten PEG. The Raman spectra of lower member short EO chain surfactants resemble that of molten PEG.

As indicated earlier, the Raman spectra of solid Igepal CO-880 and liquid Igepal CO-630 show several differences. In Igepal CO-880 there are two intense bands at 846 and 863 cm^{-1} in the methylene and methyl rocking regions. In Igepal CO-630, however, there are three peaks at 807, 848, and 892 cm^{-1}, the 807-cm^{-1} peak being more intense than the other two. For Igepal CO-880 in the methylene rocking region the 1143-cm^{-1} line is more intense than the 1128-cm^{-1} line. In Igepal CO-630 these two lines merge together, the 1126-cm^{-1} line is more intense, and the 1143-cm^{-1} line appears as a shoulder. The CH_2 bending region also shows significant changes. The four peaks at 1448, 1473, 1481, and 1488 cm^{-1} of the surfactant Igepal CO-880 merge to two peaks (at 1453 and 1467 cm^{-1}) on reduction of the ethylene oxide unit from 30 to 9. It is also noted that the peaks at 1234 and 1242 cm^{-1} merge to 1251 cm^{-1} in CO-630 with a significant increase in the intensity of the 1189-cm^{-1} line. There is also a considerable reduction in the intensity of the peaks at 945 and 1399 cm^{-1}. The shorter chain surfactants show a more intense band at 1615 cm^{-1}. These spectral differences are also observed in liquid and solid PEG. Based upon the assignments of various peaks (which in turn are based on model vibrational analysis, details are discussed at length in the reference cited above) it is concluded that on the melting of PEG (or on reduction of the EO chain length in the surfactant) that the helical EO structure opens up with the formation of new rotational motions. These motions occur mainly at the C–O bonds rather than around the C–C bonds. According to Koenig et al., this

TABLE III: Raman Frequencies for the Nonionic Surfactant Liquids Igepal CO-630 and Triton X-100 along with Those of PEG Melt

Triton X-100	Igepal CO-630	PEG melt[a]	Tentative assignments
248 w	250 w	261 w	
330 w			
393 vw			
430 vw			
		524 w	
595 w	570 vw	526 w	
641 m	641 m		
687 m	684 m		
723 vw			
736 w	735 w		
755 s	753 vw		
807 s	809 s	807 m	
822 sh			
844 m	848 sh	834 m	CH_2 rock
875 m			
893 sh	892 w	884 mw	
927 m	927 w	919 sh	
982 vw			
1000 vw			CH_2 rock, C–O, C–C stretch
1015 vw	1015 vw		
1046 w	1044 m		
1063 w	1063 sh	1052 m	C–O, C–C stretch
1103 s	1103 sh		C–O, C–C stretch, CH_2 rock
1136 m	1126 s	1134 s	C–O, C–C stretch
1170 w			
1190 m	1189 m		
1215 s			
1251 s	1251 m		CH_2 twisting
1290 s	1289 s	1283 s	
1299 s	1295 sh	1291 m	
1351 vw		1352 m	CH_2 wagging
1371 vw			
1390 vw	1380 w		
1452 sh	1453	1448 sh	CH_2 scissoring
1474 s	1467 s	1470 s	

[a] See footnote *a* to Table II.

also implies the presence of several additional rotational isomers, with the ethylene oxide configuration changing from a trans–gauche–trans sequence in the solid to a gauche–gauche–trans sequence in the liquid.

The surfactant Brij-35 has an intermediate EO chain length. Here the Raman spectrum shows features of both the longest chain Igepal CO-880 (with 30 EO unit) and that of shortest Igepal CO-630 (9 EO units). With a chain length of 23 EO units significant portions of the polyoxyethylene chains remain in a helical form with a dihedral symmetry, while a small part of the chain exhibits a disordered structure (open coil) with several gauche isomers. The nonionic amphiphile Triton X-100 is a homogeneous mixture of different EO chain lengths, with an average around 9.5. Consequently the Raman spectrum resembles that of Igepal CO-630 except that the Raman lines due to open coils are more intense.

(f) *Nonionic Surfactants in Micellar Form.* Alkyl polyoxyethylene glycol monoethers, such as Brij 35, as well as alkyl phenoxy polyethyleneoxy ethanols, such as Igepals or Tritons, aggregate together in aqueous solution to form spherical micelles. As the molecular chain lengths are quite large, large micelles are formed with aggregation numbers typically around 100–150.[5a] As in the case of ionic micelles, these nonionic micelles[18,19] have a liquidlike hydrophobic core formed by the alkyl chains, while the ethylene oxide units form a hydrophilic palisade layer. NMR studies[19] indicate that the ethylene oxide units are hydrated and that the water mole-

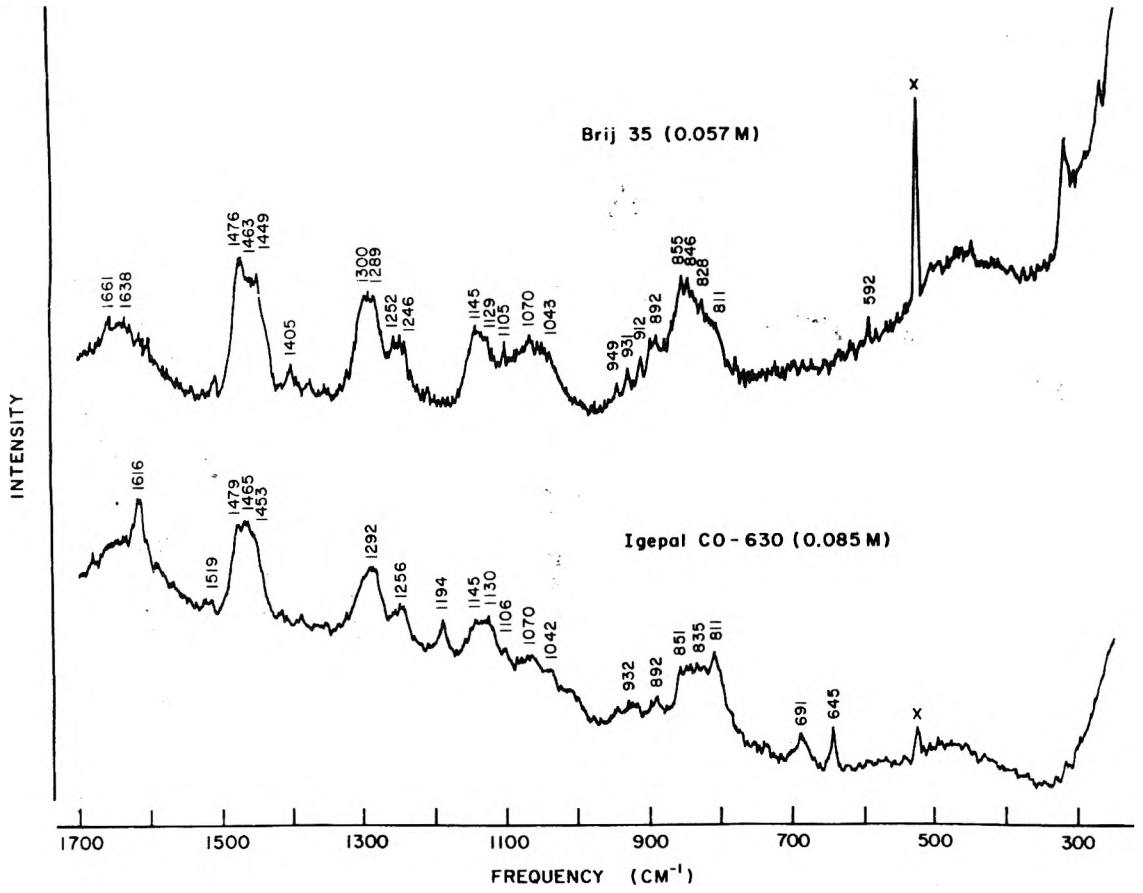

Figure 11. Raman spectra of micellar solution of Igepal CO-630 (0.059 M) and Brij 35 (0.025 M) in H_2O.

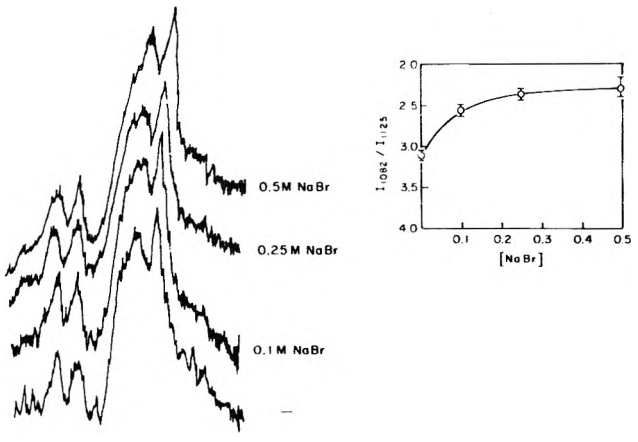

Figure 12. Raman spectrum (1000–1200-cm^{-1} region) for 0.1 M CTAB in the presence of an increasing concentration of NaBr and a plot of (I_{1082}/I_{1125}) for the series of spectra shown.

cules in the region between the polyoxyethylene chains appear to be partially immobilized. It is of interest to see whether any additional information can be obtained from Raman spectral studies.

The Raman spectra of micellized Igepal CO-630 (0.059 M) and Brij 35 (0.025 M) in H_2O are presented in Figure 11. A comparison of the spectra of Igepal CO-630, in the pure and micellar form, shows instructive differences. In micellar form, the spectrum show additional peaks at 851, 1194, 1453, 1479, and 1616 cm^{-1}. These features are characteristic of a helical structure as found in solid PEG. The peaks due to the disordered structure, as found in the pure liquid, are still present indicating that on micellization there is an ordering of the polyoxyethylene units from a random to a more ordered helical structure. For the long chain surfactant Brij 35 there are no significant differences in the Raman spectra in aqueous micellar solutions indicating no significant change in chain conformation.

(2) *Electrolyte-Induced Micellar Phase Changes.* Hither to the studies have been concerned with Raman spectra of pure surfactants and the spherical micelles formed by these compounds. Raman spectroscopy has also been utilized to probe chain conformations, in CTAB micelles, both spherical and in the bigger rodlike structures, and bilayers which are formed by the addition of electrolytes such as NaBr. The micellar change or growth into larger structures at high concentrations of surfactants, or in the presence of added electrolytes, is a well established phenomenon.

In a decimolar aqueous solution, CTAB exists in the form of "spherical" micelles with an aggregation number around 80. On addition of NaBr, these micelles grow into bigger rodlike structures.[20] We recently investigated[7c] a similar type of electrolyte-induced phase changes for DAC micelles in detail by several physicochemical techniques and observed an increase in the microviscosity of the micellar interior on introduction of the electrolyte.

The increases in the microviscosity of the interior of the CTAB micelles on addition of NaBr is also observed by observing the 1082-cm^{-1} peak in the laser-raman spectrum of CTAB. In Figure 12 the ratio I_{1082}/I_{1125} is plotted against the concentration of added NaBr. Due to the highly viscous nature of these solutions, the background scatter increases consid-

erably with increasing concentration of the electrolyte, and this was to be taken into consideration in the measurement of peak intensities. On addition of NaBr, the ratio decreases indicating an increase in rigidity of the micellar hydrocarbon core. A limiting ratio for I_{1082}/I_{1125} is reached at high electrolyte concentration. The presence of the 1082-cm^{-1} peak shows that, even in these larger rod-shaped aggregates (micellar molecular weight $\simeq$ 2 000 000), a significant amount of gauche isomers is still present. The above data are also consistent with the data of Shinitzky et al.[6] who showed that the microviscosity of the interior of the CTAB micelles increases with increasing NaBr concentration. Presumably in these larger aggregates several carbon atoms at the end of the chains retain their fluidity.

Acknowledgment. We thank Professor L. Pierce for his assistance and helpful suggestions during the course of this work. K. Kalyanasundaram wishes to acknowledge the receipt of a Peter C. Reilley Fellowship from the Department of Chemistry during the course of this work (1974–1975).

References and Notes

(1) The Radiation Laboratory of the University of Notre Dame is operated under contract with the U.S. Energy Research and Development Administration. This is ERDA Document No. COO-38-1022.
(2) J. H. Fendler and E. J. Fendler, "Catalysis in Micellar and Macromolecular Systems", Academic Press, New York, N.Y., 1975.
(3) C. Tanford, "The Hydrophobic Effect: Formation of Micelles and Biological Membranes", Wiley-Interscience, New York, N.Y., 1975.
(4) E. H. Cordes, Ed., "Reaction Kinetics in Micelles", Plenum Press, New York, N.Y., 1973.
(5) (a) K. Shinoda et al., "Colloidal Surfactants", Academic Press, New York, N.Y., 1963, Chapter 1; (b) P. H. Elworthy, A. T. McFarlane, and C. B. McFarlane, "Solubilization by Surface-Active Agents", Chapman-Hill, London, 1968, Chapter 1.
(6) M. Shinitzky, A. C. Dianoux, C. Gitler, and G. Weber, *Biochemistry*, **10**, 2106 (1971).
(7) (a) E. Williams, B. Sears, A. Allerhand, and E. H. Cordes, *J. Am. Chem. Soc.*, **95**, 4871 (1973); (b) R. T. Roberts and C. Chachaty, *Chem. Phys. Lett.*, **22**, 348 (1973); (c) K. Kalyanasundaram, M. Grätzel, and J. K. Thomas, *J. Am. Chem. Soc.*, **97**, 3915 (1975).
(8) (a) R. G. Snyder and J. H. Schachtschneider, *Spectrochim. Acta*, **19**, 85, 117 (1963); (b) R. G. Snyder, *J. Chem. Phys.*, **47**, 1316 (1967).
(9) (a) R. F. Schaufele and T. Shimanouchi, *J. Chem. Phys.*, **47**, 3605 (1971); (b) R. F. Schaufele, *ibid.*, **49**, 468 (1968); (c) Tasumi et al., *J. Mol. Spectrosc.*, **9**, 261 (1962); (d) R. G. Snyder, *ibid.*, **4**, 411 (1960); (e) R. Faiman and D. A. Long, *J. Raman Spectrosc.*, **3**, 371–377 (1975).
(10) For recent applications to phospholipid dispersions and membranes see: (a) J. L. Lippert and W. L. Peticolas, *Proc. Natl. Acad. Sci. U.S.A.*, **68**, 1572 (1971); (b) B. J. Bulkin and N. Krishnamachari, *J. Am. Chem. Soc.*, **96**, 1109 (1972); (c) J. L. Lippert and W. L. Peticolas, *Biochem. Biophys. Acta*, **282**, 8 (1972); (d) R. Mendelsolm, *ibid.*, **290**, 15 (1972); (e) K. G. Brown, W. L. Peticolas, and E. Brown, *Biochem. Biophys. Res. Commun.*, **54**, 358 (1973); (f) J. L. Lippert, L. E. Gorczyca, and G. Meiklejohn, *Biochem. Biophys. Acta*, **382**, 51 (1975). (g) D. F. H. Wallach and S. P. Varma, *ibid.*, **382**, 542 (1975).
(11) R. F. Schaufele, *J. Chem. Phys.*, **49**, 4168 (1968).
(12) S. Mizushima and T. Simanouti, *J. Am. Chem. Soc.*, **71**, 1320 (1949).
(13) J. R. Lyerla, H. M. McIntyre, and D. A. Torchia, *Macromolecules*, **7**, 11 (1974).
(14) (a) Tobin, "Raman Spectroscopy", Wiley, New York, N.Y., 1970; (b) V. H. Siebert, *Z. Anog. Allg. Chem.*, **289**, 15 (1957).
(15) M. C. Chen, R. C. Lord, and R. Mendelsohn, *J. Am. Chem. Soc.*, **96**, 3038 (1974).
(16) M. Rosch, "Nonionic Surfactants", M. J. Schick, Ed., Marcel Dekker, New York, N.Y., 1967, pp. 753–773.
(17) J. L. Koenig and A. C. Angood, *J. Polym. Sci., Part A2*, **8**, 1787 (1970).
(18) M. J. Schick, S. M. Atlas, and F. R. Eirich, *J. Phys. Chem.*, **66**, 1326 (1962).
(19) (a) J. M. Corkill, J. F. Goodman, and J. Wyer, *Trans. Faraday Soc.*, **65**, 9 (1969); (b) F. Podo, A. Ray, and G. Nemethy, *J. Am. Chem. Soc.*, **95**, 6164 (1973); (c) A. A. Riberio and E. A. Dennis, *Chem. Phys. Lipids*, **14**, 193 (1975); (d) K. Kalyanasundaram and J. K. Thomas, unpublished work.
(20) P. Debye and E. W. Anacker, *J. Phys. Chem.*, **55**, 644 (1951).

A Semiempirical Model for the Phase Transition in Polystyrene Latexes

Stephen L. Brenner

Physical Sciences Laboratory, Division of Computer Research and Technology, National Institutes of Health, Bethesda, Maryland 20014
(Received January 16, 1976)

Publication costs assisted by the National Institutes of Health

A simple model for the phase transition in polystyrene latexes has been developed. The model assumes a priori that the transition is fundamentally caused by repulsion between the spherical latex particles, i.e., it is fundamentally hard sphere in nature, but that the hard sphere diameter of the polystyrene particles is in fact ionic-strength dependent. The resulting volume fraction vs. salt concentration phase diagram is in qualitative accord with the experimental phase diagram of Hachisu and co-workers.

Introduction

Modern emulsion polymerization techniques can produce concentrated monodisperse suspensions of spherical polymer particles which, in the freshly prepared state, are typically milky white in color. Luck and coworkers[1-3] demonstrated that highly concentrated aqueous polystyrene latexes and their dried films exhibit iridescence for a certain range of particle diameters. They showed that the iridescence is due to Bragg diffraction of visible light from ordered layers of particles stacked parallel to the surface of the container. Vanderhoff et al.[4] noted that the latex particles are charged and that therefore double-layer interactions should be important in any ordering. They observed that interparticle spacing increases when an iridescent latex is diluted, order being maintained by long-range repulsion between the spheres. Krieger and co-workers[5,6] studied the diffraction in deionized aqueous latexes and found that the particles remain in a close-packed array down to volume fractions as low as 1%. Deionization of the latex removes excess salt and surfactant, resulting in a suspension of charged spheres interacting in an aqueous environment which contains (ideally) a mobile

counterion concentration just sufficient to maintain electroneutrality.

Addition of sufficient electrolyte to a deionized latex screens the interparticle repulsions and destroys the order, yielding a milky nondiffracting suspension characteristic of the "as prepared" latex. Krieger and Hiltner[5,6] found that at intermediate electrolyte concentrations ordered and disordered phases coexist at equilibrium with the volume fractions of the coexisting phases being functions of the ionic strength. They noted that the transition is strongly reminiscent of the solid–liquid melting transition, and suggested that the polystyrene system might provide insight into melting transitions in general. The interparticle forces here are of classical origin and can be continuously varied by changing the salt concentration and/or the charge density on the spheres.

Hachisu and co-workers[7-9] have attempted to map out the volume fraction vs. salt concentration phase diagram for a polystyrene latex by simple visual observation of iridescence. The general shape of the coexistence region has been determined (see ref 9, Figure 7). No theoretical study of the phase diagram has appeared to date.

In 1939 Kirkwood[10] developed an approximate theory of the radial distribution function for a liquid composed of spherical nonpolar molecules. The behavior of his approximate equations led him to the speculation that in his theory a limiting density (less than closed packed) might exist above which a liquid structure cannot exist. Only structures with crystalline long-range order would be possible above this density. This observation did *not* require the existence of attractive forces between the molecules. "Experimental" evidence for such a transition appeared in 1957, when Wood and Jacobson[11] and Alder and Wainwright[12] reported Monte Carlo and molecular dynamics computer "experiments" which indicated that a finite system of hard spheres will undergo a fluid-to-solid-like transition. The spheres begin to crystallize at a volume fraction ϕ_c (c = crystallization) of about 0.50 and the transition is complete by a volume fraction ϕ_m (m = melting) of about 0.55. No analytical proof that an infinite system of hard spheres indeed does undergo such a transition is available. de Llano and Ramiréz[13] have recently shown that equations of state for dense hard sphere fluids and solids can be used to predict transition parameters which are in excellent agreement with the computer experiments. No single equation of state, however, has yielded the transition.

It has been suggested[7-9,14] that the observed order–disorder transition in polystyrene latexes is in fact a hard-sphere type of transition. Hachisu and Kobayashi[9] have done experiments with aqueous latexes at high electrolyte concentrations (thus effectively neutralizing the charge on the spheres) which give $\phi_c = 0.39 - 0.49$ and $\phi_m = 0.48 - 0.55$ depending on electrolyte concentration and stabilizing surfactant used. They have also studied uncharged cross-linked latexes in nonaqueous solvents and find $\phi_c \approx 0.5$ and $\phi_m = 0.58 - 0.60$. Thus, the measurements in high salt and those in nonaqueous solvents yield roughly comparable transition parameters and are in approximate agreement with the computer "experiments" giving support to the hypothesis that the observed phase behavior is fundamentally a hard-sphere transition.

Long-range attractive (van der Waals) interactions between polystyrene spheres are expected to play a minimal role in the ordering phenomenon. The attractive energies are generally very small compared with the repulsive energies, and at those intersphere separations where the attractive energy does become a significant fraction of the total energy, i.e., in the region of the secondary minimum of DLVO theory,[15-17] the total energy is generally small compared to the energy of Brownian motion, kT. Examples of the total pairwise interaction energy including van der Waals forces are shown in Figure 1 for several salt concentrations. It can be seen that only at high salt concentrations, where effective screening of the repulsive force takes place, does the attractive force become more than an energetically small perturbation on the repulsive energy. At the highest volume fraction at which coexistence is observed ($\phi_c = 0.55$), the surface-to-surface distance between 1700-Å diameter spheres such as those used by Hachisu et al.[7-9] is about 177 Å. From Figure 1 it is clear that that distance is considerably larger than the position of force balance, i.e., the minimum in the potential energy curve. One therefore expects long-range attraction to be important only at very high volume fractions and when salt concentrations are high. A similar conclusion has been reached concerning the relative unimportance of long-range attraction in forming ordered arrays of rodlike proteins and protein aggregates,[18] e.g., in the formation of equilibrium gels of tobacco mosaic virus.

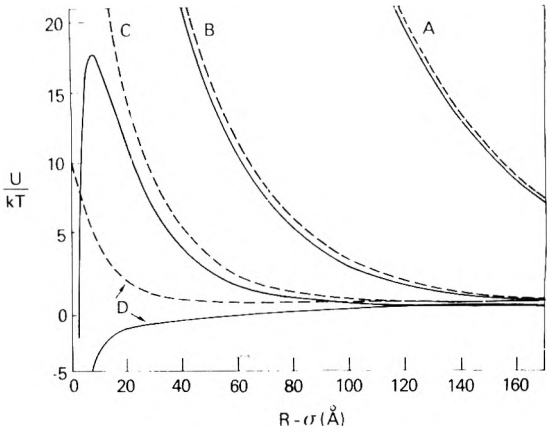

Figure 1. The pairwise interaction energy vs. separation for charged polystyrene spheres of radius 850 Å and $N = 6000$. The dashed curves are the repulsive energies only (eq 2) and the solid curves include the van der Waals attraction (see ref 17 for details). The Debye lengths ($1/\kappa$) are 50, 30, 20, and 10 Å for curves A–D, respectively.

This note proposes a simple method for modifying the hard-sphere transition parameters to take into account double-layer interactions. The transition parameters are taken to be those for hard spheres. For a given salt concentration, the hard-sphere diameter is chosen as that center-to-center distance between a pair of spheres at which the electrostatic interaction energy is on the order of the energy of Brownian motion (see Figure 2). The ionic strength dependence of the interaction energy yields an effective hard-sphere diameter that changes with salt concentration; the effective diameter increases with decreasing salt. The method produces a phase diagram in qualitative accord with observed by Hachisu et al.,[7-9] but uncertainty in the available experimental data precludes a quantitative comparison.

Theory

The hard-sphere system studied in the computer experiments is defined by specifying the pairwise interaction energy as a function of center-to-center separation of the spheres

$$U(R) = \infty \quad R \leq \sigma$$
$$U(R) = 0 \quad R > \sigma \qquad (1)$$

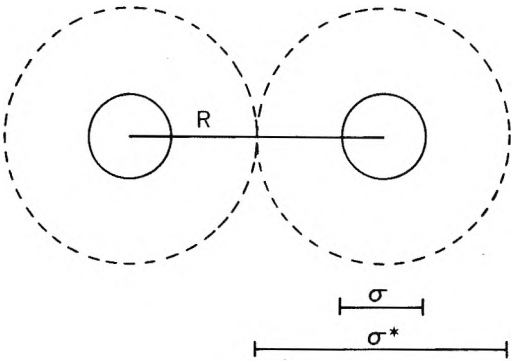

Figure 2. Two hard spheres of diameter σ a center-to-center distance R apart. The dashed lines delineate the effective hard-sphere diameter σ^* chosen such that the pairwise interaction energy at σ^* is on the order of thermal energy.

where σ is the hard-sphere diameter. Thus the spheres behave like nondeformable billiard balls. The interaction energy between a pair of uniformly charged polystyrene spheres in an aqueous salt solution is given approximately by[19-21]

$$U(R) = \infty \qquad R \leq \sigma$$

$$U(R) = \left(\frac{Ne}{1 + \frac{\kappa\sigma}{2}}\right)^2 \frac{e^{-\kappa(R-\sigma)}}{2\epsilon R} \qquad R > \sigma \tag{2}$$

where N is the number of unit charges smeared uniformly over the surface of each sphere, σ is the diameter of the sphere, ϵ is the dielectric constant of the aqueous medium, and $-e$ is the electronic charge. The Debye constant κ is given by

$$\kappa^2 = \frac{8\pi c e^2}{\epsilon k T} \qquad c = \frac{1}{2}\sum_{c_i^0} c_i^0 z_i^2 \tag{3}$$

where k is the Boltzmann constant, T is the absolute temperature, and the c_i^0 are the concentrations of ions of valence z_i in the bathing medium far from the spheres. Equation 2 is accurate when the radius $\sigma/2$ is greater than the Debye length $1/\kappa$ and when the electrostatic energy of a counterion near the sphere is smaller than thermal energy kT. Equations more general than eq 2 have been developed.[19-21] The interaction potential given by eq 2 appears at first glance to be considerably softer than that given in eq 1. It is shown below that for the purposes of studying the phase transition eq 2 can be approximated by eq 1 by choosing an effective hard-sphere diameter σ^*.

Computer experiments are not available for a potential of the form given in eq 2. There are molecular dynamics calculations for systems of soft spheres interacting with an inverse power potential[22,23]

$$U(R) = U_0\left(\frac{\sigma}{R}\right)^n \tag{4}$$

for $n = 4$, 6, 9, 12 and ∞ (clearly $n = \infty$ corresponds to the hard-sphere potential, eq 1). It might seem tempting to try to fit eq 2 to an inverse power law at some R, and then use the transition parameters for soft spheres to describe the polystyrene transition. However, as will be seen later, the potential given by eq 2 is considerably "harder" than an inverse twelfth power at "important" values of R for most values of κ.

Computer calculations show that a finite system of hard spheres undergoes a solid-to-fluid transition characterized by the densities[24]

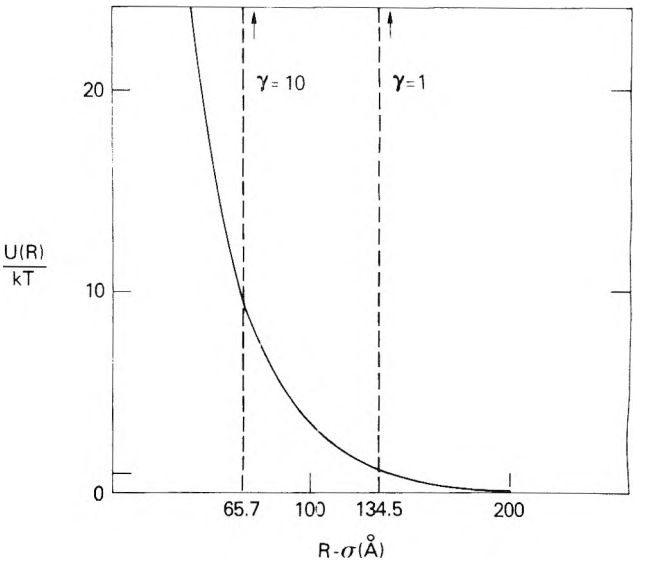

Figure 3. The electrostatic repulsive energy vs. separation for charged polystyrene spheres of radius 850 Å and $N = 6000$ for a salt concentration of 10^{-2} M 1-1 electrolyte ($1/\kappa \approx 30$ Å). Hard-sphere potentials chosen on the basis of eq 7 are indicated by dashed lines for $\gamma = 1$ and 10.

$$\rho_c = 0.736\rho_0$$
$$\rho_m = 0.667\rho_0 \tag{5}$$

(c = crystallization, m = melting) where ρ_0 is the close-packed density

$$\rho_0 = \sqrt{2}/\sigma^3 \tag{6}$$

Assume that a system of charged spheres governed by the potential in eq 2 also undergoes a transition at the densities given by eq 5 *but* that the close-packed density is determined by an *effective* hard-sphere diameter σ^* (see Figure 2). σ^* is chosen by requiring that the pairwise interaction energy at σ^* be on the order of thermal energy

$$U(\sigma^*) = \gamma kT \tag{7}$$

where U is given by eq 2. The constant γ is fixed and the values of σ^* are determined for a range of salt concentration. If $U(\sigma) < kT$ then $\sigma^* = \sigma$. An example showing the actual potential from eq 2 and effective hard-sphere potential is given in Figure 3.

The use of an effective hard-sphere diameter in colloid chemistry was suggested by Stigter.[25] The modeling of a real fluid using a hard-sphere model with a density and temperature dependent hard-sphere diameter is well known in modern statistical mechanics (see, e.g., ref 26). The choice of γkT as the value of the potential at which to fix the effective hard-sphere diameter is motivated by the fact that any force becomes important as soon as the work of that force (i.e., the potential) is on the order of thermal energy.

Results

σ^* is found from eq 7 for a given κ; calculate ρ_0 from eq 6 and ρ_c, ρ_m from eq 5. The transition volume fractions are obtained from the relation $\phi = \rho v$ where v is the volume of a polystyrene sphere of radius $\sigma/2$, $v = \frac{1}{6}\pi\sigma^3$.

The sphere radius is chosen as 850 Å and a the surface charge density as 1 μC/cm^2 to be consistent with the experiments of Hachisu et al.[7-9,35] This charge density corresponds

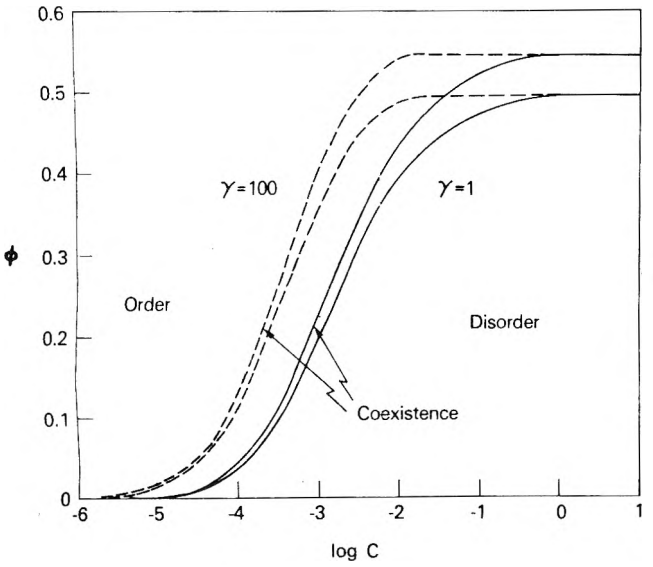

Figure 4. The volume fraction vs. salt concentration phase diagram. At high ϕ and low C there is complete order; at low ϕ and high C there is disorder, while between the curves for a given γ, there is coexistence. The volume fractions of the coexisting phase for a given C can be located by constructing a vertical tie line.

TABLE I: Effective Hard-Sphere Diameter, Power Law Exponent, and Surface Potential as a Function of Ionic Strength[a]

c, M	σ^*, Å	n[b]	$e\psi_s/kT$
1	1700	560	0.2
10^{-1}	1721	180	0.6
10^{-2}	1834	61	1.7
10^{-3}	2310	25	5.0
10^{-4}	4040	14	13.0
10^{-5}	9615	11	26.0

[a] For σ = 1700 Å, γ = 1, ϵ = 80, T = 300 °C. [b] $N = -\mathrm{d}\ \ln U/\mathrm{d}\ \ln R$ at $R = \sigma^*$ (see ref 17).

to a value of $N \approx 6000$. The resulting phase diagram is plotted in Figure 4 for values of γ = 1 and 100. Table I gives several values of the effective hard-sphere diameter σ^*, the exponent of the power law that fits U(R) at σ^*, and the reduced surface potential on the spheres where

$$\frac{e\psi_s}{kT} = \frac{Ne^2}{\epsilon akT\left(1+\frac{\kappa\sigma}{2}\right)} \tag{8}$$

At high salt concentrations the transition volume fractions are those characteristic of hard spheres of diameter $\sigma^* = \sigma$. As the salt concentration is lowered (see Figure 4) the effective diameter σ^* increases, the close-packed density decreases, and the transition volume fractions decrease. The experimentally observed sigmoid shaped coexistence region is obtained, and the absolute density difference between coexisting phases decreases with decreasing ionic strength as observed experimentally. Note that the effect of increasing γ is to shift the coexistence region to the left without markedly altering its basic shape. The pure hard-sphere transition parameter will obtain when C gets large or as $\gamma \to \infty$.

The effective power law at $R = \sigma^*$ is seen in Table I to be characterized by very large n except for extremely low salt concentrations. It is therefore not possible to fit the potential to an effective power law form comparable to those studied by Hoover et al.[23,24]

The linearized form of the Poisson–Boltzmann equation used to derive eq 2[19-21] is in principle not valid for reduced surface potentials $e\psi_s/kT > 1$. Linearization is, in fact, valid for high surface potentials as long as the ionic strength is very low[27-29,36] or when the surface-to-surface distance between the sphere is large compared to the Debye length.[20] The high surface potentials seen toward the bottom of Table I occur for very low ionic strengths and thus the use of eq 2 is less suspect than it might appear at first glance.

A quantitative comparison with the observed experimental transition parameters would be tenuous at this time for several reasons. It is clear from Figure 2 of Hachisu et al.[7] that the boundaries of the phase diagram at low salt concentrations are not unambiguously established due to experimental difficulties. Hachisu[32] comments that minute fragments of the friable ion-exchange resin beads were produced by their mechanical mixing procedure and that such fragments may have caused error in judging the starting point of order formation, effectively shifting the coexistence–disorder phase boundary to the right. A narrower transition region would be more in accord with the results obtained by this analysis. Finally, a quantitative comparison is impossible without an accurate measure of the surface charge density which is not available for those latexes used in the phase diagram work.

A more exhaustive and detailed study of the phase diagram, perhaps using the diffraction technique of Krieger et al.[5,6] is needed before a quantitative comparison with theory can be made. Computer "experiments" on a system of large charged spheres interacting with a screened Coulomb potential (eq 2) would allow critical examination of the assumption that such a system can be modeled as hard spheres with ionic strength dependent diameters.

A more refined theory of the phase transition might be developed by a modification of the method of de Llano and Ramiréz.[13] The equation of state for the solidlike phase could be constructed using a cell model (see, e.g., ref 33) and the fluidlike phase could be modeled using a virial series, or a Padé approximant to a virial series. The analysis by Stigter and Hill[34] of the second and third osmotic virial coefficients for spheres interacting with a screened Coulomb potential could provide a starting point for such an analysis.

NOTES ADDED IN PROOF: Snook and van Megen (J. Snook and W. van Megen, *J. Chem. Soc., Faraday Trans. 2*, **72**, 216 (1976)) have recently reported a Monte Carlo study of a system of spherical particles interacting via a screened Coulombic repulsion and van der Waals attraction. Ordered and disordered regions were obtained.

Andrews (F. Andrews, *J. Chem. Phys.*, **64**, 1941, 1948 (1976)) has recently studied the equilibrium statistical mechanics of Lennard-Jones fluids using a temperature-dependent hard-core diameter defined as in eq 7 with γ = 1 in two dimensions, ⅜ in three dimensions. Thus Andrews takes the hard-core diameter to be the separation distance at the classical distance of closest approach corresponding to the average kinetic energy of two particles due to their relative motion.

Acknowledgments. The author thanks William Hoover, Adrian Parsegian, and Irvin Krieger for stimulating conversations; Adrian Parsegian, Donald McQuarrie, and Ralph Nossal for reading the manuscript; and Sei Hachisu for providing some details of his experimental procedures.

References and Notes

(1) W. Luck and H. Wesslau, "Festschrift Carl Wurster", Gesamtherstellung Johannes Wiesbecker, Frankfurt am Main, W. Germany, 1980.
(2) W. Luck, M. Klier, and H. Wesslau, *Ber. Bunseges. Phys. Chem.*, **67**, 75, 84 (1963).
(3) W. A. P. Luck, *Phys. Bl.*, **23**, 304 (1967).
(4) J. W. Vanderhoff, H. J. van den Hul, R. J. M. Tausk, and J. Th. G. Overbeek in "Clean Surfaces: Their Preparation and Characterization for Interfacial Studies", G. Goldfinder, Ed., Marcel Dekkar, New York, N.Y., 1970, p 15.
(5) P. A. Hiltner and I. M. Krieger, *J. Phys. Chem.*, **73**, 2386 (1969).
(6) I. M. Krieger and P. A. Hiltner, in "Polymer Colloids", Fitch, Ed., Plenum Press, New York, N.Y., 1971, pp 63–72.
(7) S. Hachisu, Y. Kobayashi, and A. Kose, *J. Colloid Interface Sci.*, **42**, 342 (1973).
(8) A. Kose and S. Hachisu, *J. Colloid Interface Sci.*, **46**, 460 (1974).
(9) S. Hachisu and Y. Kobayashi, *J. Colloid Interface Sci.*, **46**, 470 (1974).
(10) J. G. Kirkwood, *J. Chem. Phys.*, **7**, 919 (1939).
(11) W. W. Wood and J. D. Jacobson, *J. Chem. Phys.*, **27**, 1207 (1958).
(12) B. J. Alder and T. E. Wainwright, *J. Chem. Phys.*, **27**, 1208 (1957).
(13) M. de Llano and S. Ramirez, *J. Chem. Phys.*, **62**, 4242 (1975).
(14) M. Wadati and M. Toda, *J. Phys. Soc. Jpn.*, **32**, 1147 (1972).
(15) B. S. Derjaguin and L. Landau, *Acta Physiochim. USSR*, **14**, 633 (1941).
(16) E. J. W. Verwey and J. Th. G. Overbeek, "Theory of the Stability of Lyophobic Colloids", Elsevier, Amsterdam, 1948.
(17) V. A. Parsegian, "Physical Chemistry: Enriching Topics from Colloid and Surface Science", H. Van Olphen and K. J. Mysels, Ed., Theorex, La Jolla, 1975, Chapter 4.
(18) V. A. Parsegian and S. L. Brenner, *Nature (London)*, **259**, 632 (1976).
(19) G. M. Bell, S. Levine, and L. N. McCartney, *J. Colloid Interface Sci.*, **33**, 335 (1970).
(20) S. L. Brenner and V. A. Parsegian, *Biophys. J.*, **14**, 327 (1974).
(21) B. Enos, D. A. McQuarrie, and P. Colonomos, *J. Colloid Interface Sci.*, **52**, 289 (1975).
(22) W. G. Hoover, S. G. Gray, and K. W. Johnson, *J. Chem. Phys.*, **55**, 1128 (1971).
(23) W. G. Hoover, D. A. Young, and R. Grover, *J. Chem. Phys.*, **56**, 2207 (1972).
(24) W. G. Hoover and F. H. Ree, *J. Chem. Phys.*, **49**, 3609 (1968).
(25) D. Stigter, *Recl. Trav. Chim. Pays-Bas*, **73**, 593 (1954).
(26) See, e.g., H. C. Andersen, J. D. Weeks, and D. Chandler, *Phys. Rev. A*, **4**, 1597 (1971).
(27) S. Levine, *J. Chem. Phys.*, **7**, 836 (1939).
(28) A. D. MacGillivray, *J. Theor. Biol.*, **23**, 205 (1969).
(29) S. L. Brenner and R. E. Roberts, *J. Phys. Chem.*, **77**, 2367 (1973).
(30) J. G. Kirkwood and J. C. Poirier, *J. Phys. Chem.*, **58**, 591 (1954).
(31) F. Stillinger and J. G. Kirkwood, *J. Chem. Phys.*, **33**, 1282 (1960).
(32) S. Hachisu, personal communication.
(33) B. J. Alder, W. G. Hoover, and D. A. Young, *J. Chem. Phys.*, **49**, 3688 (1968).
(34) D. Stigter and T. L. Hill, *J. Phys. Chem.*, **63**, 551 (1959).
(35) The surface charge density was not reported in the papers of Hachisu et al.[7-9] Hachisu (personal communication) estimates the charge density to be in the range 0.8–1.5 $\mu C/cm^2$.
(36) Linearization is valid in the sense that the linearized results for the pairwise potential at low salt are equivalent to those obtained by solving the nonlinear equation. However, in low salt the use of a pairwise interaction potential becomes questionable, and in fact, a cell model is more appropriate. The use of the nonlinear equation, itself is also suspect.[30,31]

Mean Adsorption Lifetimes of Cesium Chloride on Nickel Surfaces

Leo W. Huang[1]

Department of Chemistry, Illinois Institute of Technology, Chicago, Illinois 60616

and P. G. Wahlbeck*

Department of Chemistry, Wichita State University, Wichita, Kansas 67208

(Received October 6, 1975)

A pulsed-molecular-beam method was applied to the study of the mean adsorption lifetimes of adsorbed CsCl on single crystal and polycrystalline nickel surfaces. The experiments were conducted in an ultra-high vacuum system free of hydrocarbon contaminates and with pressures less than 2×10^{-8} Torr. A molecular beam of CsCl was formed from species effusing from a double-oven effusion cell equipped with a conical orifice. A rotating chopper served to pulse the molecular beam; the CsCl molecular beam was on for 10.7% of the period of the cycle. The molecular beam struck a nickel target inclined at a 45° angle. Four targets were used in these experiments: Ni(111) surface, Ni(100) surface, clean polycrystalline Ni surface, and a contaminated polycrystalline Ni surface. The mean adsorption lifetimes were determined by measuring the rate of evaporation of CsCl from the surface by means of a surface ionization detector. The desorption has been found to follow first-order kinetics in cases of single crystal targets for which equilibrium surface coverage of the adsorbate is much less than 0.001 monolayer. The activation enthalpy for the desorption process, ΔH^*, and the preexponential, τ_0, are dependent on surface structure and surface cleanliness, but they are not dependent on surface coverage. In an attempt to interpret the present values of τ_0, one must use a mobile adsorption model.

Introduction

Vaporization of bulk materials or of foreign species on another substance is an important process. The study of the kinetics of vaporization hopefully will lead to a greater understanding of the vaporization process.

The vaporization kinetics of an adsorbed species on a solid surface can be characterized by the reciprocal of the first-order rate constant, τ, the mean adsorption lifetime. The length of time an adsorbed molecule spends on a surface is important in several processes such as thermal accommodation, surface migration, condensation, chemical reaction with the surface material or other adsorbed species, and catalysis. This particular research was initiated because data for surface migration of CsCl on Ni were desired in order to perform calculations suggested by Winterbottom;[2] see also papers by Wahlbeck et al.[3,4]

The great bulk of previous determinations of mean adsorption lifetimes has been for the desorption of ions from metal surfaces. Among these are studies of the mean adsorp-

tion lifetimes of Cs^+ on polycrystalline W[5-7] and on single crystal W surfaces,[8] and of the mean adsorption lifetimes of Cs^+ when CsCl is on polycrystalline W surfaces[9] and when CsI is on polycrystalline W surfaces.[9]

There have been very few studies of the mean adsorption lifetimes of neutrals on surfaces. Shelton and Cho[10] have studied the mean adsorption lifetimes of Cu, Cr, Be, Ni, Fe, and Ti on W and oxygen covered W polycrystalline surfaces. Hudson and Sandejas[11,12] have studied the adsorption of Cd on W surfaces. The mean adsorption lifetime of Rb on single crystal W has been examined by Hughes.[13] The mean adsorption lifetimes of CO on Ni have been studied by Degras.[14,15] The adsorption of CO on Ni single crystal surfaces has been studied by Madden, Küppers, and Ertl[16] and by Tracy.[17] The system of CsI on W surfaces has been studied by Kolesnikov et al.[18]

The desorption of neutral U from polycrystalline W surfaces has been studied by Smith,[19] and the desorption of U^+ from polycrystalline W and Re surfaces has been studied by Hertel.[20]

In addition to the experimental studies, interesting theoretical studies have been performed. Molecular orbital calculations have been performed by Blyholder considering adsorption of H[21] and CO[22] on Ni atom clusters. Anderson and Hoffmann[23] have considered the case of adsorption of first period diatomic molecules on W and Ni atom clusters. These studies have provided energetics associated with the adsorption process as well as information regarding surface migration.

The temperature dependence of the τ data may be analyzed by

$$\tau = \tau_0 \exp(\Delta H^*/RT) \quad (1)$$

where ΔH^* is the activation enthalpy for the desorption process and τ_0 is a constant. The previous studies of ions and of CsI on W surfaces indicate that τ_0 values are about 10^{-13} s whereas CO on W surfaces gives a τ_0 value of 7×10^{-3} s and 7×10^{-4} s for phases 1 and 2 of adsorbed CO (see ref 14).

Equations for τ_0 may be developed from statistical mechanics using either a localized adsorption model or a mobile adsorption model. For localized adsorption, τ_0 is predicted to have a dependence on surface coverage. For mobile adsorption, τ_0 is predicted to be $1/\nu$, where ν is the vibrational frequency perpendicular to the surface, and this gives a good explanation of τ_0 being 10^{-13} s. DeBoer[24] has pointed out correctly that for mobile adsorption there is no way of changing the statistical mechanical equation to make τ_0 larger than 10^{-13} s.

The chemical system in this study was CsCl adsorbed on Ni surfaces. The mean adsorption lifetimes of neutral molecular CsCl on Ni single crystal and polycrystalline (both clean and contaminated) surfaces were measured. The experimental apparatus was developed following the design used by Cho and Hendricks.[25] A molecular beam of CsCl was formed by using an effusion cell. The beam was pulsed by using a rotating chopper. The beam has a trapezoidal time profile and was effectively on 10.7% of the beam period. The pulsed molecular beam was allowed to strike a heated Ni surface inclined to the beam at a 45° angle. The rate at which CsCl evaporated from the surface was measured by using a surface ionization detector. The ion current flowed to a signal averaging device to increase the signal-to-noise ratio. The time dependence of the ion current was analyzed to give the mean adsorption lifetime. The dependences of τ on surface temperature, crystal surface, surface coverage, and contamination were studied.

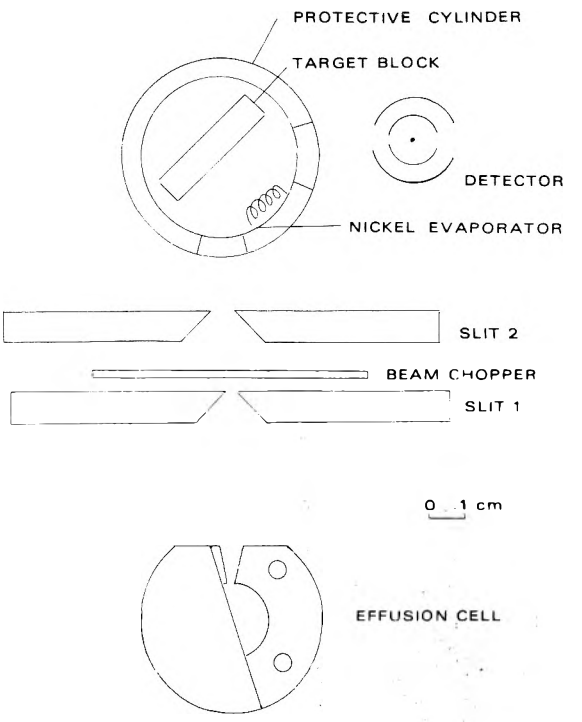

Figure 1. Top view of experimental apparatus with locations of parts of the apparatus drawn to scale as indicated. Distance from effusion cell to slit 1 was 4.4 cm; slit 1 was 0.24 × 0.60 cm. Distance from effusion cell to slit 2 was 15.1 cm; slit 2 was 0.60 × 0.60 cm. Distance from effusion cell to target was 19.4 cm. Distance from target to detector was 5.1 cm.

Experimental Section

In Figure 1 is given a schematic view of the apparatus that was used in these experiments. The different components of this apparatus are described in the following paragraphs.

Vacuum System. The apparatus represented in Figure 1 was mounted in a bell jar vacuum system pumped by vac-ion pumps and gettered by a titanium sublimator, Ultek TNB-C, Model 400-2000. The vacuum system never was exposed to oil. During experiments reported here, the pressure was maintained lower than 2×10^{-8} Torr.

Molecular Beam Source. The origin of the molecular beam was a double-oven effusion cell. The construction details of the cell are shown in Figure 2. The effusion cell was fabricated from grade A nickel. The orifice of the cell was a long divergent conical orifice located in the face of the upper oven. The smaller, entrance diameter of the orifice was 1.342 ± 0.013 mm, the larger, exit diameter of the orifice was 6.941 ± 0.045 mm, and the half-angle of the cone was 16.00 ± 0.08°. The conical orifice was chosen because small angular misalignment would not greatly change the molecular beam intensity; see angular number distribution data by Adams, Phipps, and Wahlbeck.[26] The two ovens of the effusion cell were heated independently by radiation from dc resistively heated W filaments placed in alumina thermocouple protection tubing. The temperatures of the two ovens were measured by calibrated chromel–alumel thermocouples placed at positions indicated in Figure 2.

The molecular beam species chosen for these experiments was CsCl(g). To produce CsCl(g), CsCl(s) was placed in the

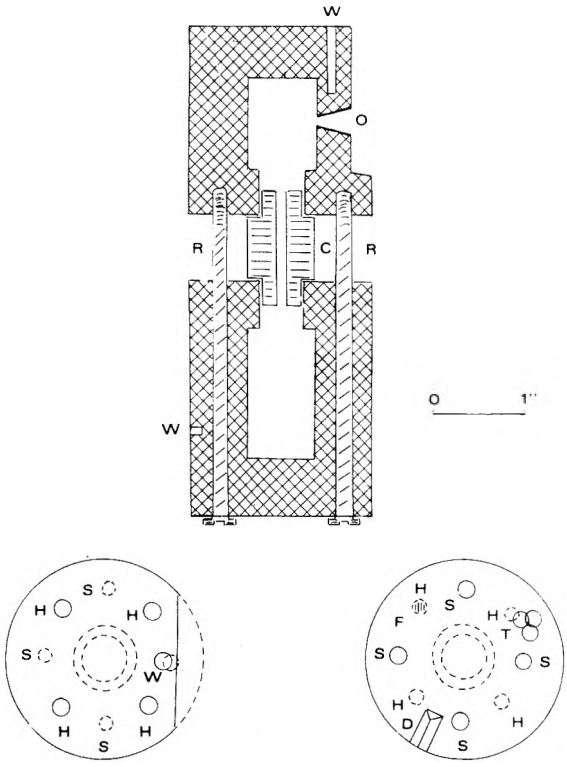

Figure 2. Details of construction of effusion cell. Solid sample was contained in lower oven. Lower left is top view of upper oven. Lower right is bottom view of lower oven: O, conical orifice; W, thermocouple well; C, piece connecting upper and lower ovens; R, bolts; H, heater hole; S, bolt hole; T, trihedral cavity for kinematic support; D, dihedral slot for kinematic support; F, flat for kinematic support.

lower oven of the effusion cell; the CsCl(s) was purchased from Alfa Inorganics, Inc. and was indicated to be 99.99+% pure with principal impurities being Rb, Na, and K. The equilibrium vapor pressure of CsCl(s) has been given by Treadwell and Werner [27] as

$$\log p_{\mathrm{Torr}} = -\frac{9970}{T} + 9.942 \qquad T \leq 915\ \mathrm{K} \qquad (2)$$

and of CsCl(l) by Kelley[28]

$$\log p_{\mathrm{Torr}} = -\frac{10\,210}{T} + 20.62 - 3.52 \log T \qquad T \geq 915\ \mathrm{K} \qquad (3)$$

The vapor species in the equilibrium vapor are principally monomer with less than 7% dimer as shown by the experimental studies by Miller and Kusch[29] and by Berkowitz and Chupka.[30]

In order to form the molecular beam from the CsCl(g) effusing from the conical orifice, molecules passed through slit 1 which was water cooled; see Figure 1. This slit eliminated molecules leaving the effusion cell at large angles. Slit 2 is the beam defining slit and determined the final geometry of the molecular beam. The dimensions of slit 2 were 0.60 by 0.60 cm. Both slits 1 and 2 were knife-edged slits. The distance from the orifice to slit 1 was 4.4 cm and from the orifice to slit 2 was 15.1 cm.

In order to produce a pulsed molecular beam, a rotating beam chopper was placed between slit 1 and slit 2. The design of the chopper blade is shown in Figure 3. From the geometries of the chopper blade, the beam is opening during 2.75%, is open fully for 5.20%, and is closing during 2.75% of the beam period. The chopper blade was made from an aluminum alloy,

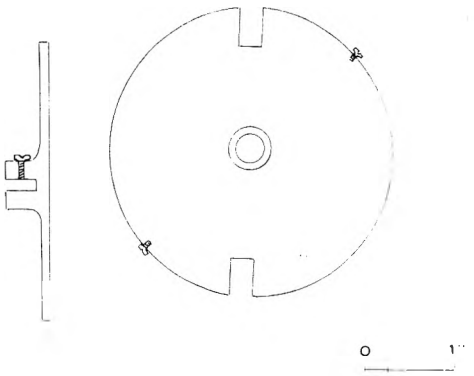

Figure 3. Construction detail of rotating chopper blade for pulsing molecular beam.

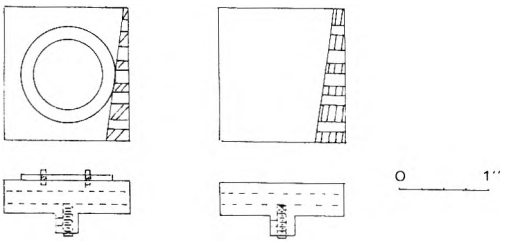

Figure 4. Construction detail of Ni targets. Left target was designed for mounting mica sheet. Right target was used for polycrystalline surface. Screw was used to secure the thermocouple for target temperature measurements.

Alcoa 2024-T3. The chopper blade was rotated by a synchronous motor, Globe Industries, Type 53A 107-2. The chopper blade was placed directly on the motor shaft. The motor was powered from a variable frequency power supply consisting of an audio oscillator, Hewlett-Packard Model 200 J, and a power amplifier. A trigger signal was generated by placing two iron screws on the periphery of the chopper blade and by mounting near the periphery a magnetic pick up obtained from Power Instruments, Inc., Model 813 BNC (this was modified for the vacuum environment). The signal from the magnetic pick-up was sent to a Hewlett-Packard tachometer, Model 500C. The tachometer could produce a large voltage pulse, which was used to trigger an oscilloscope and the signal averaging device, or could produce an analog signal which was used for chopper speed observations.

Targets. All of the targets used in experiments reported here were of Ni and were heated to various temperatures. Single crystal surfaces were mounted on a large Ni block, and polycrystalline surfaces were a face of a large Ni block. These large Ni blocks are shown in Figure 4. The large Ni blocks were heated by dc resistively heated W filaments mounted in alumina thermocouple protection tubes. The temperature of the target was measured by means of a calibrated chromel–alumel thermocouple mounted as shown in Figure 4. All targets were heated for outgassing prior to use.

Results were obtained with four surfaces: (1) Ni(111), (2) Ni(100), (3) a clean polycrystalline surface, and (4) a contaminated polycrystalline surface.

For the first three surfaces, it was necessary to obtain and maintain a clean surface. Oxygen cannot be removed from a Ni surface by flash heating because of the low volatility of nickel oxide compared to Ni. A clean surface was generated by evaporation of Ni onto the surface. Short lengths of Ni wire of 99.999% purity obtained from Leico Industries, Inc. were

wound on a W filament. The evaporator, positioned as shown in Figure 1, was heated by low voltage ac before each determination of a mean adsorption lifetime. Rough calculations indicate that with each vaporization about 50 atomic layers of Ni were deposited on the target.

With the pressure in the vacuum system being lower than 2×10^{-8} Torr, one had ca. 350 s before a monolayer would form of species from the residual gases assuming all species would stick upon their first surface collision. All experimental data for the first three targets were collected within 25 s.

Two single crystal surfaces were investigated in this study: (1) Ni(111), and (2) Ni(100). The Ni(111) surface was grown epitaxially on a mica single crystal surface. A selected piece of mica was mounted on the Ni target block as shown in Figure 4. The Ni evaporator, as described above, evaporated Ni onto the mica producing a Ni(111) single crystal surface. Detailed studies of surface structures of Ni deposited on vacuum-cleaved mica have been made by Allpress and Sanders[31] and on air-cleaved mica by Anderson and MacDonald.[32] The Ni(100) surface was produced by cutting through a single crystal boule for which the orientation was known. The single crystal boule was purchased from the Materials Research Corp. and had a purity of 99.999%. In this case, the single crystal face was polished using metallurgical polishing procedures. The Ni(100) surface was overlayed with Ni from the evaporator.

Two polycrystalline targets were studied also: (3) a clean polycrystalline Ni and (4) a contaminated polycrystalline Ni. Both of these target surfaces were surfaces of the target blocks. The target surfaces were polished using metallurgical polishing procedures. The clean target had been overlayed with Ni from the evaporator during the experiments. The contaminated target experiments were performed before the Ni evaporator was installed.

Photomicrographs of the targets, using an optical metallurgical microscope, were obtained for the four target surfaces after the experiments were performed. Magnifications up to 1000× were used. Photomicrographs of these targets are shown in Figure 5. Both the single crystal surfaces show uniform surfaces up to a magnification of 1000×. There is clear evidence for nucleation in the photomicrographs of 1000×. The nucleation sites are between 1 and 2×10^{-4} cm apart. There are a few scratches present on the Ni(100) surface. The polycrystalline targets show evidence of grain boundaries; the contaminated target surface, surface 4, shows the clearest evidence of grain boundaries. The dark spots, target surface 4, probably were caused by pits originating from Ni evaporation which occurred when the Ni was heated. The differing densities of these spots probably indicate different exposed crystal surfaces; if so, there are at least four different exposed faces present. It is highly probable that these same crystal faces are present on the clean polycrystalline surface on which Ni was evaporated.

The targets were mounted inside a stainless steel cylinder. The Ni evaporator was located inside the stainless steel cylinder. The cylinder had openings so that the molecular beam of CsCl(g) could enter and evaporating CsCl could pass to the detector. The cool walls of the cylinder acted as a sink for stray CsCl and also protected the target from stray molecules.

Detector. The detector in these experiments was a surface ionization detector using a 3 mil Re filament heated at 1300 °C. The filament was biased +22.5 V with respect to the ion collector which was at ground potential. The entrance slit of the detector was 10 mm long. Molecules from a large area of the target could strike the detector filament. An ion current

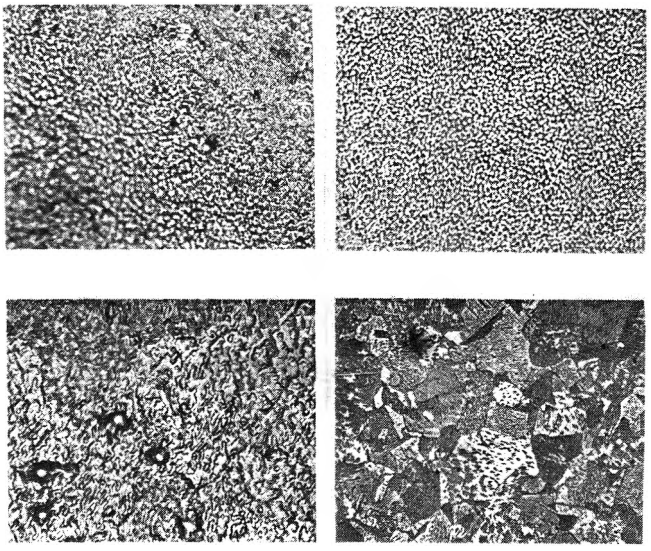

Figure 5. Optical microscopic views of surfaces: (upper left) Ni(111), 1000×; (upper right) Ni(100), 1000×; (lower left) polycrystalline Ni, with Ni deposit, 500×; (lower right) polycrystalline Ni, no Ni deposit, 200×.

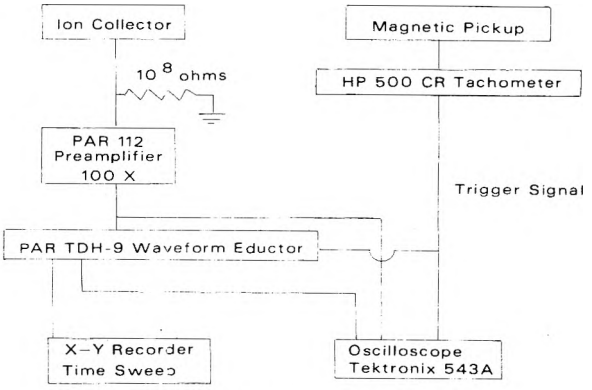

Figure 6. Circuit for signal processing.

would have resulted from the species CsCl, Cs, and Cs^+, possibly resulting from this experiment, and from other alkali and alkaline earth containing species.

Signal Circuitry. The signal generated from the surface ionization detector is an ion current of approximately 10^{-11} A. The circuit used to process this signal is shown in Figure 6. The signal is repetitive in nature with a frequency of 3.833 or 8.167 Hz.

Signal averaging was performed in order to increase the signal-to-noise ratio. A waveform eductor manufactured by Princeton Applied Research, Model TDH-9, was used. This instrument is a 100-channel analyzer. Delay times and sweep times are variable. In addition to the waveform eductor, the signal from the experiment could be observed directly on the oscilloscope, Tektronix, Model 543A, with plug-in D. The output signal, intensity vs. time, from the waveform eductor was recorded with an X–Y recorder.

Apparatus Time Constants. In order to measure a time constant for a particular process, the time constants of the signal detection system must be known.

The surface ionization detector has a time constant dependent on the mean adsorption lifetime of Cs^+ when CsCl is admitted to a Re surface which is at 1300 °C. From experi-

mental data for this case by Scheer and Fine,[7] one may compute that the time constant for the detector was 5.0×10^{-7} s.

The oscilloscope had a rise time of 0.01 μs.

Because the waveform eductor is a 100-channel analyzer, it has a resolution of 0.01 times the sweep time. In these experiments the sweep times were 200 ms giving a resolution of 2×10^{-3} s.

The time constant associated with the PAR preamplifier, the PAR waveform eductor, and the 10^8-ohm resistor was concluded to be 7.731 ± 0.172 ms. The other time constants in the data handling system are much shorter than 7.731 ms. The signal system was analyzed in detail assuming (1) a trapezoidal beam shape for which the shutter was fully open at a time t_1 after opening began, the shutter began to close at a time t_2, and the shutter was fully closed at a time t_3; (2) first-order desorption kinetics with a mean adsorption lifetime of CsCl on the Ni surface, τ; and (3) the circuit time constant, τ_a, to be 7.731 ms. If t is the time after the shutter is fully closed, the signal, $V(t)$, should obey the equation (valid when $\tau \neq \tau_a$)

$$V(t) = K\{[1 - \exp(-t_1/\tau_a) - \exp(-t_2/\tau_a) + \exp(-t_3/\tau_a)](\tau_a^2/\tau_a - \tau)\exp(-t/\tau_a) + [1 - \exp(-t_1/\tau) - \exp(-t_2/\tau) + \exp(-t_3/\tau)](\tau^2/\tau - \tau_a)\exp(-t/\tau)\} \quad (4)$$

The data for $V(t)$, with t_1, t_2, t_3, and τ_a known, can be analyzed to determine τ. A non-linear least-squares computer program, originally written by Struble,[33] was used for the determination of τ.

Experimental Procedure. Previous to initial evacuation of the apparatus, the oven was filled with CsCl(s), the target was prepared and inspected, the Ni evaporator was prepared and positioned in front of the target, the alignments of the oven, target, and detector were checked, and the electrical circuits for the heaters, thermocouples, and signal were checked.

After the vacuum system was closed by placing the bell jar in position, evacuation was begun by use of a carbon-piston pump manufactured by Bell and Gossett, Model SYC 18-1. Evacuation was continued to a pressure of 0.5×10^{-3} Torr by use of a liquid-nitrogen-cooled sorption pump. The evacuation was continued by using the vac-ion and Ti sublimation pumping. With the system cold, pressures as low as 3×10^{-9} Torr were obtained. During all collection of data, the pressure was lower than 2×10^{-8} Torr.

In order to perform an experiment, the effusion cell ovens were heated so that the back oven was 932 K and the front oven was 950 K. It would require at least 2 h to achieve stable operating temperatures of the effusion cell. A molecular beam of 7.07×10^{13} molecules/s then would strike an area of 0.58 cm^2 on the target. The target was heated to a desired experimental temperature. The detector filament was heated so that the temperature was 1300 °C, and the filament was biased. The chopper was set into motion, and its speed was stabilized.

A Ni evaporation was performed by heating the Ni evaporator for 3 min. Immediately following the evaporation, after the power to the evaporator was turned off, data were collected by the waveform eductor for 25 s.

After all data were collected for a particular day, the chopper motor, the effusion cell heaters, the target heater, and the surface ionization detector were turned off. Vacuum was not broken until the apparatus had cooled and was broken only if major internal adjustments to the apparatus were necessary.

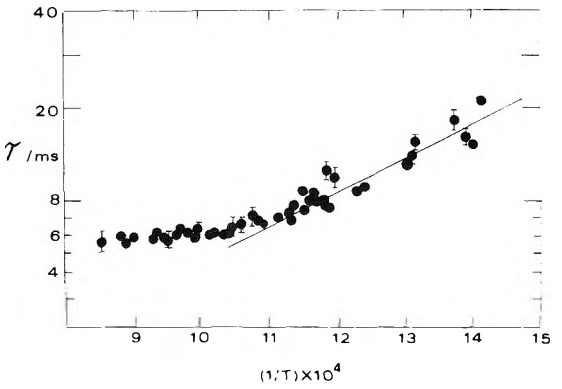

Figure 7. Apparent mean adsorption lifetimes of CsCl on clean polycrystalline Ni vs. reciprocal of target absolute temperature. Horizontal data to the left were used in establishing the time constant of the circuit.

Results

Incident Beam and Surface Coverage. The number of molecules per second effusing from the effusion cell was dependent on the effusion cell temperatures. The back oven temperature was 932 ± 5 K, and the front oven temperature was 950 ± 5 K. The number of molecules per second which struck the target depended upon the number of molecules effusing per second and upon the geometry factors of the slits. When the chopper was open, the arrival rate on the target was 7.07×10^{13} molecules s^{-1}.

If equilibrium had been achieved, then the number of molecules on the surface (centimeter)$^{-2}$ would have been the product of τ and the arrival rate when the chopper was open fully. With a value of the arrival rate given above, with a value of τ of 10 ms, and with the area of the target which was struck by the beam given above, the number of molecules adsorbed on the surface would be 1.2×10^{11} molecules cm^{-2}. Assuming ionic radii for Cs^+ and Cl^-, the fraction of the surface covered had to be ca. 2×10^{-4}. Since equilibrium was not achieved, the fraction of the surface covered was less than 2×10^{-4}.

Desorbing Species. In this experiment utilizing a surface ionization detector, an integrated signal from all alkali bearing species was obtained. With the chemical system studied here, the most probable species are CsCl, Cs, and Cs^+. The amount of dimer, Cs_2Cl_2, is less than 7%[29,30] in the original molecular beam since the vapor is not saturated; after the species strike the surface, the dimer will be insignificant (estimated to be less than 0.01%).

The thermal dissociation of gaseous CsCl using equilibrium data from the JANAF Thermochemical Tables[34] gives an amount of atomic Cs which is about 10^{-7} times the amount of CsCl. The probability of the species being Cs is very low.

The surface ionization of CsCl on a Ni surface would produce Cs^+. During these experiments, the Re filament of the detector was turned off, but the filament was biased giving an electric field in the detector. If Cs^+ was evaporating from the Ni target, the Cs^+ would have passed through the slits of the detector, entered the electric field, and passed to the ion collector. No signal was observed, and it was concluded that surface ionization was not a significant process. Sloth et al.[35] studied the surface ionization of LiCl, a species with a dissociation energy of 4.85 eV compared to CsCl which has a value of 4.6 eV, on a Re surface, a surface with a work function of 5.1 eV compared with Ni which has a work function of 4.84 eV. Sloth observed no significant surface ionization at surface temperatures less than 1200 K. The absence of Cs^+ in the present investigation is reasonable in view of the results of

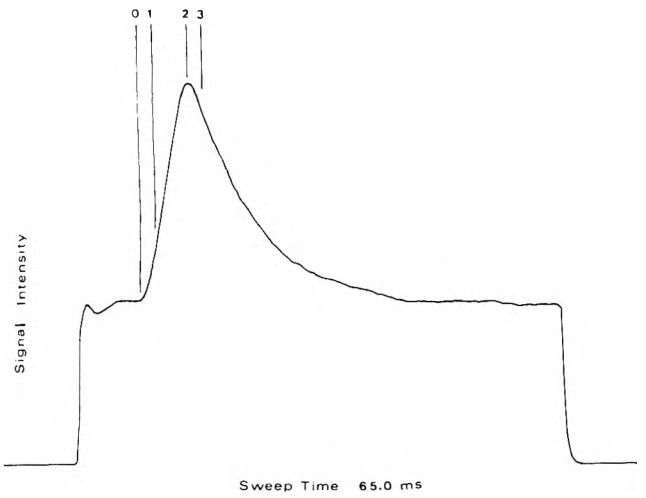

Figure 8. Sample data obtained from X-Y recording of output from PAR waveform eductor. Run 53-2. Non-linear least-squares fitting of eq 4 to this curve gave an average deviation of 1.45% with no deviation larger than 2.7%. Chopper times are indicated at the top of the figure: 0, chopper beginning to open; 1, t_1; 2, t_2; 3, t_3.

Sloth et al. since the case of CsCl on Ni is less favorable for Cs^+ formation than the case of LiCl on Re for Li^+ formation.

Determination of τ_a (Signal Circuit Time Constant). In experiments performed with a clean polycrystalline target, the data were analyzed initially with a single exponential; i.e.

$$V = V_0 \exp(-t/\tau) \tag{5}$$

In this case when the beam pulse frequency was 8.167 Hz, the τ_{exptl} values plotted as a function of temperature are given in Figure 7. There was a distinct break in the curve at $1/T = 10.5 \times 10^{-4}$. Upon analysis of the system more fully, it became apparent that the τ values at high temperatures were values appropriate for the signal circuit. The τ_{exptl} values at $T > 1000$ K were averaged to obtain a value for τ_a of 7.731 ± 0.172 ms.

The value of τ_a was found to be in approximate agreement with a directly measured value of τ_a of 10 ms obtained several months later.

First-Order Kinetics. The basic data in this experiment are ion intensity as a function of sweep time. Only data acquired after the chopper was closed completely were analyzed. A typical set of such data for experiments using a single crystal surface is shown in Figure 8; these are the output data from the waveform eductor. All data were fitted by a non-linear least-squares computer program to eq 4. Agreement between the experimental curve and the fitted curve gave an average deviation of 1.45% with no deviation larger than 2.7%. It is concluded that the assumption used in the derivation of eq 4, i.e., the evaporation process can be treated by first-order kinetics, is correct. The first-order rate constants are the reciprocals of the τ values which shall be presented.

With a polycrystalline surface, it was expected that one would have evaporation kinetics much more complex because of the several crystallites on the surface, see Figure 5. There is some evidence that such complexity results. The τ values were determined assuming first-order kinetics, and these values will be presented.

Single Crystal Surfaces. The values of the mean adsorption lifetimes, the τ values, are given in Figure 9 for a Ni(111) surface and in Figure 10 for a Ni(100) surface. All data were acquired with a pulse frequency of 3.833 Hz. The dependence of the τ values upon target temperature may be analyzed using a linear least-squares computer program with

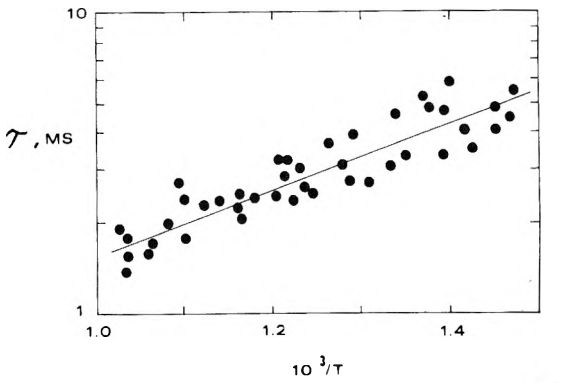

Figure 9. Mean adsorption lifetimes of CsCl on Ni(111) vs. reciprocal of target absolute temperature.

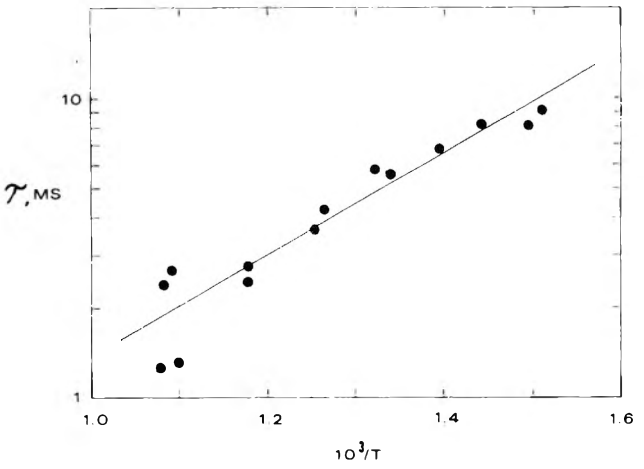

Figure 10. Mean adsorption lifetimes of CsCl on Ni(100) vs. reciprocal of target absolute temperature.

$$\ln \tau = \ln \tau_0 + \Delta H^*/RT \tag{6}$$

where τ_0 is a constant and ΔH^* is the activation enthalpy for the desorption process at the average experimental target temperature. Values of τ_0 and ΔH^* are given in Table I.

Clean Polycrystalline Surface. The temperature dependence of the values of τ is given in Figure 11 for a chopper speed of 3.833 Hz. The values of τ_0 and ΔH^* are given in Table I. It is to be noted that the values of τ_0 and ΔH^* are intermediate between those of Ni(111) and Ni(100).

Contaminated Polycrystalline Surface. With a contaminated polycrystalline Ni target, the data were fitted to eq 5. The τ values were observed to be significantly smaller than the τ values derived from the data for the clean polycrystalline surface. A quantitative value for τ was not determinable in this case.

Discussion

Model. There are several models which may be considered for the desorption process. The localized model would demand that $V(t)$ be dependent on surface coverage which would lead to desorption kinetics of non-first order. The experimental data do not support non-first-order desorption. The nonlocalized model which allows quasi-free translation and rotation of adsorbed species is the most reasonable model to select. With the assumption that translational and rotational motions are unhindered and that internal vibrations are not changed, one may show that

TABLE I: Desorption Data for CsCl on Ni

Surface[a]	τ_0, s	ΔH^*, cal/mol
(111)	$(1.22 \pm 0.31)10^{-4}$	5039 ± 407
(100)	$(2.38 \pm 0.18)10^{-5}$	7992 ± 772
Polycrystalline	$(9.60 \pm 2.99)10^{-5}$	6485 ± 632

[a] All surfaces are believed to be clean since Ni was deposited on them immediately prior to data collection.

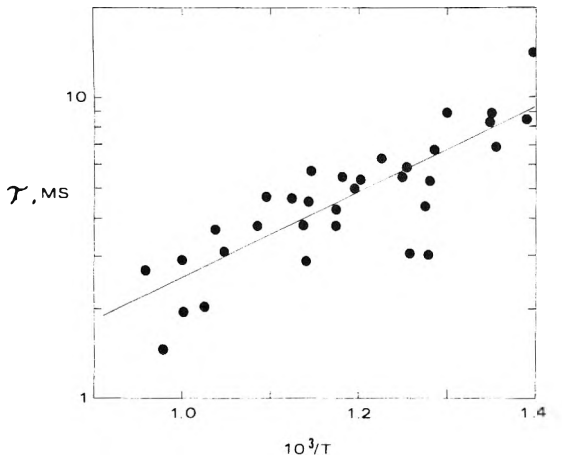

Figure 11. Mean adsorption lifetimes of CsCl on clean polycrystalline Ni vs. reciprocal of target absolute temperature.

$$\tau_0 = (h/kT)\ {}_af_{\mathrm{vib}_z} \tag{7}$$

where h, k, and T have their usual meanings and ${}_af_{\mathrm{vib}_z}$ is the partition function for vibrational motion perpendicular to the surface.

Evaporation of molecules from a surface of the bulk solid has been shown to occur with a mechanism involving atom motion from a kink site to a ledge site to a terrace site to the gas phase.[36] The rate-determining step is the motion from the kink site to the ledge site. In the case of desorption of a species from a surface of a different substance, the rate-determining step appears to be desorption from particular sites on the terrace. The identity of such sites is not known. Several types of sites on the terrace including nucleation sites, grain boundary sites, dislocation sites, and impurity sites are possible.

Dependence of ΔH^* on Surface Structure. From the data for ΔH^* presented in Table I, it is clear that there is a significant dependence of ΔH^* upon the surface structure. For Ni(111), ΔH^* is ca. 5039 cal/mol, and for Ni(100), ΔH^* is ca. 7992 cal/mol. It is to be noted that $\Delta H^*(111)/\Delta H^*(100) = 0.631$.

Blyholder[22] has recently reported results from a CNDO study of CO adsorption on Ni surfaces. These calculations indicated that the ratio of the binding energies of CO adsorbed on Ni(111) to Ni(100) is 2/3. This ratio is in good agreement with the experimental observation for CsCl adsorbed on the Ni surfaces.

τ_0 Values. The experiments with CsCl on Ni surfaces gave rise to τ_0 values given in Table I. These values of τ_0 are between 0.02 and 0.12 ms.

Values of τ_0 are predicted by eq 7. Making a substitution for ${}_af_{\mathrm{vib}_z}$, one finds that τ_0 should be $1/\nu$, where ν is the vibrational frequency perpendicular to the surface; this indicates that τ_0 should be 10^{-13} s. As indicated earlier, any change in the model for nonlocalized adsorption will make τ_0 even smaller. Thus, for the largest value of τ_0 possible, τ_0 must be given by $1/\nu$.

The large experimental values can be understood if desorption occurs only at specific sites. The molecules of CsCl adsorbed on the surface must migrate to the desorption sites. This desorption model will be discussed more fully by Liu and Wahlbeck.[37]

Polycrystalline Data. By examining the photomicrographs of the polycrystalline surface after the targets had been used, Figure 5, the existence of several small crystallites with different crystal faces exposed was evident. One would expect the mean adsorption lifetimes to be a sum of exponentials with each surface having its own characteristic τ_0 and ΔH^*. In approximating the data with a single exponential, intermediate values of ΔH^* and τ_0 between single crystal surfaces data would be effected.

Effect of Contamination. From observations presented earlier, it is apparent that contaminants on a surface lower the value of τ. An increase in τ has been observed with Cs^+ on W surfaces when Cs, CsCl, and CsI were the adsorbed species by Scheer and Fine.[7,9] This may be explained if the contaminants weaken the bonding of the adsorbed gas on the surface.

Acknowledgments. The authors wish to acknowledge gratefully the support of this research by the U.S. National Science Foundation under Grant No. GH-36938 and its predecessor No. GP-30706. Previous support from the U.S. Atomic Energy Commission under Contract No. AT(11-1)-1029 is acknowledged.

The authors also wish to thank Professor W. R. Warke and the Metallurgical Engineering Department at the Illinois Institute of Technology for valuable assistance. Thanks are given to Mr. Harlan Hertrich for his help in the machine shop.

The authors express their appreciation to Dr. Ming Biann Liu and Mr. Vincent Mathews for computational aid performed at Wichita State University.

References and Notes

(1) Based on a thesis by L. W. Huang submitted in partial fulfillment of the requirements for the Ph.D. Degree, Illinois Institute of Technology, Chicago, Ill., 1973.
(2) (a) W. L. Winterbottom, *J. Chem. Phys.*, **49**, 106 (1968); (b) **51**, 5610 (1969).
(3) S. J. Wey and P. G. Wahlbeck, *J. Chem. Phys.*, **57**, 2932 (1972), and earlier papers.
(4) M. B. Liu and P. G. Wahlbeck, *J. Chem. Phys.*, **59**, 907 (1973).
(5) R. C. Evans, *Proc. R. Soc. London Ser. A*, **139**, 604 (1933).
(6) F. Knauer, *Z. Phys.*, **125**, 278 (1948).
(7) M. D. Scheer and J. Fine, *J. Chem. Phys.*, **37**, 107 (1962).
(8) T. Lee and R. E. Stickney, *Surface Sci.*, **32**, 100 (1972).
(9) M. D. Scheer and J. Fine, *J. Chem. Phys.*, **38**, 307 (1963).
(10) H. Shelton and A. Y. Cho, *J. Appl. Phys.*, **37**, 3544 (1966).
(11) J. B. Hudson and J. S. Sandejas, *J. Vac. Sci. Technol.*, **4**, 230 (1967).
(12) J. B. Hudson and J. S. Sandejas in "Fundamentals of Gas-Surface Interactions", H. Saltsburg, J. N. Smith, Jr., and M. Rogers, Ed., Academic Press, New York, N.Y., 1967, pp 271–283.
(13) F. L. Hughes, *Phys. Rev.*, **113**, 1036 (1959).
(14) D. A. Degras, *Adv. Vac. Sci. Technol., Proc. Int. Congr., 3rd., 1965*, **2**, 673 (1965).
(15) D. A. Degras, *Vacuum*, **18**, 122 (1968).
(16) H. H. Madden, J. Küppers, and G. Ertl, *J. Chem. Phys.*, **58**, 3401 (1973).
(17) J. C. Tracy, *J. Chem. Phys.*, **56**, 2736 (1972).
(18) B. Ya. Kolesnikov, A. M. Kolchin, and G. M. Panchenkov, *Zh. Tekh. Fiz.*, **40**, 868 (1970).
(19) D. H. Smith, *J. Chem. Phys.*, **53**, 299 (1970).
(20) G. R. Hertel, *J. Chem. Phys.*, **47**, 133 (1967).
(21) G. Blyholder, *J. Chem. Phys.*, **62**, 3193 (1975).
(22) G. Blyholder, *J. Phys. Chem.*, **79**, 756 (1975).
(23) A. B. Anderson and R. Hoffmann, *J. Chem. Phys.*, **61**, 4545 (1974).
(24) J. H. DeBoer, *Vacuum*, **16**, 309 (1966).
(25) A. Y. Cho and C. D. Hendricks, *J. Appl. Phys.*, **40**, 3339 (1969).
(26) J. Q. Adams, T. E. Phipps, and P. G. Wahlbeck, *J. Chem. Phys.*, **51**, 920 (1969).
(27) W. D. Treadwell and W. Werner, *Helv. Chim. Acta*, **36**, 1436 (1953).

(28) K. K. Kelley, *U.S., Bur. Mines, Bull.*, **383**, 39 (1935).
(29) R. C. Miller and P. Kusch, *J. Chem. Phys.*, **25**, 860 (1956).
(30) J. Berkowitz and W. A. Chupka, *J. Chem. Phys.*, **29**, 653 (1958).
(31) J. G. Allpress and J. V. Sanders, *Surface Sci.*, **7**, 1 (1967).
(32) J. R. Anderson and R. J. MacDonald, *J. Catal.*, **13**, 345 (1969).
(33) G. Struble, "Non-Linear Least Squares Curve Fitting Program", IBM 1620 General Program Library, 6.0.134.
(34) D. R. Stull, Ed., JANAF Thermochemical Tables, 2d ed, Tables and dates: CsCl(g), 30 June 1968; Cs(g), 30 June 1968; Cl(g), 31 March (1961).
(35) E. N. Sloth, M. H. Studier, and P. G. Wahlbeck, *J. Phys. Chem.*, **78**, 820 (1974).
(36) See C. A. Hultman and G. M. Rosenblatt, *Science*, **188**, 145 (1975); O. Knacke and I. N. Stranski, *Prog. Metal Phys.*, **6**, 181 (1956).
(37) M. B. Liu and P. G. Wahlbeck, *J. Phys. Chem.*, following article in this issue.

Mean Adsorption Lifetimes of Cesium and Cesium Iodide on Nickel Surfaces

Ming Biann Liu[1] and P. G. Wahlbeck*

Departments of Chemistry, Wichita State University, Wichita, Kansas 67208 and Illinois Institute of Technology, Chicago, Illinois 60616
(Received October 6, 1975)

Mean adsorption lifetimes of Cs and CsI adsorbed on Ni(111) and Ni(100) surfaces have been determined by a pulsed-molecular-beam technique using ultra-high vacuum techniques and clean surfaces. Molecules effusing from a double-oven Knudsen cell were collimated with slits and chopped with a rotating wheel. The molecular beam was on for 11.086% of the period of the pulsing cycle. The desorption process was found to be first order. The mean adsorption lifetimes have been determined as a function of surface temperature. Surface populations have been varied in some cases, but in all cases they were less than 0.001 monolayer. A mechanism for the desorption process has been proposed which utilizes surface migration of the physically adsorbed species to particular desorption sites. The nature of the possible desorption sites is considered.

Introduction

The mean adsorption lifetimes of Cs and CsI on single crystal surfaces have been determined experimentally. These determinations were part of a continuing effort which began with studies reported by Huang and Wahlbeck.[2] Reasons for interest in the mean adsorption lifetime of species on surfaces and related previous studies have been given by Huang and Wahlbeck.[2]

Huang and Wahlbeck[2] determined the mean adsorption lifetime of CsCl adsorbed on Ni(111), Ni(100), and polycrystalline Ni. They analyzed their data using

$$\tau = \tau_0 \exp(\Delta H^*/RT) \quad (1)$$

where τ is the mean adsorption lifetime, τ_0 is a preexponential factor, T is the absolute temperature, R is the gas constant, and ΔH^* is the activation enthalpy for the desorption process. The values of ΔH^* indicated that CsCl is physically adsorbed on Ni surfaces, and the values showed a dependence on surface structure. The mobile adsorption model was concluded to be correct rather than the model for localized adsorption. The values of τ_0 were much larger than theoretically expected. For mobile adsorption τ_0 is expected to be approximately equal to the reciprocal of the vibrational frequency for the vibrational motion perpendicular to the surface; i.e., 10^{-12} to 10^{-13} s. However, values of τ_0 were found to be 10^{-4} to 10^{-5} s. Reasons for the difference of a factor of 10^8 have been sought.

To aid in the understanding of mean adsorption lifetimes, it was decided to study Cs and CsI adsorbed on Ni surfaces. The selection of Cs was made since there would be no influence of a diatomic molecule in this case. The species CsI was chosen because of the increased size of the I atom and because of the changes in bonding characteristics. In this paper, the new experimental results will be presented. A possible mechanism will be given as an explanation of the experimental results.

* Address correspondence to this author at Wichita State University.

Experimental Section

The experimental apparatus that was used in this study was the same one described by Huang and Wahlbeck.[2] A pulsed molecular beam was produced from vapor effusing from a double-oven effusion cell. The beam molecules passed through two collimating slits with a rotating chopper positioned between the slits. The pulsed molecular beam struck a Ni target which was heated resistively. Desorbed molecules were detected by a surface ionization detector as a function of time.

The following changes were made to the apparatus used by Huang and Wahlbeck:[2] (1) The apparatus was mounted inside an Ultek table top vacuum system Model TNB-X instead of Model TNB-C. (2) A new beam chopper was made on which the slots were cut along radial lines; the beam was opening during 2.750%, was open fully for 5.584%, and was closing during 2.750% of the beam period. (3) The size of the stainless steel protection cylinder around the surface target was increased from 1.34 in. i.d. to 2.25 in. i.d. (4) The detector signal circuit was modified in order to reduce the time constant of the electronic circuit; this eliminated the complex analysis of the experimental data as performed by Huang and Wahlbeck.[2]

In experiments performed with CsI(g), the first collimating slit was water-cooled. When experiments were performed with Cs(g), the first collimating slit was cooled with liquid nitrogen.

Samples. The sample of anhydrous CsI with a stated purity of 99.9% was purchased from Research Organic/Inorganic

Chemical Co. The sample was dried initially at 150 °C before being placed in the apparatus.

Vapor pressure data were measured by Cogin and Kimball[3a] and by Scheer and Fine.[3b] The results of Scheer and Fine[3b] are given by

$$\log P_{atm} = 7.775 - 10\,106/T \quad (2)$$

The composition of the vapor was measured by Rothberg, Eisenstadt, and Kusch;[4] the amount of dimer was found to be less than 0.5%.

Experiments were performed with Cs. Because cesium metal is so reactive, it was decided to generate Cs in the apparatus by chemical reaction. The reaction mixture consisted of Cs_2CrO_4 and Si in a molar ratio of 1:2. A mass spectrometric study indicated that Cs(g) was the only volatile reaction product. The chemical reaction occurs rapidly at 710 °C.

The sample of Cs_2CrO_4 was purchased from Research Organic/Inorganic Chemical Co., and the Si in powder form of 100 mesh was purchased from Alfa Inorganics.

The reaction mixture was placed in the back oven of the effusion cell, the back oven only was heated, and the cesium produced by the reaction could be used for a few days.

Cesium is produced by the chemical reaction involving Cs_2CrO_4 and Si. The equilibrium vapor pressure associated with this reaction has not been studied to the authors' knowledge. The dependence of the Cs pressure upon oven temperature has not been used, but experiments have been performed by heating the ovens to temperatures at which useable intensities have been found.

Targets. Nickel targets were used in this study. The targets were described by Huang and Wahlbeck.[2] In this study, only single crystal surfaces were studied. A Ni(111) surface was prepared by deposition of Ni on air-cleaved mica. A Ni(100) surface was cut from a single crystal boule purchased from Materials Research Corp. The stated purity of the boule was 99.999%. The orientation of the boule was checked by von Laue x-ray diffraction. The Ni(100) surfaces were prepared by spark cutting followed by electropolishing. Spark cutting was done with a rotating slotted disk lowered by a servomechanism. The electropolishing was performed with an electrolyte of 70% concentrated H_2SO_4 and 30% H_2O by volume. A current of 2 A cm^{-2} was used for 30 s to 2 min.

As in the case of the experiments by Huang and Wahlbeck,[2] clean surfaces were obtained by vaporization of Ni onto the mica or the Ni(100) boule before each datum collection. The Ni wire used for these vaporizations was obtained from Leico Industries Inc. and had a stated purity of 99.999%.

Before the targets were used, they were outgassed between 550 and 600 °C for 5 h at pressures in the 10^{-8} Torr range. The target was returned to room temperature before the initial Ni deposition. The initial deposition was performed with the target at room temperature and a vacuum of ca. 6×10^{-9} Torr.

After experiments were performed, the surfaces were examined by optical microscopy with magnifications up to 1600×. The instrument used was a Unitron series N metallograph, Unitron Instruments Co. Selected targets were examined with a scanning electron microscope in the SEM laboratory at the Illinois Institute of Technolgoy.

Detector Circuit. The circuit to handle the ion currents from the surface ionization detector, with final signal averaging analysis performed by a waveforn eductor (Princeton Applied Research Model TDH-9), was modified from that of Huang and Wahlbeck[2] by changing the 10^8-ohm resistor to a 10^6-ohm resistor and by adding an additional operational amplifier with a gain of 100; see Figure 6 of Huang and Wahlbeck.[2] These changes reduced the time constant of the electronic circuit. It was possible, therefore, to treat the experimental data of $V(t)$, desorbing species current as a function of time, with a single exponential; i.e.

$$V(t) = V(t = 0) \exp(-t/\tau) \quad (3)$$

Apparatus Checks. In order to ascertain whether the molecular beam source, the detector, and the signal circuitry were functioning properly, the detector was placed directly in the molecular beam; i.e., the position normally occupied by the surface target. In all other ways, the apparatus was functioning normally. With the chopper running, the beam profile should be observed with a trapezoidal shape as described earlier and with additional flight time effects. With a beam pulse frequency of 10 Hz, the most often used frequency, the time between beam pulses was 100 ms. The most probable flight time was less than 0.1 ms; flight time effects consequently were expected to be insignificantly small. The beam profile was found to be trapezoidal; it was concluded that the beam source, the detector, and the signal circuitry were functioning properly with an apparatus time constant which was much smaller than the mean adsorption lifetimes.

Another apparatus check was performed by allowing CsCl molecules to strike a hot Re target. Scheer and Fine[5] have studied this case determining the τ values of Cs^+ desorption. They observed the mean adsorption lifetimes with a surface cleaned by flash heating to 2400 K and with a contaminated surface. They found

$$\tau(s) = (2.8 \times 10^{-13}) \exp(1.95\ eV/RT) \quad (4)$$
(clean surface)

$$\tau(s) = (2.8 \times 10^{-11}) \exp(1.55\ eV/RT) \quad (5)$$
(contaminated surface)

With the apparatus used in these studies, ions were detected by the surface ionization detector when the Re filament of the detector was not heated. The Re target surface was not capable of being heated to 2400 K. The dependence of τ upon Re target temperature gave

$$\tau(s) = (1.1 \times 10^{-9}) \exp(2.1\ eV/RT) \quad (6)$$

These results are most probably valid for a contaminated surface as indicated by the larger τ_0, or preexponential, value. The ΔH^* values, numerators of the exponents, are all approximately the same. The results indicate that the apparatus is functioning correctly.

Results

Surface Coverage. The number of molecules per second which struck the target depended upon the number of molecules effusing per second and upon the geometry factor of the beam defining slits. The rate of effusion was dependent upon the oven temperatures and upon the vapor pressure of the effusing species. The dimensions of the beam defining slits and other dimensions are provided on Figure 1 of Huang and Wahlbeck.[2]

If equilibrium on the adsorbing surface had been achieved, the number of molecules $(centimeter)^{-2}$ on the surface would have been the product of τ and the arrival rate. The largest values of τ observed were less than 30 ms.

For experiments performed for CsI, the maximum incident flux was 1.4×10^{14} molecules $cm^{-2}\ s^{-1}$ which gave a surface population of 4.2×10^{12} molecules cm^{-2}. Using ionic radii for

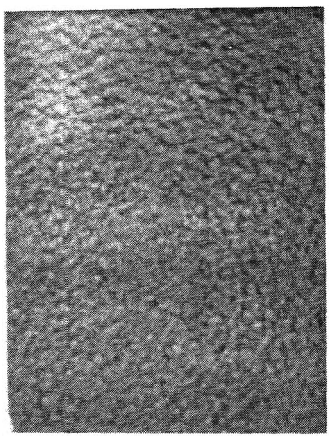

Figure 1. Optical microscopic view of Ni(111) surface at a magnification of 1600×. This surface was used in experiments designated OP-16, 17.

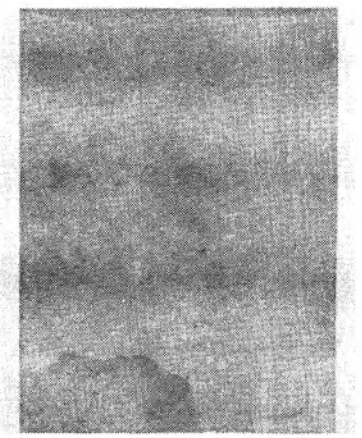

Figure 2. Optical microscopic view of Ni(100) surface at a magnification of 1600×. This Ni(100) surface was designated as single crystal no. 1.

Cs^+ and I^-, one computes that under equilibrium conditions the fraction of the surface covered would be 0.001. Since equilibrium is not achieved, the surface coverage fraction must have been less than 0.001.

Desorbing Species. The detector for desorbing species was a surface ionization detector; the signal would be an integrated signal for all alkali bearing species. For the case where Cs was desorbed, the signal could have been from Cs, Cs_2, and Cs^+. For the case of desorbing CsI, the signal could have been from CsI, Cs_2I_2, Cs, and Cs^+.

In order to detect positive ions desorbed from the Ni surfaces, the heating power for the Re filament of the detector was turned off leaving the bias to the filament on. No signals were detected in the cases of CsI and Cs impinging on the surface indicating that no ions were desorbing from the Ni targets. Using this technique in experiments with CsCl impinging on a hot Re target surface, ion desorption was easily detected.

For the case of Cs, the equilibrium amount of dimer in the gas phase is indicated to be small according to the "JANAF Thermochemical Tables";[6] the ratio of dimer to monomer would have been at least as small as 10^{-5} at 1000 K. The desorbed species from the Ni surfaces are indicated to have been neutral Cs(g).

For the case of CsI, the equilibrium amount of dimer in the gas phase was indicated to be small by Rothberg, Eisenstadt, and Kusch.[4] Calculations were performed to estimate the amount of dissociation of CsI on the Ni surface. These calculations utilized thermodynamic properties for Cs(g) and I(g) from the "JANAF Thermochemical Tables"[6] and thermodynamic properties for CsI(g) calculated by statistical mechanics using the harmonic-oscillator, rigid-rotor model. The spectroscopic data are given by Rice and Klemperer,[7] Barrow and Caunt,[8] and Honig et al.[9] The dissociation energy of CsI, $D_0°$ [CsI(g)], was taken from Gaydon[10] as 3.4 eV. With an incident intensity of CsI molecules of 1.4×10^{14} molecules $cm^{-2}\ s^{-1}$ and with a target temperature of 907 K, the dissociation fraction was calculated to be 2×10^{-5} which is negligibly small.

Surfaces. All single crystal surfaces used in these studies were examined after measurements were completed. The surfaces were examined by optical microscopy to magnifications of 1600×. Photomicrographs of typical surfaces are shown in Figures 1 and 2. From the photomicrographs, the surfaces show a uniform appearance over the entire surface. All of the surfaces show the same type of macroscopic structure; i.e., the surfaces show patches which are typical when deposit growth occurs by two-dimensional nucleation phenomenon.

The same targets which are shown in Figures 1 and 2 using optical microscopy were studied using a scanning electron microscope. As with the optical micrographs, the surfaces appeared to be highly uniform with a hillock structure. The size of the hillocks shown in Figure 1 are about 5×10^{-5} cm in radius. On the Ni(111) surface, energy analysis of secondary electron emission showed no detectable amounts of W, Cs, or Mg (from mica). Contamination of the surface by the W heater of the Ni evaporator or by condensation of Cs bearing species appears to have not occurred. Since no Mg was observed, it is concluded that the Ni surface which was grown epitaxially was continuous.

Detailed studies of surface structures of Ni deposited on vacuum-cleaved mica have been made by Allpress and Sanders[11] and on air-cleaved mica by Anderson and MacDonald.[12]

First-Order Kinetics. All $V(t)$ data were examined for adherence to first-order kinetics. It is believed that the desorption process should be a first-order process; the data analysis should verify that this assumption is valid. Malfunctioning of the apparatus occasionally gave results which appeared not to be first order.

Plots of log $V(t)$ vs. time were made, and the data should fall on straight lines if the process obeys first-order kinetics. Examples of such plots are given in Figures 3 and 4. All data which are reported are first-order data.

Mean Adsorption Lifetime Data. The experimental data of $V(t)$ vs. time were treated by use of eq 3 to derive τ values. The dependence of τ on target temperature for CsI is given in Figures 5 and 6 for the Ni(111) and Ni(100) targets, respectively, and for Cs in Figures 7 and 8 for the Ni(111) and Ni(100) targets, respectively.

The data for the dependence of τ on target temperature may be treated according to eq 1, and values for ΔH^* and τ_0 may be derived. Table I summarizes data which have been obtained in this study.

Independence of the values of τ of chopper speed should occur if one truly has first-order kinetics. Data from runs with CsI labeled OP-16 and OP-17 were acquired with chopper speeds of 12.5 and 20 Hz, respectively. From data presented in Figure 5, one may see that the τ values are independent of chopper frequency. At low surface coverages, one would not expect the desorption process to be higher order.

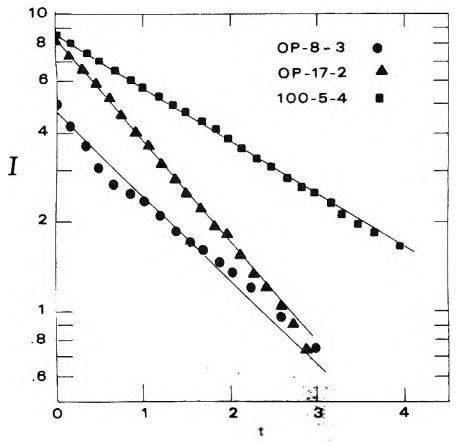

Figure 3. Intensity vs. time. Time scale was: OP-8-3, 1.742 ms/unit; OP-17-2, 4.59 ms/unit; 100-5-4, 5.50 ms/unit. These plots were used to test first-order kinetics. Data from OP-8 were not used.

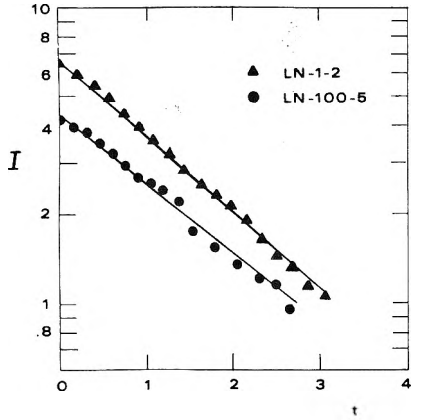

Figure 4. Intensity vs. time. Time scale was: LN-1-2, 5.02 ms/unit; LN-100-5, 3.39 ms/unit. These plots were used to test first-order kinetics.

Discussion

Mean Adsorption Lifetime Data. A summary of data obtained by Huang and Wahlbeck[2] and data obtained in this study is given in Table II.

These data have varying reliability. Uncertainties found from least-squares analyses are reported with the values of ΔH^* and τ_0. The data obtained in this study are believed to have higher reliability because of the simpler data treatment to calculate τ values. In this study the basic experimental data were fitted to eq 2 whereas Huang and Wahlbeck[2] had to use a much more complex equation because of the importance of the time constant associated with the apparatus.

The data are believed to be reliable because of results from apparatus checks described earlier.

Surfaces. The surfaces which were used in this study were single crystalline. It is believed that the surfaces were clean since fresh nickel was evaporated onto the surfaces before each datum point was determined and since the vacuums were below 1×10^{-7} Torr. Data on sticking coefficients of different gases on nickel surfaces under low pressure conditions show that oxygen[13,14] has a sticking coefficient of 0.01 on Ni(111) and Ni(100), nitrogen[15] has a sticking coefficient of zero on Ni surfaces at temperatures above room temperature and pressures less than 10^{-3} Torr, and carbon monoxide has a sticking coefficient on Ni of 5×10^{-4} according to Degras[16] and 1.0 according to Horgen and King.[17] The times required

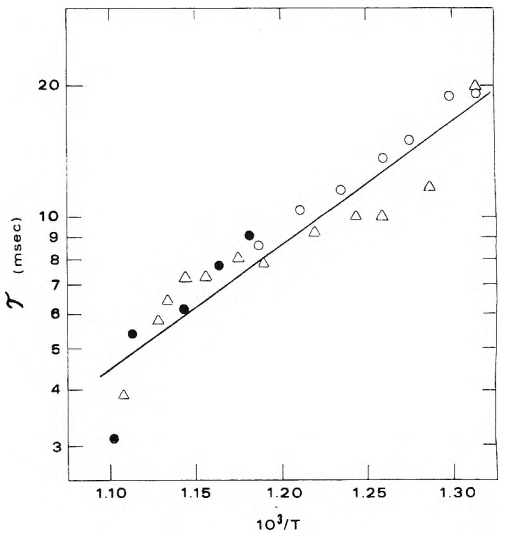

Figure 5. Mean adsorption lifetimes of CsI on Ni(111) vs. reciprocal of target absolute temperature: (●) OP-16, beam pulsed at 20 Hz; (○) OP-16, beam pulsed at 12.5 Hz; (△) OP-17, beam pulsed at 12.5 Hz.

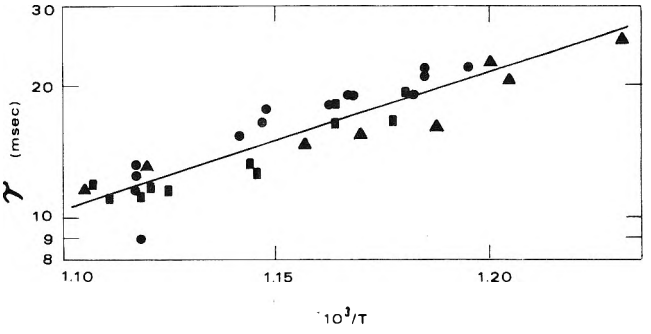

Figure 6. Mean adsorption lifetimes of CsI on Ni(100) vs. reciprocal of target absolute temperature: (▲) run 100-2; (●) run 100-5; (■) run 100-7.

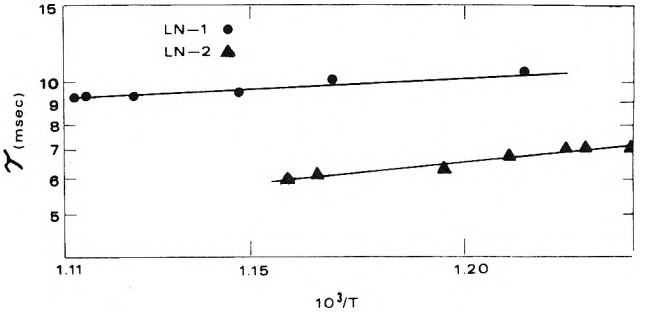

Figure 7. Mean adsorption lifetimes of Cs on Ni(111) vs. reciprocal of target absolute temperature.

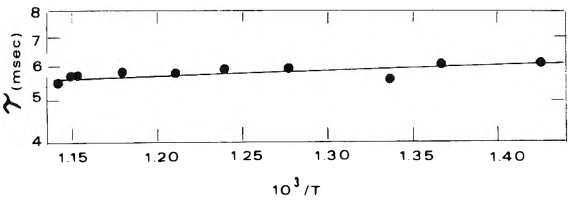

Figure 8. Mean adsorption lifetimes of Ni(100) vs. reciprocal of target absolute temperature. Run LN-100.

TABLE I: Mean Adsorption Lifetimes of CsI and Cs on the Nickel Surfaces

Run no.	System	Target temp, K	Vacuum, Torr	Temp, °C: Front oven	Temp, °C: Back oven	τ_0, s	ΔH^*, kcal/mol	Remarks
OP-16 OP-17	CsI/ Ni(111)	761–907	8×10^{-8} to 2×10^{-7}	609	591	$(3.20 \pm 1.84) \times 10^{-6}$	13.1 ± 0.9	20 and 12.5 Hz, 140 monolayers per deposit (total 1.9 mg)
100-2 100-5 100-7	CsI/ Ni(100) No.1	812–905	8×10^{-8} to 2×10^{-7}	615	608	$(4.17 \pm 2.81) \times 10^{-6}$	14.2 ± 1.2	10 Hz
100-4	CsI/ Ni(100) No. 1	842–888	8×10^{-8} to 2×10^{-7}	629	621	$(4.72 \pm 4.28) \times 10^{-7}$	17.8 ± 1.6	10 Hz, no nickel deposition in this experiment
LN-1	Cs/Ni(111)	824–902	1×10^{-7}	573	612	$(3.00 \pm 0.59) \times 10^{-3}$	2.0 ± 0.3	10 Hz, diameter of hillocks $\sim 2 \times 10^{-4}$ cm; 3×10^7 hillocks cm^{-2}
LN-2	Cs/Ni(111)	807–858	7×10^{-8} to 1×10^{-7}	579	620	$(4.31 \pm 0.97) \times 10^{-4}$	4.5 ± 0.4	10 Hz, 250 monolayers per deposit (total 1.1 mg), diameter of hillocks ca. 1×10^{-4} cm; 1×10^8 hillocks cm^{-2}
LN-100	Cs/Ni(100) No. 2	702–870	$(1–4) \times 10^{-7}$	620	625	$(4.46 \pm 0.45) \times 10^{-3}$	0.5 ± 0.2	10 Hz, repolished surface of nickel single crystal No. 2 using alumina and cloth. Probably not reliable

TABLE II: Experimental Data for τ_0 and ΔH^*

Adsorbent[a]	Target[b]	ΔH^*, kcal	τ_0, s
Cs	Ni(111)	3.3 ± 0.4	$(1.7 \pm 1.6)10^{-3}$
CsCl	Ni(111)	5.04 ± 0.41	$(1.22 \pm 0.31)10^{-4}$
CsCl	Ni(100)	7.99 ± 0.77	$(2.38 \pm 1.18)10^{-5}$
CsCl	Ni, poly	6.50 ± 0.63	$(9.60 \pm 2.99)10^{-5}$
CsI	Ni(111)	13.1 ± 0.9	$(3.20 \pm 1.84)10^{-6}$
CsI	Ni(100)	14.2 ± 1.2	$(4.17 \pm 2.81)10^{-6}$

[a] Data for adsorbed CsCl is from Huang and Wahlbeck.[2] [b] All surfaces are believed to be clean since Ni was deposited on them immediately prior to data collection.

for a monolayer of contaminants to deposit from the residual gases in vacuo is difficult to estimate from the above data. One would expect it to be longer than the time calculated (perhaps by a factor of 10) assuming all gases have a sticking coefficient of unity. If the sticking coefficients were unity and the pressure was 1×10^{-7} Torr, it would take 35 s for a monolayer of contaminants to be deposited.

Allpress and Sanders[11] studied Ni surfaces grown on vacuum-cleaved mica. These surfaces consisted of crystallites which had (111) faces oriented well with the mica surface. The orientations of other axes of the crystallites on the mica surface were excellent, and the crystallites grew together to form a homogeneous film. Anderson and MacDonald[12] studied Ni deposits on air-cleaved mica. In the air-cleaved case, the crystallites were oriented well so that (111) faces were parallel to the mica surface. However, in this case, the other axes of the crystallites were not well oriented. There were a number of dislocations formed where the crystallites grew together. Since the mica was cleaved in air in experiments reported here, it is believed that the (111) surfaces which were used better fit the latter class.

The photomicrographs shown in Figures 1 and 2 and the scanning electron micrographs show the small hillocks which are the crysallites which have grown. From the study of Anderson and MacDonald[12] it is concluded that there are dislocations in the regions where the crystallites have grown together. The number of such defects would be directly proportional to the number of crystallites on the surface.

It is assumed that the deposits of Ni on the Ni(100) boule surface has (100) surfaces well oriented with the boule surface.

Types of surface sites can be classified as follows: (1) ledge and kink sites which are associated with the contours of the hillocks; (2) dislocations caused by the intergrowth of slightly misaligned hillocks where there are about 10^8 hillocks cm^{-2}; and (3) impurity sites (about 10^{10} impurity sites cm^{-2}) which are expected since the impurity levels in the Ni wire used on the evaporator and in the single crystal boule was 1 in 10^5 Ni atoms. These surface sites are believed to play an important role in the desorption process.

ΔH^*. From the data presented in Table II, the values of ΔH^* increase as one goes from atomic Cs to CsCl to CsI.

In all cases represented in Table II, the ΔH^* values are such as to be classified as belonging to physical adsorption; i.e., a weakly adsorbed material.

CNDO calculations reported by Blyholder for H[18] and for CO[19] adsorption on Ni surfaces have revealed the following interesting conclusions. (1) The binding energy of either H or CO is greatest over a surface hole, less when the adsorbed species is in a bridged position between two Ni atoms, and least when the adsorbed species is directly over a Ni atom. (2) For H atoms, the binding energies for different Ni surfaces are such that (111) > (110) > (100), whereas for CO, (111) < (100) and (111)/(100) = 2/3. (3) The d electrons of the Ni atoms do not play a significant role in the binding of adsorbed species. (4) The surface migration energy is the binding energy of the adsorbed species over a hole minus the binding energy in the bridged position; the surface migration energy is smaller than the binding energy over a hole position.

TABLE III: Mean Times Calculated for Steps of the Proposed Mechanism

Step no.	Process	N	ΔH,[d] kcal	τ, s	Note
1	A(kink) → A(ledge)	1	26	4.8×10^{-8}	
2	A(ledge) → A(ledge)	100	22	6.4×10^{-7}	*a*
	A(ledge) → A(terrace)	1	24	1.7×10^{-8}	
3	A(terrace) → A(desorp)	10^6	13.1	7.3×10^{-5}	*b*
4	A(desorp) → A(g)	1	20	2.3×10^{-9}	
1′	A(ledge) → A(ledge)	100	22	6.4×10^{-7}	*a*
	A(ledge) → A(kink)	1	22	6.4×10^{-9}	
2′	A(terrace) → A(ledge)	3000	13.1	2.2×10^{-7}	*c*
4′	A(g) → A(terrace)	$[\bar{Z} = \alpha_{trap} P/(2\pi mkt)^{1/2}]$			

[a] For the adsorbed species to go from its initial ledge position to a terrace position requires multiple random walk steps involving ledge to ledge positions. It has been estimated that no more than 100 such steps would be required. [b] For the adsorbed species to go from its initial terrace position to a desorption site requires multiple random walk steps involving terrace to terrace positions. An estimate of this number is given in the text. [c] For the adsorbed species to go from its initial terrace position to a ledge site requires multiple random walk steps involving terrace to terrace positions. An estimate of this number of steps was obtained by considering that the average distance covered was about 50 Å. [d] ΔH for step 3 and step 2′ were taken from the experimental data for the desorption of CsI. Values for ΔH for the other steps were estimated by incrementing the values according to the number of nearest neighbor Ni atoms.

From the above conclusions, dislocation sites, in which there are more atoms present than the usual perfect array allows, would be less binding for H atoms but more binding for CO molecules.

From data presented in Table II, the ratio of ΔH^* values for CsCl adsorbed on Ni(111) to Ni(100) is 0.631 which is close to the ratio found theoretically by Blyholder[19] for CO adsorbed on Ni.

τ_0 Values. In the introduction of this paper, it was remarked that one of the purposes of this work was the search for an explanation of the large τ_0 values found by Huang and Wahlbeck[2] for CsCl adsorbed on Ni. In this study with Cs and CsI adsorbed on Ni, large values of τ_0 again have been found. It is believed that the explanation for this must be sought in the detailed mechanism of the desorption process.

Proposed Mechanism. With physical adsorption, surface migration can occur readily as has been observed in field emission microscope experiments such as those performed by Ehrlich and Hudda.[20] This is consistent with the discussion by Huang and Wahlbeck[2] in which localized adsorption was ruled out and a mobile adsorption model was selected. The following mechanism is proposed which is consistent with the kink–ledge–terrace mechanism[21,22] usually used for bulk vaporization processes, with the observations of surface migration, and with the experimental data reported from this study:

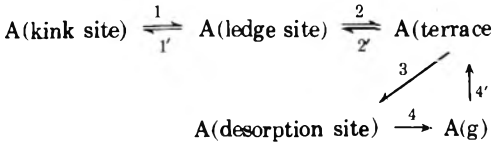

In the experiments reported in this study, most molecules will strike the surface on terrace sites (step 4′) since the molecular beam is uniform in intensity and most of the surface consists of terrace sites.

Step 3 consists of surface migration to a desorption site. The desorption site would have to be a site associated with the Ni surface for which the adsorbed species has a smaller binding energy.

All motions of the adsorbed species on the surface from one surface site to the next are assumed to occur because of vibrational motions associated with the lattice potential surface. Each change of site will have a τ value of

$$\tau = \tau_0^\circ \exp(\Delta H/RT) \tag{7}$$

where $\tau_0^\circ = 10^{-13}$ s and ΔH is related to the depth of the potential well. For ledge motion and surface migrational motion, multiple (N) random walk steps are required with

$$\tau = N\tau_0^\circ \exp(\Delta H/RT) \tag{8}$$

In Table III are estimated values of the parameters associated with CsI adsorbed on Ni(111). From the calculated τ values, it is concluded that step 3, the surface migration of the adsorbed species from the first terrace site to the desorption site, is the rate-determining step in the process. A large N value for the rate-determining step is required for the predicted τ_0 ($= N\tau_0^\circ$) value to agree with experimental data reported in Table II. In order for step 1 to be rate determining, ΔH for step 1 would have to be greater than 40 kcal.

In order to explore this proposed mechanism, an identification of the desorption sites would be most helpful. Of the sites considered under the discussion of surface characterization, ledge and kink sites and dislocation sites probably would have a greater binding energy for the adsorbed species. The impurity sites could serve as desorption sites if the impurity atoms lowered the binding energy. There are about 10^{10} impurity sites cm^{-2}. The average area served by a defect would be 10^{-10} cm^2 defect^{-1}. Assuming circular geometry, the average radius served by such a defect would be 5.6×10^{-6} cm^2. For a random walk motion on the surface, the average displacement, r, is given by

$$r^2 = Nd^2/3 \tag{9}$$

where N is the number of jumps in the random walk and d is the jump distance. If the average jump distance for Ni is taken to be 1.24 Å, then there would be 6×10^5 jumps.

The average surface migrational speed of the adsorbed molecules would be given by

$$\bar{C} = d/\tau = (d/\tau_0) \exp(-\Delta H^*/RT) \tag{10}$$

For the case of adsorbed Cs, $\bar{C}$ would be 1×10^4 cm s^{-1}. This surface migrational speed is in approximate agreement with that calculated from $\bar{C} = (\pi kT/2m)^{1/2}$, see Moelwyn-Hughes,[23] which gives a value of $\bar{C}$ of 2.8×10^4 cm s^{-1}. With the approach for the average surface migrational speed given by d/τ, the values of $\bar{C}$ would decrease as ΔH^* increases. This

is a reasonable result. As the number of desorption sites decreases, the observed value of τ_0 would increase.

Contamination Effects. A decrease in τ values with contaminated surfaces has been observed in these studies with desorption of CsCl and CsI as well as in the case of desorption of U^{24} and U^{+}.[25] Studies by Scheer and Fine[5] of desorption of Cs^{+} resulting from Cs, CsCl, and CsI adsorbed on W and Re surfaces showed that τ increased when the surface was contaminated. An explanation of the decrease observed in the present studies with contamination of the surface is given by considering that more desorption sites are present with more impurities on the surface. Fewer random walk steps would be required in step 3. In the studies of Scheer and Fine, large values of ΔH^* were observed which would lead one to believe that step 1 is probably the rate-determining step in their desorption process. The addition of contaminates to the surface in the studies of Scheer and Fine would not be expected to have the same effect since the rate-determining step is step 1 rather than step 3.

Acknowledgments. The authors gratefully acknowledge financial support for this research from the National Science Foundation through Grants No. GH-35938 and GH-42513.

Thanks are given also to Dr. Leo W. Huang for his work on preparation of the Ni(100) surfaces and some scanning electron microscopy performed at the University of Wisconsin—Milwaukee. Professor William Warke of the Illinois Institute of Technology is thanked for his help with scanning electron microscopy of the surfaces used in this study.

References and Notes

(1) Based on a thesis by M. B. Liu submitted in partial fulfillment of the requirements for the Ph.D. Degree, Illinois Institute of Technology, Chicago, Ill., 1974.
(2) L. W. Huang and P. G. Wahlbeck, *J. Phys. Chem.*, preceding paper in this issue.
(3) (a) G. E. Cogin and G. E. Kimball, *J. Chem. Phys.*, **11**, 1035 (1948). (b) M. D. Scheer and J. Fine, *ibid.*, **36**, 1647 (1962).
(4) G. M. Rothberg, M. Eisenstadt, and P. Kusch, *J. Chem. Phys.*, **30**, 517 (1959).
(5) M. D. Scheer and J. Fine, *J. Chem. Phys.*, **38**, 307 (1963).
(6) D. R. Stull and H. Prophet, *Natl. Stand. Ref. Data Ser., Natl. Bur. Stand.*, **No. 37**, 2nd ed (1971).
(7) S. A. Rice and W. Klemperer, *J. Chem. Phys.*, **27**, 573 (1957).
(8) R. F. Barrow and A. D. Caunt, *Proc. R. Soc. London, Ser. A*, **219**, 120 (1953).
(9) H. Honig, M. Mandel, M. L. Stitch, and C. H. Townes, *Phys. Rev.*, **96**, 629 (1954).
(10) A. G. Gaydon, "Dissociation Energies and Spectra of Diatomic Molecules", 3d ed, Chapman and Hall, London, 1968.
(11) J. G. Allpress and J. V. Sanders, *Surface Sci.*, **7**, 1 (1967).
(12) J. R. Anderson and R. J. MacDonald, *J. Catal.*, **13**, 345 (1969).
(13) L. H. Germer, E. J. Scheibner, and C. P. Hartman, *Phil. Mag.*, **5**, 222 (1960).
(14) L. H. Germer and A. V. MacRae, *J. Appl. Phys.*, **33**, 2923 (1962).
(15) L. H. Germer and A. V. MacRae, *J. Chem. Phys.*, **36**, 1555 (1962).
(16) D. A. Degras, *Suppl. Nuovo Cim.*, **5**, 408 (1967).
(17) A. M. Horgen and D. A. King in "The Structure and Chemistry of Solid Surfaces", G. A. Somorjai, Ed., Wiley, New York, N.Y., 1969.
(18) G. Blyholder, *J. Chem. Phys.*, **62**, 3193 (1975).
(19) G. Blyholder, *J. Phys. Chem.*, **79**, 756 (1975).
(20) G. Ehrlich and F. G. Hudda, *J. Chem. Phys.*, **35**, 1421 (1961).
(21) O. Knacke and I. N. Stranski, *Prog. Metal Phys.*, **6**, 181 (1956).
(22) C. A. Hultman and G. M. Rosenblatt, *Science*, **188**, 145 (1975).
(23) E. A. Moelwyn-Hughes, "Physical Chemistry", 2d ed, Pergamon Press, New York, N.Y., 1961, p 959.

An Electron Spin Resonance Study of the Pressure Dependence of Ordering and Spin Relaxation in a Liquid Crystalline Solvent[1]

James S. Hwang, K. V. S. Rao, and Jack H. Freed*

Department of Chemistry, Cornell University, Ithaca, New York 14853 *(Received December 17, 1975)*

An ESR study of ordering and relaxation as a function of pressure is reported for the perdeuterated Tempone nitroxide radical probe in phase V solvent. The study of ordering focuses on the nature of the intermolecular interactions between the probe and solvent (and between solvent molecules), which lead to the weak ordering of the probe. The results are suggestive of longer range interactions than were previously found by McColl in an NMR study on a pure solvent. The spin relaxation results have been analyzed in terms of activated-state theory to obtain values of ΔH_a and ΔV_a as a function of T and P for the rotational reorientation. Anomalous features of the spin relaxation previously reported by Polnaszek and Freed in a temperature-dependent study of this system are reported here as a function of pressure. These anomalies are most pronounced for rotational correlation times (τ_R) large enough that ESR line shapes are no longer motionally averaged (i.e., they are characteristic of the slow motional region). In general, the anomalous behavior depends mainly on τ_R and appears to be nearly independent of the particular combination of T and P. A mechanism in which the local structure around the probe relaxes more slowly than the probe, as proposed by Polnaszek and Freed, is taken to be the most likely explanation. Rapid motional effects in the rigid solvent are also reported. Details of the high-pressure accessory are given.

1. Introduction

ESR relaxation studies can supply useful information about molecular dynamics in condensed media. We have actively conducted careful studies of such processes in both isotropic and anisotropic (liquid crystalline) environments,[2-6] over a wide range of temperatures, embracing the fast motional region to the rigid limit. Some NMR studies have demonstrated the utility of experiments over a wide range of pressures to learn about molecular dynamics.[7,8] However, there are few comparable ESR studies.[9] In this work, we complement our previous experiments on temperature dependence, in which

line shapes consistent with non-Brownian reorientational motion (e.g., large angle jump diffusion) and anomalous frequency dependences of the rotational reorientational correlation functions were observed, with a study of pressure dependence. This complementary study has yielded results which aid in interpreting the previous observations. For example, we can ask such questions as to whether "pressure-induced" slow-motional spectra will be consistent with the same or different non-Brownian motional models; or whether anomalous frequency-dependent line width behavior also exists as a function of pressure.

The primary effect of increasing pressure at constant temperature is to increase the intermolecular potentials, while measurements at constant pressure, in which temperature is varied, include combined effects of molecular kinetic energies and intermolecular potentials. Thus, the pressure-dependent experiments are more directly amenable to analysis in terms of molecular models. [Of course representations of the experiments at constant volume are of considerable utility, but this requires the knowledge of PVT data.] Furthermore, as reviewed by Jonas,[7] pressure-dependent experiments are very useful in distinguishing between spin relaxation effects due to internal motions from those due to overall motions. This is of particular importance in assigning anomalous relaxation behavior.

We have, in this work, studied the spin-probe PD-Tempone in the liquid crystalline solvent phase V. We have shown in previous extensive studies at atmospheric pressure with a variety of isotropic and nematic liquid solvents that, by the use of this perdeuterated spin probe, one removes most of the undersirable width inhomogeneity typical of spin probes. This yields better resolved spectra, which can be analyzed with much greater confidence and accuracy. Also, it was found in our previous studies with this probe that the magnetic tensors are very nearly identical in a variety of nonhydrogen-bonding solvents, including nematic solvents,[3-5] and we take this to imply that there are little or no specific interactions with the nitroxide entity in such solvents that might confuse our interpretations. We chose phase V solvent for this initial study as a function of pressure, because it was the only nematic solvent that in our previous studies[5] had the properties of (1) having a nematic phase over a wide temperature range and (2) being viscous enough at its lower temperatures that spectra characteristic of the slow motional region were observed. These properties were expected to be manifested as a function of pressure.

It is possible, with nematic solvents, to study thermodynamic properties related to the measured order parameter as a function of T and P (or T and V), and one may interpret them in terms of statistical theories of the nematic state. There have been a few such NMR studies of nematics,[10-12] although this work is the first such ESR study. Thus, while our experiments were conceived primarily for studies of molecular dynamics, we also discuss our results on ordering to indicate their relevance to nematic equations of state.

The experimental aspects, including a description of the high-pressure system, are given in section 2. Our results on ordering vs. T and P are given in section 3, where they are discussed in terms of simple mean field theory. The spin relaxation results are presented and discussed in section 4. Conclusions appear in section 5.

2. Experimental Methods

Spectra of PD-Tempone in phase V at X-band were obtained with a Varian E-12 spectrometer modified for high pressures and interfaced with a PDP-9 computer. The details of interfacing are discussed in ref 3. The high-pressure experiments were carried out in a thermostated Be–Cu vessel containing a slow-wave helix, and a pair of modulation coils mounted on a Teflon modulation capsule. The high-pressure system was designed for 10 kbars maximum pressure, but the actual maximum pressures required in this work (e.g., 4.5 kbars for phase V at 45 °C) were determined by the freezing point of the nematic phase of phase V.

The high-pressure generating system is capable of delivering 14 l. of high-pressure fluid continuously without being disconnected from the vessel. The schematic of the high-pressure generating system is given in Figure 1. Pressures up to 4 kbars can be conveniently generated with a Haskel DSXHW-602 air driven liquid pump. This is performed with valves 1 and 2 closed and valve 3 open. For pressures in excess of 4 kbars (and up to 10 kbars), a Harwood A2.5J high-pressure intensifier is brought into the circuit by closing valve 3 and opening valve 2.

We show in Figure 2 the assembled ESR high-pressure vessel which was tested up to 7 kbars. The vessel is machined from a 2-in. rod of temper H Berylco 25. The rod was tested ultrasonically before machining using an immersion method. After machining, the finished parts were heat treated (at 600 °F for 2 h) using a precipitation hardening process. Earlier work on the use of Berylco 25 for a high-pressure ESR vessel has been discussed by Plachy and Schaafsma[13] and by Doyle et al.[14] for a high-pressure ENDOR cavity. The microwave and pressure plugs, which seal the ESR vessel at both ends, employ true Bridgman seals,[15] which cause minimal wear on the seals and yield a vessel virtually free of leaks.[16] The microwave plug was designed for variable frequency experiments from S-band to X-band.

Variable temperature and high pressure experiments were performed using a brass temperature control jacket constructed to fit around the pressure vessel. This system was made leak tight by means of a rubber sealant. The temperature of the solution in the variable temperature jacket was monitored with a copper–constantan thermocouple or (when accurate temperature reading to 0.1 °C is required) a precision thermistor. The solution, which flows into the copper tubings of the temperature control jacket, is from a Tamson constant temperature bath, with temperature stability to within 0.01 °C. The temperature in the temperature control jacket is constant to within 0.1 °C and has a temperature range from −25 to 75 °C.

The sample preparation and sample holder containing a helix are similar to the description given elsewhere.[9] The solutions of PD-Tempone in phase V were somewhat more concentrated than previously used in I in order to enhance sensitivity. Some spin exchange, therefore, was present at the higher temperatures near atmospheric pressure, but it was still possible to introduce the appropriate line shape corrections for inhomogeneous deuteron broadening[3,5] in the presence of spin exchange in the manner of Lang and Freed.[17]

Most of the other aspects of the experimental methods are as discussed in I; e.g., the magnetic tensor components used for PD-Tempone in phase V are those given in I.

3. Order Parameters and Statistical Thermodynamic Relations

The nominal ordering parameters $\langle \boldsymbol{D}^2_{00} \rangle_z \equiv S^{(p)}$ determined for PD-Tempone in phase V, appropriate for a one parameter potential,[5] are plotted vs. pressure in Figure 3. [The $\boldsymbol{D}^L_{KM}(\Omega)$ are the generalized spherical harmonics, cf. ref 2–5, and the

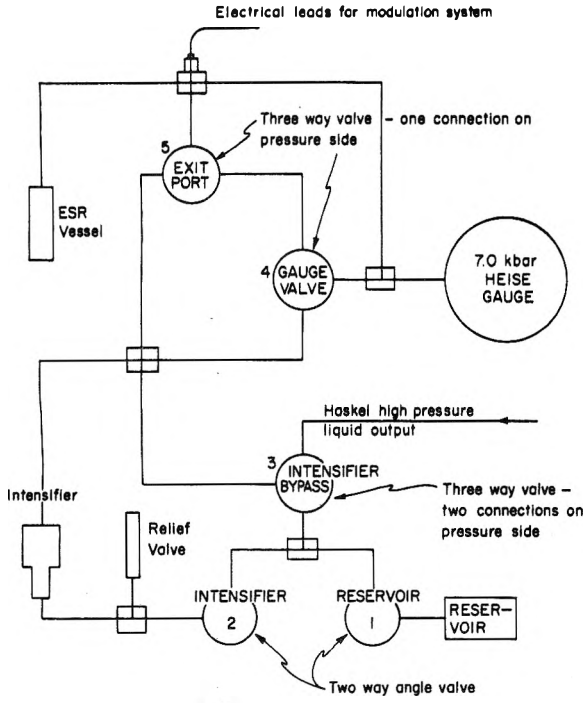

Figure 1. Schematic of the high pressure generating system.

angular brackets imply ensemble averaging.] These results are from the measured hyperfine shifts and are computed from eq 2.27a of I (with β' the tilt angle of the magnetic z axis with respect to the ordering z' axis set equal to zero). It is seen to vary linearly with pressure. (The significant deviations from linearity at high pressures are due to the fact that the data have not been corrected for the effects of slow tumbling and are not otherwise anomalous, cf. I.) In an NMR study on PAA of $S^{(s)}$ (the order parameter of the pure solvent) with pressure at more elevated temperatures, the graphs were generally nonlinear.[11]

It was shown in I, that the ordering of the spin probe is usually not axially symmetric, so that a pair of order parameters $\langle \boldsymbol{D}^2_{0,0} \rangle_z$ and $\langle \boldsymbol{D}^2_{2,0} + \boldsymbol{D}^2_{-2,0} \rangle_z$ (and the principal axes) must be specified. These may be determined from combined hyperfine and g shift measurements and eq 2.26 of I. However, it was not conveniently possible to measure very accurate g values in the high-pressure vessel. It was therefore assumed for convenience that the nominal $\langle \boldsymbol{D}^2_{0,0} \rangle_z$ value shown in Figure 3 may be replaced by the associated pair of order parameters found in I for the same nominal $\langle \boldsymbol{D}^2_{0,0} \rangle$ in the same system at atmospheric pressure (or more precisely the vapor pressure of solvent) and different temperatures. This would follow if, while the extent of ordering is affected by T and P, the "symmetry" of the molecular alignment remains about the same for a given extent of ordering. The basis of the two-term ordering tensor is[5]

$$\langle \boldsymbol{D}^L_{KM}(\Omega) \rangle = \int d\Omega P_0(\Omega) \boldsymbol{D}^L_{KM}(\Omega) \tag{3.1}$$

where $P_0(\Omega)$, the equilibrium distribution in Euler angles Ω between the molecular coordinate system and the laboratory system, is given by

$$P_0(\Omega) = \exp(-U(\Omega)/kT)/\int d\Omega \exp(-U(\Omega)/kT) \tag{3.2}$$

with $U(\Omega)$ the mean restoring potential of the probe in the field of nematic solvent molecules, which is given by

$$U(\alpha, \beta, 0)/kT \simeq -\lambda \cos^2 \beta - \rho \sin^2 \beta \cos 2\alpha \tag{3.3}$$

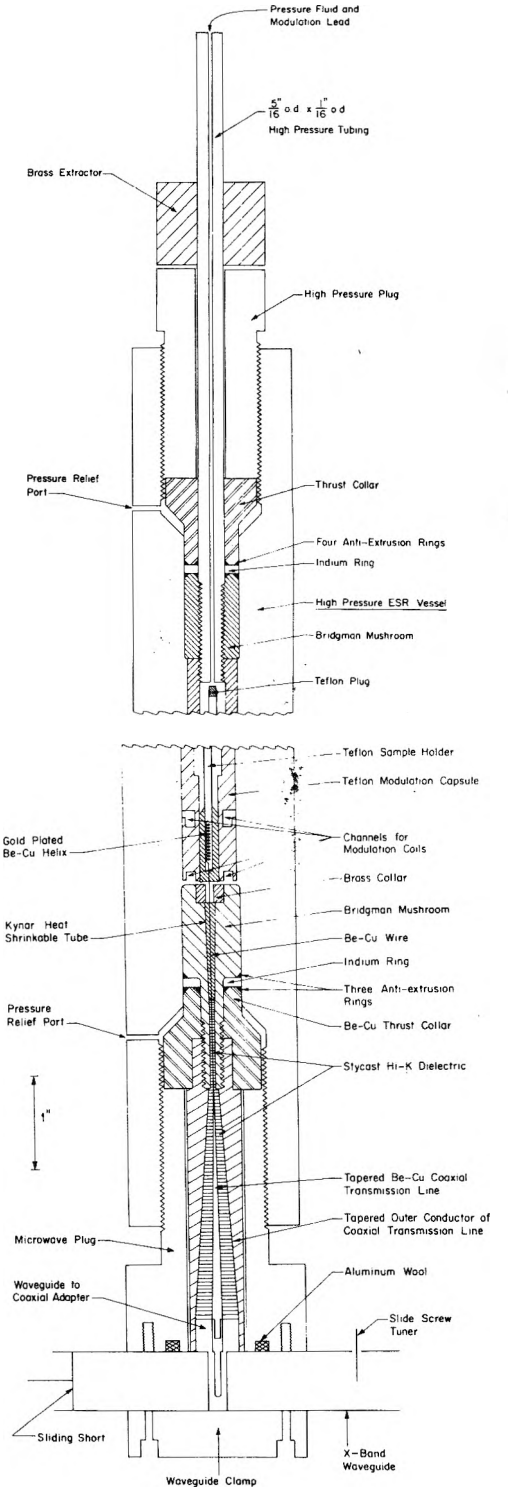

Figure 2. ESR high pressure vessel fully assembled. (The upper and lower halves are shown separately but are actually joined at the break lines.)

The Maier–Saupe-type form of the potential comes about when $\rho = 0$ in eq 3.3. Note that the mean torque on the probe is derived by taking the appropriate gradient of $U(\Omega)$, i.e.

$$\mathbf{T} = +i\mathbf{M}U(\Omega) \tag{3.4}$$

where $\mathbf{M}$ is an angular gradient operator defined in I. Thus $U(\Omega)$ is statistically the potential of mean torque[18] (within an arbitrary energy zero) for the spin probe.

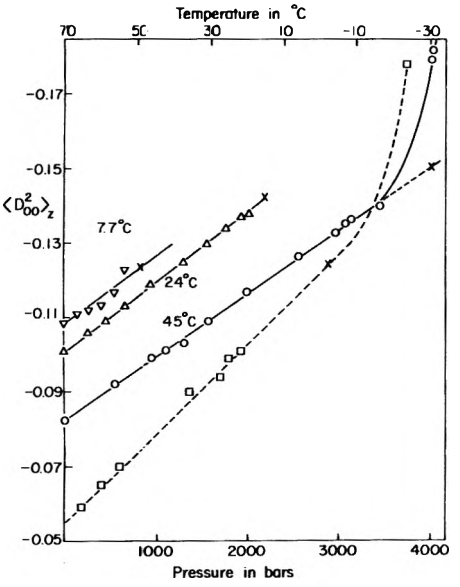

Figure 3. Nominal ordering parameter $\langle D^{(2)}_{00} \rangle_z$ vs. pressure for PD-Tempone in phase V. The solid lines show least-squares fits. The dashed curve is for the temperature variation at 1 atm from Polnaszek and Freed. The nonlinear effects for larger ordering are due to onset of slow motion. The X's mark the melting points from the least-squares fits given in the text.

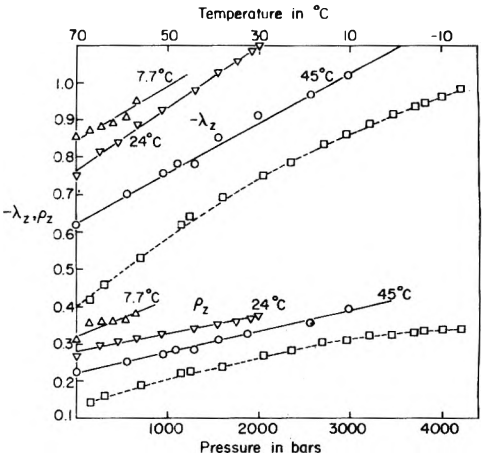

Figure 4. Asymmetric ordering, potential parameters, vs. pressure for PD-Tempone in phase V. The ordering parameters are defined with respect to the z molecular axis. The solid lines show least-squares fits. The dashed curve is for the temperature variation at 1 atm from Polnaszek and Freed.

The values of $-\lambda_z$ and ρ_z obtained in this manner are shown in Figure 4. [The subscript z means that the molecular magnetic z axis is taken as the primary orientation axis.] They are linear in P, just as $S^{(p)}$ was. It was noted in I that the probe orients weakly with the magnetic z axis tending to be perpendicular to the director, the y axis tending to be parallel to the director, and the x axis tending to be oriented nearly at the magic angle.

Our results on ordering of the spin probe ($S^{(p)}$) as a function of T and P has some relevance for theories of the nematic state. First we note that, while the PD-Tempone spin probe is ordered to a lesser extent than the nematic solvent molecules themselves, it is indeed a probe of the surroundings. One often employs a "mean field" theory to estimate the true potential of mean torque U which is measured experimentally. Then one may make use of orientation-dependent expansions such as[19-23]

$$U^{(s)}_{mf}(\Omega) \simeq \sum_{\text{even L,K}} \bar{u}^{(ss)}_{L,K}(r) \langle D^{L(s)}_{K,0}(\Omega') \rangle D^{L(s)}_{K,0}(\Omega) \qquad (3.5)$$

and

$$U^{(p)}_{mf}(\Omega) \simeq \sum_{\text{even L,L';K,K'}} \bar{u}^{(sp)}_{L,L',K,K'}(r) \langle D^{L(s)}_{K,0}(\Omega') \rangle D^{L'(p)}_{K',0}(\Omega) \qquad (3.6)$$

where the subscripts mf imply mean field approximation, the superscripts (s) and (p) refer to solvent and probe, and we are assuming low concentrations of probe molecules, so the latter only interact with solvent molecules. The solvent order parameters $\langle D^{L(s)}_{K,0}(\Omega') \rangle$ are determined by self-consistency considerations. The coefficients $\bar{u}^{(ij)}_{L,K}(r)$ are a measure of the strengths of the anisotropic interaction between molecules of species i and j and they are averages over the pair distribution function $n^{(2)}(r)$, e.g.

$$\bar{u}^{(ss)}_{L,K} = \rho^2 \int u^{(ss)}_{L,K}(r) n^{(2)}(r)\, dr \qquad (3.7)$$

where ρ is the number density. The other assumptions of such "mean field" approaches are discussed in numerous places.[19-23] Note however the eq 3.5 for $U^{(s)}_{mf}$ assumes a spherically symmetric pair distribution function for simplicity, while for $U^{(p)}_{mf}$ this is not invoked to better allow for anisotropic ordering. The Maier-Saupe potential[19] is based on the assumption that only $\langle D^{(2)(s)}_{00} \rangle$ is important and due to weak attractive forces, although more recent theories have included $\langle D^{4(s)}_{00} \rangle$, but in different ways.[21,22] In general, for long rodlike solvents the $K \neq 0$ terms in eq 3.5 should not be important, although for the probe they will generally have to be considered. While it is, in general, possible to represent all types of attractive and repulsive pairwise intermolecular forces by equations such as eq 3.5 and 3.6, some theories have introduced repulsive forces as a purely entropic, excluded volume between hard spheres.[10,20,24]

One general feature of the various theories is that each predicts a universal value for $S^{(s)} \equiv \langle D^{2(s)}_{00} \rangle$ for the isotropic–nematic, and possibly for the nematic–solid phase transitions. NMR studies on the liquid crystal PAA as a function of T and P have confirmed this.[10] Our results at the nematic–solid phase transition for the different temperatures and pressures yield $S^{(p)}_{mp} = -0.14 \pm 0.017$, at the melting point. (However, there appears to be a definite trend such that $S^{(p)}_{mp}$ increases somewhat with increasing pressure.) This value is, as expected, smaller than the value 0.55 ± 0.015 obtained for $S^{(s)}_{mp}$ for PAA. Our results appear to indicate that the ordering of the probe is a definite monitor of the thermodynamic properties of the liquid crystalline solvent. Note that it has recently been shown that the presence of small amounts of impurities does not normally change the value of $S^{(s)}$ at the nematic–isotropic transition, and we may expect this to be true at the melting point as well.

The observed pressure dependence of the solid–nematic melting point for phase V is

$$T_{mp}(P) = -2.5\ ^\circ\text{C} + 12\ ^\circ\text{C/kbar} \times P \qquad (3.8)$$

(While substantial supercooling of the freezing point was noted in the temperature-dependent studies involving samples in thin capillary tubes, cf. I, it was not observed in this work.) This pressure dependence is smaller than that reported for PAA:[10]

$$T_{mp}(P) = 116\ ^\circ\text{C} + 24.5\ ^\circ\text{C/kbar} \times P \qquad (3.9)$$

Note that solutions of nematics with small amounts of impurity are known to be ideal, and they will cause a freezing point depression predicted in the usual fashion.

Our result can be interpreted, with the Clausius–Clapeyron equation (neglecting the small impurity effect) to yield at the melting point

$$\Delta H/\Delta V = T\left(\frac{dP}{dT}\right) = [T\,°\text{k})/12]\ \text{kbars} \qquad (3.10)$$

Unfortunately there is no latent heat (ΔH) or specific volume (ΔV) data available for phase V (or the similar MBBA solvent) at the melting point. [If we were to use the ΔV for PAA,[10,19] then we would get $\Delta H \sim 4.3$ kcal/mol.]

McColl[11] has introduced the thermodynamic quantity γ

$$\gamma \equiv \left(\frac{\partial \ln T}{\partial \ln \rho}\right)_S = -\left(\frac{\partial \ln T}{\partial \ln V}\right)_S \qquad (3.11)$$

as a measure of the relative importance of density (or specific volume) vs. temperature in establishing nematic order. This parameter is best calculated by converting data of $S^{(i)}$ taken as a function of T and P to results as a function of T and V by means of data on the T and P dependences of molar volume.[12] However, one may rearrange eq 3.11 for γ to obtain

$$\frac{1}{\gamma} = T\beta_T\left[\left(\frac{\partial P}{\partial T}\right)_S - \left(\frac{\partial P}{\partial T}\right)_\rho\right] \qquad (3.12)$$

where $\beta_T \equiv (\partial \ln \rho/\partial P)_T$ is the isothermal compressibility. Thus, while the slopes $(\partial P/\partial T)_S$ may be determined from our experiments, β_T and $(\partial P/\partial T)_\rho$ must be determined by other measurements. No such data have as yet been obtained for phase V, so we make use of published data on sonic velocity,[26] heat capacity,[27,28] and thermal expansion[29,30] for the liquid crystal MBBA, since in our previous work (I), we found that phase V and MBBA yielded similar results for ordering of the probe and for viscosity at the same temperatures. Our results for $(\partial P/\partial T)_S$ with some results on γ are given in Table I. Note that McColl and Shih[12] have found $\gamma = 4$, and it is constant over a range of temperatures (at 1 bar). Our estimates from less data amount to $\gamma \approx 1.9 \pm 0.4$. Note that this difference is directly traceable to our values of $(\partial P/\partial T)_S = 45$ bars/K, which is fairly constant, as shown in Figure 5 where nearly straight lines curves of T vs. P at constant $S^{(p)}$ have been obtained.[31] McColl[12] also found a near constancy, but with $(\partial P/\partial T)_S \simeq 23$ bars/K or nearly half our result. We also give results for another useful thermodynamic derivative, $(\partial S/\partial T)_V$, which may be obtained from our measurement, as was γ, using

$$\left(\frac{\partial S}{\partial T}\right)_V = \left(\frac{\partial S}{\partial T}\right)_P + \frac{\alpha}{\beta_T}\left(\frac{\partial S}{\partial P}\right)_T \qquad (3.13)$$

with $\alpha \equiv (\partial \ln V/\partial T)_P$ also computed from the published data.[26-30]

The theoretical importance of these quantities may be illustrated in the context of eq 3.5–3.7. The pair-interaction coefficients $u^{ij}_{L,K}(r_{ij})$ will in general depend on inverse powers of r_{ij} or r_{ij}^{-n}, e.g., $n = 6$ for dispersion forces which were the only forces introduced by Maier and Saupe.[19] More general treatments of attractive and repulsive forces yield more complex dependences on r_{ij}. One can hope to estimate a "mean" n from experiment to shed some light on the relative importance of these terms. This is done as follows. One *assumes* that

$$\bar{u}^{ij}_{L,K}(r_{ij}) \propto V^{-n/3} \qquad (3.14)$$

since an r_{ij}^{-n} dependence implies a $V^{-n/3}$ dependence. Now

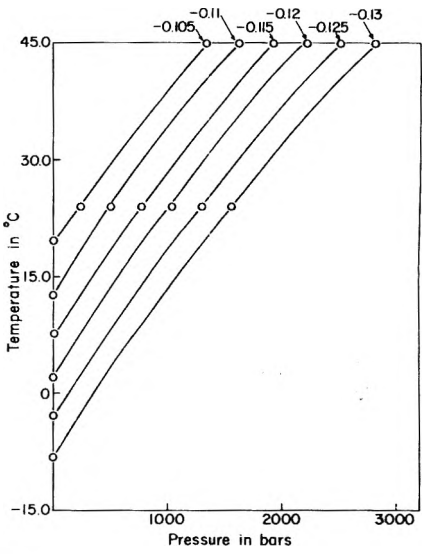

Figure 5. Graph of temperature vs. pressure showing contours of constant $\langle D^{(2)}_{00}\rangle_z$. The results shown are for the pressure runs at 24 and 45 °C, and the atmospheric pressure experiments of Polnaszek and Freed (ref 5).

the minimization of the Helmholtz free energy of orientation in the limit of very dilute solution of probes, for the mean field potentials of eq 3.5 and 3.6 leads to the result that $P^{(s)}_{mf}(\Omega)$ is given by the form of eq 3.2, but with $U^{(s)}_{mf}$ given by eq 3.5. Then, in the mean field of the aligned solvent molecules, the distribution function for the probe molecules, $P^{(p)}_{mf}(\Omega)$, is also given by the form of eq 3.2, but with $U^{(p)}_{mf}$ of eq 3.6. Thus our measurements of $S^{(p)}$ are to be interpreted in the mean field theory by

$$S^{(p)} = \int D^{2(p)}_{00}(\Omega) P^{(p)}_{mf}(\Omega)\, d\Omega \qquad (3.15)$$

Let us, purely for simplicity, assume Maier–Saupe-type potentials (i.e., only $D^2_{00}(\Omega)$ terms in the expansions of eq 3.5 and 3.6). Furthermore we assume, $u^{sp}_2/kT = a^{sp}/V^{\gamma_p}T$ and $u^{ss}_2/kT = a^{ss}/V^{\gamma_s}T$ with a^{sp} and a^{ss} independent of T and V. Also a^{ss} is negative for rods and a^{sp} is positive for PD-Tempone. Then from the functional relation

$$S^{(i)}(T,V) = g_i(T,V,S^{(s)}) \qquad (3.16)$$

where i = s or p, (and, e.g., g_p is given by the right-hand side of eq 3.15) we obtain

$$\left(\frac{\partial S^{(i)}}{\partial T}\right)_V = \left(\frac{\partial g_i}{\partial S^{(s)}}\right)_{T,V}\left(\frac{\partial S^{(s)}}{\partial T}\right)_V + \left(\frac{\partial g_i}{\partial T}\right)_{S^{(s)},V} \qquad (3.17)$$

with a similar expression for $(\partial S^i/\partial V)_T$. We then obtain for this simple mean field model

$$\left(\frac{\partial \ln S^{(s)}}{\partial \ln T}\right)_V = \frac{(\Delta S^s)^2 a^{ss}/V^{\gamma_s}T}{1 + (\Delta S^s)^2 a^{ss}/V^{\gamma_s}T} \qquad (3.18)$$

where $(\Delta S^{(s)})^2$ is the mean square fluctuation in order parameter given by

$$(\Delta S^{(s)})^2 \equiv \langle (D^{2(s)}_{00})^2\rangle - \langle D^{2(s)}_{00}\rangle^2 \qquad (3.19)$$

Then utilizing

$$\left(\frac{\partial T}{\partial V}\right)_{S^{(s)}} = -\left(\frac{\partial S^{(s)}}{\partial V}\right)_T \Big/ \left(\frac{\partial S^{(s)}}{\partial T}\right)_V \qquad (3.20)$$

we obtain

$$\left(\frac{\partial \ln T}{\partial \ln V}\right)_{S^{(s)}} = -\gamma_s \qquad (3.21)$$

TABLE I: Thermodynamic Quantities of PD-Tempone Dissolved in Phase V

					$(T/S^{(p)})(\partial S^{(p)}/\partial T)_V$	
T, K	$(\partial P/\partial T)_{S^{(p)}}$, mol/cm s^2 K	γ_p'	$S^{(p)}$	$S^{(s)}$ [a]	Exptl value	Predicted value from eq 3.22
298	1.68×10^5	2.28	−0.101	0.58	−1.85	−2.75
313	1.68×10^5	1.9	−0.0824	0.5	−2.58	−4.34

[a] The values given are for MBBA from ref 32.

Actually it is easy to show that eq 3.21 is obtained from more general mean field distribution functions utilizing eq 3.5, provided only that the $\bar{u}^{(ss)}_{L,K}/kT$ for all L and K show the same $1/V^{\gamma_s}T$ dependence; but eq 3.18 would then become more complicated. McColl and Shih[12] compare in a graph the Maier–Saupe prediction for $S^{(s)}$ vs. T at constant V with their actual experimental results. One sees that, in general, the $(\partial S^{(s)}/\partial T)_V$, which are *negative*, are predicted to be too large in magnitude by a Maier–Saupe theory. Note that $-(\Delta S^{(s)})^2 u^{ss}/kT$ is predicted from Maier–Saupe theory to range from ~1 to ¾ over the nematic range (with the values near unity in the vicinity of the isotropic–nematic phase transition). Thus, only small changes in the equivalent of $(\Delta S^s)^2 u^{ss}/kT$ resulting from including other terms in the potential (cf. eq 3.5, e.g., $\boldsymbol{D}^4_{00}(\Omega)$) will have a significant effect on the denominator of eq 3.18. Thus, we would expect that the equivalent of $(\Delta S^s)^2 u^{ss}/kT$ must be corrected to smaller values to agree with experiment by the inclusion of other terms in the potential.

The similar results for the probe ordering are given by

$$\left(\frac{\partial \ln S^{(p)}}{\partial \ln T}\right)_V = \frac{(\Delta S^{(p)})^2 a^{sp} S^{(s)}/V^{\gamma_p} T S^{(p)}}{1 + (\Delta S^{(s)})^2 a^{ss}/V^{\gamma_s} T} \tag{3.22}$$

and

$$-\left(\frac{\partial \ln T}{\partial \ln V}\right)_{S^{(p)}} = \gamma_p\left[1 + \frac{a^{ss}}{V^{\gamma_s} T}(\Delta S^s)^2\left(1 - \frac{\gamma_s}{\gamma_p}\right)\right] \tag{3.23}$$

where for PD-Tempone probe, $S^{(p)}$ is negative. Thus the mean field theory, wherein the ordering potential of the probe is taken to be proportional to $S^{(s)}$ (cf. eq 3.6), aptly shows from eq 3.23 that the volume dependence at constant $S^{(p)}$ depends on both γ_p and γ_s. And, in general, the thermodynamic dependence of $S^{(p)}$ is a function of both u^{sp} and u^{ss}. We list, in Table I, the results for $(\partial \ln S^{(p)}/\partial \ln T)_V$ predicted from eq 3.22 from our measurements on $S^{(p)}$ and published results on MBBA[32] for $S^{(s)}$ (recall that the results in I implied very similar ordering behavior in MBBA and phase V). These predictions are qualitatively in reasonable agreement with the experimental values, but tend to be 50–70% high. However, our previous discussion of $(\partial \ln S^{(s)}/\partial \ln T)_V$ indicated that a "corrected" $(\Delta S^{(s)})^2 u^{ss}/kT$ that is smaller than the prediction from a Maier–Saupe potential is needed to produce agreement with experiment. This also clearly applies to eq 3.22, and the order of the correction in this parameter (i.e., about 25% lower) is also similar. Thus, the thermodynamic properties of the probe ordering $S^{(p)}$ appear to be amenable to the same kind of analysis as $S^{(s)}$. The expression of eq 3.23 suggests that our measurement of γ (call it γ_p') is roughly $\gamma_p' \sim (\frac{1}{4}\gamma_p + \frac{3}{4}\gamma_s)$, for $(\Delta S^{(s)})^2 u^{ss}/kT \sim -\frac{3}{4}$, but with a "corrected" $(\Delta S^{(s)})^2 u^{ss}/kT$, it would, from the above indications, be closer to $\gamma_p' \sim \frac{1}{2}(\gamma_p + \gamma_s)$. Thus, it may well be that our result of $\gamma_p' \sim 2$ compared to McColl's $\gamma_s = 4$ in PAA reflects either a $\gamma_p < \gamma_s$ in phase V (or "quasi"-MBBA) or else if $\gamma_p = \gamma_s$ in this solvent, then the overall result is different from PAA.

Note, however, that our observed trend of $S^{(p)}_{mp}$, viz., that it appears to show a systematic increase with increasing P_{mp} would in the context of the mean-field theory used here, imply $\gamma_p < \gamma_s$, provided $S^{(s)}_{mp}$ is constant as one expects.[10]

4. Relaxation and Rotational Reorientation

(A) *Line Width Analysis. Motional Narrowing Region.* The observed motional narrowing line widths are fit to the usual quadratic in m_I, the z component of the ^{14}N nuclear spin quantum number:

$$T_2^{-1}(m_I) = A + Bm_I + Cm_I^2 \tag{4.1}$$

The results for the variation of A, B, and C plotted logarithmically with pressure are shown in Figure 6. The ln A, ln B, and ln C are found to be linear with pressure except for the higher pressures consistent with the onset of slow tumbling. The results are found to be very similar to the results in I obtained as a function of T. The overall similarity in results for the different pressures and the work of I is emphasized in Figure 7 where the important C/B ratio[2-5] is plotted vs. τ_R (the determination of τ_R, the rotational correlation time, is discussed below). The increase in C/B with τ_R is due to some extent to the increase in ordering as either the pressure is raised or the temperature is lowered. (For an isotropic liquid C/B should remain constant.) However, there is a substantial increase in C/B with τ_R not attributable to the ordering. As in I, this may be interpreted in terms of (1) anisotropic viscosity; (2) anisotropic diffusion; (3) modification of the pseudo-secular spectral densities to

$$j(\omega_a) = \frac{\tau_R}{1 + \epsilon'\omega_a^2\tau_R^2} \tag{4.2}$$

where, for $\epsilon' = 1$, one recovers the well-known Debye spectral density. We summarize these (and other) mechanisms in Table II. None of these explanations are really satisfactory, and again for the same reason given in I. We summarize some of these reasons. When the results are analyzed in terms of anisotropic viscosity, the value of $\hat{N} \equiv \hat{\tau}_{R\perp}/\hat{\tau}_{R\parallel}$ continues to increase with increasing $\hat{\tau}_{R\perp}$ (i.e., $\hat{\tau}_{R\parallel}$ remains nearly equal while $\hat{\tau}_{R\perp}$ increases considerably). [Here $\hat{\tau}_{R\perp}$ and $\hat{\tau}_{R\parallel}$ are the components of the rotational correlation time that are respectively perpendicular and parallel to the director.] When the results are analyzed in terms of anisotropic diffusion, one finds that $N_y \equiv \tau_{R\perp}/\tau_{R\parallel}$ must be increasing as $\tau_{R\perp}$ increases, and this is "turned on" only for $\tau_{R\perp} > 2 \times 10^{-10}$ s. Furthermore, when $\tau_R \gtrsim 10^{-9}$ s, A' is predicted to be negative. This is totally unexpected; typically A' is found to increase with increasing τ_R.[2-5] [Here $\tau_{R\perp}$ and $\tau_{R\parallel}$ are referred to a symmetry axis of the molecule.] The modification of the pseudo-secular spectral density with $\epsilon' \sim 13$–20 yields results for τ_R equal to that of the values of $\hat{\tau}_{R\perp}$ for the anisotropic viscosity model. However, in this case, a single, constant parameter (viz., ϵ') adequately explains a range of results. [More precisely $\epsilon_{ps} \approx$

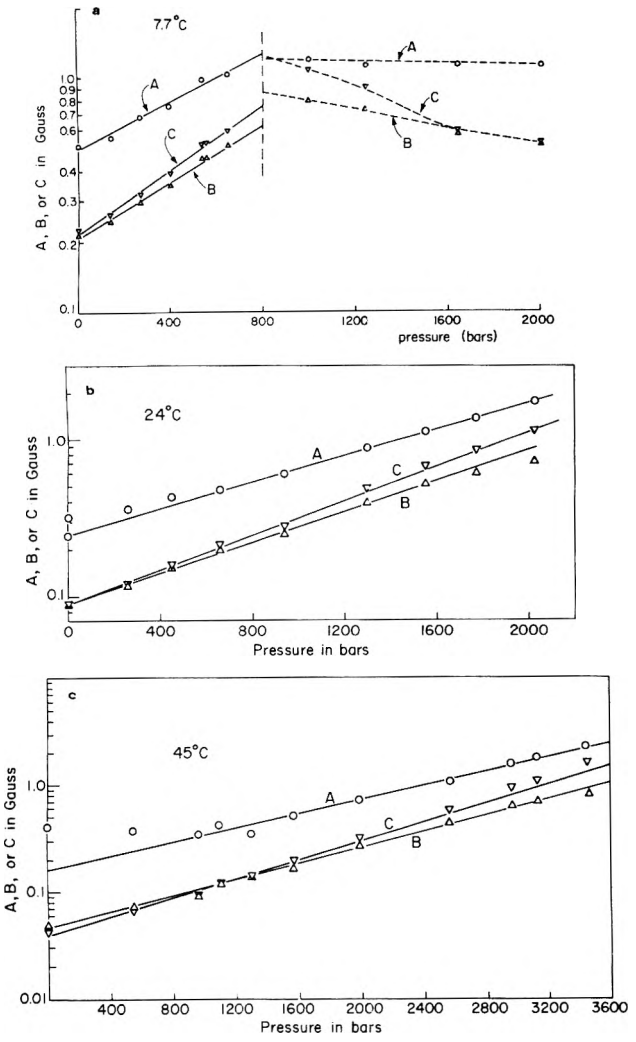

Figure 6. Line width parameters A, B, or C from fit of line width to expression $A + BM_N + CM_N^2$ (where M_N is the ^{14}N nuclear spin quantum number) plotted vs. pressure. The solid lines are the least-square fits. Parts a, b, and c are respectively for 7.7, 24, and 45 °C. The dashed lines in part a are results for the solid phase; the phase transition is indicated by the vertical dashed line.

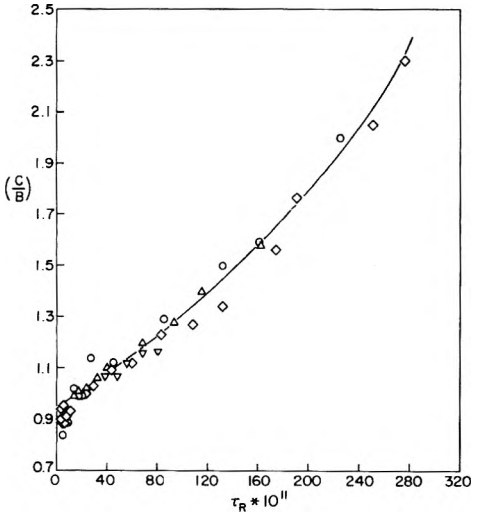

Figure 7. Graph of (C/B) vs. τ_R for PD-Tempone in phase V. The points marked by O, Δ, and ∇ are for 45, 24, and for 7.7 °C, respectively. The points marked ◊ are for the temperature variation at 1 atm from Polnaszek and Freed.[5]

20 effectively "explains" the low temperature lower pressure results, while $\epsilon'_{ps} \approx 13$ is better for the higher temperature, high pressure results.] Thus the analysis in terms of ϵ' is a useful way of representing the data and, as discussed in I and in Section C below, it has certain theoretical implications. Its limitations will be discussed below.

The results of an analysis of C and B to yield τ_R for the different models according to the procedures in I are given in Figure 8. That is, the analysis was based on the appropriate diffusion solutions under the two-term potential, eq 3.3, with the values of λ_z and ρ_z given in Figure 4. The theoretical expressions for the line widths $(A - A')$, B, and C are given by eq 2.31 of I, and computer programs for their computation are given elsewhere.[33] It is seen from Figure 8 that the actual results for τ_R are not very sensitive to the particular model (no more than 10% difference). Since the anomalies, presumably due to model-dependent effects, become much greater in the slow-motional region, we defer further discussion of this.

(B) *Activation Energy and Volume.* The variation of τ_R with pressure at 8, 24, and 45 °C is shown in Figure 8. One finds that ln τ_R is linear in P (as well as in $1/T$). It is possible to obtain the usual activation enthalpies ΔH_a and volumes ΔV_a from the P and T dependences, respectively.[7,8,34,35a] That is, if we assume activated-state theory for convenience, we may write

$$\tau_R = \tau_{R,0} \exp[\Delta G_a/RT] \tag{4.3}$$

where ΔG_a is the difference in Gibbs function between the initial and the activated state. One expects $\tau_{R,0}$ to be almost T and P independent, and we assume that it is. Then, from the thermodynamic relations

$$\Delta G_a = \Delta H_a + T(\partial \Delta G_a/\partial T)_P = \Delta H_a - T\Delta S_a \tag{4.4}$$

and

$$\Delta V_a = (\partial \Delta G_a/\partial P)_T \tag{4.5}$$

one easily finds that

$$\Delta H_a = R\left[\frac{\partial \ln \tau_R}{\partial(1/T)}\right]_P = -RT^2\left[\frac{\partial \ln \tau_R}{\partial T}\right]_P \tag{4.6}$$

and

$$\Delta V_a = RT\left(\frac{\partial \ln \tau_R}{\partial P}\right)_T \tag{4.7}$$

respectively. Our data analyzed in this way yield

$$\Delta H_a = (9.37 + 0.001\,02P) \text{ kcal/mol} \tag{4.8}$$

with P in bars (e.g., ΔH_a is 9.43, 9.55, 10.28, 10.92 kcal/mol for P = 1, 200, 1000, and 1500 bars, respectively). [The linear variation of ln τ_R with $1/T$ results in a temperature independent ΔH_a.] Also

$$\Delta V_a = (53.7 - 0.079T) \text{ cm}^3\text{/mol} \tag{4.9}$$

and T is in K (i.e., ΔV_a is 31.3, 30.4, 28.5 cm^3/mol for T = 281, 297, 318 K, respectively). [The linear variation of ln τ_R with P results in a pressure independent ΔV_a.] By analogy to eq 4.6 one typically defines

$$\Delta E_{V,a} \equiv R\left[\frac{\partial \ln \tau_R}{\partial(1/T)}\right]_V \tag{4.10}$$

Then, since

$$\left(\frac{\partial \Delta G_a}{\partial T}\right)_V = -\Delta S_a + \left(\frac{\partial P}{\partial T}\right)_V \Delta V_a \tag{4.11}$$

one easily shows that

TABLE II: Summary of Rotational Relaxation Mechanisms

Mechanism	Characteristic	Parameters	Ref
(1) Anisotropic diffusion	Unequal reorientation rates about principal axis system fixed in molecule. When the reorientation rates are equal this becomes isotropic Brownian rotational diffusion.	$R_\parallel = (6\tau_{R\parallel})^{-1}$ rotational diffusion coefficient about molecular symmetry axis. $R_\perp = (6\tau_{R\perp})^{-1}$ rotational diffusion coefficient about molecular axes perpendicular to symmetry axis. $N = \tau_{R\perp}/\tau_{R\parallel}$	2a; J. H. Freed, *J. Chem. Phys.*, **41**, 2077 (1964)
(2) Anisotropic viscosity	Unequal reorientation rates about principal axis system fixed in the laboratory (e.g., dc magnetic field axis).	$\hat{R}_\parallel = (6\hat{\tau}_{R\parallel})^{-1}$ rotational diffusion coefficient about orienting axis in lab frame. $\hat{R}_\perp = (6\hat{\tau}_{R\perp})^{-1}$ rotational diffusion coefficient perpendicular to orienting axis in lab frame. $\hat{N} = \hat{\tau}_{R\perp}/\hat{\tau}_{R\parallel}$	4; 5; C. F. Polnaszek, G. V. Bruno, and J. H. Freed, *J. Chem. Phys.*, **58**, 3185 (1973)
(3) Fluctuating torques	Anisotropic torques which induce reorientation are themselves relaxing at a rate that is not much faster than the reorientation of the probe molecule.	τ_R = relaxation time for rotational diffusion of probe molecule. τ_M = relaxation time for fluctuating torques inducing reorientation of probe molecule. $\epsilon' \equiv (1 + \tau_M/\tau_R)^2$. May be combined with analogues of models 1 (requiring additional specification of $\tau_{M\parallel}$ and $\tau_{M\perp}$) or 2 (requiring $\hat{\tau}_{M\parallel}$ and $\hat{\tau}_{M\perp}$).	3; 18
(4) SRLS	Probe molecule relaxes in a local potential field, while the latter averages out isotropically at a significantly slower rate than the rate of probe molecule reorientation.	$S_1 = \frac{1}{2}(3\cos^2\theta - 1)$ the order parameter of the probe relative to the local anisotropic potential field (i.e., local structure). This ordering is assumed to be cylindrically symmetric for simplicity. τ_x = the relaxation rate of the local structure. (May also be combined with the analogues of models 1 or 2.)	5
(5) Jump diffusion	Molecule reorients by random jumps of arbitrary angle.	$R = (\epsilon^2)_{av}/6\tau$ where τ is the time between jumps and $(\epsilon^2)_{av}$ is the mean-square jump angle. Can be generalized to include anisotropic diffusion tensors, by analogy with models 1 or 2.	2a
(6) Free diffusion	Molecular reorientation is partially due to free gaslike motion which is perturbed by the frictional effects of the surroundings.	τ_R and τ_J where τ_J is the angular-momentum relaxation time. They are often related by the Hubbard–Einstein relation: $\tau_R\tau_J = I/6kT$ with I the moment of inertia. Also $\tau_J^{-1} = \beta$ the friction coefficient.	2a; 3; G. V. Bruno and J. H. Freed, *J. Phys. Chem.*, **78**, 935 (1974).
(7) Director fluctuations	A hydrodynamic effect in which the nematic director fluctuates in its orientation with respect to the applied magnetic field.	$\tau_q^{-1} = Kq^2/\eta$ where τ_q is the relaxation time of the qth Fourier component of the director fluctuation, with K the average elastic constant of the liquid crystal and η is the viscosity.	5

$$\Delta E_{V,a} = \Delta H_a - T\left(\frac{\partial P}{\partial T}\right)_V \Delta V_a \qquad (4.12)$$

The partial derivative $(\partial P/\partial T)_V = \alpha/\beta$ where $\alpha \equiv (1/V)(\partial V/\partial T)_P$ and $\beta \equiv -(1/V)(\partial V/\partial P)_T$ have already been used in section 3. We have estimated α and β from the appropriate data on MBBA (cf. section 3) to obtain

$$\Delta E_{V,a} \approx 0.803 + 0.001\,02P + 0.0126T \text{ kcal/mol} \qquad (4.13)$$

which is applicable only for $T \simeq 313$ K and $P \sim 1$ bar. To the extent that one accepts activated state theory, ΔH_a and $\Delta E_{V,a}$ are measures of the energy required to reorient a molecule under conditions of constant P and V, respectively. Then eq 4.8, 4.9, and 4.13 are consistent with the intuitive picture[35a] that (1) the restoring torques exerted on the probe (hence ΔH_a) increase as P increases, since the free volume is reduced; and (2) the kinetic molecular fluctuations increase as T increases so the activation volume that is needed decreases. The T and P dependence of $\Delta E_{V,a}$ is then a composite of these reasons, cf. eq 4.12.

(C) *Slow Motional Region and the Various Reorientational Models.* Typical spectra obtained at the highest pressures for which the nematic solvent has not frozen are shown in Figures 9–11. The largest values of τ_R occurred, surprisingly enough, at the higher temperatures, as a result of the nature of the pressure dependence of the phase transition (cf. eq 3.8) vs. the activation free energy of τ_R (cf. eq 4.3, 4.6–4.9). Also shown in those figures are the theoretical spectra predicted for an isotropic Brownian motion model with the λ_z and ρ_z from Figure 4, and the τ_R's from Figure 8 (extrapolated where necessary).

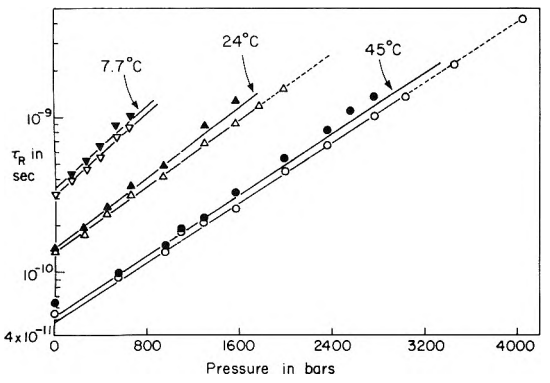

Figure 8. Graph of τ_R vs. pressure for PD-Tempone in phase V. The best fits with an asymmetric potential (i.e., either anisotropic viscosity or $\epsilon' \neq 1$) are shown by ∇, Δ, O, while the best fits with an anisotropic rotation model are showr by ▼, ■, ●. See text. The dashed lines represent extrapolated values used for the slow tumbling simulations.

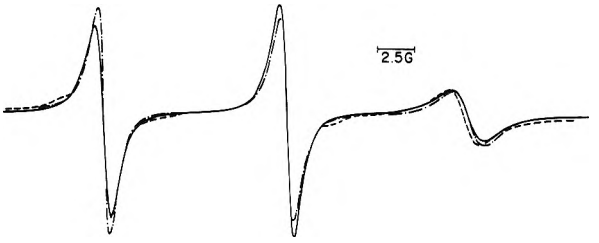

Figure 9. Comparison of experimental and simulated spectra at 7.7 °C and 652 bars for PD-Tempone in phase V: (- - - -) experimental result; (- O - O -) theoretical result based on isotropic Brownian diffusion with $\tau_R = 8.0 \times 10^{-10}$ s, $\lambda_z = -0.945$, $\rho_z = 0.38$, and $A' = 1.18$ G; (—) theoretical result based upon model with $\epsilon_s' = 1$, $\epsilon_{ps}' = 20$, $A' = 0.33$ G but other values given by the Brownian model.

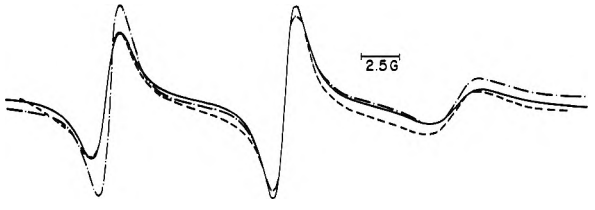

Figure 10. Comparison of experimental and simulated spectra at 24 °C and 1974 bars for PD-Tempone in phase V: (- - - -) experimental result; (- O - O -) theoretical result based on isotropic Brownian diffusion with $\tau_R = 1.59 \times 10^{-9}$ s, $\lambda_z = -1.096$, $\rho_z = 0.37$, and $A' = 0.12$ G; (—) theoretical result based upon model with $\epsilon_s' = 1$, $\epsilon_{ps}' = 13$, $A' = 0.52$ G, but other values given by the Brownian model.

It is clear that there are large discrepancies between experimental and predicted spectra, and they become worse as τ_R increases. These discrepancies are virtually the same as was observed in I for temperature-dependent studies. As in I, it was possible to get satisfactory fits with the anisotropic viscosity model but with anomalously large values of $\hat{N}$ (and with $\hat{\tau}_{R\parallel}$ eventually having to become negative for the slower motions). The anisotropic diffusion model is not satisfactory and it requires that A' become negative.

As in I, it was possible to satisfactorily fit the spectra with a model based upon frequency-dependent diffusion coefficients, which result from having fluctuating intermolecular torques that induce the reorientation but are not fluctuating at a rate which is much faster than the reorientation. However, it was again necessary to distinguish between components which are parallel and perpendicular to the director. This

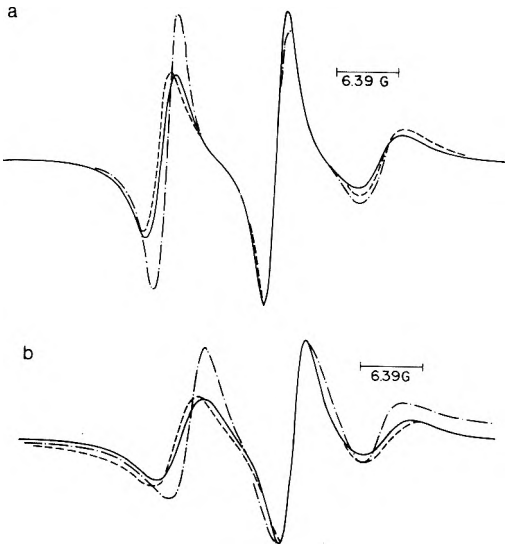

Figure 11. Comparison of experimental and simulated spectra at 45 °C for PD-Tempone in phase V: (a) 3450 bars, (- - - -) experimental result; (- O - O -) theoretical result based on isotropic Brownian diffusion with $\tau_R = 2.25 \times 10^{-9}$ s, $\lambda_z = 1.124$, $\rho_z = 0.40$, and $A' = 0$; (—) theoretical result based upon model with $\epsilon_s' = 1$, $\epsilon_{ps}' = 13$, and $A' = 0.95$ G, but other values given by the Brownian model; (b) 4031 bars, (- - - -) experimental result; (- O - O - O -) theoretical result based on isotropic Brownian diffusion with $\tau_R = 4.3 \times 10^{-9}$ s, $\lambda_z = -1.21$, $\rho_z = 0.43$, and $A' = 0$; (—) theoretical result based upon model with $\epsilon_s' = 1$, $\epsilon_{ps}' = 13$, and $A' = 1.35$ G but other values given by the Brownian model.

matter is discussed in more detail in I. Here we just note the simplified formulae in the limit of zero ordering for L = 2:

$$j_{2,s}(\omega) = \hat{\tau}_{R\perp}/[1 + \epsilon_s'\hat{\tau}_{R\perp}\omega^2] \tag{4.14a}$$

$$\epsilon_s' = (1 + \hat{\tau}_{M\perp}/\hat{\tau}_{R\perp})^2 \tag{4.14b}$$

and

$$j_{2,ps}(\omega) = \hat{\tau}_{R,1}/[1 + \epsilon_{ps}'\hat{\tau}_{R,1}\omega^2] \tag{4.15a}$$

$$6\hat{\tau}_{R,1}^{-1} = 5\hat{\tau}_{R\perp}^{-1} + \hat{\tau}_{R\parallel}^{-1} \tag{4.15b}$$

and

$$\epsilon_{ps}' = \left(1 + \frac{5}{6}\hat{\tau}_{M\perp}/\hat{\tau}_{R\perp} + \frac{1}{6}\hat{\tau}_{M\parallel}/\hat{\tau}_{R\parallel}\right)^2 \tag{4.15c}$$

In these expressions $\hat{\tau}_{M\perp}$ and $\hat{\tau}_{M\parallel}$ are the relaxation times for the fluctuating torques inducing the reorientation, i.e., for those components parallel and perpendicular to the director. The subscripts s and ps refer to secular and pseudo-secular (or nuclear-spin flip) contributions, respectively.[5] In general, we require $\epsilon_s' \sim 1$ or 2 and $\epsilon_{ps}' \sim 20$ for low T and low P slow tumbling while $\epsilon_{ps}' \sim 13$ for high T and high P slow tumbling. These results are consistent with the motional narrowing analysis, but they are more dramatic in the slow tumbling case. This is evidenced in Figures 9–11, where the results of such an analysis are presented.[35b]

We have carried out an analogous analysis in terms of anisotropic fluctuating torques referred to the molecular, as opposed to the director frame. Here one specifies $\tau_{R\parallel}$, $\tau_{R\perp}$, $\tau_{M\parallel}$, and $\tau_{M\perp}$, and one obtains expressions analogous to (but different from) those for the director frame. However, we could find no set of values of the adjustable parameters which could yield predictions in satisfactory agreement with experiment.

Despite the fact that the analysis based upon fluctuating

torques as described above and shown in Figures 9–11 yielded satisfactory agreement with experiment, it was argued in I that such large values of ϵ_{ps}' are inconsistent with the physical model; i.e., it implies $\hat{\tau}_{M\|} \gg \hat{\tau}_{R\|}$. Thus another model was considered there, viz., one assumes that significant components of the fluctuating torque persist for times long compare to τ_R. Then, on a longer time scale, τ_X, these components relax isotropically or nearly isotropically. This "slowly relaxing local structure" (SRLS) mechanism was analyzed in I and approximate expressions were given for their contribution to the line width. These comments also apply to our present results. The SRLS is an effective mechanism for explaining an anomalous increase in C/B. Order of magnitude estimates yield $S_l^2 \equiv \langle \boldsymbol{D}_{00}^2(\Omega) \rangle_l \sim 1/16$, where S_l measures the ordering of the probe relative to the temporarily static torque components, while $\tau_X/\tau_R \sim 10$. In particular, for motionally narrowed spectra, and where S_l is not large, one can derive expressions for the spectral densities $j_0(\omega)$ and $j_2(\omega)$

$$j_0(\omega) = \frac{\tau(0)}{1 + \omega^2\tau(0)^2} \rightarrow \left[D_0(\omega) + \frac{S_l^2\tau_X}{1 + \omega^2\tau_X^2} \right] \quad (4.16a)$$

$$j_2(\omega) = \frac{\tau(2)}{1 + \omega^2\tau(2)^2} \rightarrow D_2(\omega) \quad (4.16b)$$

where the first equality is the usual definition of the spectral density for anisotropic diffusion in an isotropic liquid[2] and the arrow points to the new result.[36] Also the $D_0(\omega)$ and $D_2(\omega)$ are given in I, and for $\omega\tau(0), \omega\tau(2) \ll 1$, and $S_l \lesssim 0.8$ one has (using a more accurate expansion than in I):

$$D_0(\omega = 0) \simeq [1 + 0.27S_l - 2.87S_l^2 + 1.522S_l^3]\tau(0) \quad (4.17a)$$

$$D_2(\omega = 0) \simeq [1 + 0.052S_l + 0.264S_l^2 + 0.177S_l^3]\tau(2) \quad (4.17b)$$

while for negative $S_l \gtrsim -0.4$ one has

$$D_0(\omega = 0) \simeq [1 - 0.180S_l - 3.11S_l^2 - 6.34S_l^3]\tau(0) \quad (4.18a)$$

$$D_2(\omega = 0) \simeq [1 - 0.134S_l - 0.601S_l^2 - 2.654S_l^3]\tau(2) \quad (4.18b)$$

As in I, we assume that the molecular magnetic z axis orients perpendicular relative to the local ordering, so eq 4.18 apply. Then the hyperfine tensor is very nearly axially symmetric in this molecular reference frame, so at X-band we can neglect in a first approximation the terms contributing to A, B, and C from $D_2(\omega)$. Then for our rough estimates of $S_l^2 \sim 1/16$ and $\tau_X/\tau_R \sim 10$, the terms $D_0(\omega)$ and $S_l^2\tau_X/[1 + \omega^2\tau_X^2]$ contribute roughly comparably for $\omega^2\tau_X^2 \ll 1$ (more precisely $D_0(0) \sim 0.95\tau(0)$ and $S_l^2\tau_X \sim 0.6\tau(0)$, while for $S_l^2 \sim 0.1$, $D_0(0) \sim 0.8\tau(0)$ and $S_l^2\tau_X \sim \tau(0)$). Thus, this analysis indicates that τ_R calculated from $j_0(\omega)$ might be about 60% larger than the true value. (We have not attempted a total reanalysis based on such an observation given the other approximations in our analysis.)

One can explain the anomalous part of the C/B increase which begins to develop for $\tau_R > 2 \times 10^{-10}$ s by the choice of $\tau_X/\tau_R \sim 10$. This requires the analysis of the SRLS mechanism for $\tau_X > 2 \times 10^{-9}$ s, which is near the incipient slow-motional region for nitroxides. However, the analysis of A, B, and C near the incipient slow motional region becomes complicated because of the need to precisely distinguish the relevant secular and pseudo-secular frequencies for the spectral densities associated with the $S_l^2\tau_X/[1 + \omega^2\tau_X^2]$ term. The more complex calculations which are required are summarized elsewhere.[4,5,33] We show in Figure 12, the results of the contributions to A, B, and C from the SRLS mechanism, which were only briefly summarized in I. It should be emphasized that these results have been calculated neglecting any effects from the actual mean potential (cf. eq 3.3), so one must analyze the results assuming additivity of its effects with that of the SRLS mechanism. Note that the increase in C/B is indeed predicted for $\tau_X > 2 \times 10^{-9}$ s from this contribution to the width, and it becomes very dramatic for $\tau_X \sim 10^{-8}$ s, corresponding to $\tau_R \sim 10^{-9}$ s (according to our analysis) and this is indeed consistent with our experimental observations both in I and in the present work. Since a careful analysis based upon slow tumbling becomes important for $\tau_X \gtrsim 2.5 \times 10^{-9}/S_l$ (or $\sim 2.5 \times 10^{-8}$ s in the present case) the results shown in Figure 12 should not be used for the slower values of τ_X. It is seen from results quoted in I that more dramatic effects may be obtained, hence smaller values of S_l^2 and/or τ_X/τ_R would be needed, if there is substantial anisotropy in the relaxation of the local structure. Furthermore, one would expect S_l^2 to increase somewhat as the temperature is lowered and the pressure is increased.

Clearly, it is somewhat arbitrary to distinguish models in which the fluctuating torques are relaxing at rates comparable to or significantly greater than the reorienting probe molecule. Fluctuating torque components must be relaxing over a very wide range of frequencies.[37] However it seems reasonable that, for a small spherical probe in a solvent of long rodlike nematic solvent molecules, there will indeed exist local structure around the probe, which can relax only by the more improbable reorientation of the solvent molecules about axes perpendicular to the director (however, for typical values of $S^{(s)} \sim 0.35$–0.55; the Maier–Saupe-type theory prediction is $(\Delta S^{(s)})^2 \sim 0.2$–$0.15$ roughly corresponding to root-mean square angular fluctuations of ~37–40°; however, the actual values are probably somewhat smaller, cf. section 3). Or, perhaps even more likely, the translational diffusion of the rodlike solvent molecules directly affects the local structure about the probe.

We have discussed in I the de Gennes–Pincus-type hydrodynamic model for fluctuations in the director[38] and its potential effect on ESR relaxation.[5] There it was concluded that it was both qualitatively and quantitatively of the wrong character to explain the observed anomalies. Our pressure-dependent results reinforce these conclusions. It is perhaps useful to distinguish between the two models or mechanisms: SRLS, and hydrodynamic director fluctuations. In simple physical terms, the former is a model involving molecular dimensions and molecular diffusion, while the latter involves coupled modes or waves with dimensions much greater than molecular dimensions. Partly as a result of this, the rotational reorientation of the probe molecule should be more significantly affected by the former molecular-type process. The frequency and temperature dependence of the latter model has been worked out,[38,39] and it is substantially different from that for molecular reorientation. Our combined temperature and pressure studies show that the relaxation anomalies are closely related in their T and P dependence to the rotational reorientation, τ_R, while τ_R exhibits very similar activation energies as the twist viscosity of the liquid crystal (cf. I). It is reasonable to expect that the SRLS mechanism is closely coupled to the rotational and translational diffusion processes of the solvent molecules. The frequency dependence of such a mechanism has not been analyzed yet; the discussion above

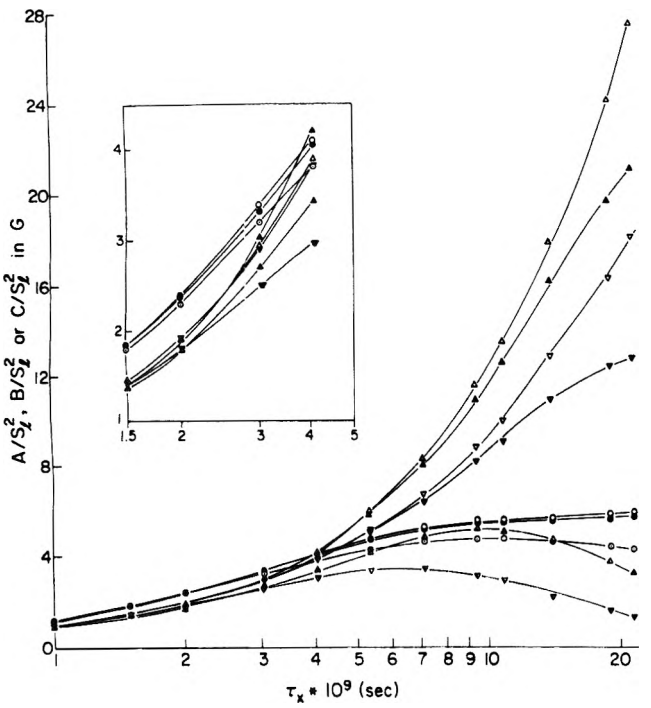

Figure 12. Graph of the contributions of the slowly relaxing local structure (SRLS) mechanism to the nitroxide line widths as a function of τ_X, the relaxation time for the local structure. The results are given as A/S_l^2, B/S_l^2, C/S_l^2, where S_l is the local structure order parameter, and these are the additional contributions to be added to the main contributions due to the overall molecular reorientation. The O, ●, ⊙ are the A/S_l^2 values for S_l = ⅛, ¼, and 1, respectively; the ▽, ▼, ▽ are the B/S_l^2 values for S_l = ⅛, ¼, and 1, respectively; and the △, ▲, ▲ are the C/S_l^2 values for S_l = ⅛, ¼, and 1, respectively. The insert shows a portion of the main graph on an expanded scale.

assumes a simple Debye-type spectrum from the relaxing local structure. The qualitative effects of the two mechanisms on ESR relaxation (i.e., the relative magnitudes *and* signs of the contributions to A, B, and C) need not necessarily be different. For the analysis yielding Figure 12, it is assumed that the local structure about the probe is distributed isotropically; i.e., one averages the persistent local torque over an isotropic distribution. This is not at all unreasonable for a spherical probe weakly ordered in the liquid crystal. The director fluctuation model is not isotropic in this sense. The director fluctuations are small increments from the mean director. [One could, of course, incorporate such a feature into the local structure mechanism, as was shown in I.] Because of this feature, it is predicted to make just a pseudo-secular (and nonsecular, or $M = \pm 1$ terms in general) contribution to the ESR, A, B, and C terms. In particular it would reduce C, hence C/B, which is opposite to the observed effect. An isotropic model can contribute just as effectively to secular ($M = 0$) and pseudo-secular ($M = \pm 1$) terms, and, as shown in Figure 12, lead to an *increase* in C/B for appropriate values of τ_X.

Our analysis of the SRLS mechanism on the ESR line shapes is still very approximate, and the complicating features of slow tumbling in τ_R and τ_X have not as yet been adequately dealt with, although the methods have been outlined in I. This is, in part, why the theoretical fits of the incipient and slow tumbling spectra in Figures 9–11 have been based mainly on the probably less important frequency-dependent diffusion model (or mechanism). It represents, nevertheless, an effective "semiempirical" method for fitting our results.

We turn now to what appears to be a somewhat larger effect ($\epsilon' \sim 20$) at low T and P compared to high T and P ($\epsilon' \sim 13$). In the context of the activation analysis of the previous section, this would imply that the increase in the local structure (or restoring torques), due to the reduction in free volume as P is increased, is somewhat more than offset by the effects of the kinetic molecular fluctuations as T increases, which permits larger fluctuations of the probe, hence reduced ordering with respect to the local structure, as well as more rapid relaxation.

(D) *Frozen Solutions.* When the pressure is increased above the values at the freezing point (shown in Figure 3), a metastable form of phase V is observed. The motion of the spin probe slows down considerably. This metastable form decays to a stable solid within about 10 min. Because of this rapid change, we were not able to obtain well-defined reproducible spectra for possible simulation.[40]

The spectrum of PD-Tempone in the solid phase is like that in isotropic liquids in the motional narrowing region, i.e., there are three fairly sharp unshifted lines. It was noted in I, where the frozen solutions yielded ESR spectra characteristic of the rigid limit, that these spectra showed no preferential ordering. Line width parameters for this frozen phase are displayed in Figure 6a. One notes (1) that B and C appear to change discontinuously at the freezing point and (2) that B and C are *decreasing* as the pressure is increased above its value at the freezing point. Observation (1) requires some explanation. Our theoretical estimates are that ordering potentials typical of PD-Tempone in the nematic phase should lead to values of B and C that are about 30% lower than for the isotropic phase, provided τ_R remains the same. The isotropic and nematic values of B, when extrapolated to the freezing point, actually do lead to comparable estimates of τ_R (1.0×10^{-9} and 9.1×10^{-10} s for the nematic and isotropic phases, respectively). Now observation (2) implies that τ_R decreases as the pressure is increased in the solid phase, as though the probe is located in a cavity (or clathrate) and, from the estimates of τ_R from B, this structure is like that in the nematic phase, except that increasing the pressure freezes out movement of solvent molecules, and the motion of the spin probe becomes less hindered. At still higher pressures, the free volume of the cavity should be reduced, and τ_R should again increase.[41]

We have not yet considered the increase in C upon freezing, which is larger than expected from the change in B discussed above. In the context of the SRLS mechanism, one notes from Figure 12 that an enhanced C/B ratio results from its large relative contributions to C. If the local structure is relaxing more slowly, i.e., τ_x is longer in the solid phase, and/or S_l becomes larger, then one might expect an enhanced C/B ratio. However, in our analysis of SRLS, we have assumed that in the nematic phase, its effects and those of the macroscopic director are additive. This may not be true, so we cannot at present be confident of the proposed explanation for the large increase in C upon freezing. Note, however, that when the pressure has been increased substantially (and τ_R has decreased) in the solid phase, then $C/B \approx 1$, which is expected if the SRLS is not important.

5. Conclusions

In this work, it was shown that pressure-dependent ESR studies can supply useful information about molecular ordering and dynamics in liquid crystalline solvents. The results on molecular ordering could be discussed in terms of simple mean field theory to show how they reflect, in general, the combined effects of the orientation dependent interactions between solvent molecules as well as between solvent and

probe. The present results for a spherical probe molecule are consistent with somewhat longer range interactions ($\gamma_P' = 1.9 \pm 0.4$) than the results of McColl on a pure solvent (PAA with $\gamma_s = 4.0 \pm 0.1$), although the present results are somewhat of a preliminary nature.

The pressure-dependent spin-relaxation studies both amplify and support the previous temperature-dependent studies on this system, and the results have been subjected to an activated state theory analysis. The anomalous relaxation behavior previously noted for the temperature-dependent studies in the incipient slow-tumbling region has been confirmed as a function of pressure. It is shown that this anomalous behavior is nearly independent of what combination of T and P is required to achieve a given τ_R. The strong dependence of the anomaly on τ_R, and its virtual independence of the particular combination of T and P, is taken as strong evidence that the anomalous behavior is directly related to the *viscous* modes of motion associated with the reorientation of the spin probe in its surroundings of rodlike molecules. It has been argued that the most likely explanation for the anomaly is a slowly relaxing local structure mechanism, in which the rodlike solvent molecules present a persistent local structure for the probe, which relaxes on a time scale much slower than the reorientation of the probe. Furthermore, this would be consistent with an apparent cagelike structure which appears to be frozen in as the nematic phase solidifies. Also, it would be consistent with longer range orientation-dependent interactions acting on the probe than on the rodlike solvent molecules. This mechanism of a probe or solute molecule reorienting relative to a persistent potential, which then relaxes on a slower time scale, is expected to be a very general one in liquid crystals and plastic crystals, structured liquids, and biological systems.

It would, of course, be of considerable interest to study the effects of the size and the shape of a variety of spin probes on both the molecular ordering as reflected in γ_P', as well as on the molecular dynamics and the proposed SRLS mechanism. Such experiments are currently planned.

Acknowledgments. We wish to acknowledge helpful discussions with Dr. C. F. Polnaszek. We wish to thank Mr. R. E. Terry for his considerable help in constructing the high pressure vessel.

References and Notes

(1) Supported in part by a grant from the National Science Foundation and by the Cornell University Materials Science Center.
(2) (a) S. A. Goldman, G. V. Bruno, C. F. Polnaszek, and J. H. Freed, *J. Chem. Phys.*, **56**, 716 (1972); (b) S. A. Goldman, G. V. Bruno, and J. H. Freed, *ibid.*, **59**, 3071 (1973).
(3) J. S. Hwang, R. P. Mason, L. P. Hwang, and J. H. Freed, *J. Phys. Chem.*, **79**, 489 (1975).
(4) J. H. Freed in "Spin Labelling Theory and Applications", L. J. Berliner, Ed., Academic Press, New York, N.Y., 1975, Chapter 3.
(5) C. F. Polnaszek and J. H. Freed, *J. Phys. Chem.*, **79**, 2283 (1975). Hereafter referred to as I.
(6) D. S. Leniart, H. D. Connor, and J. H. Freed, *J. Chem. Phys.*, **63**, 165 (1975).
(7) J. Jonas, *Adv. Magn. Reson.*, **6**, 73 (1973).
(8) J. Jonas, *Ann. Rev. Phys. Chem.*, **26**, 167 (1975).
(9) J. S. Hwang, D. Kivelson, and W. Z. Plachy, *J. Chem. Phys.*, **58**, 1753 (1973).
(10) B. Deloche, B. Cabane, and D. Jerome, *Mol. Cryst. Liq. Cryst.*, **15**, 197 (1971).
(11) J. R. McColl, *Phys. Lett.*, **38A**, 55 (1972).
(12) J. R. McColl and C. S. Shih, *Phys. Rev. Lett.*, **29**, 85 (1972).
(13) W. Z. Plachy and T. J. Schaafsma, *Rev. Sci. Instrum.*, **40**, 1590 (1969).
(14) W. T. Doyle, T. F. Dutton, and A. B. Wolbarst, *Rev. Sci. Instrum.*, **43**, 1668 (1972).
(15) P. W. Bridgman, "The Physics of High Pressure", Dover Publications, New York, N.Y., 1970.
(16) The high pressure vessel has held a pressure of 5 kbars for 1 month with no noticeable change.
(17) J. C. Lang, Jr., and J. H. Freed, *J. Chem. Phys.*, **56**, 4103 (1972). Equation A1 of that reference is given incorrectly, but the actual analysis used the correct expressions. The correct form of eq A1 is

$$\left[[\Delta\omega_{N,M} - i\left[T_2(0)^{-1} + \omega_{HE}\left(1 - \frac{1}{3}P_M\right)\right]\right] \bar{Z}_{N,M} + i\omega_{HE}\frac{1}{3}P_M \sum_{M' \neq M} \bar{Z}_{N,M'} = D_M A$$

We wish to thank Mr. A. E. Stillman for helpful correspondence on this point.
(18) L. P. Hwang and J. H. Freed, *J. Chem. Phys.*, **63**, 118 (1975).
(19) W. Maier and A. Saupe, *Z. Naturforsch. A*, **13**, 564 (1958); **14**, 882 (1959); **15**, 287 (1960).
(20) P. G. de Gennes, "The Physics of Liquid Crystals", Oxford University Press, New York, N.Y., 1974.
(21) (a) S. Chandrasekhar and N. V. Madhusudana, *Acta Crystallogr., Sect. A*, **27**, 303 (1971); (b) *Mol. Cryst. Liq. Cryst.*, **24**, 179 (1973).
(22) (a) R. L. Humphries, P. G. James, and G. R. Luckhurst, *J. Chem. Soc., Faraday Trans. 2*, **68**, 1031 (1972); (b) R. L. Humphries and G. R. Luckhurst, *Chem. Phys. Lett.*, **17**, 514 (1972).
(23) G. R. Luckhurst and M. Setaka, *Mol. Cryst. Liq. Cryst.*, **19**, 279 (1973). We employ the notation similar to that of these authors.
(24) L. Onsager, *Ann. N.Y. Acad. Sci.*, **51**, 627 (1949).
(25) J. R. McColl, *J. Chem. Phys.*, **62**, 1593 (1974).
(26) D. Eden, C. W. Garland, and R. C. Williamson, *J. Chem. Phys.*, **58**, 1861 (1973).
(27) J. Mayer, T. Waluga, and J. A. Janik, *Phys. Lett.*, **41A**, 102 (1972).
(28) J. A. Janik et al., *J. Phys. (Paris)*, Colloquium CI, 159 (1975).
(29) M. J. Press and A. S. Arrott, *Phys Rev.*, **8A**, 1459 (1973).
(30) E. Gulari and B. Chu, *J. Chem. Phys.*, **62**, 795 (1975).
(31) The graphs in Figure 5 do not include the results on the pressure sample used for the 7.7 °C runs. The results for $S^{(p)}$ from this sample are systematically 0.005 too low for agreement with the atmospheric pressure samples of I and with the other pressure samples. This could be due to an impurity in this high pressure sample. This small deviation is not of significant importance in the relaxation studies.
(32) Y. S. Lee, Y. Y. Hsu, and D. Dolphin, *Liq. Cryst. Ordered Fluids*, **2**, 357 (1974).
(33) C. F. Polnaszek, Ph.D. Thesis, Cornell University, 1976. Note eq 2.18d of ref 5 has a misprint: $2R_\perp\lambda/7$ should replace $2R_\parallel\lambda/7$. It appears correctly in this reference and in ref 4.
(34) J. G. Powles and M. C. Gough, *Mol. Phys.*, **16**, 349 (1969).
(35) (a) R. L. Armstrong and P. A. Speight, *J. Magn. Reson.*, **2**, 141 (1970). (b) The spectra obtained with the high pressure apparatus are slightly asymmetric. Also there is a small amount of base line shift. We partially compensated for both these effects in our simulations. However, small discrepancies resulting from these effects do show up in our comparisons between the experimental and simulated spectra in Figures 9–11.
(36) In I it was pointed out that one could estimate an ϵ' from this mechanism. It would only apply to $j_0(\omega)$ and not to $j_2(\omega)$. One obtains

$$j_0(\omega) \approx j_0(0)[1 + \epsilon'\omega^2\tau_R^2]^{-1}$$

with

$$\epsilon' \approx 1 + S_l^2(\tau_X^3/\tau_R^3)\frac{1 + \omega^2\tau_R^2}{1 + \omega^2\tau_X^2}$$

which is appropriate for $(\tau_R/\tau_X)^2 \ll 1$ and $S_l^2\tau_X/\tau_R < 1$. This form is a little more accurate than given in I.
(37) Very rapidly relaxing torque components can be expected to induce angular momentum, hence spin rotational relaxation (given by τ_J) without substantially affecting the overall reorientation. This may be the explanation for the anomalies in the product $\tau_R\tau_J$ observed in ref 6.
(38) (a) P. G. de Gennes, *Mol. Cryst. Liq. Cryst.*, **7**, 325 (1969); (b) P. Pincus, *Solid State Commun.*, **7**, 415 (1969).
(39) J. W. Doane, C. E. Tarr, and M. A. Nickerson, *Phys. Rev. Lett.*, **33**, 620 (1974).
(40) We have attempted to simulate a spectrum obtained at 2000 bars and 7.7 °C with an estimated $\tau_R \sim 7 \times 10^{-9}$ s. The value of ϵ' required seemed to be greater than 1, but less than 13. The intensity ratio of the lines in the experimental spectrum was found to change with time. Hence no reliable value of ϵ' could be obtained.
(41) A closely related observation for DTBN in the plastic crystal camphene has recently been made by Glarum and Marshall, *J. Chem. Phys.*, **62**, 956 (1975).

Use of Ketones as Probe Molecules for the Detection of Acid Strength Distribution on Oxide Surfaces

Wolfgang Schulz and Helmut Knözinger*

Institut für Physikalische Chemie, Universität München, 8 München 2, West Germany *(Received January 19, 1976)*

The Lewis acid sites on surfaces of polycrystalline oxides are energetically heterogeneous. It is shown that this site heterogeneity shows up in the band width and asymmetry of the carbonyl stretching band of suitably substituted ketones which are coordinately adsorbed on the Lewis acid sites of a δ-Al_2O_3. It follows from the experimental studies that ketones bearing electron-releasing substituents such as isopropyl or *tert*-butyl groups are chemically stable at temperatures up to approximately 100 °C. They are therefore suitable probe molecules. Acetone and hexachloroacetone on the other hand readily undergo chemical transformations even at room temperature and thus cannot be used as probes for surface Lewis acid sites.

Lewis acid sites on surfaces of polycrystalline oxides, on aluminas in particular, are generally believed to be energetically heterogeneous. One should therefore expect that characteristic infrared bands of Lewis bases, which are coordinately adsorbed on these Lewis acid sites, should reflect the site heterogeneity in the band width and/or a continuous shift of the band position with surface coverage. Pyridine has often been used as a probe molecule,[1-3] but steric restrictions between the large pyridine ring and surface anions in the immediate vicinity of the Lewis acid site have been shown to be the reason for an activated chemisorption of pyridine.[4] We have therefore chosen nitriles as alternative probe molecules.[5] These have the advantage of their functional group being small and unshielded so that steric restrictions cannot interfere with the interaction with the surface sites. However, acetonitrile is very reactive and undergoes various surface reactions even under very mild conditions.[6,7] One of these reactions is a nucleophilic attack of basic surface hydroxyl groups onto the nitrile C atom of the coordinated molecule and leads to surface amide structures.[6] Since this reaction is facilitated by the polarization of the coordinated nitrile, the reactivity of the probe molecule can effectively be reduced by substitution with electron-releasing substituents. Thus, *tert*-butyl cyanide was found to be stable on alumina surfaces at temperatures up to 200 °C.[5] The surface heterogeneity, however, could again not be detected with this probe molecule with certainty, since the position of the C≡N stretching band of the coordinatively adsorbed molecule was unaffected within the limits of resolution by the surface coverage as well as by the dehydroxylation temperature of the oxide and the band width of this band was only slightly larger than in the liquid. The insensitivity of the C≡N stretching vibration of nitriles vs. differences in the coordination bond strength is most probably due to two opposing effects which occur on coordination, namely, a rehybridization (which leads to a net increase in bond order) and the polarization of the C≡N bond.[5]

We have therefore decided to study the behavior of ketones as probe molecules for the detection of Lewis acid sites on oxide surfaces, since in these molecules rehybridization does not take place on coordination and the polarization of the carbonyl group leads to a shift of the carbonyl stretching band toward lower frequencies. Hair and Chapman[8] have proposed hexachloroacetone as a probe molecule that fulfills a variety of criteria necessary for the unequivocal detection of acid sites. However, ketones very easily undergo surface reactions by nucleophilic attack of surface hydroxyl groups.[3,6] Thus, acetone forms surface acetate anions and methane is detected in the gas phase.[9,10] These reactions are facilitated by the coordination of the ketone and by the substitution of the ketone with electron-withdrawing substituents. Thus, hexachloroacetone is in fact much more reactive than acetone and the formation of trichloroacetic acid anions can readily be detected on alumina surfaces by their characteristic infrared bands at 1630 and 1430 cm^{-1} which appear on adsorption of hexachloroacetone at room temperature while chloroform and secondary reaction products are detected in the gas phase.[6] We have therefore concluded that ketones bearing electron-releasing alkyl groups as substituents might, in analogy to the reduced reactivity of substituted nitriles, be less reactive than hexachloroacetone and acetone. The adsorption of diisopropyl ketone and hexamethylacetone on aluminas has therefore been studied by the conventional infrared transmission technique.[1,2,11] Figure 1 shows the carbonyl stretching region for the liquid ketones and after addition of $AlCl_3$ to the liquid ketones (solvent CCl_4). A shift toward lower wave numbers of the carbonyl stretching band by 65 cm^{-1} is observed on formation of the $AlCl_3$ complex of hexamethylacetone. The band half-width of the carbonyl stretching band in the complex is 30 cm^{-1}. In the case of diisoprolyl ketone, two shifted carbonyl stretching bands are observed in the $AlCl_3$ complex, their origin being not quite clear. The bands appear at 1657 and 1637 cm^{-1}, respectively, and correspond to wave number shifts of 58 and 78 cm^{-1}. The occurrence of this doublet may be interpreted as being due to the existence of conformational isomers in the $AlCl_3$ complex. On adsorption of these two ketones on δ-Al_2O_3 (dehydroxylated at 500 °C), surface reactions are much reduced as compared to hexachloroacetone or acetone, although not completely suppressed. As shown in Figure 2, the stepwise adsorption of diisopropyl ketone in small doses leads to the development of a broad asymmetric carbonyl stretching band, the position of which shifts toward higher wave numbers as the coverage increases. Finally, a band maximum is obtained at 1680 cm^{-1}. At further increasing ketone pressure an additional band grows at 1695 cm^{-1}. The corresponding species is readily desorbed and must therefore be weakly adsorbed, most probably via H bonds as indicated by the reversible perturbation of the surface OH groups. Desorption at room temperature leaves a carbonyl band which is centered at 1680 cm^{-1} (i.e., shifted by 35 cm^{-1} with respect to the liquid) and which is asymmetric toward lower wave

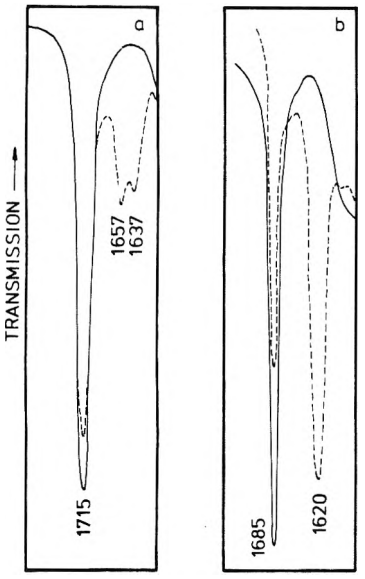

Figure 1. Carbonyl stretching bands of alkyl-substituted ketones and their $AlCl_3$ complexes in CCl_4: (a) —, diisopropyl ketone; - - - -, $AlCl_3$ complex of diisopropyl ketone; (b) —, hexamethyl ketone; - - -, $AlCl_3$ complex of hexamethyl ketone.

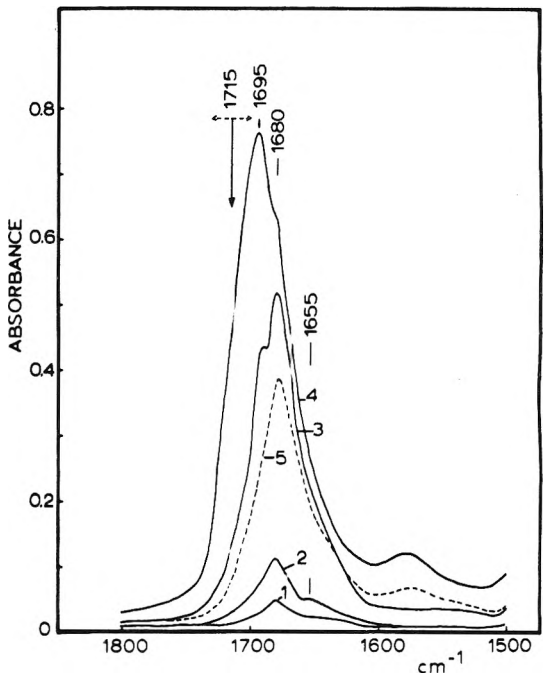

Figure 2. Carbonyl stretching region of diisopropyl ketone adsorbed on δ-Al_2O_3 (pretreated at 500 °C). Spectra 1 to 4 develop at successive doses of the ketone, spectrum 5 is obtained after desorption at ambient temperature for 1 h at 10^{-4} mmHg. The arrows at 1715 cm^{-1} indicate position and band half-width of the liquid ketone.

numbers and has a shoulder around 1630 cm^{-1}. The band half-width being 45 cm^{-1} is larger than in the homogeneous $AlCl_3$ complex. A small band near 1580 cm^{-1} is the result of slight surface reactions and is assigned as the asymmetric stretching vibration of a surface carboxylate species. The development of the carbonyl stretching band and its feature clearly indicates the coordinative interaction of the ketone with Lewis acid sites representing a fairly wide range of acid strengths. A completely analogous behavior is observed on adsorption of the hexamethylacetone. The carbonyl stretching band is shifted by 39 cm^{-1} from 1685 cm^{-1} in the liquid hexamethylacetone to 1646 cm^{-1} in the chemisorbed state after desorption at ambient temperature. The corresponding band half-width is 55 cm^{-1} as compared to 30 cm^{-1} in the homogeneous $AlCl_3$ complex. It can thus be concluded that the carbonyl stretching band is in fact sensitive enough for the detection of acid strength distributions, as proposed by Hair.[2] The halogen-substituted ketones, however, are not suited as probe molecules because of their high reactivity; alkyl-substituted ketones on the other hand can be used at least at sufficiently low temperatures, e.g., below 100 °C.

References and Notes

(1) H. Little, "Infrared Spectra of Adsorbed Species", Academic Press, London, 1966.
(2) M. L. Hair, "Infrared Spectroscopy in Surface Chemistry", Marcel Dekker, New York, N.Y., 1967.
(3) H. Knözinger, *Adv. Catal.*, **25**, 184 (1976).
(4) H. Knözinger and H. Stolz, *Fortschr. Kolloid. Polym.*, **55**, 16 (1971).
(5) H. Knözinger and H. Krietenbrink, *J. Chem. Soc., Faraday Trans. 1*, **71**, 2421 (1975).
(6) H. Knözinger, H. Krietenbrink, H. D. Müller, and W. Schulz, paper accepted for the Sixth International Congress on Catalysis, London, 1976.
(7) H. Krietenbrink and H. Knözinger, *Z. Phys. Chem. (Frankfurt am Main)*, in press.
(8) M. L. Hair and J. D. Chapman, *J. Phys. Chem.*, **69**, 3949 (1965).
(9) P. Fink, *Rev. Roum. Chim.*, **14**, 811 (1969).
(10) A. V. Deo, T. T. Chuang, and J. G. Dalla Lana, *J. Phys. Chem.* **75**, 234 (1971).
(11) H. Knözinger, *Acta Cient. Venez., Suppl. 2*, **24**, 76 (1973).

Semiempirical Calculations for Metal Clusters. Isolated and Adsorbed to Carbon and Silicon Dioxide Models

R. C. Baetzold

Research Laboratories, Eastman Kodak Company, Rochester, New York 14650 *(Received December 17, 1975)*

Publication costs assisted by Eastman Kodak Company

Histograms of calculated valence-band density of states for isolated and adsorbed clusters of Cu, Ag, and Au are reported. The features shown indicate that d bands continue spreading in size up to 13 atoms and when the metal cluster is adsorbed to carbon or silicon dioxide the band width becomes much greater. Minima in the curves for binding energy per atom vs. size are observed at a few atoms by CNDO and extended Hückel calculations for Ag, Cu, Au, and Pd. This property is important in determining critical catalytic size for some reactions. Calculations for icosahedral clusters, thought to be important in catalytic reactions, show properties differing little from fccub clusters.

Introduction

The objective of this work is to determine electronic properties of metal clusters. This information will be compared with and used to explain various experimental properties now being measured for this type of system. Included in these measurements are the ESCA studies of valence-band structure[1] and catalytic studies of critical sizes.[2] The eventual aim of this work is to gain a better understanding of heterogeneous catalysis.

This report examines electronic properties of Ag, Au, and Cu isolated and in interaction with a carbon or silicon dioxide model using complete neglect of differential overlap[3] (CNDO) molecular orbital theory. It is an extension of previous work on isolated Ag and Pd metal clusters[4] and those interacting with a 10-atom carbon model.[5] In the present work a larger, 16-atom carbon model is employed and adsorption on a Si_2O_4 model is treated by CNDO. In addition, extended Hückel theory[6] (EH) is used to examine binding energies of various metal clusters to compare with critical catalytic size. The icosahedral metal cluster geometry, thought to be important in some catalytic reactions,[7] is compared in stability to other geometries including fccub, which we have previously investigated.[8] A comparison will be made of isolated vs. adsorbed-cluster results and EH with CNDO results.

The electronic properties that determine catalysis in metal clusters are not completely understood. Valence-band structure information is thought to be of importance since this feature determines which orbitals can best interact with the wave functions of an adsorbate. Other properties including binding energies, ionization potentials (IP), and electron affinities (EA) are investigated in this report. The properties investigated here are similar to those examined by Blyholder[9,10] in studies of chemisorption on nickel particles using CNDO and by Anderson and Hoffman[11] in extended Hückel calculations of transition-metal clusters.

Method

The method of calculation using CNDO[3] has been employed for transition elements before.[4,5] The resonance parameters (β) and all other parameters employed by Pople and Segal[12] for Si, O, and C were used here. Values of β used for the transition elements were determined by fit to experimental data of diatomic molecules as described before.[4] The ionization potential (IP) values were taken from atomic spectral tables,[13] and atomic electron affinities (EA) were taken from experiment, when available, or estimated. These values are listed in Table I.

The exponents of the Slater orbitals were taken from atomic Hartree–Fock calculations.[14] This procedure works well for s and p orbitals, but not for d orbitals: it gives a band of d molecular orbitals that are too narrow and are located too far from the vacuum level. Therefore, to correct these problems partially, the d orbitals were made more diffuse by reducing the d exponent values to those shown in Table I.

The EH calculations have been performed using two parameterizations. When single Slater orbitals were employed, the exponents of Clementi[14] were used and the Wolfsberg–Helmholz constant was optimized by fit to experimental data for diatomic molecules.[4] Alternatively, when double ζ d orbitals were employed,[15] the Wolfsberg–Helmholz constant was assigned the standard value 1.75. The use of two sets of parameters serves to provide a check on the reliability of the calculation.

The 16-atom carbon model (C_{16}) and the six-atom silicon dioxide model (Si_2O_4) are shown in Figure 1, as well as sites (marked ×) where the transition-metal atom was adsorbed. The placement of atoms were determined by potential energy minima for the most symmetric sites. Sites of low symmetry were not considered owing to computer time limitations. We expect to determine only general trends in properties by this process.

Results

A. *Isolated Clusters—CNDO.* Various metal cluster geometries were examined by determining potential energy curves while all nearest-neighbor bonds retain equal lengths. Straight linear chains were found to be the most stable for Cu and Ag, whereas symmetric three-dimensional structures were more stable for Au. Values for both types of geometries are reported in Table II, in which the sequence of three-dimensional geometries is: 4-pyramid, 5-bipyramid, 6-square bipyramid, 7-bicapped pentagon, 8-cube, and 9,13-fccub structure. It is observed that even-size clusters generally have higher BE/n values than odd-size ones for Ag, Cu, and Au. In these cases there is a general increase in BE/n with n. The values of HOMO reflect the trend in IP values based upon Koopmans' theorem.[16] Since relaxation effects due to hole

TABLE I: Input Parameters—CNDO

Atom	$-\beta^0$	Orbital	½(IP + EA) eV	Slater exponent
Ag	1	5p	2.39	1.35
		5s	4.26	1.35
		4d	6.27	1.90
Au	1	6p	2.18	1.82
		6s	5.11	1.82
		5d	6.55	2.10
Cu	1	4p	2.56	1.46
		4s	4.45	1.46
		3d	6.46	1.90

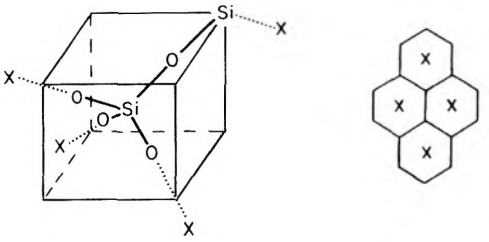

Figure 1. Sketches of the carbon and silicon dioxide models used in this work. Adsorption sites marked by X.

formation are not included in these calculations, experimental IP values would be expected to be 1–2 eV less than the HOMO value. The LUMO reflects the trend in EA with size. Here it is observed that the LUMO and HOMO tend to approach one another with increasing n, but a large energy gap exists between the two.

The band structures of the occupied levels of Au and Ag clusters are shown in the histograms of Figures 2 and 3. The d bands of Au spread with increasing size to ~2.25 eV at Au_{13} and the s molecular orbitals spread even more in energy. For Ag, the d-band spreading depends upon size and geometry, but the d bands are spread over a 1.25-eV energy range at nine atoms. Bulk Ag and Au have the experimental d-band widths 3.0 and 6.0 eV, respectively.[17] In these calculations molecular orbitals composed primarily of s orbitals do not appear at lower energy than the d molecular orbitals although there is considerable spreading of the s levels. Some s orbitals are mixed into the d states, however. In the EH-type calculations s states have been observed at lower energy than d states for Au_{13} and Ag_{13}. The features of the Cu density-of-states histogram are similar to the Ag case.

B. *Clusters on Si_2O_4.* The Si_2O_4 model consists of only six ions as shown in Figure 1. It was found that larger models did not give convergent results with the CNDO scheme. Thus, this small model having one fully coordinated Si and one Si with only one coordination is employed. Other calculations using SiO_2 models have been successful with only a few ions, so this provides some justification for the small model chosen here. The previous calculations for SiO_2 include the EH study of defect electronic structure by Bennett and Roth,[18] X_α calculations for silicates,[19] and the linear combination of localized orbitals (LCLO) approach employed by Yip and Fowler[20] for characterizing the valence-band structure.

The most favorable site for adsorption of transition-metal atoms of Ag, Cu, or Au on Si_2O_4 is near an oxygen ion. The greatest binding energy results when the metal atom bridges two oxygen ions. The data shown in Table III refer to this site for one metal atom and linear bonding to oxygen ions for two and three metal atoms. The fourth atom is added to form a pyramidal-shape metal cluster.

The data in Table III indicate considerable interaction between metal cluster and Si_2O_4 substrate. Electron transfer to Si_2O_4 and a decreasing trend in BE/n with n takes place.

Histograms showing the density of occupied states for Ag clusters on Si_2O_4 are shown in Figure 4. The Si_2O_4 cluster has several molecular orbitals composed of p orbitals on O, which interact with the metal cluster. The d states on Ag are shifted considerably depending upon whether the atom is next to a Si or an O ion. This difference is expected as deduced from the charge of neighboring ions and based upon Madelung considerations. As the cluster increases in size the d states form a band that contains only minor amounts of orbital contributions from SiO_2 orbitals. Considerable mixing of these orbitals is seen for states on both sides of this band.

The shape of the energy-level histograms for Ag_n clusters isolated and adsorbed to Si_2O_4 can be compared by referring to Figures 2 and 4. We see that the major component of the d band is relatively unshifted in energy, but several d states split off from the main band upon adsorption. These states usually contain contributions from the substrate orbitals. Similar histograms for Au and Cu have been constructed and the general features observed are similar to those in the Ag case.

C. *Au_n and Cu_n Adsorbed to C_{16} Model.* We examined the properties of gold and copper clusters adsorbed to the 16-atom carbon model (C_{16}) because of the possibility of making comparative ESCA measurements in this system. The C_{10} model was used to find adsorption sites and distances before doing the calculations with the C_{16} model. The sites of greatest binding were at hexagon centers with the bond distance 2.37 Å for AuC and CuC. Using the resonance parameter (β^0) for C, employed previously by Pople,[12] gives the best convergence. This represents a condition of strong C–C and metal–C interaction. The binding energy per C atom in the model is 26.1 eV, which is about four times the bulk experimental value of graphite, 7.4 eV. The ionization potential of the carbon model is 7.7 eV; the experimental value for bulk carbon is 5.0 eV.

The valence structure for a series of Au and Cu clusters on C_{16} is shown in the histograms of Figures 5 and 6. Comparison with Figure 3 shows that the d band in gold is ~3 eV wide for Au_5 on C_{16}, but only ~1 eV for small, isolated clusters. In addition, the d orbitals of a single gold atom are mixed strongly with the 2p orbitals of C resulting in considerable spreading of density for the single atom. Similar effects are found for Cu_n on C_{16}.

The properties of the adsorbed metal clusters are shown in Table IV. Note that the values of binding energy per atom are much greater for the clusters interacting with C_{16} than for isolated ones. This is a consequence of the interaction with substrate orbitals, although this effect is believed to be overestimated by a factor of 4. For most of the values in Table IV BE/n decreases with increasing n, which suggests that during nucleation experiments aggregation does not occur as long as substrate sites are open for single atoms to be bound. It is interesting that this effect is also found with other parameterizations for carbon, such as the set giving weaker carbon–metal interactions studied before.[5] There is a considerable gap between HOMO and LUMO for the closed shell clusters, which decreases with increasing n, as was observed for the isolated clusters. Cu and Au show very little electron transfer with the substrate.

The results reported here may be compared with results

TABLE II: Properties of Isolated Clusters—CNDO

Size	Req, Å	Nonlinear BE/n, eV	Nonlinear HOMO, eV	Nonlinear LUMO, eV	Linear BE/n, eV	Linear HOMO, eV	Linear LUMO, eV
			Cu				
2	3.0	2.33	7.19	1.61			
3	3.2	1.91	4.09	4.09	1.91	4.47	4.47
4	3.2	2.14	5.97	2.07	2.18	6.68	2.24
5	3.2	1.98	4.25	4.25	2.07	4.46	4.46
6	3.2	2.22	6.22	2.07	2.30	6.55	2.41
7	3.2	2.00	4.35	4.35			
8	3.2	2.22	6.33	2.26	2.28	6.34	2.60
			Au				
2	2.8	1.68	8.16	2.13			
3	2.8	1.21	5.09	5.09	1.24	4.64	4.64
4	3.0	1.71	7.20	2.37	1.63	7.79	2.56
5	3.0	1.54	5.04	5.04	1.42	5.04	5.04
6	3.0	1.82	7.25	2.60	1.68	7.62	2.73
7	3.0	1.66	4.90	4.90	1.50	5.02	5.02
8	3.0	1.77	7.29	2.78	1.33	6.01	4.61
9	3.0	1.77	4.88	4.88			
13	3.0	1.95	5.15	5.15			
			Ag				
2	3.2	1.52	7.00	1.53			
3	3.4	1.14	3.76	3.76	1.10	4.27	4.27
4	3.4	1.50	5.80	1.86	1.51	6.68	2.02
5	3.4	1.46	4.02	4.02			
6	3.4	1.88	6.25	2.02	1.68	6.51	2.20
7	3.4	1.57	4.02	4.02			
8	3.4	1.68	6.24	2.06	1.51	6.37	2.31
9	3.4	1.71	4.03	4.03			
13	3.4	1.87	4.07	4.07			

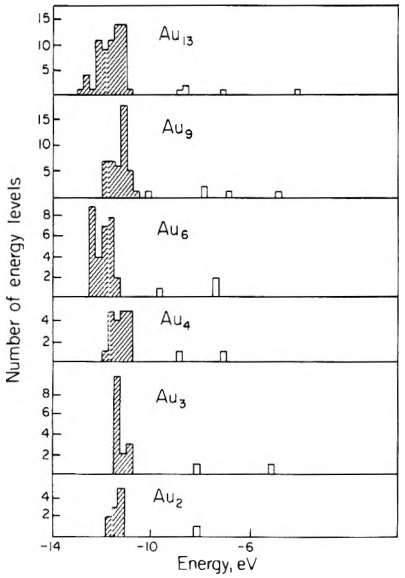

Figure 2. Histogram of the number of energy levels per 0.25-eV energy interval for Au clusters as a function of energy. Geometries were linear, equilateral triangle, pyramid, square bipyramid, bccub unit cell, and fccub cell. Shaded areas indicate d states on Au.

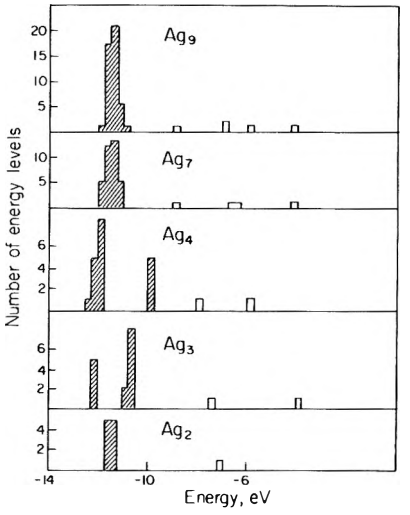

Figure 3. Histogram of the number of energy levels per 0.25-eV energy interval for Ag clusters as a function of energy. Geometries were linear, equilateral triangle, pyramid, bicapped pentagon, and bccub unit cell. Shaded areas indicate d states on Ag.

employing a 16-atom carbon model with the $\beta^0 = -4$ parameterization for carbon. This represents a case of weaker C–C and C–metal interaction. It is found that the d states are centered at the same energy in the two types of calculation, but they are narrowed considerably in the $\beta = -4$ case, bearing a strong resemblance to histograms in Figures 2 and 3. At Au_4 adsorbed to C_{16} the d width is 1.75 eV compared to 5 eV using these two parameterizations. The general shape of the d states is bimodal in each case.

D. *Isolated Metal Clusters—EH.* Isolated metal clusters have been investigated by EH because of the better d-orbital

TABLE III: Properties of Metal Atoms Adsorbed to Si_2O_4

No. of atoms	BE, eV	Av charge	HOMO, eV	LUMO, eV
Ag	12.87	+0.65	3.91	3.91
Ag_2	15.78	+0.33	7.42	1.68
Ag_3	36.98	+0.30	3.41	3.41
Ag_4	22.55	+0.14	5.00	1.44
Cu	11.26	+0.29	5.11	5.11
Cu_2	16.13	+0.30	8.05	1.93
Cu_3	35.58	+0.28	3.45	3.45
Cu_4	20.61	+0.16	5.18	2.10

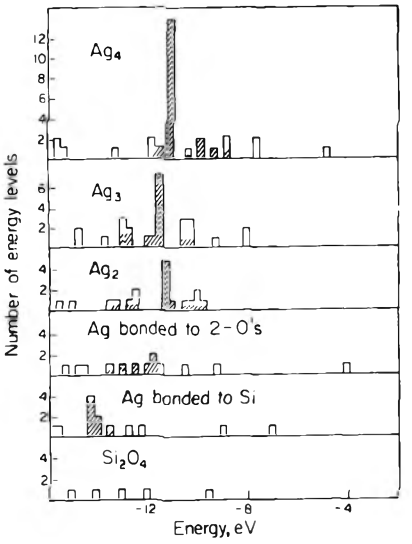

Figure 4. Histogram showing number of energy levels per 0.25-eV energy interval for Ag clusters bonded to Si_2O_4 model. Shaded areas indicate d orbitals on Ag.

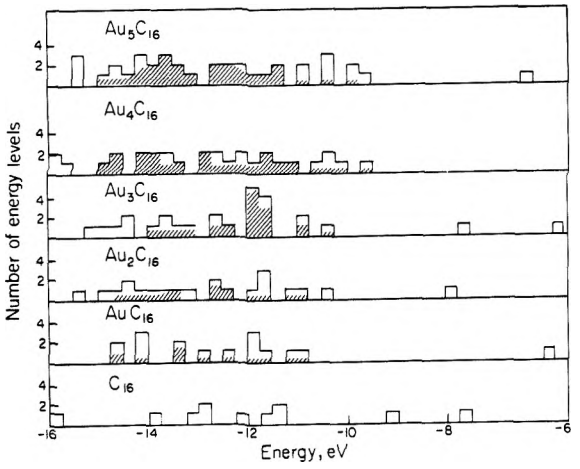

Figure 5. Histogram showing number of energy levels per 0.25-eV energy interval for Au clusters adsorbed to C_{16} model. Shaded area *denotes d orbitals on Au.*

representations and larger cluster sizes that can be studied in this case relative to CNDO. It is also of interest to compare results calculated by the two methods as a means of judging reliability of the calculations. The several different types of parameterization for EH discussed before can be used.

The binding energy per atom is a fundamental property of

TABLE IV: Properties of Adsorbed Metal Atoms on C_{16}

Cluster	BE/n, eV	HOMO, eV	LUMO, eV	Av metal atom charge
Au	31.08	5.39	5.39	+0.16
Au_2	27.35	7.78	3.17	+0.07
Au_3	18.40	5.66	5.66	+0.05
Au_4	24.12	9.69	4.34	+0.20
Au_5	19.13	6.45	6.45	+0.12
Cu	10.81	6.55	6.55	−0.03
Cu_2	13.43	8.52	3.37	+0.01
Cu_3	9.31	4.87	4.87	+0.01
Cu_4	10.65	8.63	4.86	+0.04
Cu_5	6.87	6.06	6.06	−0.04
Cu_6	7.88	7.46	4.64	+0.02

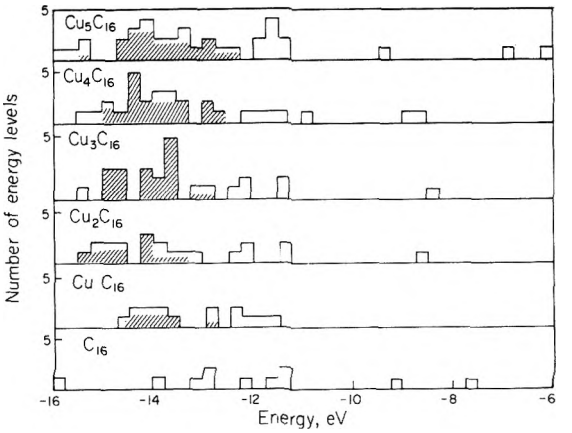

Figure 6. Histogram showing number of energy levels per 0.25-eV energy interval for Cu clusters adsorbed to C_{16}. Shaded areas denote d orbitals on Cu.

metal clusters determining their cohesion. Figure 7 shows this property for several different three-dimensional metal clusters using the double-ζ parameters. For several of these metals, including Ag, Cu, and Au, linear chains are predicted to be more stable than the three-dimensional structures. Nevertheless, we examine here only the three-dimensional properties because these are most likely to be formed on substrates. Note that a minimum in BE/n as a function of size is found for Pd, Cu, Au, and Ag. Such behavior is found also in the CNDO data for Au and Ag reported in Table I. The minima do not occur at the same size for each calculation. This type of behavior is also found when the Clementi-type parameterization is employed as shown for Ag and Pd in Figure 8. This behavior of the binding energy per atom could determine a critical size for nucleation or catalysis involving stabilization of metal atoms.[2]

The binding energies of the icosahedral structure and the fccub structure of large Pd and Ag clusters are also compared in Figure 8. This icosahedral structure is interesting because of the pair-potential calculations of Allpress and Sanders,[21] Burton,[22] and Briant and Burton[23] suggesting its stability and catalytic properties. In addition, electron microscopic studies of rhodium[24] and gold clusters on mica[25] have given evidence for the existence of this geometry in some situations. The icosahedral structure is more stable than fccub for Pd, but the reverse is true for Ag as shown in Figure 8. This effect is also found using the double-ζ parameterization. Examination of

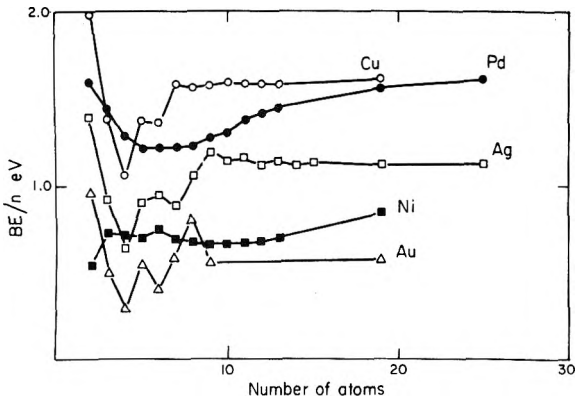

Figure 7. Binding energy per atom for three-dimensional Ni (■), Pd (●), Cu (O), Ag (□), and Au (△). The double ζ parameterization with $K = 1.75$ is used in these calculations. Large clusters with 13 or more atoms have the fccub geometry.

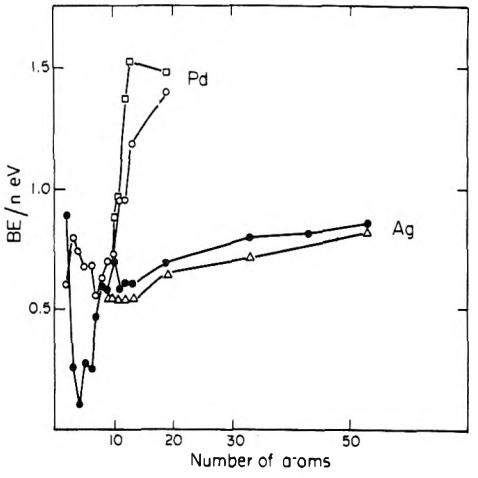

Figure 8. Binding energy per atom for fccub Ag (●), fccub Pd (O), icosahedral Ag (△), and icosahedral Pd (□) as a function of size. Clementi orbital exponents with $K = 1.44$ for Pd and $K = 1.30$ for Ag were employed.

this phenomenon for Ni and Cu shows similar behavior for members of a given column in the periodic table. Thus, the molecular orbital calculations indicate a greater stability for Pd and Ni geometries, which are unlike that of the bulk fccub metal. In the case of Ag and Cu small clusters, fccub is more stable than icosahedral geometry.

The electronic properties do not vary greatly between icosahedral and fccub geometries. In the case of 1B metal clusters, ionization potential values are about 0.2 eV smaller for icosahedral than fccub across the range of sizes investigated. For the group 8 metal clusters, ionization potentials are smaller for icosahedral than for fccub geometry, but the average number of d holes per Pd atom is the same (0.8) for both geometries. The calculations thus do not suggest any different catalytic activity for one cluster geometry than for the other

Differences in the preferred geometry of Ag and Pd clusters may be discussed in terms of the surface structure of icosahedral and fccub particles described by Burton.[7] More closely packed surfaces are observed in icosahedral vs fccub particles and lead to a broader valence band and smaller ionization potential as reported above. The average electron configuration found here is $4d^{10}\,5s^{1}$ for Ag and $4d^{9.2}\,5s^{0.8}$ for Pd. Since filled bands are slightly destabilizing, the broader 4d band of the Ag icosahedral particle would lead to less stability than for the fccub particle. In the case of Pd, the 4d band is only partly filled and would be stabilized upon broadening. This favors the icosahedral structure. Of course, the effect of structure on 5s bands must also be considered in determining the total relative stability.

Conclusions

Histograms representing the density of states of metal clusters as a function of size have been reported for isolated and adsorbed metal clusters. It is observed that the substrate can severely distort the shape of the cluster density of states through mixing of wave function. Isolated metal particles have narrower d-band widths than their bulk counterparts, and linear geometries are predicted to be more stable for some metals, including Cu and Ag, by CNDO and EH molecular orbital theories.

A comparison of specific results of EH and CNDO methods is not always comforting as the results reported here for absolute values of binding energies show. Many general features do agree, such as the presence of increasing BE/n with n, the gap between HOMO and LUMO, the presence of weakly stable, small clusters, and the narrow d band found for small metal clusters. Electron transfer from Au, Ag, and Cu to SiO_2 and carbon are predicted by both models. The general features of the valence-band spectrum shown here can be tested experimentally by measurement of the density of states. As before,[5] absolute values of binding energies for metal atoms adsorbed to the carbon model are expected to be about four times the experimental ones. The values reported for the adsorbed clusters in Tables III and IV are much larger than the values reported for isolated clusters in Table II reflecting the strong interaction with substrate. The trends in BE/n with n are different for isolated and adsorbed clusters. The binding energy of adsorbed cluster is strongly dependent upon sites of adsorption so there may be more favorable sites for growth of the metal cluster on the substrate.

This treatment of metal clusters by semiempirical MO theories requires that all absolute values calculated be treated cautiously. Trends in a set of data for clusters or comparisons of data for similar properties are likely to be calculated with the most reliability.

Acknowledgments. I am grateful for the stimulation of my colleagues, particularly J. F. Hamilton, who took part in many helpful conversations. I wish to thank J. J. Burton and C. L. Briant for providing the coordinates used in their calculations for icosahedral structures.

References and Notes

(1) M. G. Mason and R. C. Baetzold, *J. Chem. Phys.*, **64**, 271 (1976).
(2) J. F. Hamilton and P. C. Logel, *Photogr. Sci. Eng.*, **18**, 507 (1974).
(3) J. A. Pople, D. P. Santry, and G. A. Segal, *J. Chem. Phys.*, **43**, S 129 (1965).
(4) R. C. Baetzold, *J. Chem. Phys.*, **55**, 4363 (1971).
(5) R. C. Baetzold, *Surf. Sci.*, **36**, 123 (1972).
(6) R. Hoffmann, *J. Chem. Phys.*, **39**, 137 (1963).
(7) J. J. Burton, *Catal. Rev.-Sci. Eng.*, **9**, 209 (1974).
(8) R. C. Baetzold and R. E. Mack, *J. Chem. Phys.*, **62**, 1513 (1975).
(9) G. Blyholder, *Surf. Sci.*, **42**, 249 (1974); *J. Vac. Sci. Technol.*, **11**, 865 (1974).
(10) G. Blyholder, *J. Phys. Chem.*, **79**, 756 (1975).
(11) A. B. Anderson and R. Hoffmann, *J. Chem. Phys.*, **61**, 4545 (1974).
(12) J. A. Pople and G. A. Segal, *J. Chem. Phys.*, **44**, 3289 (1966).
(13) C. E. Moore, *Natl. Bur. Stand. (U.S.), Circ.* No. 467, Vols. 1–3 (1949).
(14) E. Clementi, D. L. Raimondi, and W. P. Reinhardt, *J. Chem. Phys.*, **47**, 1300 (1967).
(15) H. Basch and H. B. Gray, *Theor. Chim. Acta*, **4**, 367 (1966).

(16) T. Koopmans, *Physica*, **1**, 104 (1933).
(17) R. A. Pollak, S. Kowalczyk, L. Ley, and D. A. Shirley, *Phys. Rev. Lett.*, **29**, 274 (1972); D. Shirley, *Phys. Rev. B*, **5**, 4709 (1972).
(18) A. J. Bennett and L. M. Roth, *J. Phys. Chem. Solids*, **32**, 1251 (1971).
(19) J. A. Tossell, D. J. Vaughan, and K. H. Johnson, *Chem. Phys. Lett.*, **20**, 429 (1973).
(20) K. L. Yip and W. B. Fowler, *Phys. Rev. B*, **10**, 1391, 1400 (1974).
(21) J. G. Allpress and J. V. Sanders, *Aust. J. Phys.*, **23**, 23 (1970).
(22) J. J. Burton, *J. Chem. Phys.*, **52**, 345 (1970).
(23) C. L. Briant and J. J. Burton, *Nature (London), Phys. Sci.*, **243**, 100 (1973).
(24) E. B. Prestridge and D. J. C. Yates, *Nature (London)*, **234**, 345 (1971).
(25) J. G. Allpress and J. V. Sanders, *Surf. Sci.*, **7**, 1 (1967).

Diffusion of Hexane Isomers in Argon

Eli Grushka* and P. Schnipelsky

Department of Chemistry, State University of New York at Buffalo, Buffalo, New York 14214 *(Received October 9, 1975)*

The diffusion of hexane isomers in argon confirms previous observations that diffusion coefficients increase with increased branching. The position and number of side chain groups affect the diffusion of the isomers, in agreement with the shielding theory. Group diffusion volumes, which are empirical quantities in the Fuller–Schettler–Giddings predicting equation, substantiate qualitatively the arguments of the shielding theory. The present results indicate that methyl group diffusion volumes decrease slightly in going from octane to hexane isomers. The reasons for the decrease, if indeed real, are not yet known. By use of the Lennard-Jones (6–12) potential model (admittedly oversimplified for hexane isomers), it is shown that changes in the magnitudes of the diffusion coefficients are a function of the molecular geometry and not of the interaction energy.

Introduction

In a series of papers[1,2] we have discussed the effect of molecular structure on the gaseous diffusion coefficients of octane and heptane isomers. Such studies have practical significance in the designing of various systems where diffusion is important: i.e., gas adsorption beds, distillation columns, pollution studies, etc. In addition, much theoretical information can be ascertained from the dependence of the diffusion of isomers on the molecular geometry. Previous investigations have indicated that the diffusion coefficients of octane and heptane isomers increase with increased branching. Elliot and Watts'[3] studies of *n*-pentane and isopentane show the same trend. However, both Elliot and Watts,[3] and Wakeham and Slater[4] found that isobutane diffused slower than the normal homologue.

It was also found previously that the position of the side chain on the long alkane backbone affects the diffusion coefficients. For example, the diffusion coefficient of 2,4-dimethylpentane in He was significantly different from D_{12} of 2,2-dimethylpentane. Vandensteendam and Piekarski[5] studied the effect of the position of an ester group in a series of molecules having the formula $CH_3(CH_2)_{M_1}COO(CH_2)_{M_2}CH_3$, where $M_1 + M_2 = 6$. Contrary to our findings, and the prediction of the shielding theory,[6] the position of the COO group did not greatly affect the diffusion coefficients. Vandersteendam and Piekarski,[5] however, did not give the precision of their measurements, and consequently, final conclusions based on their data cannot be made. The importance of the dependence of D_{12} on the position of the side group lies in the fact that some predicting equations can be modified to better estimate diffusion coefficients. One of the better predicting equations, namely, the one suggested by Fuller, Schettler, and Giddings,[7] fails in the case of structural isomers. The present work, in conjunction with previous data,[1,2] will indicate how the equation can be modified to include geometric features.

With structural isomers, the molecular weights are constant. It is then of theoretical importance to ascertain whether changes in the diffusion coefficients, as a function of molecular shape, are due to changes in the size of the isomers or to changes in the interaction energies between the isomer molecules and other gas molecules. It is difficult, however, to choose a correct potential model which can adequately describe large polyatomic molecules. A great deal of work has been done on spherical molecules using the Lennard-Jones (6–12) potential (for review, see ref 8 and 9). For polyatomic molecules Dahler and co-workers[10–13] and Sandler and Mason[14] developed the loaded sphere and spherocylindrical models, while Hoffman[15] described an ovaloid model. More recently, Verlin, Matzen, and Hoffman[16] have further discussed the ovaloid system.

It was decided to utilize the Lennard-Jones (6–12) potential, simply because this model was, and still is, extensively used for nonspherical molecules. Values of the collision integrals for the (6–12) potential are readily available.[8] The Lennard-Jones potential yields the collison distance σ_{12} and the depth of the interactive potential ϵ_{12}. Even though this model does not accurately describe molecular interactions, the trends observed are useful for qualitative discussions on the effects of molecular structure. It must be recognized, as pointed out very elegantly by Kestin, Ro, and Wakeham,[17] that the analysis of diffusion data (or any other transport property for that matter) does not result in the validation of a potential model. Additional justifications for the use of this potential for large molecules is given by Svehla.[18]

Hirschfelder, Curtiss, and Bird[8] indicate that because no combining rules are required, diffusion data, provided it is accurate, are inherently a more reliable measure of the force constants σ_{12} and ϵ_{12}. All that is needed is the temperature dependence of the diffusion coefficients. Weismann and Mason[19] calculated gaseous diffusion coefficients from viscosity data. They recognized the loss in accuracy when calculating D_{12} from viscosity. However, due to the ease of obtaining accurate viscosity data, Weismann and Mason[18] indicated that "the accuracy in the calculated diffusion coefficients is little worse than the accuracy obtainable by direct measurements". However, due to recent developments and improvements in the so-called "chromatographic broadening technique" [20] accurate diffusion coefficients can be measured rapidly with great ease. Instrumental improvements were discussed previously by Grushka and Maynard,[1] Grushka and Schnipelsky,[2] and by Wakeham and Slater.[4] The mathematical relationships between the zone spreading in the chromatograph and the diffusion coefficient are discussed elsewhere (i.e., ref 1, 2, 4, 20).

Experimental Section

Apparatus and Procedure. The specially designed diffusion apparatus, as well as the procedure, were described elsewhere.[2] In the present study, diffusion coefficients were measured at 306.5 ± 0.1 and 372.9 ± 0.1 K.

Reagents. The hexane isomers, purchased from Chemical Sample Co., were (a) n-hexane (99.9%), (b) 2-methylpentane (99.9%), (c) 3-methylpentane (99.9%), (d) 2,2-dimethylbutane (99.9%), and (e) 2,3-dimethylbutane (99%). The argon carrier gas (Grade A), purchased from Liquid Carbonic, was passed over molecular sieves The H_2 and air were of ordinary commercial grade.

Results and Discussion

The data collection and reduction were carried out as previously mentioned.[2] Possible sources of errors and their elimination, as well as a discussion on the reliability of the method, are described elsewhere.[1,2]

Diffusion of Hexane Isomers in Ar. Table I shows the diffusion coefficients of all the hexane isomers in Ar at two temperatures.

Since some of the diffusion cbefficients are very close in magnitude, a statistical examination of the data is required. An F test shows that, for all the data at each temperature, the standard deviation within 95% confidence level are not different. More important perhaps is a t test for the differences between the reported D_{12} values. At 306.5 K the difference between the diffusion coefficients of 3-methylpentane and 2-methylpentane is significant to within a 90–95% confidence level. The difference in D_{12} of the same compounds at 372.9 K is significant at the 95% confidence level. The difference in D_{12} values of 2,3-dimethylbutane and 2,2-dimethylbutane at 306.5 K is significant at the 80–90% confidence level. The difference in D_{12} values of the same two compounds at 372.9 K is significant at the 90–95% confidence level. From the t test, it could be surmised that statistically the dimethylalkanes, at 306.5 K, have virtually identical diffusion coefficients. This perhaps is not surprising since the two molecules are quite similar in size and shape. Nonetheless, given the fact that the difference in the diffusion coefficients is significant at confidence levels above 75% (below which, customarily, no statistical inferences can be made), the discussion in this paper will assume that the D_{12}'s of the dimethylalkanes are different.

The data confirm previous observations; D_{12} increases with increasing molecular branching. Unlike the results shown in Table I, Cummings and Ubbelohde found[21] that at 288.6 K 2,3-dimethylbutane has a lower diffusion coefficient than n-hexane in Ar. The present results are not only in agreement with previous studies using different homologous isomers,[1,2] but also the trend in the present data is consistant at two different temperatures. It is to be noted that while the change in D_{12} when going from n-hexane to the methylpentanes and the dimethylbutanes is relatively large, the change in the diffusion coefficients within a class of isomers is much smaller. Moreover, the order is similar to that observed with the heptane isomers diffusion in He:[2] the 3-methylalkanes diffuse slower than the 2-methylalkanes, and the more symmetrical dimethylalkanes diffuse faster than other dimethylalkanes.

TABLE I: Diffusion Coefficients (cm^2/s) of Hexane Isomers in Argon

Compound	$D_{1,2}$[a,b] 306.5 K	$D_{1,2}$[a,b] 372.9 K
Hexane	0.0734 (0.71%)	0.1049 (0.60%)
3-Methylpentane	0.0742 (0.44%)	0.1061 (0.50%)
2-Methylpentane	0.0747 (0.63%)	0.1068 (0.42%)
2,3-Dimethylbutane	0.0773 (0.81%)	0.1105 (0.36%)
2,2-Dimethylbutane	0.0778 (0.73%)	0.1112 (0.54%)

[a] Diffusion coefficients are corrected to 1 atm. [b] The numbers in parentheses are percent relative standard deviation (i.e., standard deviation divided by D_{AB} times 100).

Together with the data previously obtained,[1,2] the above results substantiate Giddings' shielding theory.[6] As the number of methyl group increases, shielding of the methylene groups on the backbone of the molecule is more effective. According to the theory, the contribution of the latter to the molecular cross section is minimal. Consequently, the branched molecules are smaller than the linear ones. This results in the higher diffusion coefficients of the straight alkanes. As the proximity of the two methyl side groups decreases, the linear portion of the molecule (an ethyl group) can shield these two units more effectively. The case of 3- and 2-methylpentane is more complex. In the latter, the long linear portion of the molecule can shield the methyl group to a greater extent than in the former (propyl vs. ethyl straight chain segments). On the other hand, the 2-methyl group shields a smaller portion of the straight chain part of the molecule than does the 3-methyl unit. Space filling models and experimental results given here (as well as in the case of the heptane isomers study) seem to favor the first explanation.

The consistency in the behavior of the diffusion coefficients in three classes of parent compounds is noteworthy. This fact, if indeed correct, should find utility in modifying such a predictive equation as the FSG relationship.[7] Grushka and Maynard[1] have introduced the concept of group diffusion volumes, and have shown that the FSG equation can be rearranged to yield such diffusion volumes. In the case of an alkane with n carbon atoms, the methyl group diffusion volume of a methylalkane is given by

$$\left[\left(\frac{A}{D_{12}}\right)^{1/2} - V_S^{1/3}\right]^3 - \sum V_{C_{n-1}H_{2n-1}} = V_{CH_3}$$

where A is a function of temperature, pressure, and molecular weights of the solute and the carrier, V_S is the atomic diffusion

volume of the carrier (Ar in the present paper), $\Sigma V_{C_{n-1}H_{2n-1}}$ is summation of the atomic diffusion volumes of $n-1$ carbon atoms and $2n-1$ hydrogen atoms, and V_{CH_3} is the group diffusion volume of the methyl group. Similar equations can be set up for dimethylalkane or for other alkyl side groups. Table II shows the group diffusion volumes for the methyl groups at two temperatures. As was found with heptane[2] and octane[1] isomers, the contribution of each methyl group at a given temperature is a function of its position and the number of groups. Inner groups have larger diffusion volumes; CH_3– in dimethyl isomers have smaller V_{CH_3} values than in methylalkanes. This is in qualitative agreement with the shielding theory. For example, the fact that the CH_3– group on the 3 position has a larger group diffusion than that on the 2 position might be indicative of the fact that the former is not shielded as well by other groups in the molecule than the latter. This contribution to the molecular dimension being large results in a smaller diffusion coefficient of 3-methylpentane as compared to that of 2-methylpentane.

The effect of temperature on group diffusion volumes is also of interest. The smaller group diffusion volumes at the higher temperature may reflect a change in the conformation of the molecules. As the temperature increases, not only translational motions of the molecules increase, but so do the internal vibrational motions. *Atomic* diffusion volumes as described by Fuller, Schettler, and Giddings[7] do not have any temperature dependence. The same may not be true with *group* diffusion volumes. It should also be emphasized that the 1.75 power dependence of D_{12} and T suggested by Fuller et al.[6,7] is based solely on empirical grounds. Thus, the observed behavior in the *group* diffusion volumes as the temperature changes might indicate that these volumes are not true molecular parameters. With regard to the temperature dependence of D_{12}, Massero and Mason[22] recently have demonstrated how the power-law dependence can be improved upon. It is interesting to note that the volume difference between the two methylpentanes is approximately the same at the two temperatures. The same is true for the two dimethylbutanes, but not for the volume difference between the methyl and dimethyl isomers. More experimental data are needed to verify the importance of this observation.

A comparison of group diffusion volumes for equivalent positional isomers of hexane, heptane,[2] and octane[1] at about 373 K is given in Table III. Several observations can be made and empirically explained. (a) The group diffusion volumes for the 3-methyl, 2-methyl, and 2,3-dimethyl isomers decrease in going from octane to hexane. An exception occurs with the 2,2-dimethyl isomer. It should be realized that the present data were obtained with Ar as the mobile phase while previous work utilized He. It is conceivable that, unlike He, the bulkier Ar could not probe closely the molecular structure of the alkanes. At this point it is not clear whether the decreasing trend is a real one.

(b) The group diffusion volume for 2,3-dimethylbutane is greater than 2,2-dimethylbutane, while the inverse is true in the case of the analogous heptane isomers. This might be due to the fact that with the later solutes the backbone chain is longer and, consequently, the shielding effect on or by the methyl groups is a strong function of their positions. In the case of the dimethylbutanes, the molecules are so compact that the shielding effect in the 2,3 or 2,2 isomer is not much different. The previous discussion on the statistical analysis of the data should be kept in mind. This may explain the observation of Wakeham and Slater[4] that isobutane diffused slower than n-butane in Ar. (c) The differences in the magnitude of group diffusion volumes of the positional isomers is smaller for the hexane series. This may be explained by (1) the general compactness of the isomers or (2) the effect of using a larger probe molecule, namely, argon.

TABLE II: Methyl Group Diffusion Volumes

Compound	Diffusion volume, cm³ at 306.5 K	Diffusion volume, cm³ at 372.9 K
3-Methylpentane	26.0	22.0
2-Methylpentane	24.1	20.1
2,3-Dimethylbutane	18.7	17.0
2,2-Dimethylbutane	17.8	16.1

TABLE III: Group Diffusion Volumes (cm³) for Some Octane (1), Heptane (2), and Hexane Isomers at 100 °C

	2-Methyl	3-Methyl	2,3-Dimethyl	2,2-Dimethyl
Hexane	20.1	22.0	17.0	16.1
Heptane	22.4	25.5	17.8	19.1
Octane		26.2	20.5	

Interaction Parameters. As indicated in the Introduction, it is of interest to ascertain whether the changes in the diffusion coefficients are due to changes in molecular shape (geometric factor) or to changes in the attractive and repulsive forces between the isomers and Ar (energetic factors). Diffusion data can be utilized to calculate interaction parameters provided that a particular potential model is assumed. The model used here is the Lennard-Jones (6–12) potential. The advantages and disadvantages of this model were discussed previously. It is stressed again that though the model is not entirely applicable to nonspherical molecules, the results, in a qualitative manner, still convey the trends in the behavior of the data.

Diffusion data were used to obtain ϵ_{12}/k and σ_{12} by several workers.[4,23–30] In general, a least-square fit procedure was used to compare experimental data with theoretical calculations. The present method is a modification of the least-square technique which, while perhaps not as accurate, allows rapid calculation of ϵ_{12}/k and σ_{12}. It is based on measuring diffusion coefficients at two temperatures as discussed in ref 8. It is realized that a procedure using only two experimental points can be inferior to a least-squares fit scheme over a range of temperatures. However, the current method is fast, simple, and, as will be shown in a subsequent publication, yields results which are in close agreement with literature values.

From the diffusion data in Table I, ϵ_{12}/k and σ_{12} values for the hexane isomers are calculated, and shown in Table IV. Within the limitation of the applicability of the Lennard-Jones (6–12) potential, Table IV appears to indicate that while ϵ_{12}/k values do not show any particular trend, σ_{12} values decrease as branching increases. It can be assumed, then, that geometrical factors, rather than energetic interaction, are more important in determining the order of diffusion. The same conclusion can be reached by noticing that the ratios of the D_{12}'s at the two temperatures are a constant, having the value of 1.43. The ϵ_{12}, or energetic factor, affects the temperature dependence of the diffusion coefficient, whereas σ_{12} affects only the magnitude of D_{12}. Hence, since the ratios of the D_{12}'s at the two temperatures are the same for each com-

TABLE IV: Interaction Parameters for Hexane Isomers–Argon

Isomer	σ_{12}, Å	(ϵ_{12}/k), K
n-Hexane	4.78	171
3-Methylpentane	4.76	173
2-Methylpentane	4.74	175
2,3-Dimethylbutane	4.67	171
2,2-Dimethylbutane	4.65	166

TABLE V: Force Constants for Hexane Isomers

Compound	(ϵ/k), K	σ, Å
n-Hexane	240	6.15
3-Methylpentane	246	6.11
2-Methylpentane	251	6.08
2,3-Dimethylbutane	241	5.92
2,2-Dimethylbutane	225	5.89

pound, they all have the same energy factors, and the magnitude of the diffusion coefficients is a function of the molecular geometry.

Using combining rules such as suggested in ref 8, in conjunction with literature values of σ and ϵ/k for Ar, the Lennard-Jones (6–12) force constants for the individual isomers can be obtained. The best values of σ and ϵ/k for Ar are perhaps the average values of the compilation on p 1212 of ref 8: $\sigma = 3.41$ Å, $\epsilon/k = 122$ K. Table V shows σ and ϵ/k values for the various hexanes. A word of caution about the accuracy of these values should again be mentioned, especially since in obtaining the data for Table V, values of σ and ϵ/k from two different measurement techniques were used. The σ and ϵ/k values for *n*-hexane can be compared with those on p 1213 of ref 8. The tabulated values of the force constants of *n*-hexane, obtained from viscosity measurements, are out of line with other alkanes. The values in Table V follow the behavior depicted in the above reference much better. The trend of decreasing σ with increasing molecular branching should be taken as a trend only in view of the simplicity of the model. Nonetheless, the fact that ϵ/k is, within experimental errors constant, while σ appears to be a function of the molecular geometry is indicative of the relative importance of the molecular structure in determining the magnitude of D_{12}.

Conclusion

The increase in diffusion coefficients of hexane isomers as the molecular branching increases is similar to the behavior of octane and heptane isomers. However, the difference in D_{12} between the isomers is smaller in the present study. This might be due to (a) the fact that here the probe molecule is Ar while previously He was used, or to (b) the fact that hexane isomers are more compact than octane or heptane isomers, and thus the size of e.g., 2,3-dimethylbutane, is very close to that of 2,2-dimethylbutane. Space filling models and CH_3– group diffusion volumes for these isomers tend to support the latter supposition.

Analysis of the data in terms of the Lennard-Jones (6–12) potential model in an admittedly oversimplified manner also indicates that the diffusion behavior is a function of molecular geometry of the isomers and not of changes in attractive or repulsive forces. In the future, more sophisticated potential models, along with better data fitting procedures, should be used in order to obtain more meaningful interaction parameters.

References and Notes

(1) E. Grushka and V. R. Maynard, *J. Phys. Chem.*, **77**, 1437 (1973).
(2) E. Grushka and P. Schnipelsky, *J. Phys. Chem.*, **78**, 1428 (1974).
(3) R. W. Elliot and H. Watts, *Can. J. Chem.*, **50**, 31 (1972).
(4) W. A. Wakeham and D. H. Slater, *J. Phys. B.*, 7, 297 (1974).
(5) C. Vandensteendem and S. Piekarski, *C. R. Acad. Sci. Paris, Ser. C*, **277**, 817 (1973).
(6) E. N. Fuller, K. Ensley, and J. C. Giddings, *J. Phys. Chem.*, **73**, 3679 (1969).
(7) E. N. Fuller, P. D. Schettler, and J. C. Giddings, *Ind. Eng. Chem.*, **58**, 19 (1966).
(8) J. O. Hirschfelder, C. F. Curtiss, and R. B. Bird "Molecular Theory of Gases and Liquids", Wiley, New York, N.Y., 1964.
(9) T. R. Marrero and E. A. Mason, *J. Phys. Chem. Ref. Data*, **1**, 3 (1972).
(10) J. S. Dahler and N. F. Sather, *J. Chem. Phys.*, **38**, 2363 (1962).
(11) S. I. Sandler and J. S. Dahler, *J. Chem. Phys.*, **43**, 1750 (1965).
(12) S. I. Sandler and J. S. Dahler, *J. Chem. Phys.*, **46**, 3520 (1967).
(13) S. I. Sandler and J. S. Dahler, *J. Chem. Phys.*, **47**, 2621 (1967).
(14) S. I. Sandler and E. A. Mason, *J. Chem. Phys.*, **47**, 4653 (1967).
(15) D. K. Hoffmann, *J. Chem. Phys.*, **50**, 4823 (1969).
(16) J. D. Verlin, M. K. Matzen, and K. K. Hoffman, *J. Chem. Phys.*, **62**, 4146 (1975).
(17) J. Kestin, S. T. Ro, and W. Wakeham, *Physica*, **58**, 165 (1972).
(18) R. A. Svehla, NASA Technical Report No. T-132, 1962.
(19) S. Weissman and E. A. Mason, *J. Chem. Phys.*, **37**, 1289 (1962).
(20) J. C. Giddings and S. L. Seager, *J. Chem. Phys.* **33**, 1579 (1960).
(21) G. A. McD. Cummings and A. R. Ubbelhobde, *J. Chem. Soc.*, 3751 (1953).
(22) T. R. Massero and E. A. Mason, *AIChE J.*, **19**, 498 (1973).
(23) I. Amdur, J. Ross, and E. A. Mason, *J. Chem. Phys.*, **20**, 1620 (1952).
(24) I. Amdur and T. F. Schatzki, *J. Chem. Phys.*, **27**, 1049 (1957).
(25) I. Amdur and T. F. Schatzki, *J. Chem. Phys.*, **30**, 1425 (1959).
(26) I. Amdur and L. M. Shuler, *J. Chem. Phys.*, **38**, 188 (1963).
(27) R. J. J. van Heijningen, J. P. Harpe, and J. J. M. Beenakker, *Physica*, **38**, 1 (1968).
(28) B. Khouw, J. E. Morgan, and H. I. Schiff, *J. Chem. Phys.*, **50**, 66 (1969).
(29) S. Gotoh, M. Manner, J. P. Sorensen, and W. E. Stewart, *J. Chem. Eng. Data*, **19**, 172 (1974).
(30) W. A. Wakeham and D. H. Slater, *J. Phys. B.*, **6**, 886 (1973).

Binding of Counterions to the Polyacrylate Anion at Varying Charge Densities

R. J. Eldridge and F. E. Treloar*

Department of Physical Chemistry, University of Melbourne, Parkville, Victoria 3052, Australia *(Received May 7, 1973; Revised Manuscript Received December 29, 1975)*

Ultraviolet spectrophotometric measurements were used to investigate ion association in solutions containing hexaamminecobalt(III) perchlorate, supporting electrolyte, and either partially neutralized poly(acrylic acid) or acrylic acid–methyl acrylate copolymer with all the carboxylic acid groups neutralized. Several detailed models of the binding site are considered, and all but one rejected. It is concluded that the binding site is composed of adjacent carboxylate groups. When the polyion carries only short sequences of charged groups, the triply charged counterion is associated with fewer than three such groups. In contrast to Cu^{2+}, it is unable to force a redistribution of charged and uncharged groups to create binding sites.

The association of di- and trivalent cations with polyanions has been widely regarded as chelation of the cation by neighboring[1-4] or widely separated[5,6] anionic groups. However, Begala and Strauss[7] have presented evidence against the chelation of Mg^{2+} and Ba^{2+} by polyacrylate (PA). The structure of the polyion–counterion adduct is thus uncertain.

Optical studies of the binding of nonlabile complexes can help clarify the nature of the binding site. We have previously reported[8] the results of a spectrophotometric study of the association of the hexaamminecobalt(III) cation (M) with PA in the presence of added $NaClO_4$ or $LiClO_4$. The ratio of bound to unbound M varies as the first power of the carboxylate concentration, and inversely as the cube of the concentration of added salt. From these observations we concluded that M is site-bound by three carboxylate groups on a single polymer chain. We further concluded tentatively that the carboxylate groups composing a binding site are close together. This model can be tested by examining the effect of interrupting the sequence of carboxylate groups.

We now report the results of an extension of this work to samples of polyacrylic acid (PAA) in which the numbers of binding sites (carboxylate anions) have been limited either by partial neutralization or by partial esterification followed by complete neutralization of the remaining carboxylic acid groups. In the former case the "partitions" between sequences of carboxylate groups are free to move; in the latter case they are not. A comparison of the amounts of M bound by these substances should reveal the local requirements for the binding of a trivalent cation and thus provide a test of our model.

Experimental Section

The preparation of PAA ($\langle M_w \rangle$ = 710 000) and hexaamminecobalt(III) perchlorate, and the spectrophotometric technique have been described previously.[8] Absorbance measurements were made at 235.8 nm and 30.0 °C in 1-cm cells using a Hilger and Watts Uvispek fitted with a circulating water thermostat. The concentration of M was 5×10^{-4} M in all cases.

Mandel and Stadhouder[9] have partially methylated polymethacrylic acid (PMAA) using dimethyl sulfate, but in this work we prepared the analogous PAA derivative by copolymerizing acrylic acid (AA) with methyl acrylate (MA).

Copolymers containing 62.2 and 77.24 mol % acid (calculated on total monomer units) were dissolved in an equivalent quantity of aqueous NaOH for the ion-binding study. The pH of these stock solutions (C_{COO^-} = 0.1–0.2 M) was 7–8, and titration of aliquots with acidified $KMnO_4$ showed that a negligible proportion of ester groups hydrolyzed over a period of several months.

PAA solutions at different degrees of neutralization α were made by addition of aliquots of standard NaOH or LiOH solution.

Sequence Length of Carboxylate Groups in the Copolymers. These are calculated from standard copolymer theory.[10] The fraction of *all* monomer units occurring in a sequence of n successive acid units is

$$P_n^A = P_{AA}^n(1 - P_{AA}) \quad (1)$$

where

$$P_{AA} = r_A/(r_A + f_E/f_A) \quad (2)$$

$r_A = k_{AA}/k_{AE}$ the ratio of rate constants for addition of acid and ester to a growing chain ending in acid. f_E and f_A are the fractions of ester and acid in the reaction mixture. The values of r_A and r_E used are 1.44 and 1.0, respectively.[11]

The fraction of acid groups occurring in a sequence of n is

$$P_n' = P_n^A/\sum_{n=1}^{\infty} P_n^A = P_{AA}^{n-1}(1 - P_{AA}) \quad (3)$$

Another quantity of interest is the mean length of acid sequences, given by[12]

$$\bar{m}_A = 1/(1 - P_{AA}) \quad (4)$$

Results and Discussion

The spectrophotometric results for the binding equilibrium

$$M^{3+} + nCOO^- \rightleftarrows MS$$

where M^{3+} represents a free, and MS a site bound hexaamminecobalt(III) ion, are plotted in terms of the dimensionless absorbance increment

$$\Delta = [MS]\epsilon_{MS} + [M^{3+}]\epsilon_{M^{3+}} + [COO^-]\epsilon_p - C_{M^{3+}}\epsilon_{M^{3+}} - C_p\epsilon_p \quad (5)$$

where the ϵ are molar absorbances, C the stoichiometric molar concentrations, and the subscript p indicates polymer.

Figures 1–3 show the absorbance increment Δ as a function of the stoichiometric carboxylate concentration C_{COO^-} for eight series of solutions containing 5×10^{-4} M $M(ClO_4)_3$ and varying concentrations of polyelectrolyte and added perchlorate. Curves for fully neutralized PA (α = 1) are included for comparison. It can be seen that decreasing the charge

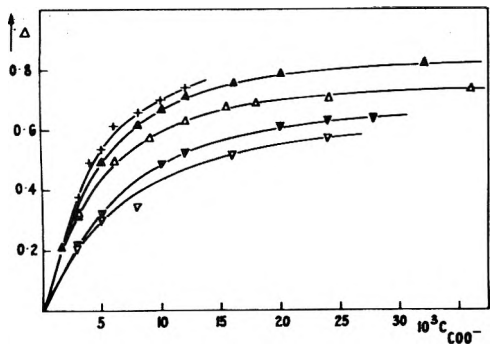

Figure 1. Absorbance increment Δ vs. stoichiometric carboxylate concentration (M) in NaPA–$NaClO_4$ solutions, $[Na^+]$ = 0.41 M: NaPA 100% (+), 75% (▲), and 50% (▽) neutralized; 23% (Δ) and 38% (▼) methylated.

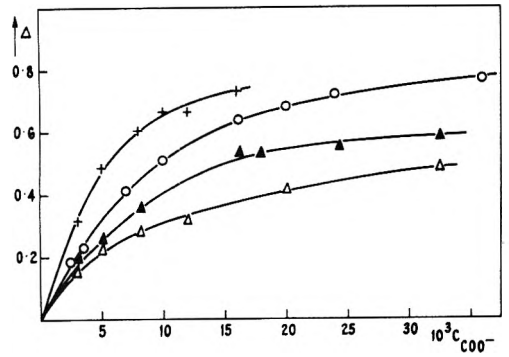

Figure 2. Absorbance increment Δ vs. stoichiometric carboxylate concentration in LiPA–$LiClO_4$ solutions: $[Li^+]$ = 0.41 M, LiPA 100% (+) and 50% (▼) neutralized; $[Li^+]$ = 0.51 M, LiPA 100% (O) and 50% (Δ) neutralized.

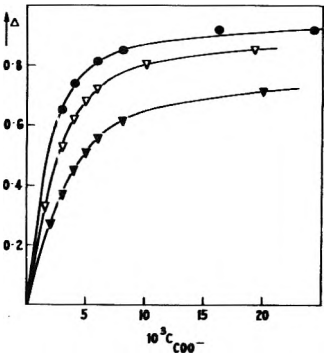

Figure 3. Absorbance increment Δ vs. stoichiometric carboxylate concentration (M) in NaPA–$NaClO_4$ solutions, $[Na^+]$ = 0.26 M: NaPA 100% neutralized (●); 23% (▽) and 38% (▼) methylated.

density on the polyion reduces the absorbance increment, but even at the lowest charge density studied (α = 0.5), Δ is sufficiently large to indicate the occurrence of site binding.

The binding ability of the sodium polysalts is greater than that of the lithium at all charge densities, showing that binding must still be regarded as a competition between trivalent and univalent counterions for binding sites as was previously seen for fully neutralized polymer.

The structure of the binding site can be elucidated by considering the following possible types of site binding to a polyion with short sequences of charged monomer units: (a) attachment of M only to three adjacent carboxylate groups; (b) the redistribution of carboxyl and carboxylate groups with the creation of binding sites consisting of three adjacent carboxylate groups; (c) the bringing of three carboxylate groups close to a trivalent cation by changes in the conformation of the polyion; or (d) binding to fewer than three carboxylate groups when triads are not available. Models (b) and (c) predict for the effective concentration C^* of binding sites $C^* = \frac{1}{3}C_{COO^-}$. Thus Δ should depend only on C_{COO^-} (and C_{NaClO_4}). However, the spectrophotometric data in Figure 1 show Δ at any C_{COO^-} to depend on the linear charge density of the polyion.

The similarity of the partly esterified and the incompletely neutralized polyacrylates is further evidence against model (b). The order of binding ability is $\alpha = 1 >$ 23% esterif > α = 0.75 > 38% esterif > α = 0.50 showing that esterification does not block binding more effectively than does incomplete neutralization. The available intrinsic viscosity molecular weight data suggest that the unperturbed dimensions of PAA and poly(methyl acrylate) are not very different.[13] Because of the high electrolyte concentration used in this work, the polyelectrolyte will not be expanded greatly above its unperturbed dimensions. Thus the free energy gain from forming electrically neutral $M(COO)_3$ units is insufficient to alter either the polyion conformation or the distribution of –COOH and $-COO^-$ groups. The binding of M to PA is therefore qualitatively different from the binding of Cu^{2+} to carboxylic polyacids. The observations of Morawetz[3] suggest that binding of Cu^{2+} to PA involves a redistribution of charged and uncharged monomer units as postulated in model (b). A further difference between M and Cu^{2+} is seen in the dependence of the extent of binding of M on ionic strength (Figure 2). Mandel and Leyte[14] have shown the association constant in the Cu(II)–PMA system to be independent of ionic strength up to 0.1 M. The difference in binding behavior between M and Cu^{2+} may presumably be attributed to the exceptionally strong covalent bonding between Cu(II) and polycarboxylic acids. Leyte et al.[15,16] have demonstrated the existence of metal-to-metal bonds in the Cu(II)–PMA adduct at low degrees of neutralization showing that Cu^{2+} ions are able to bind on adjacent sites. This would almost certainly require a forced redistribution of –COOH and $-COO^-$ groups.

For type (a) binding, the hypothetical extent of association can be calculated from the absorbance data. In ref 8, we assumed the limiting value (0.942) of Δ at high C_{COO^-} to correspond to complete binding of M. Model (a) thus predicts for the fraction f of M bound to three $-COO^-$ groups,

$$f = \Delta/0.942 \qquad (6)$$

Equation 6 assumes that the M–PA adduct has the same molar absorbance at all charge densities as it does at α = 1. The work of Mathews[17,18] provides some support for this assumption. This work showed sites for the binding of M to anionic polysaccharides to consist of three or more charged groups, not all of which were able to approach very closely to the bound cation. Mathews found the adducts of M with chitosan derivatives having both one and two sulfate groups per saccharide unit to show the same absorbance increment, equal to 0.40 at 235 nm, under his experimental conditions. Chondroitin sulfates, which have $-OSO_3^-$ and $-COO^-$ units on alternate saccharide units, also showed Δ = 0.40 at 235 nm. However, different binding behavior was observed with heparin, which has a greater number of anionic substituents per monomer unit. Several heparin samples yielded more strongly absorbing adducts than did either the chondroitin sulfates or the chitosan derivatives, and further sulfation increased still

TABLE I: Distribution of Carboxylate Groups in Copolymers

Mole fraction COO^-	Fraction of these occurring			Mean COO^- sequence length	Concn of binding sites from eq 7, C^*/C_{COO^-}
	Singly (P_1')	In pairs (P_2')	In triads (P_3')		
0.622	0.378	0.235	0.146	2.64	0.111
0.772	0.228	0.176	0.136	4.38	0.171

further the absorbance of the heparin–$[Co(NH_3)_6]$ adduct. These observations suggest that the association of M with three anionic groups results in the same increase in absorbance at several charge densities. Only when more than three anionic groups are close to a trivalent ion, as in the case of heparin, does the absorbance become even greater.

For model (a), the stoichiometric concentration C^* of binding sites in the copolymer solutions can be calculated from eq 4. If we assume that a sequence of three to five adjacent charged groups provides one binding site, a sequence of six to eight provides two, and so on, then

$$C^* = C_{COO^-}\left\{\frac{1}{3}P_3' + \frac{1}{4}P_4' + \frac{1}{5}P_5' + \frac{2}{6}P_6' + \frac{2}{7}P_7' + \frac{2}{8}P_8' + \frac{3}{9}P_9' + \ldots\right\} \quad (7)$$

This series converges rapidly for the values of P_{AA} characterizing the copolymers used in this work, and the values of C^* obtained are shown in Table I. It is apparent that most acrylate monomer units occur in short sequences, and C^*/C_{COO^-} is small.

The distribution of sequence lengths in the partly neutralized polyacids cannot be calculated in this way, but C^* must be smaller than $\frac{1}{3}C_{COO^-}$.

For the case of NaPA ($\alpha = 1$) in $NaClO_4$ solution, plots of $f/(1-f)$ against $[COO^-]$ are linear,[8] with slope given by $K/3[Na^+]$ where K is the equilibrium constant for the association of M with a triad of $-COO^-Na^+$ units.

Figure 4 shows $f/(1-f)$ plotted against the hypothetical concentration of binding sites $C^* - fC_M$, where C_M is the stoichiometric concentration of M. For the partly neutralized polyacrylates C^* was approximated by $\frac{1}{3}C_{COO^-}$. The picture is similar when the neutralizing ion is Li^+. Clearly interpreting the data according to model (a) leads to the conclusion that more binding occurs to the copolymers than to PA ($\alpha = 1$) at a given concentration of carboxylate triads (at least at low carboxylate concentrations). Thus model (a) may be rejected, leaving only model (d). The curvature of the plots in Figure 4 is further proof that the absorbance increase is not due to the formation of a single adduct, as is the fact that the gradients of the linear portions of these curves at low C_P depend on some power smaller than the third of the salt concentration.

Our conclusion that the binding is type (d) can be tested by deriving an expression for the absorbance of a system containing M associated with one, two, and three carboxylate ligands, in the presence of extraneous Na^+ ions. The model to be used is essentially that of ref 8, the only change being a generalization to enable n to vary from one to three. Using A to represent the $-COO^-$ ligands, and denoting the stepwise association constants by k, we have

$$k_1 = [MA][Na^+]/[A][M] \quad (8a)$$

$$k_1k_2 = [MA_2][Na^+]^2/[A][M] \quad (8b)$$

$$k_1k_2k_3 = K/3 = [MA_3][Na^+]^3/[A][M] \quad (8c)$$

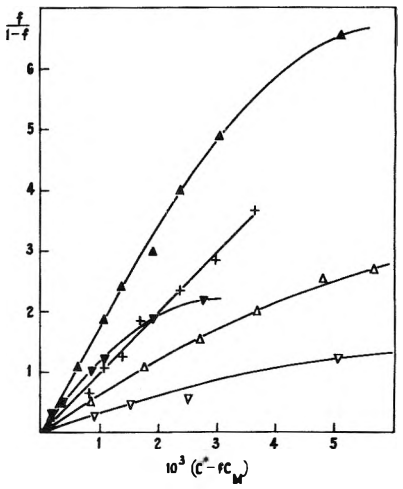

Figure 4. Test of model (a): $f/(1-f)$ vs. hypothetical concentration of binding sites, $[Na^+] = 0.41$ M; NaPA 100% (+), 75% (△) and 50% (▽) neutralized; 23% (▲) and 38% (▼) methylated.

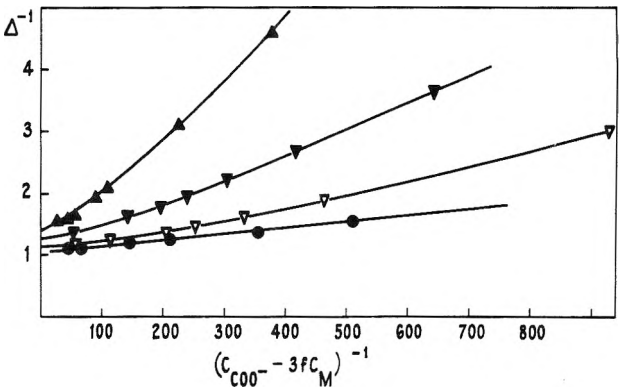

Figure 5. General model of the binding equilibrium: reciprocal of the absorbance increment vs. reciprocal of the concentration of free ligands: $[Na^+] = 0.26$ M, NaPA 100% neutralized (●); 23% (▽) and 38% (▼) methylated; $[Na^+] = 0.41$ M NaPA, ▲ 38% methylated.

It must be recognized that k_2 and k_3 (or K) incorporate "effective" carboxylate concentrations[3,14] and may therefore depend on the charge fraction $[A]/C_p$, decreasing as $[A]/C_p$ decreases. Activity coefficients are also incorporated in the association constants. This procedure should be quite satisfactory at constant ionic strength. The activity coefficient of M may vary significantly between 0.26 and 0.58 M although this is unlikely at the low concentration of M used in this work.

The absorbance increment then becomes

$$\Delta = [MA_3]\epsilon_{MA_3} + [MA_2]\epsilon_{MA_2} + [MA]\epsilon_{MA} + [M]\epsilon_M + [A]\epsilon_A - C_M\epsilon_M - C_p\epsilon_A \quad (9)$$

$$\Delta = \left(\frac{k_1k_2k_3}{[Na^+]^3}\epsilon_{MA_3} + \frac{k_1k_2}{[Na^+]^2}\epsilon_{MA_2} + \frac{k_1}{[Na^+]}\epsilon_{MA}\right)[A][M] - \epsilon_M(C_M - [M]) - \epsilon_A(C_p - [A]) \quad (10)$$

where the ϵ are molar absorbances. However

$$C_M - [M] = \left(\frac{k_1k_2k_3}{[Na^+]^3} + \frac{k_1k_2}{[Na^+]^2} + \frac{k_1}{[Na^+]}\right)[A][M] \quad (11)$$

i.e.

$$[M] = C_M/\left(1 + [A]\sum_{n=1}^{3} k_1 \ldots k_n/[Na^+]^n\right) \quad (12)$$

and

$$C_P - [A] = \left(\frac{3k_1k_2k_3}{[Na^+]^3} + \frac{2k_1k_2}{[Na^+]^2} + \frac{k_1}{[Na^+]}\right)[A][M] \quad (13)$$

therefore

$$\Delta = \frac{C_M[A]}{1 + [A]\sum_{n=1}^{3}\frac{k_1 \ldots k_n}{[Na^+]^n}} \sum_{n=1}^{3} \frac{k_1 \ldots k_n}{[Na^+]^n} \epsilon_{MA_n}$$

$$- \epsilon_A \Sigma_n{}^3{=}1 \frac{nk_1 \ldots k_n}{[Na^+]^n} - \epsilon_M \sum_{n=1}^{3} \frac{k_1 \ldots k_n}{[Na^+]^n} \quad (14)$$

$$= \frac{C_M[A]}{1 + [A]\sum_{n=1}^{3}\frac{k_1 \ldots k_n}{[Na^+]^n}} \sum_{n=1}^{3} \frac{k_1 \ldots k_n}{[Na^+]^n}$$

$$\times (\epsilon_{MA_n} - n\epsilon_A - \epsilon_M) \quad (15)$$

$$= \frac{A_{[A]}}{1 + B[A]} \quad (16)$$

$$1/\Delta = 1/A[A] + B/A \quad (17)$$

The model reduces to that of ref 8 if the first and second terms of the series in the numerator and denominator of the right-hand side of eq 16 are much smaller than the third.

A plot of Δ^{-1} against $[A]^{-1}$ would be linear under these conditions, with the gradient at any value of [A] increasing as the concentration of 1:1 electrolyte increases. In fact the second and third association constants are not negligible. They should diminish as the fraction of carboxylate groups on the polymer which are charged decreases, since the effective concentration of ligands about a $-COO^-M^{3+}$ group will be smaller. (This would not be so if charges were able to move freely along the polyion.) Thus the gradient of the Δ^{-1} vs. $[A]^{-1}$ plots would be expected to increase with decreasing charge density. $[A]^{-1}$ is not known, but Figure 5 shows Δ^{-1} plotted against $(C_{COO^-} - 3fC_M{}^{-1})$. This quantity approaches $[A]^{-1}$ at high polymer concentrations and is a better approximation to $[A]^{-1}$ than is $C_{COO^-}{}^{-1}$. The curvature of these plots shows that the effective ligand concentration is dependent on $[A]/C_P$.

The gradient A^{-1} of each curve decreases as $[A]^{-1}$ decreases, that is, as the polyion becomes less densely covered with trivalent ions. Also, the gradients of the various curves are least for the most highly charged polyions, showing that the second and third association constants indeed diminish as $[A]/C_P$ diminishes. Finally, it is seen that increasing the concentration of added salt increases the steepness of the curves, as expected.

However Figure 5 and Figures 1–3 show that at low charge densities Δ remains small even when the polyion is greatly in excess. Thus binding to fewer than three carboxylate groups persists even when sufficient triads are available to accommodate all the trivalent cations present so that binding depends on the overall charge density of the polyion.

Acknowledgments. We are indebted to Mr. J. Charlesworth, who collaborated in the development of the copolymerization procedure and prepared some of the samples. One of us (R.E.) gratefully acknowledges financial support from the Commonwealth Department of Education and Science. This work has been supported by the Australian Research Grants Committee.

References and Notes

(1) F. T. Wall and S. J. Gill, *J. Phys. Chem.*, **58**, 1128 (1954).
(2) H. P. Gregor, L. B. Luttinger, and E. M. Loebl, *J. Phys. Chem.*, **59**, 990 (1955).
(3) H. Morawetz, *J. Polym. Sci.*, **23**, 247 (1957).
(4) J. J. O'Neill, E. M. Loebl, A. Y. Kandanian, and H. Morawetz, *J. Polym. Sci. A*, 3, 4201 (1965).
(5) S. A. Rice and M. Nagasawa, "Polyelectrolyte Solutions", Academic Press, New York, N.Y., 1961, p 443.
(6) V. Crescenzi, F. Quadrifoglio, and B. Pispisa, *J. Chem. Soc. A*, 2175 (1968).
(7) A. J. Begala and U. P. Strauss, *J. Phys. Chem.*, **76**, 254 (1972).
(8) R. J. Eldridge and F. E. Treloar, *J. Phys, Chem.*, **74**, 1446 (1970).
(9) M. Mandel and M. G. Stadhouder, *Makromol. Chem.*, **80**, 141 (1964).
(10) G. E. Ham, "Copolymerization", High Polymers Series, Vol. XVIII, Interscience, New York, N.Y., 1964, Chapter 1.
(11) R. J. Eldridge and F. E. Treloar, *J. Polym. Sci., Polym. Chem. Ed.*, in press.
(12) G. Goldfinger and T. Kane, *J. Polym. Sci.*, **3**, 462 (1948).
(13) J. Brandrup and E. H. Immergut, Ed., "Polymer Handbook", Interscience, New York, N.Y., 1966, pp IV21–22.
(14) M. Mandel and J. C. Leyte, *J. Polym. Sci.*, **56**, S23 (1962); *J. Polym. Sci. A*, **2**, 2883, 3771 (1964).
(15) J. C. Leyte, *Kolloid-Z.*, **212**, 168 (1966).
(16) J. C. Leyte, L. H. Zuiderweg, and M. van Reisen, *J. Phys. Chem.*, **72**, 1127 (1968).
(17) M. B. Mathews, *Biochim. Biophys. Acta*, **37**, 288 (1960).
(18) M. B. Mathews, *Arch. Biochem. Biophys.*, **104**, 394 (1964). (In ref 8 we pointed out that eq 6 of ref 17 is incorrect. The correct form of this equation was given by Mathews in ref 18.)

COMMUNICATIONS TO THE EDITOR

Vibrational Assignment and Force Constants of the Tetrasulfide Ion, $S_4{}^{2-}$

Sir: Recently Daly and Brown[1] investigated the Raman spectra of solid Na_2S_4 and its aqueous solution. They observed six frequencies and assigned these to the six fundamentals of $S_4{}^{2-}$ assuming the molecular symmetry C_2. They also made a normal-coordinate treatment using a valence force field with six force constants ($2f_r, f_{rr'}, f_\alpha, f_{r\alpha}$, and f_τ) and assuming reasonable values for the geometrical parameters. However, these parameters do not agree with the values found by x-ray crystal structure analysis of Na_2S_4,[2] and some of the force constants

have unlikely values. For example, the two stretching force constants, f_r = 1.6 and 1.9 mdyn/Å for the central and terminal bonds, respectively, are too different from each other and too low compared with the values 2.3–2.4 mdyn/Å obtained for S_6,[3] S_8,[4] and S_{12}[5] which contain bonds of very similar distances, d. From the linear relationship

$$\log f_r = 2.66 - 7.26 \log d$$

which has been derived from 14 experimental values,[6] one expects f_r = 2.32 mdyn/Å for S_4^{2-}. Furthermore, the interaction constant for the two terminal bonds, f_{rr}' = −0.31 mdyn/Å, calculated by Daly and Brown,[1] contrasts with the very small values (−0.005 to +0.049) found for S_6,[3] S_8,[4] S_8O,[7] and S_{12}.[5] The interaction between neighboring bonds which is very strong in sulfur rings and chains (f_{rr} = 0.3–0.6 mdyn/Å[3-7]) was neglected by Daly and Brown. To find the reasons for these discrepancies we made a new normal-coordinate treatment.

The calculations were made using a modified Urey–Bradley force field (MUBFF) of the same type as has been applied successfully to S_6,[3] S_8,[4] and S_{12}:[5]

$$2V = \Sigma K(\Delta r)^2 + 2\Sigma K' r\Delta r + \Sigma H(r\Delta\alpha)^2 + 2\Sigma H' r^2\Delta\alpha + \Sigma F(\Delta q)^2 + 2\Sigma F' q\Delta q + Y(r\Delta\tau)^2 + 2Y' r^2\Delta\tau + 2\Sigma P\Delta r\Delta r' + C(\Delta q')^2 + 2C' q'\Delta q'$$

with the force constants K (bond stretching), H (valence angle bending), F (next nearest neighbor repulsion), Y (torsion), P (bond–bond interaction), and C (repulsion between atoms separated by two other atoms). The force constants K', H', and Y' are eliminated in the removal of the redundant coordinates, q and q', and F' and C' were constrained by the conventional assumptions $F' = -0.1F$ and $C' = -0.1C$. The geometrical parameters r, α, τ, q, and q' are given in Table I, the symmetry coordinates are listed in Table II.

For the first calculations[9] we used the force constants of S_8 since S_4^{2-} and S_8 have very similar r, α, and τ values (see Table I). These force constants are K = 1.849, H = 0.038, F = 0.329, Y = 0.025, P = 0.301, and C = 0.077 mdyn/Å.[4] The S_4^{2-} frequencies obtained with these force constants are shown in column 4 of Table II. In column 5 the six frequencies of the S_4 unit of H_2S_4 are listed which has been studied by ir and Raman spectroscopy.[10] The comparison between the two sets of frequencies shows good agreement supporting the calculated values.

The Raman lines observed by Daly and Brown[1] for solid Na_2S_4 and its solution in water are listed in Table III together with the lines observed by Ward[11] for a solution of S_8 in aqueous Na_2S which had the approximate composition Na_2S_6 but which he believed to contain mainly S_4^{2-}.

From Table III one can see that the spectra of solid and aqueous Na_2S_4 are considerably different. There are not only frequency differences of up to 33 cm^{-1} but also substantial changes of some intensities. Since it is well known[12,13] that in aqueous polysulfide solutions equilibria of type

$$S_nS^{2-} + S_mS^{2-} + H_2O \rightleftharpoons S_{n+m}S^{2-} + HS^- + OH^-$$

exist we feel that proof has still to be given that the solution spectra obtained by Ward[11] and Daly and Brown[1] are in all details (frequencies, intensities, polarization behavior) those of S_4^{2-}. Especially the line at about 420 cm^{-1} whose intensity increases very much on dissolution of Na_2S_4 in water and which becomes as intense as the 448-cm^{-1} line in dilute solution[1] must belong to some other species S_n^{2-} ($n > 4$, probably 5) which is formed when the pH of the alkaline solution decreases[13] because of dilution.[14] Unfortunately, no vibrational spectra of higher polysulfide anions have been reported so far but from the spectra of sulfur rings the stretching vibrations can be expected in the region 400–490 cm^{-1}.[15] Using the same force field as for S_4^{2-} and taking the force constants from S_8 we calculated the frequencies of all fundamental modes of S_5^{2-}, S_6^{2-}, S_7^{2-}, and S_8^{2-} for many different conformations assuming the following geometrical parameters: d = 2.06 Å, α = 108°, and τ = 68 or 98°.[16] The stretching frequencies turned out to be almost independent of the conformation and were found in the region 417–477 cm^{-1}. The number of observable frequencies is expected to be lower than the number of bonds because of an increasing number of incidental degeneracies. In all cases, however, one mode near 420 cm^{-1} is to be expected supporting our assignment of the corresponding Raman line in the spectra of Na_2S_4 to S_n^{2-} ($n > 4$). Obviously, small amounts of S_n^{2-} ($n > 4$) were also present in solid Na_2S_4 prepared by Daly and Brown causing the weak Raman line at 424 cm^{-1}. The remaining solid state frequencies can be assigned to the S_4^{2-} ion as shown in the last

TABLE I: Geometrical Parameters of the S_4^{2-} Ion in Solid Na_2S_4[2] and of S_8[8] [a]

	S_4^{2-}	S_8
Central bond, r_2, Å	2.061	2.060
Terminal bonds, r_1, r_3, Å	2.074	
Valence angle, α, deg	109.76	108.0
Dihedral angle, τ, deg	97.81	98.8
Nonbonded distance, q, Å	3.38	3.33
Nonbonded distance, q', Å	4.54	4.5

[a] The molecular symmetries are C_2 and D_{4d}, respectively, and q and q' are the distances between atoms separated by one and two atoms, respectively.

TABLE II: Symmetry Coordinates and Frequencies of S_4^{2-} [a]

Symmetry species		Symmetry coordinate	Frequencies, cm^{-1} Na_2S_4 calcd	H_2S_4 (in CS_2)	Na_2S_4 obsd
A	ν_1	Δr_2	462	484	481
	ν_2	$(1/\sqrt{2})(\Delta r_1 + \Delta r_3)$	429	450	448
	ν_3	$(1/\sqrt{2})(\Delta\alpha_1 + \Delta\alpha_2)$	179	184	209
	ν_4	$\Delta\tau$	96	77	123
B	ν_5	$(1/\sqrt{2})(\Delta r_1 - \Delta r_3)$	458	487	481
	ν_6	$(1/\sqrt{2})(\Delta\alpha_1 - \Delta\alpha_2)$	194	225	278

[a] The calculated values were obtained using the S_8 force constants,[4] the observed frequencies are from solid Na_2S_4.[1] For comparison the corresponding H_2S_4 frequencies[10] are given.

TABLE III: Raman Lines and Intensities Observed for Solid Na_2S_4 and Polysulfide Solutions[1,11] (Frequencies in cm^{-1})

Na_2S_4, solid: 481s, 448vs, 424w, 278m, 209m, 123w
Na_2S_4 in H_2O: 497m, 448vs, 414s, 245m, 191vw, 115vw
"Na_2S_6" in H_2O: 493m, 454s, 419m, 251m 193w

column of Table II assuming an incidental degeneracy of ν_1 and ν_5 as has been observed for H_2S_4 also.[10] This assignment is further supported by the observation that ν_1 and ν_5 are less intense than ν_2 in the Raman spectrum of S_2Cl_2, too, which belongs to the same point group.[18]

Since there are not enough frequencies to determine six force constants and since we have some doubts whether the 278-cm^{-1} Raman line is a fundamental of S_4^{2-} we adjusted the stretching frequencies only by varying only the force constants K and P. The large gap of 170 cm^{-1} between stretching and bending modes justifies this approximation. After the force constant corrections became zero a maximum difference of 2 cm^{-1} between calculated[19] and observed stretching frequencies was obtained with K = 2.036 and P = 0.340 mdyn/Å. From the F matrix, whose elements are simple linear combinations of the valence force constants, f_r = 2.32 and 2.37 for the central and terminal bonds, respectively, were calculated. The interaction constant f_{rr} amounted to 0.61 mdyn/Å. All three values are in excellent agreement with the force constants calculated for sulfur rings.[15]

To prove our results we also tried to adjust the calculated and observed frequencies using the assignment given by Daly and Brown[1,20] (a = 448, 414, 191, 115; b = 497, 245 cm^{-1}) but after the force constant corrections became zero large differences of up to 31 cm^{-1} remained for all stretching frequencies. The same happened with the assignment a = 497, 448, 191, 115; b = 414, 245 cm^{-1}.

The results of Ward,[11] Daly and Brown,[1] and of this work show that further investigations of the Raman and infrared spectra of tetrasulfides are necessary to establish all fundamental modes and force constants of the S_4^{2-} ion. Until this work has been done attempts to detect S_4^{2-} or other polysulfides in the complex solutions of S_8 in aqueous Na_2S[1,11] or in amines[1] by means of Raman spectroscopy should be done with caution.

References and Notes

(1) F. P. Daly and Ch. W. Brown, *J. Phys. Chem.*, 79, 350 (1975).
(2) R. Tegman, *Acta Crystallogr., Sect. B*, **29**, 1463 (1973).
(3) L. A. Nimon and V. D. Neff, *J. Mol. Spectrosc.*, **26**, 175 (1968).
(4) D. W. Scott, J. P. McCullough, and F. H. Kruse, *J. Mol. Spectrosc.*, **13**, 313 (1964).
(5) R. Steudel and D. F. Eggers, *Spectrochim. Acta, Part A*, **31**, 879 (1975).
(6) R. Steudel, *Z. Naturforsch. B*, **30**, 281 (1975).
(7) R. Steudel and D. F. Eggers, *Spectrochim. Acta, Part A*, **31**, 871 (1975).
(8) A. Caron and J. Donohue, *Acta Crystallogr.*, **18**, 562 (1965).
(9) The calculations were made on a CD 6300 computer using the programs BGLZ and LSMA by Shimanouti (Tokyo 1968) and UBZM by Schachtschneider (Emeryville, Calif., 1964).
(10) H. Wieser, P. J. Krueger, E. Muller, and J. B. Hyne, *Can. J. Chem.*, **47**, 1633 (1969).
(11) A. T. Ward, *Mat. Res. Bull.*, **4**, 581 (1969).
(12) A. Teder, *Acta Chem. Scand.*, **25**, 1722 (1971).
(13) W. Giggenbach, *Inorg. Chem.*, **11**, 1201 (1972).
(14) Daly and Brown reached the same conclusion but nevertheless they assigned this frequency to S_4^{2-}, also.
(15) R. Steudel, *Spectrochim. Acta, Part A*, **31**, 1065 (1975).
(16) See the x-ray structure of $(NH_4)_2S_5$ (d_{SS} = 2.06 Å, α = 107.5°, τ = 67.5° [17]).
(17) N. K. Goh, Dissertation, Universität Münster, Germany, 1974.
(18) S. G. Frankiss and D. J. Harrison, *Spectrochim. Acta, Part A*, **31**, 161 (1975).
(19) The calculated values are a = 482, 449, 179, 96; b = 479, 194 cm^{-1}.
(20) These authors obtained a good agreement between calculated and observed frequencies since they used *three* independent variable force constants for the stretching modes ($2f_r$ and f_{rr}'). However, they assigned the highest a-type frequency to the symmetry coordinate $S = \Delta r_1 + \Delta r_3$ whereas our calculations show clearly that the potential energy of the highest symmetric stretching vibration arises mainly from the coordinate $S = \Delta r_2$ which is in agreement with the vibrational analyses of S_2Cl_2[21] and H_2S_4.[10] Ward[11] also calculated force constants for S_4^{2-} neglecting the constant f_{rr} and using f_{rr}' instead (interaction between bonds r_1 and r_3).
(21) R. Forneris and C. E. Hennies, *J. Mol. Struct.*, **5**, 449 (1970).

Institut für Anorganische und Analytische Chemie
Technische Universität Berlin
D-1 Berlin-12
Federal Republic of Germany

Ralf Steudel

Received May 7, 1975; Revised Manuscript Received December 1, 1975

Comment on "Vibrational Assignment and Force Constants of the Tetrasulfide Ion, S_4^{2-}" by R. Steudel

Publication costs assisted by the University of Rhode Island

Sir: In the above communication Steudel suggests that the band at 424 cm^{-1}, which we observe in the Raman spectrum of solid Na_2S_4, is due to an impurity. The solid was prepared by the method reported by Eibeck,[2] who clearly showed by x-ray diffraction that pure S_4^{2-} was obtained by the procedure. We are aware that in aqueous and amine solutions a band due to another sulfur species appears at 400 cm^{-1}, and recently we have shown that this band is due to S_8^{n-}.[3] However, the depolarization ratio for the band at 400 cm^{-1} in the spectrum of S_8^{n-} is 0.37, whereas it is 0.619 for the band at 419 cm^{-1} in the spectrum of an aqueous solution of S_4^{2-}.[4] This suggests that the two bands are due to two different species, and supports assignment of the band at 420 cm^{-1} to S_4^{2-}.

References and Notes

(1) F. P. Daly and C. W. Brown, *J. Phys. Chem.*, **79**, 350 (1975).
(2) R. E. Eibeck, University Microfilms, L.C. Card No. Mic 61-1608; *Diss. Abst.*, **21**, 3254-5 (1961).
(3) F. P. Daly and C. W. Brown, *J. Phys. Chem.*, **80**, 480 (1976).
(4) A. T. Ward, *Mat. Res. Bull.*, **4**, 581 (1969).

Department of Chemistry
University of Rhode Island
Kingston, Rhode Island 02881

Francis P. Daly
Chris W. Brown*

Received June 18, 1975; Revised Manuscript Received December 11, 1975

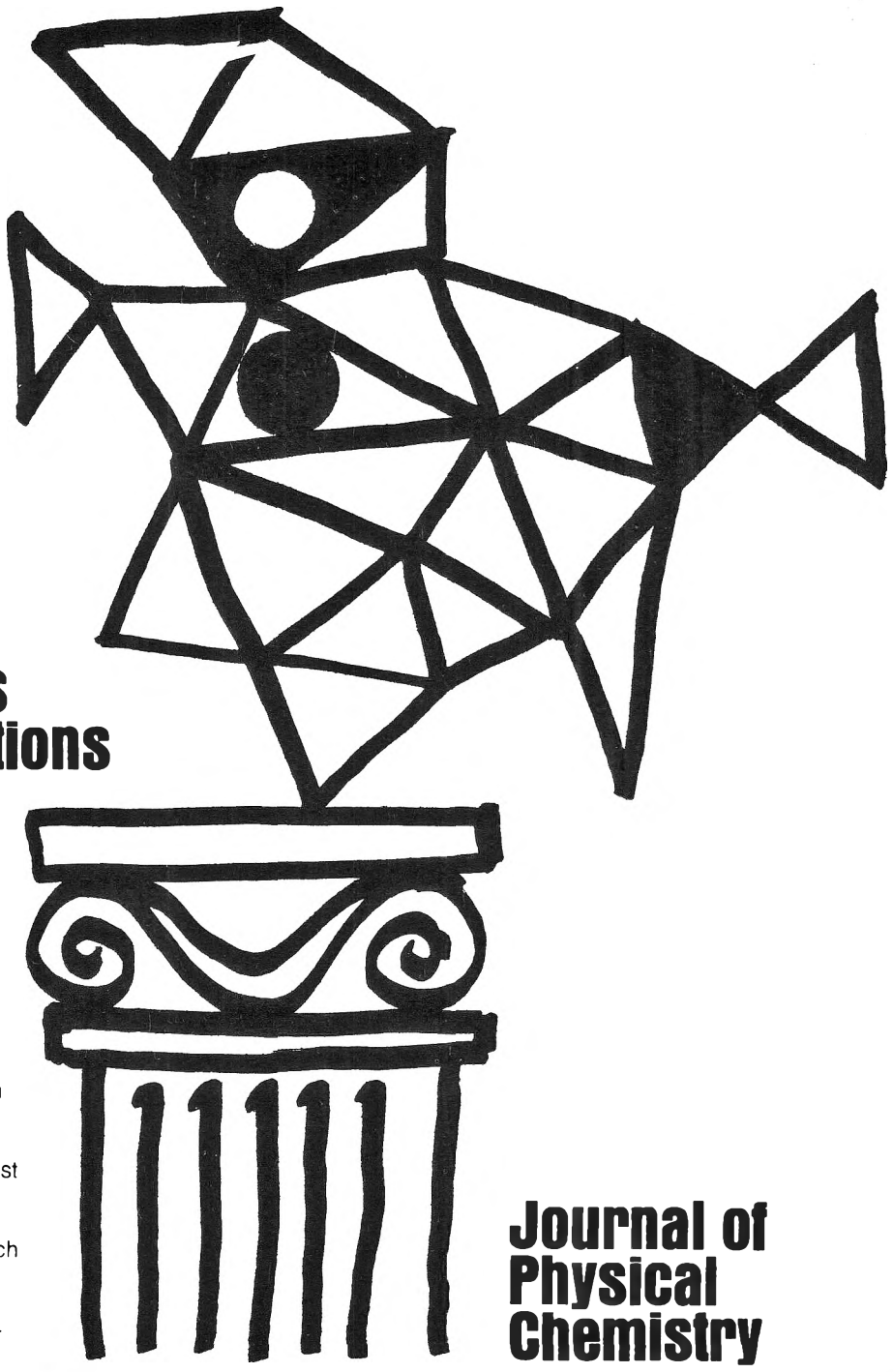

New concepts new techniques new interpretations

. . . together with valuable reports on classical areas

They are all waiting for you between the covers of our well-balanced JOURNAL OF PHYSICAL CHEMISTRY. Whatever your particular interest in physical chemistry, you'll find the JOURNAL's broad range of experimental and theoretical research reports are relevant and beneficial to your work. Each biweekly issue brings you an average of 30 authoritative, comprehensive reports on fundamental aspects of atomic and molecular phenomena, as well as timely notes, communications and reports plus the proceedings of selected symposia.

Join your fellow physical chemists who rely on JPC as an excellent biweekly source of data in both new and classical areas. Just complete and return the form to start your own subscription.

. . . *another ACS service*

Journal of Physical Chemistry

The Journal of Physical Chemistry
American Chemical Society **1976**
1155 Sixteenth Street, N.W.
Washington, D.C. 20036

Yes, I would like to receive the JOURNAL OF PHYSICAL CHEMISTRY at the one-year rate checked below:

	U.S.	*Canada***	*Latin America***	*Other Nations***
ACS Member One-Year Rate*	☐ $24.00	☐ $30.25	☐ $29.75	☐ $30.25
Nonmember	☐ $96.00	☐ $102.25	☐ $101.75	☐ $102.25

Bill me ☐ Bill company ☐ Payment enclosed ☐

Air freight rates available on request.

Name _____

Street _____ Home ☐ Business ☐

City _____ State _____ Zip _____

Journal subscriptions start January '76

*NOTE: Subscriptions at ACS member rates are for personal use only. **Payment must be made in U.S. currency, by international money order, UNESCO coupons, U.S. bank draft, or order through your book dealer.

RADIONUCLIDES IN THE ENVIRONMENT

ADVANCES IN CHEMISTRY SERIES NO. 93

Twenty-eight papers from a symposium sponsored by the Division of Nuclear Chemistry and Technology, chaired by E. C. Freiling.

Pollution . . . a growing concern . . . a concept not generally associated with radionuclides. The successful control of this hazardous waste product of nuclear energy is essential to the continued use and development of nuclear power. Critical to this problem is an understanding of the processes by which radionuclides are produced, dispersed, and retained in the environment.

The papers in this volume discuss and evaluate the properties and problems relating to radionuclides, including

- mechanisms of release, absorption, uptake, transport
- behavior, measurement and characterization, specific weapons tests
- specific activity, public health aspects, fallout
- new methods and equipment

522 pages with index Clothbound (1968) $15.00
Set of L.C. cards with library orders upon request.

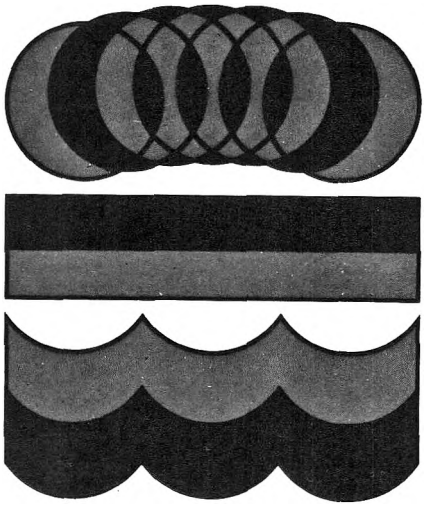

Other books in the ADVANCES IN CHEMISTRY SERIES OF related interest include:

No. 89 Isotope Effects in Chemical Processes. Methods of separating isotopes and labeled molecules—chemical exchange, electromigration, photochemical processes, and distillation—are examined, along with factors that suit a process to isotope separation—single stage fractionation, exchange rate, and reflux.
278 pages cloth (1969) $13.00

No. 82 Radiation Chemistry—II. Thirty-six papers and 17 abstracts on radiation chemistry in gases, solids, and organic liquids. Includes three plenary lectures. 558 pages cloth (1968) $16.00

No. 81 Radiation Chemistry—I. Forty-one papers and 17 abstracts on radiation chemistry in aqueous media, biology, and dosimetry. From the international conference at Argonne National Laboratory. 616 pages cloth (1968) $16.00. No. 81 and 82 ordered together $30.00

No. 72 Mass Spectrometry in Inorganic Chemistry. A basic tool for chemical manipulations, the mass spectrometer is a conventional monitor for any stage in a research problem to help establish what is going on. 21 Research reports. 329 pages cloth (1968) $12.00

No. 68 The Mössbauer Effect and Its Application in Chemistry. Ten papers that will familiarize chemists with Mössbauer spectroscopy as an analytical tool for studying chemical bonding, crystal structure, electron density, magnetism, and other properties.
178 pages cloth (1967) $8.00

No. 66 Irradiation of Polymers. Eighteen papers survey radiation mechanics in polymers, the chemical nature of reactive species produced, crosslinking and scission, homopolymerization, graft copolymerization, and the effects of ultraviolet light radiation.
275 pages cloth (1967) $10.00

No. 58 Ion–Molecule Reactions in the Gas Phase. Eighteen papers survey spectrometric and other methods for producing and studying ion–molecule reactions such as pulsed sources for studying thermal ions, reactions in flames and electrical discharges.
336 pages cloth (1966) $10.50

No. 50 Solvated Electron. Reviews of theory, structure, reactions of solvated and hydrated electrons; detailed papers on electrical transport properties, photochemistry, theory of electron transfer reactions, structure of solvated electrons, hydrated electron research. 304 pages cloth (1965) $10.50

Postpaid in U. S. and Canada; plus 30 cents elsewhere.
Order from:

SPECIAL ISSUES SALES
AMERICAN CHEMICAL SOCIETY
1155 SIXTEENTH ST., N.W.
WASHINGTON, D. C. 20036